UNIVERSITY OF SOUTHAMPTON

FACULTY OF NATURAL AND ENVIROMENTAL SCIENCES

School of Ocean and Earth Sciences

Investigating drivers of phytoplankton blooms in the North Atlantic Ocean using high-resolution in situ glider data

by

Anna Sergeevna Rumyantseva

Thesis for the degree of Doctor of Philosophy

October 2016

UNIVERSITY OF SOUTHAMPTON

ABSTRACT

FACULTY OF NATURAL AND ENVIRONMENTAL SCIENCES

Ocean and Earth Sciences

Thesis for the degree of Doctor of Philosophy

INVESTIGATING DRIVERS OF PHYTOPLANKTON BLOOMS IN THE NORTH ATLANTIC OCEAN USING HIGH-RESOLUTION IN SITU GLIDER DATA

Anna Sergeevna Rumyantseva

Autonomous buoyancy-driven underwater gliders represent a powerful tool for studying marine phytoplankton dynamics due to their ability to obtain frequent depth-resolved profiles of bio-optical and physical properties over inter-seasonal time scales, even under challenging weather conditions and low light. This thesis is based on a unique year-long deployment of pairs of gliders at the Porcupine Abyssal Plain Sustained Observatory located in the Northeast Atlantic Ocean, complemented by remotely sensed chlorophyll and photosynthetically active radiation (Aqua MODIS products), surface net heat (NCEP/NOAA reanalysis), surface wind stress (ASCAT products) and in situ measurements of nutrients, chlorophyll, microscale turbulence and meteorological parameters. The data were used to study drivers of autumn and spring phytoplankton blooms.

In the beginning of the deployment, the gliders captured the upper ocean dynamics during an autumnal storm. The onset of an autumn phytoplankton bloom due to nutrient intrusion was detected. Additional data collected during a simultaneous sampling campaign allowed quantification of the nutrient supply by two physical mechanisms associated with a storm event: entrainment of nutrients during a period of high wind forcing and subsequent shear-spiking at the pycnocline due to interactions of storm generated inertial currents with wind. The importance of the two mechanisms is discussed, and I conclude that storms play an important role in fuelling ocean primary production during periods of nutrient depletion.

The glider data from winter and spring captured the onset and development of the phytoplankton spring bloom. Mechanisms controlling the bloom onset were studied in light of the main competing hypotheses: the critical depth, the critical turbulence, and the dilution-recoupling hypotheses. The bloom onset was consistent with the critical depth hypothesis, if the decoupling

between the actively mixing layer and the mixed layer is considered. However, the observed bloom developed slowly and was relatively low in magnitude. The frequent passage of storms and periods of convective mixing can significantly decrease mean growth rate for phytoplankton populations affecting the rate of bloom development.

Finally, the impact of biotic factors, such as zooplankton grazing, on spring bloom dynamics is discussed. In order to address potential zooplankton variability that underlies the observations, the glider data was coupled with a simple phytoplankton-zooplankton model. The model was forced with the phytoplankton growth rate evaluated based on the observational data. It is shown that gradual phytoplankton growth in winter results in tight coupling between phytoplankton and zooplankton that can hamper the formation of high-magnitude spring blooms in the North Atlantic Ocean.

Table of Contents

List of Tables

List of Figures

DECLARATION OF AUTHORSHIP

I, ANNA SERGEEVNA RUMYANTSEVA declare that this thesis entitled

INVESTIGATING DRIVERS OF PHYTOPLANKTON BLOOMS IN THE NORTH ATLANTIC OCEAN USING HIGH-RESOLUTION IN SITU GLIDER DATA

and the work presented in it are my own and has been generated by me as the result of my own original research.

I confirm that:

1. This work was done wholly or mainly while in candidature for a research degree at this University;
2. Where any part of this thesis has previously been submitted for a degree or any other qualification at this University or any other institution, this has been clearly stated;
3. Where I have consulted the published work of others, this is always clearly attributed;
4. Where I have quoted from the work of others, the source is always given. With the exception of such quotations, this thesis is entirely my own work;
5. I have acknowledged all main sources of help;
6. Where the thesis is based on work done by myself jointly with others, I have made clear exactly what was done by others and what I have contributed myself;
7. Parts of this work have been published as:
   Rumyantseva, A., Lucas, N., Rippeth, T., Martin, A., Painter, S. C., Boyd, T. J., & Henson, S. (2015). Ocean nutrient pathways associated with the passage of a storm. *Global Biogeochemical Cycles*, **29**(8), 1179-1189.
   - Attached as Appendix A

Signed: .....

Date: .....

Acknowledgements

First of all, I would like to express my gratitude to my scientific advisers, Stephanie and Adrian. Their expertise, understanding, support, motivation and a good sense of humour made my PhD enjoyable and rewarding. I cannot wish for better mentors! I would also like to thank Eleanor Frajka-Williams for being my panel chair and providing helpful comments on our advisory panel meetings.

I am grateful to Karen Heywood, Jan Kaiser and Gillian Damerell from the University of East Anglia. It was a great pleasure for me to visit Norwich during my PhD and learn about glider technologies from the true glider experts. Also I would like to thank Natasha Lucas, Tom Rippeth and Stuart Painter who were co-authors of my first scientific publication. It was a big pleasure to work with you. Additionally, I would like to acknowledge John Taylor and Andrew Thompson for helpful discussions and suggestions throughout my project. I am also grateful to Richard Lampitt for his support and his tips on giving talks at scientific conferences.

I would like to thank all the people involved in the OSMOSIS project, the staff of Ocean Biogeochemistry & Ecosystems Group, the crew of RRS “James Cook” and fellow PhD students in the National Oceanography Centre, Southampton.

I would like to express my sincere gratitude to Trevor Platt and Shubha Sathyendranath who inspired me to pursue a PhD in Ocean and Earth Science.

Last but not the least, I would like to thank my friends and family for their invaluable support, encouragement and understanding. It would not be possible without you!

This thesis is dedicated to the memory of my grandmother Anna.

List of Abbreviations

ADCP	Acoustic Doppler Current Profiler
ASCAT	Advanced Scatterometer (ASCAT) Surface Wind Fields
CDH	Critical Depth Hypothesis
Chl *a*	Chlorophyll *a*
COARE	Coupled Ocean Atmosphere Research Experiment
CT	Conductivity, Temperature
CTD	Conductivity, Temperature, Depth
CTH	Critical Turbulence Hypothesis
DC	Dark Counts
DRH	Dilution Recoupling Hypothesis
ECOpuck	Environmental Characterization Optics puck
HNLC	High Nutrient Low Chlorophyll
JGOFS NABE	Joint Global Ocean Flux Study – North Atlantic Bloom Experiment
LES	Large Eddy Simulation
LNHC	Low Nutrient High Chlorophyll
MLD	Mixed Layer Depth
MODIS	Moderate Resolution Imaging Spectroradiometer
NABE08	North Atlantic Bloom Experiment 2008
NCEP	National Centres for Environmental Prediction
NERC	Natural Environment Research Council
NO_3	Nitrate
NOAA	National Oceanic and Atmospheric Administration
OSMOSIS	Ocean Surface Mixing, Ocean Submesoscale Interaction Study
PABIM	Platforms for Biogeochemical studies: Instrumentation and Measure

PAP	Porcupine Abyssal Plain
PAR	Photosynthetically Active Radiation
QC	Quality Control
R^2	Coefficient of Determination
SCM	Subsurface Chlorophyll Maxima
TOGA	Tropical Ocean Global Atmosphere program

List of Symbols

b	Phytoplankton mortality rate
B_0	Surface buoyancy flux
c_1	Maximum zooplankton growth rate
c_2	Grazing half-saturation
c_3	Ingestion efficiency
c_4	Zooplankton non-predation mortality
c_5	Zooplankton quadratic mortality
c_d	Drag coefficient
c_p	Seawater heat capacity
C_x	Dimensionless constants
D	Eddy diffusivity
E	Light intensity
E_0	Surface light intensity
f	Coriolis parameter
F_{NO3}	Nitrate flux
g	Acceleration due to gravity
I(Chl a)	Integrated Chlorophyll a
K	Light attenuation coefficient
k_{vK}	von Karman constant
l	Phytoplankton loss rate
N	Buoyancy frequency
P	Phytoplankton concentration
Q	Net surface heat flux
Q_l	Latent heat flux

Q_{lw}	Net longwave radiation
Q_s	Sensible heat flux
Q_{sw}	Net shortwave radiation
r	Phytoplankton net accumulation rate
$\vec{s}$	Bulk shear
S	Salinity
S(Chl a)	Surface Chlorophyll a concentration
T	Temperature
t	Time
u_*	Friction velocity
$\vec{U}$	Horizontal velocity of the flow
z	Depth
Z	Zooplankton concentration
z_{cr}	Critical depth
z_{eu}	Euphotic depth
z_{mixed}	Mixed layer depth
z_{mixing}	Mixing layer depth
z_{MO}	Monin-Obukhov length scale
α^{chl}	Chlorophyll-specific slope of phytoplankton-irradiance curve
ε	Energy dissipation rate
ϑ	Cellular chlorophyll-to-carbon mass ratio
λ	Coefficient of thermal expansion for seawater
μ	Phytoplankton specific growth rate
ρ	Seawater density
τ	Wind stress

Chapter 1: Introduction

This thesis aims to study mechanisms underlying phytoplankton seasonal blooms using data from autonomous buoyancy-driven gliders complemented by satellite data, atmospheric forcing reanalysis and in situ measurements. A unique year-long glider data set introduced in this project was collected in the temperate Northeast Atlantic Ocean. The temperate and subpolar North Atlantic Ocean is a region where phytoplankton seasonality has been studied for decades but still many aspects remain uncertain. This introduction emphasizes the importance of marine phytoplankton in the global carbon cycle and marine food webs, provides an overview of the current state of knowledge on the topic of phytoplankton blooms and shows how measurements from gliders can deepen understanding of factors controlling phytoplankton variability and manifestation of blooms.

1.1 Importance of marine phytoplankton

The surface layer of the global ocean is inhabited by free-floating, single-celled organisms called phytoplankton. In the same way as terrestrial plants, phytoplankton are responsible for production of organic compounds from carbon dioxide (primary production) through the process of photosynthesis. Rates of ocean primary production vary geographically and tend to be higher in temperate, sub-polar and polar regions (Figure 1.1). The satellite-based estimates of ocean primary production suggest that marine phytoplankton fix approximately 50 Pg of carbon per year that is roughly equivalent to carbon uptake by terrestrial plants (Field 1998). Since the start of the Industrial Revolution the global ocean has removed up to 30% of the anthropogenic CO_2 from the atmosphere (Siegenthaler & Sarmiento 1993; Raven & Falkowski 1999). As further increases of carbon dioxide emission are expected, understanding the processes controlling atmospheric carbon sequestration is highly important.

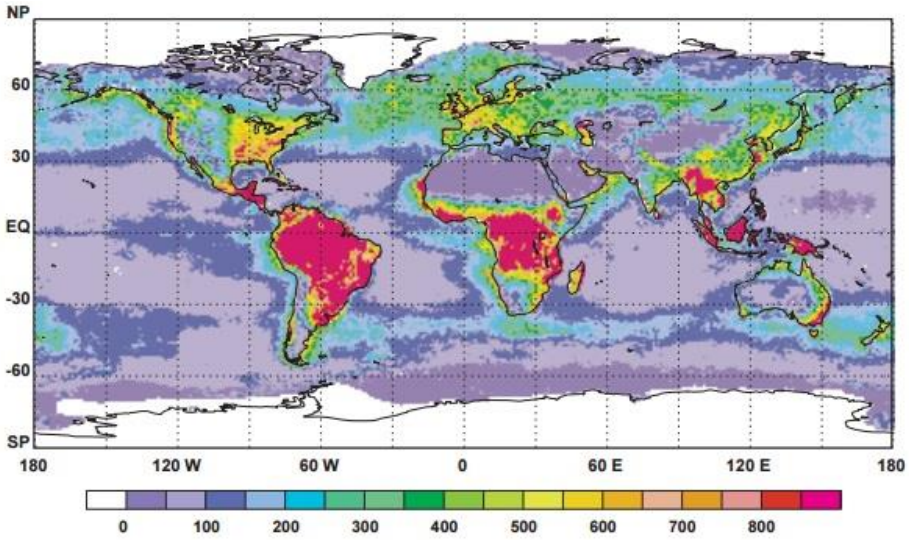

Figure 1.1 Global annual net primary production (in grams of carbon per m^{-2}). From Field et al. (1998).

Carbon uptake by the ocean is driven by the *solubility pump* and the *biological pump* (Volk & Hoffert 1985). The solubility pump is a mechanism of carbon sequestration through deep water formation in high latitudes. Cooling of surface waters increases the solubility of CO_2. Eventually, cold waters with high concentrations of dissolved inorganic carbon sink and sequestrate carbon away from the atmosphere. The biological pump is a process through which a fraction of the carbon fixed by phytoplankton is transferred to the ocean interior via biological activity. The main processes involved in the biological carbon pump are sketched in Figure 1.2. Dead phytoplankton sink contributing to the particle flux out of the ocean surface layer. In addition, phytoplankton are grazed by zooplankton that generate waste forming another pathway for carbon to the deep ocean. If not remineralized, sinking particles accumulate on the ocean floor and stay out of contact with the atmosphere over centuries. The downward particle flux from the euphotic zone is also the vital food source for benthic organisms (Hawkins & Hartnoll 1982; Smetacek 1984). Small changes in primary production can significantly affect the strength of the biological pump and therefore concentrations of CO_2 in the atmosphere and benthic ecosystems.

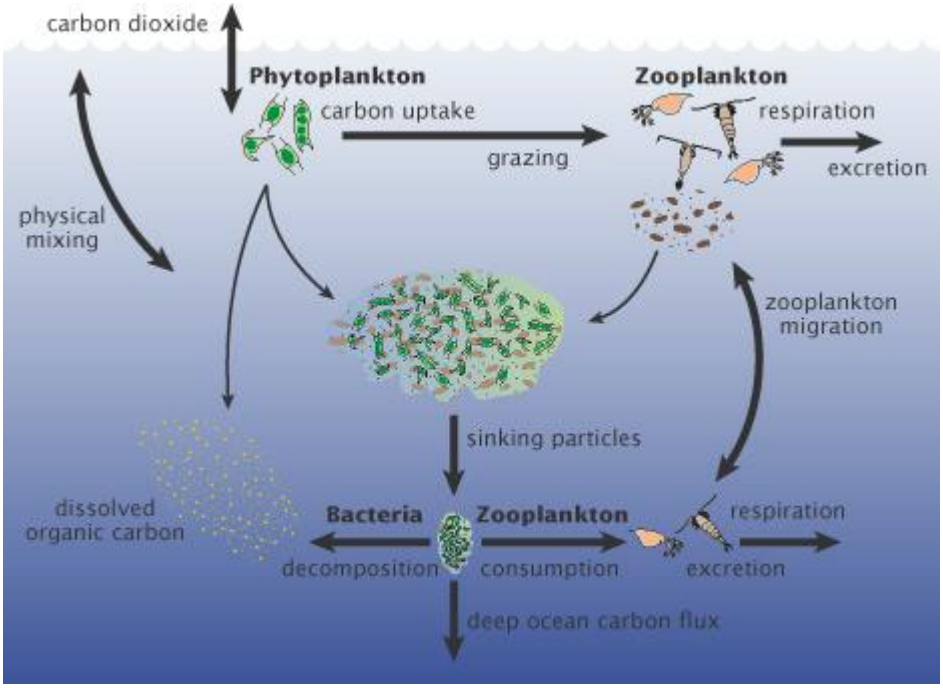

Figure 1.2 The biological carbon pump (adopted from "A New Wave of Ocean Science" brochure composed by U.S. Joint Global Ocean Flux Study).

In addition to the drawdown of atmospheric CO_2 as a part of the biological carbon pump, phytoplankton form the base of nearly all marine food chains and regulate pelagic ecosystem functioning. Consistent measurements of phytoplankton variability can be used as ecological indices for monitoring possible changes in the ocean pelagic ecosystem under natural or anthropogenic climate variability (Platt et al. 2009).

The seasonal changes of phytoplankton abundance have also a profound impact on recruitment rates of many commercially important fish species (Platt et al. 2003; Koeller et al. 2009). During metamorphosis, fish larvae rely on zooplankton or in some cases phytoplankton as a food source (Kane 1984). Food availability during a crucial period of fish larvae development determines rates of larval survival and subsequent recruitment success (Leggett & Deblois 1994). Therefore, understanding of phytoplankton variability and its effect on trophodynamics has important implications for fisheries management.

1.2 Phytoplankton growth controls

To convert inorganic carbon to organic compounds through photosynthetic reactions, phytoplankton require nutrients (such as nitrate, phosphorus, silica, iron) and light as a source of energy. Sunlight is attenuated very rapidly by water; therefore, phytoplankton are confined to the thin (10-100 m) sunlit ocean layer called the *euphotic zone*. Nutrients arise from remineralization of sinking organic matter and tend to accumulate in the subsurface waters. Phytoplankton

organisms are drifters, and so their proximity to the essential factors for growth is controlled by movement of ambient water masses. Physical mixing in the upper ocean layer regulates light and nutrient availability that affects spatial and temporal variations of phytoplankton abundance.

Light and nutrient availability regulate phytoplankton cell division rate and represent bottom-up controls of the population. Zooplankton predation is an important loss term in phytoplankton dynamics. Seasonal cycles of phytoplankton and zooplankton affect one another. For instance, enhanced grazing pressure can supress accumulation of phytoplankton biomass regardless of high cell division rates (Strom 2002). In addition, marine algal viruses can infect phytoplankton populations leading to higher mortality and preventing rapid growth (Suttle et al. 1990).

Under certain conditions phytoplankton growth overcomes losses due to grazing, mortality and other factors and, as a result, an accumulation of phytoplankton biomass (i.e. phytoplankton bloom) takes place. The temperate and subpolar North Atlantic Ocean represents the most productive open ocean region (Figure 1.1). Therefore, the emergence of phytoplankton blooms in this region gained great attention in oceanographic research. In the next sections, factors controlling the formation of seasonal phytoplankton blooms in the North Atlantic are discussed in detail.

1.3 Phytoplankton spring blooms

In the temperate and subpolar North Atlantic Ocean phytoplankton abundance is low in winter due to strong winter convective mixing and low sun angle. At the same time, deepening of the mixed layer enriches the ocean surface layer with nutrients (Koeve 2001). As the season advances, dramatic growth increase in spring (known as the phytoplankton spring bloom) takes place. Spring blooms in the North Atlantic are the most pronounced of any open ocean region and highly important for carbon flux to the deep ocean and regional trophodynamics (Legendre 1990). The timing of initiation, magnitude and duration of spring blooms vary interannually (Racault et al. 2012) and affected by variability in physical conditions (Henson et al. 2009a). In addition, the predicted climate change can alter spring bloom dynamics (Doney 2006).

Even after decades of research (Mills 2011), mechanisms underlying the initiation of phytoplankton spring blooms are debated (Behrenfeld & Boss 2014). Therefore, it remains unclear how the spring bloom phenomenon can respond to climate perturbations and what are the possible

effects on the pelagic ecosystem and the ocean carbon uptake. Sections 1.3.1 – 1.3.7 provide an overview of the ongoing debate.

1.3.1 Critical depth hypothesis

The critical depth hypothesis (CDH) (Sverdrup 1953) was the first conventional framework that described necessary conditions for initiation of phytoplankton spring blooms in the temperate and subpolar North Atlantic Ocean. The hypothesis was formulated by Harald Sverdrup based on the earlier ideas introduced by Gran & Braarud (1935). According to the CDH, the start of the phytoplankton spring bloom corresponds to shoaling of the ocean mixed layer depth above a critical depth.

The concept of a critical depth is illustrated in Figure 1.3. The critical depth is defined as the depth to which phytoplankton can be mixed and at which the total photosynthesis (area "AEC" on Figure 1.3) for the water column is equal to the total respiration (area "ABDC" on Figure 1.3). Sverdrup also introduced the concept of a compensation depth (or a compensation irradiance) defined as a depth (or irradiance level) at which the rate of photosynthesis equals the rate of respiration. The compensation irradiance term in the CDH characterizes losses due to phytoplankton respiration as well as grazing, sinking, viral infections and other factors (Smetacek and Passow 1990).

Sverdrup based the CDH on several assumptions:

- phytoplankton cells are equally distributed within the mixed layer,
- nutrients are replete,
- phytoplankton respiration is constant with depth,
- primary production is linearly related to light intensity that exponentially decays in the water column,
- and the value of compensation irradiance is known.

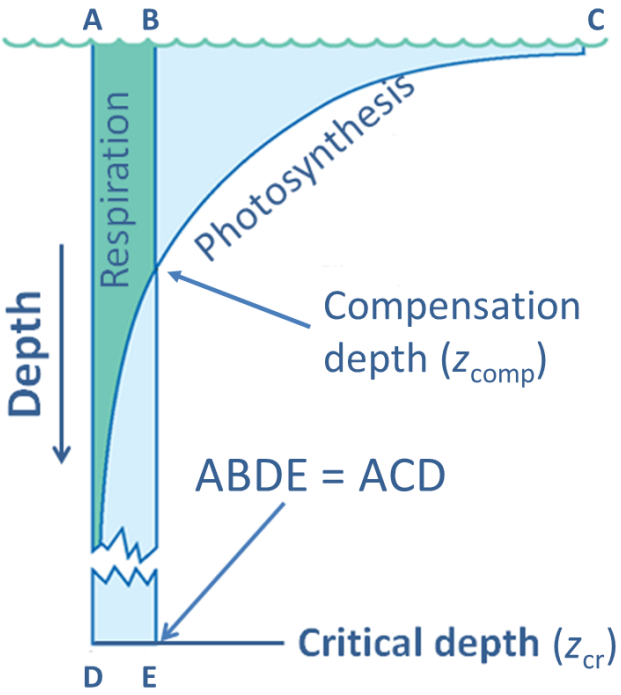

Figure 1.3 The sketch demonstrating Sverdrup's critical depth hypothesis of phytoplankton spring bloom initiation.

Sverdrup suggested that the critical depth criterion was achieved during seasonal stratification of the upper ocean layer in spring when light conditions for phytoplankton populations improve dramatically. Sverdrup tested the CDH by comparing changes in phytoplankton and zooplankton abundances, mixed layer depth and estimated critical depths using ship-based observations in the Norwegian Sea. The collected data indicated a dramatic increase in phytoplankton abundance following formation of a very shallow mixed layer in the middle of May. Variability in zooplankton abundances during the pre-bloom period was relatively low, supporting Sverdrup's assumption of constant losses.

Subsequently, the critical depth framework has been used for decades to explain spring bloom onset in the North Atlantic Ocean and other aquatic systems (Mills, 1989). However, it is important to note that the CDH is not universally applicable. For example, in subtropical regions phytoplankton growth is nutrient-limited due to well established water column stratification (Dutkiewicz et al. 2001). Nutrient limitation contradicts one of the assumptions of the CDH.

The CDH was greatly criticized and revisited over the years. Townsend et al. (1992) and Eilertsen et al. (1981) observed initiation of spring blooms under nutrient replete conditions in the absence of water column stratification. These observations were considered as strong evidence

against the CDH. Since then, the interest in the CDH has been growing (Sathyendranath et al. 2015) (Figure 1.4) and many research groups have attempted to verify the CDH, refine it or propose alternative explanations.

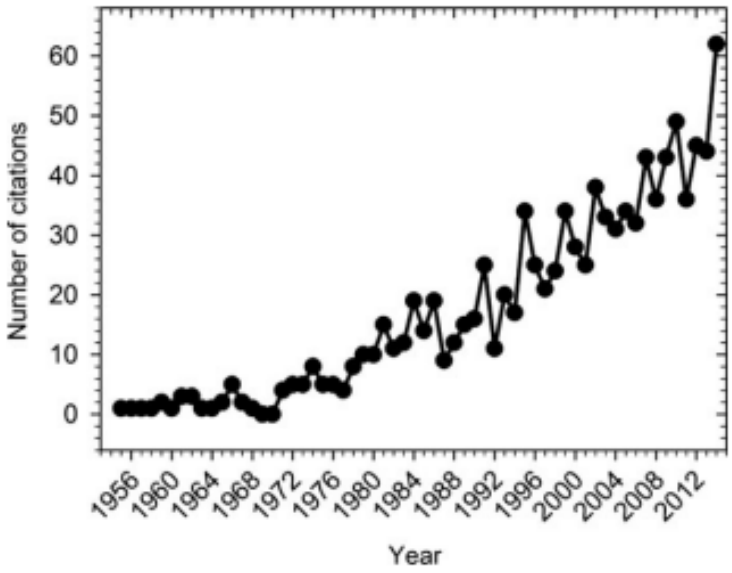

Figure 1.4 The absolute number of citations of Sverdrup (1953) per year (1953–2014). From Sathyendranath et al. (2015).

1.3.2 Mixed layers and mixing layers

Initiation of spring blooms in the absence of water column stratification can be explained by shoaling of the layer where mixing is currently active above a critical depth. Formulating the CDH, Sverdrup defines a mixed layer as the layer *"thoroughly mixed"* and "*below which the density increases so rapidly with depth that turbulence is suppressed*". According to this formulation, gradients in a vertical distribution of phytoplankton should be matched by strong gradients in density profiles. But, a mixed layer defined based on temperature or density gradients (e.g. de Boyer Montegut et al. 2004) can be a poor proxy for the layer where mixing is currently active (Franks, 2014). For clarity, the following definitions of mixed and mixing layers are widely used in literature:

- **Mixed layer** is a layer formed by the history of mixing and associated with a strong vertical gradient in hydrographic profiles.
- **Mixing layer** is a layer where mixing is currently active.

The difference between mixed and mixing layers has been discussed in depth by Brainerd and Gregg (1995). They analysed vertical profiles of temperature, salinity, density and turbulence energy dissipation rate obtained during several cruises off the California coast. The analysis showed

that strong gradients in vertical profiles of turbulence can correspond to extremely small (0.0025–0.005 kg m^{-3}) changes in density. According to their observations, vertical distribution of turbulence was relatively homogeneous during convective-driven mixing. However, under surface heating, the region of high energy dissipation rate was significantly shallower than a hydrographically-defined mixed layer. The part of the mixed layer below the mixing layer is relatively stable and has been referred to as the "remnant layer" (Brainerd & Gregg 1993). Brainerd and Gregg (1995) concluded that actively mixing layers are not easily detectable in vertical hydrographic profiles and overturning turbulent length scales give the most suitable estimation of the mixing layer depth.

Brody & Lozier (2014, 2015) considered divergence between mixing and mixed layers and its effect on the spring bloom onset in the subpolar North Atlantic Ocean. In particular, the studies analysed the difference in turbulence conditions under wind-driven and convective-driven mixing regimes that were differentiated based on the Monin-Obukhov length scale. The length scale is calculated based on atmospheric forcing data and can be used to describe relative effect of buoyancy and shear on turbulence in the ocean surface layer. Satellite and in situ data coupled with atmospheric forcing reanalysis showed that shoaling of a mixing layer above a critical depth under wind-driven regime can be a more precise criterion for an onset of phytoplankton spring blooms than the traditional critical depth framework.

Chiswell (2011) further emphasized that phytoplankton can be trapped near the surface by weak stratification that corresponds to small, sometimes indistinguishable gradients in hydrographic profiles. Using a historical data on chlorophyll a (hereafter Chl *a*) and temperature collected off the east coast of New Zealand, he explicitly showed that the depth of strong vertical gradients in temperature profiles can significantly deviate from the depth of maximum vertical gradients in phytoplankton distribution (Figure 1.5).

In summary, shoaling of a mixing layer and associated formation of weak vertical stratification can trigger a spring bloom before strong seasonal stratification fully develops.

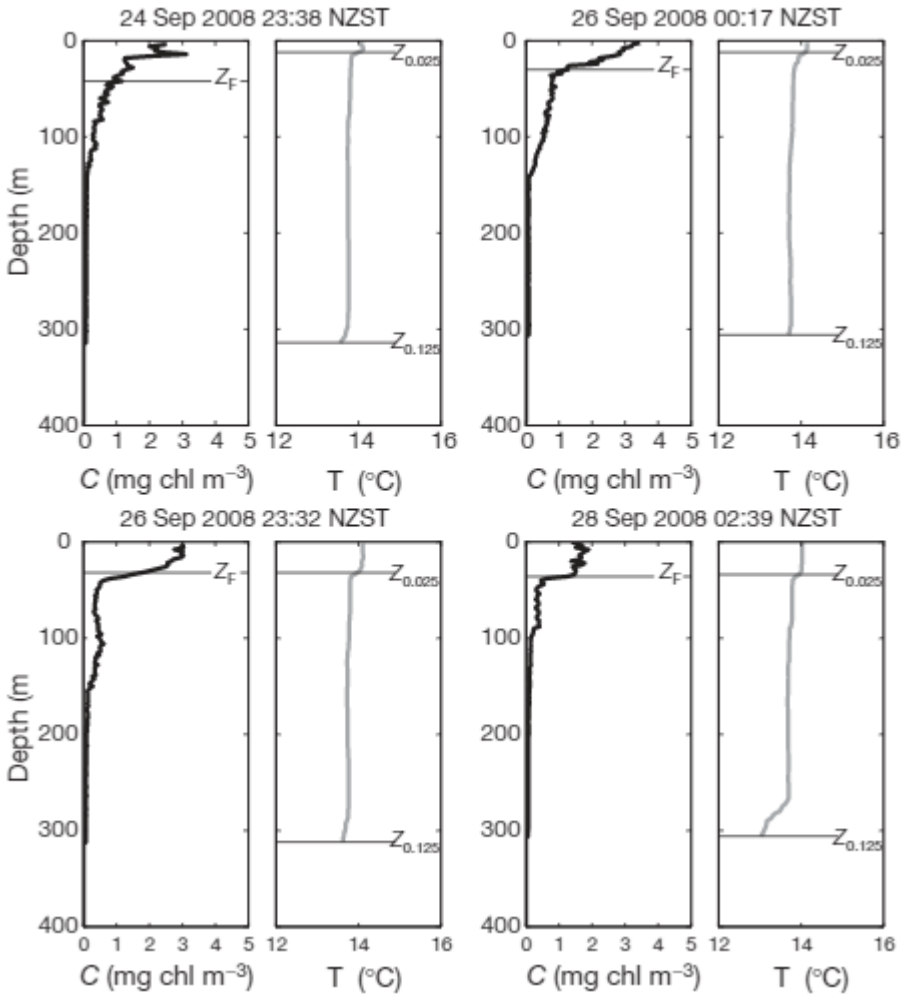

Figure 1.5 Temperature (T) and Chl *a* (C) profiles from CTD casts during a cruise off the east coast of New Zealand. $Z_{0.125}$ and $Z_{0.025}$ indicate depths at which density exceeds the surface value by 0.125 kg m^{-3} and 0.025 kg m^{-3} respectively. Z_F is the depth of maximum vertical gradient in Chl *a* profiles. Taken from Chiswell (2011).

1.3.3 Critical turbulence hypothesis

Huisman (1999) proposed a critical turbulence hypothesis (CTH), another mechanism explaining the occurrence of phytoplankton blooms in deep mixed layers. According to this hypothesis, spring blooms can start in arbitrarily deep layers due to changes in mixing intensity rather than in mixing depth. Using a phytoplankton growth-diffusion model (Okubo 1980), he demonstrated that low values of vertical eddy diffusivity (a proxy for mixing intensity) allow phytoplankton growth near the surface to outpace mixing. In this scenario, a bloom develops resulting in an uneven vertical distribution of phytoplankton within a mixing layer. Interestingly, the CTH was somehow foreseen by Sverdrup who wrote in his paper: "*a phytoplankton population may increase independently of the thickness of the mixed layer if the turbulence is moderate*". Huisman (1999) concludes that the phytoplankton bloom in spring can be triggered either through the critical

depth mechanism or through the critical turbulence mechanism (Figure 1.6). In his model, Huisman (1999) considered only neutrally buoyant phytoplankton species. Subsequently, Ebert et al. (2001) extended his work by incorporating sinking and buoyancy of phytoplankton. The study concluded that sinking phytoplankton species cannot form a bloom through the critical turbulence mechanism since they cannot persist in the ocean surface layer under low turbulence conditions.

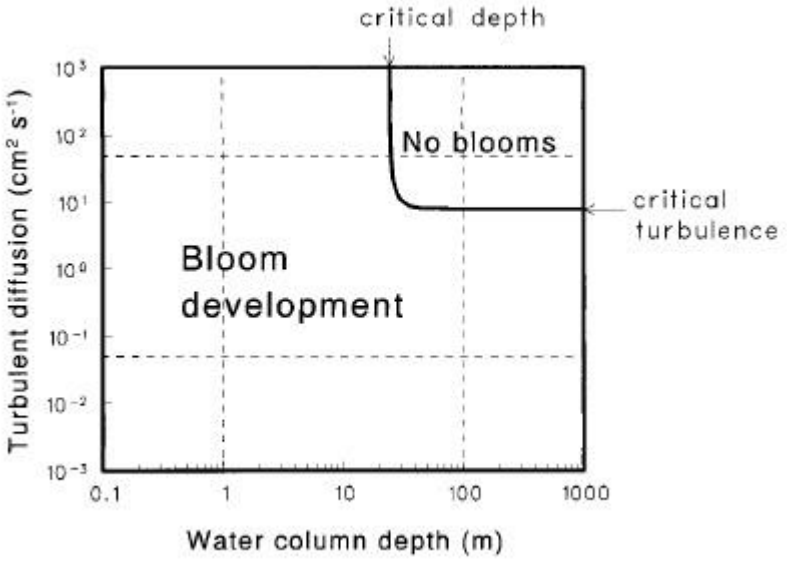

Figure 1.6 The combinations of water-column depth and vertical eddy diffusivity that allow a phytoplankton bloom and the combinations that prevent a phytoplankton bloom. From Huisman et al. (1999).

Verification of the CTH would require measurements of ocean microstructure in order to estimate vertical eddy diffusivity. On the other hand, turbulence conditions in the upper ocean layer are largely regulated by the overlying atmosphere. Data on heat flux and wind speed are easily available from various reanalysis products (Kalnay et al. 1996). In this regard, Taylor and Ferrari (2011a) attempted to link the critical turbulence criterion to the surface heat flux. Taylor and Ferrari (2011a) focused on the turbulence forced by thermal convection and obtained an analytical expression for the critical heat flux. They showed that net positive growth of phytoplankton was observed only for very small values of the surface heat flux $<O(1\ W\ m^{-2})$, indistinguishable from zero in practice. The predictions from the theory were tested using a large-eddy simulation (LES) model coupled with a phytoplankton population model that resolved the three-dimensional velocity field and corresponding variability in phytoplankton. The numerical simulations confirmed that the bloom onset occurs when the surface heat flux approaches zero. Therefore, Taylor and Ferrari (2011a) concluded that the onset of the spring bloom in the temperate and subpolar North Atlantic Ocean should coincide with the termination of convective mixing. The finding was further

supported by Ferrari et al. (2015) and Cole et al. (2015) who found a good agreement between timing of spring bloom onset derived from satellite ocean colour data and timing of surface heat flux becoming positive.

Enriquez and Taylor (2015) extended the work of Taylor & Ferrari (2011a) by considering the impact of wind forcing and surface heating on phytoplankton spring bloom initiation. Under wind-driven mixing, both the mixing depth and mixing intensity change depending on the surface forcing. Therefore, a spring bloom can start either through critical turbulence mechanisms (decreasing mixing intensity) or through critical depth mechanism (decreasing mixing depth). Enriquez and Taylor (2015) conducted a series of numerical simulations and concluded that under wind driven conditions shoaling of the mixing layer would most likely result in net phytoplankton growth.

In summary, the analysis of the phytoplankton growth-diffusion model showed that spring blooms can start near the surface in arbitrarily deep layers due to a decrease in mixing intensity. Subsequently, turbulence conditions necessary for bloom initiation were linked to atmospheric forcing parameters. It was shown that under convective-driven conditions, the net growth of phytoplankton starts when surface heat flux approaches zero. Under wind-driven mixing conditions, the spring bloom is more likely to develop through shoaling of a mixing layer above a critical depth.

1.3.4 Impact of lateral dynamics

The research work highlighted in the previous sections explained the initiation of spring blooms in the one-dimensional framework. However, a number of recent studies have brought attention to the impact of lateral dynamics on spring bloom initiation in the temperate and subpolar North Atlantic Ocean (Mahadevan et al. 2012; Taylor & Ferrari 2011a) and other ocean regions (Thomalla et al. 2015; Olita et al. 2014; Swart et al. 2014; Lévy et al. 1999; Lévy et al. 2000). This group of studies mainly discusses physical mechanisms operating at ocean density fronts that can stratify the upper ocean layer or reduce the intensity of vertical mixing.

Mahadevan et al. (2012) showed that submesoscale (1-10 km) mixed layer eddies arising from slumping of lateral density gradients trigger phytoplankton spring blooms in the subpolar North Atlantic Ocean prior the onset of surface heating. Slumping of horizontal density gradients can stratify the upper ocean layer even under relatively strong (-100 W m^{-2} as shown in the study) net cooling of the ocean surface. The role of wind forcing in this case is defined by the wind direction: it can either support or prevent stratification by a front slumping. Nevertheless, localized stratification driven by mixed layer eddies forming at density fronts can trigger a patchy phytoplankton bloom before the onset of surface warming. In situ observations from gliders and a

Lagrangian float obtained in the framework of the North Atlantic Bloom Experiment 2008 (NABE08) corroborated this view.

Taylor & Ferrari (2011b) showed that frontal instabilities can also suppress turbulent mixing and drive localized phytoplankton blooms through the critical turbulence mechanism under net cooling of the ocean surface. They performed LES simulations (Figure 1.7) reproducing conditions at a relatively strong ocean front (~0.25°C/km) such as the one between the Gulf Stream and the Labrador Current. It was noted that the mechanism is potentially applicable for weaker, more prevalent fronts in the ocean. The study concluded that density fronts can contribute to sustaining phytoplankton populations in winter when surface cooling is strong and conditions are particularly unfavourable for phytoplankton growth.

Patches of high phytoplankton growth associated with ocean fronts were also detected in glider data collected in the Atlantic Subantarctic Zone (Thomalla et al. 2015; Swart et al. 2014). The glider data show the occurrence of intermittent short-term blooms of phytoplankton 1-2 months before the onset of solar heating and manifestation of the seasonal spring bloom event.

Lévy et al. (1999; 2000) considered the impact of mesoscale eddies (10-100 km) on the initiation of phytoplankton blooms in the north-western Mediterranean Sea, the region characterized by intense mesoscale activity in winter. Stratification prompted by the mesoscale activity drove an increase in light exposure of phytoplankton. Enhanced growth was observed at the periphery of eddies before the onset of stratification due to solar heating.

Thus, horizontal density gradients and regions of intense mesoscale activity support localized phytoplankton blooms through a reduction in mixing intensity and/or depth even under net surface cooling. This can be considered as an initial trigger of seasonal phytoplankton blooms or as a mechanism for maintaining phytoplankton populations in winter.

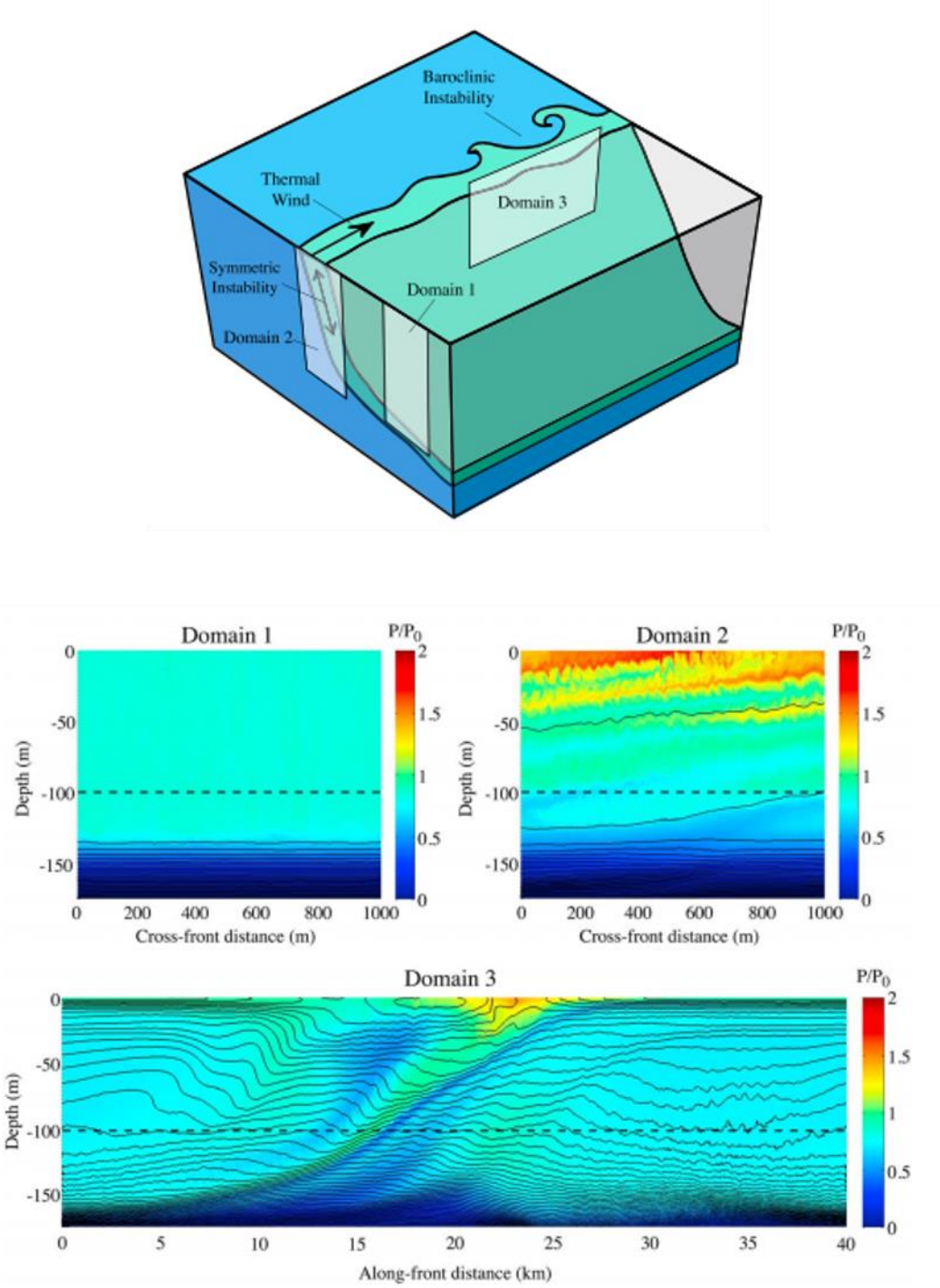

Figure 1.7 Results of numerical simulations by Taylor & Ferrari (2011a). Phytoplankton concentration (*P*, normalized to initial conditions P_0) is colour-coded and density contours are shown as black lines. The figure shows that phytoplankton blooms develop at the frontal zones (Domain 2 and Domain 3). Phytoplankton concentration is unvarying outside of the frontal region (Domain 1). In the simulations, surface heat flux was set to -100 W m^{-2}.

1.3.5 Top-down view on bloom initiation

The studies cited in the previous sections invoke a bottom-up view of the process of spring bloom initiation. Under nutrient-replete conditions, phytoplankton growth rate depends on light and temperature (e.g. Edwards et al. 2013). The CDH and CTH focus on the processes that regulate phytoplankton cell division rate and assume that loss rates are constant during the pre-bloom period.

The impact of loss terms (e.g. zooplankton grazing) on the North Atlantic spring bloom initiation has received significantly less attention in literature compared to mixing and light conditions (Fischer et al. 2014). However, there is ample evidence that grazing by zooplankton regulate phytoplankton seasonal cycles (Banse 2011) and therefore can play an important role in the process of bloom initiation. For instance, the examination of the CDH performed by Platt et al. (1991) explicitly showed that losses due to zooplankton grazing substantially affect estimations of critical depths.

In fact, seasonal dynamics of phytoplankton and zooplankton are concurrent. The occurrence of phytoplankton blooms can be attributed to environmental perturbations of predator-prey coupling (Cushing 1959). In other words, phytoplankton blooms can be considered as events that occur when zooplankton grazing fails to keep up with phytoplankton biomass accumulation (Irigoien et al. 2005). Tight predator-prey coupling results in low seasonality of phytoplankton but it can be disturbed by rapidly increasing phytoplankton growth rate due to changes in stratification, light or nutrient conditions.

A significant part of losses in phytoplankton populations is attributed to micro-zooplankton grazing (Strom et al. 2001; Tillmann 2004; Burkill et al. 1987). Micro-zooplankton have high division rates and can rapidly respond to increasing stocks of phytoplankton (Banse K. 1992). Several observational studies reported that enhanced grazing by micro-zooplankton at the early stages of spring bloom development prevented the formation of phytoplankton blooms (Watras et al. 1985; Weisse & Scheffel-Möser 1990).

Using a modelling approach, Evans & Parslow (1985) also demonstrated that enhanced phytoplankton growth in winter can maintain a population of grazers large enough to suppress phytoplankton blooms in spring. Albeit, Evans & Parslow (1985) emphasized that in the North Atlantic Ocean the mixed layer in winter is deep and phytoplankton concentrations are too low to support significant zooplankton growth.

Sverdrup's observations in the Norwegian Sea also showed low variability in zooplankton during the pre-bloom period. It is important to note, however, that Sverdrup (1953) reported observations of copepod abundances. Copepods are meso-zooplankton that mainly feed on large phytoplankton species and micro-zooplankton. To survive periods of food shortage in winter, copepods migrate to deep waters, undergo diapause and re-emerge in spring close in time to a spring bloom event (Hirche 1996). Winter hibernation results in low grazing by meso-zooplankton that could in part explain the invariant abundance of copepods during the pre-bloom period observed by Sverdrup.

1.3.6 Dilution-recoupling hypothesis

The dilution-recoupling hypothesis (DRH) proposed by Behrenfeld (2010) attributes the formation of phytoplankton spring blooms in the subpolar North Atlantic Ocean to predator-prey interactions, suggesting decreasing grazing pressure as the main factor for the bloom onset. The hypothesis states that deepening of the mixed layer in winter causes physical perturbation of predator-prey coupling. Deep mixing and low light intensity in winter result in low phytoplankton cell division rates. But at the same time, these conditions reduce encounter rates of phytoplankton with zooplankton leading to subsiding grazing pressure. Thus, according to the DRH a phytoplankton bloom starts due to decreasing losses to grazing rather than due to enhanced phytoplankton growth rate. A blooming period begins in deep mixed layers and terminates when stratification advances (Figure 1.8) and coupling between phytoplankton and zooplankton becomes tight. The hypothesis has not been verified using any direct comparison of phytoplankton growth and loss rates since it is very difficult to obtain time-resolved data on zooplankton grazing in the high-latitude North Atlantic Ocean in winter. However the positive net growth of phytoplankton during deep winter mixing derived from satellite (Behrenfeld 2010; Figure 1.8) and in situ data sets (Boss and Behrenfeld 2010) has been used as evidence to support the DRH.

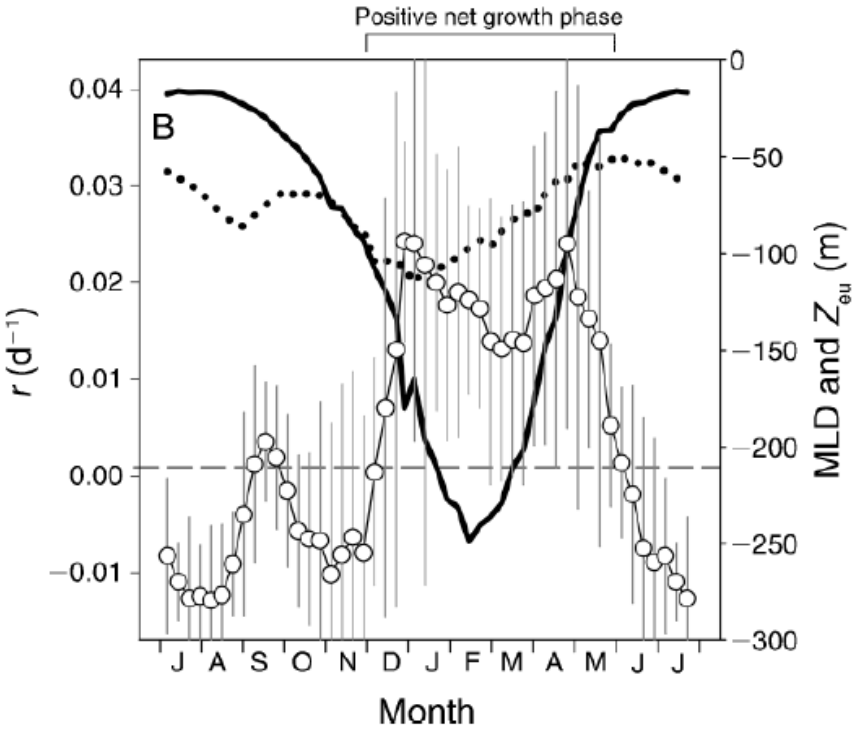

Figure 1.8 Annual mean cycles of phytoplankton net accumulation rate (*r;* white circles with grey bars indicating standard deviation of *r*), mixed layer depth (MLD; heavy black line), and euphotic depth ($Z_{eu;}$ dotted black line) for an area in the North Atlantic Ocean lying between 25-35 °W and 45-50°N. From Behrenfeld (2010).

1.3.7 Unifying perspectives

The previous sections showed that the debate around spring blooms in the North Atlantic Ocean brought up several alternative hypotheses and refinements to the original critical depth framework. However, different hypotheses might be valid during different times of year and the process of bloom initiation might consist of multiple stages.

In their paper "Seasonal diary of phytoplankton in the North Atlantic", Lindemann & St. John (2014) proposed a conceptual model of spring bloom initiation in the North Atlantic Ocean that moves beyong the "single mechanism" view (Figure 1.9). In winter strong convective mixing dilutes phytoplankton, reducing grazer pressure, and prevents sinking of phytoplankton out of the surface layer, sustaining the algal population. Periods when convective mixing ceases increase growth of phytoplankton near the surface through the critical turbulence mechanism even though the hydrographically defined mixed layer is still deep. When stratification advances, the mixed layer shoals and the further development of the phytoplankton bloom proceeds through the critical depth mechanism. Lindemann & St. John (2014) suggest that before the seasonal stratification,

phytoplankton and zooplankton are decoupled, therefore grazing pressure is unlikely to suppress phytoplankton growth in deep mixed layers.

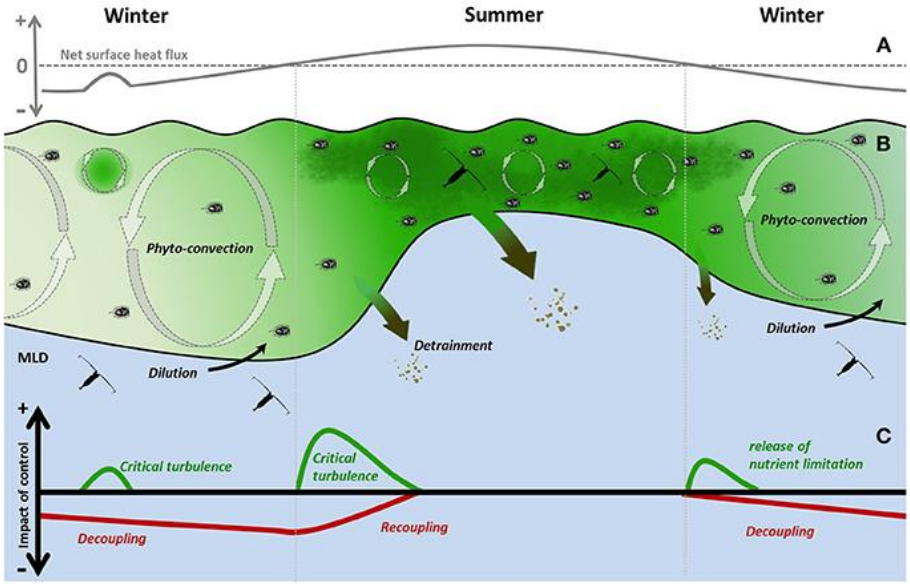

Figure 1.9 The conceptual model of the physical and biological controls and their impacts on the seasonal cycle of phytoplankton in the open subarctic North Atlantic. From Lindemann and St. John (2014).

Another unifying conceptual model was proposed by Chiswell et al (2015) (Figure 1.10). In their view, deepening of the mixed layer in autumn due to convection and increasing wind forcing entrains new nutrients to the surface layer prompting an increase in phytoplankton stocks. After that, two scenarios of phytoplankton dynamics are possible. In one case (Ocean 1 on Figure 1.10) phytoplankton stocks gradually increase over winter since the mixed layer depth remains above the critical depth throughout the whole annual cycle. In Ocean 2 (Figure 1.10) the phytoplankton population becomes light limited and stocks decrease in winter. Before the onset of surface warming, phytoplankton stocks can increase through the critical turbulence mechanism. Subsequently, the surface heat flux becomes positive and stratification forms, further advancing the development of the phytoplankton bloom in spring. Initially the stratification is weak and a mixing layer (see section 1.3.2) is shallower than the mixed layer. This framework mainly considers how abiotic factors (e.g. nutrients, stratification, mixing) influence spring bloom manifestation, giving less attention to zooplankton grazing and other biotic factors.

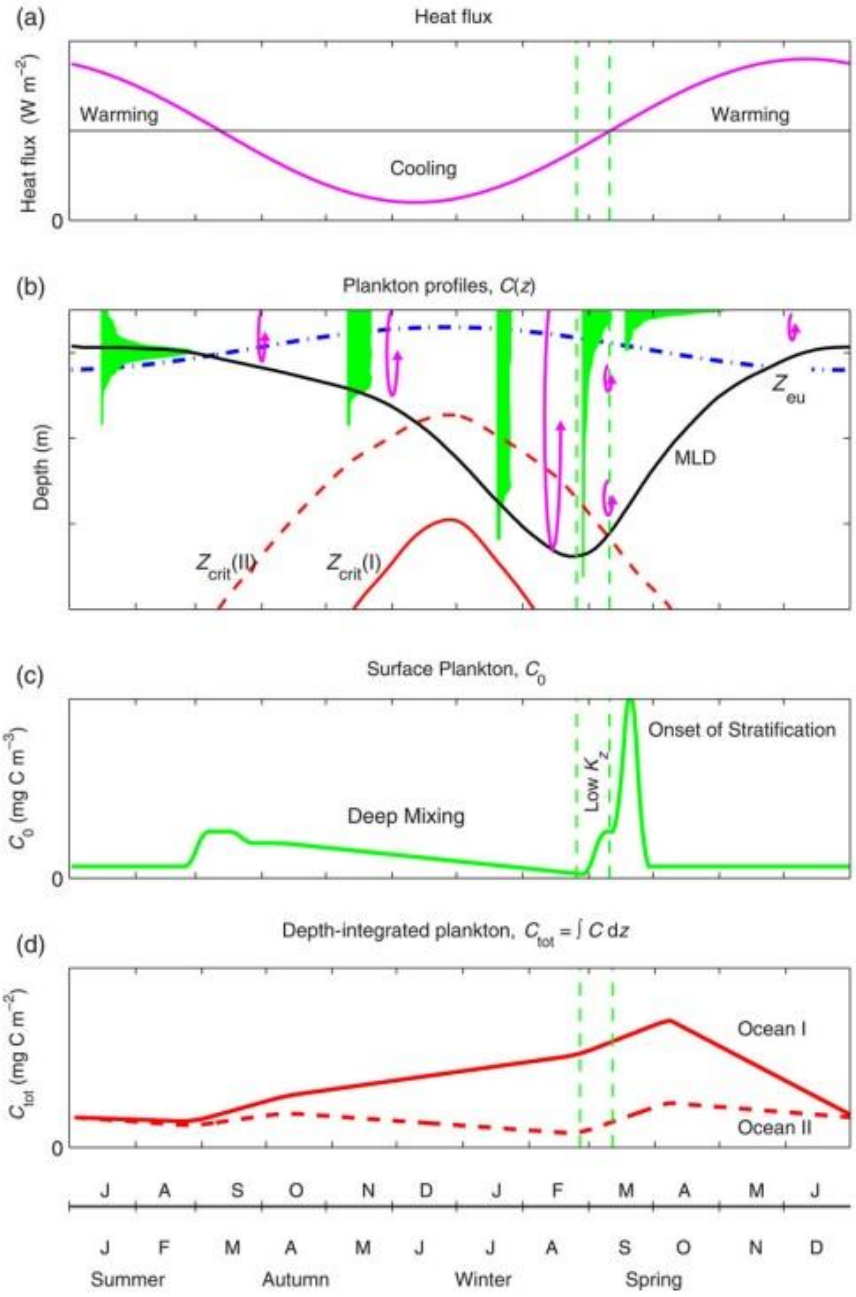

Figure 1.10 Schematic annual cycles for the temperate and subpolar oceans: (a) surface heat flux; (b) phytoplankton concentration profiles (filled green profiles), along with the mixed layer depth (black solid line) and the depth of the euphotic zone (blue dash-dotted line). Also shown are critical depths (Z_{crit}, dashed and continuous lines) for hypothetical Oceans I and II, where Ocean II is light-limited in winter, whereas Ocean I is not. The vertical scale of the mixing is indicated by overturning arrows; (c) surface plankton concentration, C_0; and (d) depth-integrated phytoplankton, C_{tot}, for the two hypothetical Oceans. Vertical dashed lines show the times of deepest mixed layer and the cessation of convective mixing. From Chiswell et al. (2015).

1.4 Autumn phytoplankton blooms

In the temperate and subpolar North Atlantic Ocean, phytoplankton spring blooms typically terminate due to depletion of nutrients and/or overgrazing. During the post-spring bloom a well-established pycnocline inhibits the upward flux of nutrients to the euphotic zone. Under these conditions primary production is predominantly fuelled by regenerated forms of nitrogen such as ammonium and urea unless physical re-supply of nutrients occurs. Developed stratification and depletion of nutrients result in a non-uniform vertical distribution of phytoplankton with a pronounced subsurface chlorophyll maximum (SCM) (Cullen 1982). Formation of the SCM can be explained by an accumulation of phytoplankton at a depth where conditions are favourable for growth - at the base of the euphotic zone in the vicinity to the nutricline (Lorenzen, 1966).

In autumn, cooling of the ocean surface and passage of storms erodes vertical stratification, deepening the mixed layer and causing an influx of nutrients into the surface layer. At the same time, deepening of the mixed layer reduces light levels experienced by phytoplankton. The formation of autumn blooms is attributed to an increase in growth due to new entrainment if light conditions are still favourable (Findlay et al. 2006). In the North Atlantic Ocean, autumn blooms are lower in magnitude compared to spring blooms (Martinez et al. 2011) and, therefore, less studied.

Initiation of autumn blooms in the temperate and subpolar North Atlantic Ocean is similar to initiation of phytoplankton blooms in subtropical gyres where the flux of nutrients is prohibited by strong stratification. Several studies reported a significant increase in surface Chl *a* concentration in nutrient depleted regions after storms' passage (Marra et al. 1990) and hurricanes (Babin et al. 2004). On the other hand, an increase in surface Chl *a* can be associated with redistribution of biomass from the SCM and can be misinterpreted as a bloom in remote sensing imagery (Foltz et al. 2015; Perry et al. 2008). In general, it remains uncertain if storms initiate net phytoplankton growth and what their contribution to the nutrient budget is.

1.5 Autonomous gliders in phytoplankton studies

Phytoplankton seasonality and bloom dynamics have been extensively studied using satellite ocean colour data (e.g. Cole et al. 2015; Henson et al. 2009b; Racault et al. 2012). Remote sensing of ocean colour provides synoptic maps of surface Chl *a* concentration and allows monitoring of phytoplankton variability over the global ocean. However, there are some well-known limitations of this technique. Global satellite images of phytoplankton distribution are limited to the first optical depth. Therefore, features like the SCM are not directly detectable by ocean remote sensing (Ardyna et al. 2013). Moreover, the satellite data record contains gaps due to periods of cloud cover

and low sun angle (Cole et al. 2012). In the temperate and subpolar North Atlantic Ocean the percentage of missing data in satellite record reaches >50% (Figure 1.11).

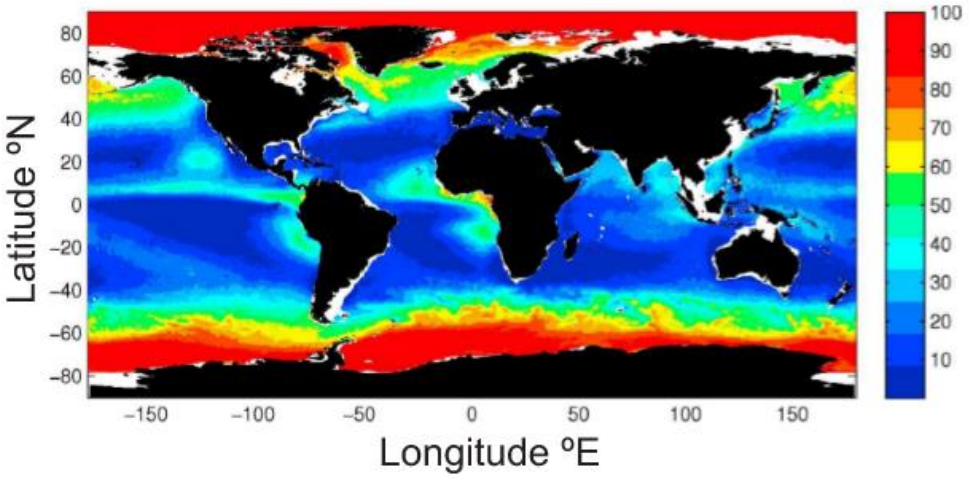

Figure 1.11 Map of the percentage of missing data in the satellite ocean colour record over the time span 2002–2006. From Cole et al. (2012).

Ocean colour remote sensing techniques retrieve surface Chl *a* concentrations using visible electromagnetic radiation coming from the ocean. Measuring in vivo Chl *a* fluorescence intensity is another established method of determining its concentration in seawater (Lorenzen, 1966). Fluorescence sensors can be easily mounted on in situ autonomous platforms such as buoyancy-driven gliders.

Gliders represent a new powerful platform for studying phytoplankton dynamics due to their ability to obtain frequent depth-resolved profiles of bio-optical and physical properties for long (inter-seasonal) periods of time, even under challenging weather conditions regardless of surface light levels. Gliders are capable of retrieving information from remote areas of the ocean and during the time of year when satellite data is unavailable. Changes in both surface concentrations of Chl *a* as well as depth-integrated Chl *a* inventories can be quantified by measuring the vertical structure of phytoplankton in the water column, overcoming the limitations of the satellite ocean colour data.

Being operated remotely, gliders dive and ascend in the ocean by regulating their buoyancy (Eriksen et al. 2001). Wings on a glider (Figure 1.12) are designed to control its tilt in the water to allow horizontal movement. When the glider comes to the surface, it communicates with a satellite, receives flight parameters for the next descent and transmits data collected on the latest dive. The average time of one dive (descent and ascent) to the maximum depth of 1000 meters is 4 hours. Duration of a mission can be several months and depends on the sampling resolution and type of

sensors mounted on a glider. During one deployment, a glider can collect more than 1000 vertical profiles of seawater properties and cover a distance up to thousands of kilometres.

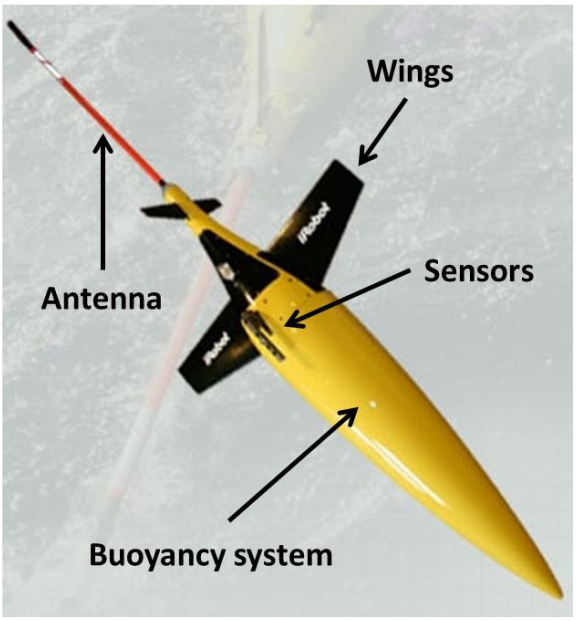

Figure 1.12 IRobot glider

The standard optical Wet Labs ECO puck often mounted on gliders contains a fluorometer, CDOM (coloured dissolved organic matter) sensor and an optical sensor that measures the intensity of light scattered in the water. The latter provides estimates of volume scattering and particulate optical backscatter that can be interpreted as an index of phytoplankton biomass (Huot et al. 2007). However, the backscatter signal in seawater involves scattering from bacteria, heterotrophs, bubbles, detritus and other suspended material, introducing complications in relating particulate optical backscatter to phytoplankton carbon content (Stramski et al. 2004). Gliders can be also equipped with PAR and oxygen sensors.

Gliders have been successfully applied in studies of phytoplankton spring blooms, SCM and general seasonal variability during the North Atlantic Bloom Experiment in 2008 (Cetinić et al. 2014; Briggs et al. 2011; Mahadevan et al. 2012), in the Labrador Sea (Frajka-Williams et al. 2009), at the shelf break – offshore zone off the Washington coast (Perry et al. 2008) and in the Southern Ocean (Swart et al. 2014; Thomalla et al. 2015). New sensors and techniques related to glider measurements are rapidly developing. Some recent achievements in this field involve determining of vertical velocities in the ocean using the glider's flight model (Frajka-Williams et al. 2011), estimation of particulate organic carbon fluxes and mean particle size using bio-optical sensors (Briggs et al. 2011; Briggs et al. 2013) and detecting krill swarms using an echo-sounder mounted on a glider (Guihen et al. 2012).

1.6 Summary points

- Marine phytoplankton play an important role in sequestration of atmospheric CO_2, represent the base of nearly all marine food webs, and affect recruitment rates of many commercially important species.
- The temperate and subpolar North Atlantic Ocean is the most productive open ocean region where phytoplankton blooms emerge in autumn and in spring. Phytoplankton spring blooms tend to be the most pronounced and of high ecological significance.
- Mechanisms of spring bloom initiation are keenly debated in the oceanographic community and several hypotheses have been proposed. Many studies suggest that spring blooms start when the mixed layer defined based on hydrography is relatively deep, contrary to Sverdrup's interpretation. It remains uncertain under which atmospheric conditions spring blooms start and what the role of zooplankton grazing is.
- Autumn blooms of phytoplankton arise from nutrient influx to the euphotic zone associated with storm passage and/or surface cooling. However, a surface increase in phytoplankton concentration can be driven by redistribution of phytoplankton biomass from an SCM. In general, it remains uncertain if storms initiate in situ phytoplankton growth and how significant a nutrient flux associated with them is.
- Autonomous underwater platforms, like gliders, represent a new powerful technology for studying phytoplankton variability. Gliders provide depth resolved measurements of biophysical parameters in the upper ocean over long time scales. Data collected by gliders can provide a new perspective on mechanisms underlying bloom formation. In particular, measurements from autonomous gliders can
    1) map changes in phytoplankton distribution along with hydrographic parameters during storms and periods of cloud cover (relevant for studies of autumn phytoplankton blooms) and
    2) provide high-resolution depth-resolved measurements of phytoplankton distribution during winter and spring when satellite data is limited (relevant for studies of spring phytoplankton blooms).

The next chapter provides details of the glider mission, data processing and lists additional data sets used in this study. Chapter 3 gives an overview of the obtained data set, describes general patterns observed in the data and specifies parts of the data set analysed in Chapter 4 (focused on an autumn bloom event), Chapter 5 (addresses the impact of atmospheric forcing and light on

spring bloom initiation) and Chapter 6 (analyses the role of zooplankton grazing on the spring bloom). Synthesis of results and future research directions are provided in Chapter 7.

Chapter 2: OSMOSIS glider mission

The glider data set for this study was collected in the framework of NERC funded UK OSMOSIS (Ocean Surface Mixing, Ocean Submesoscale Interaction Study) project. The aim of the OSMOSIS project was to study processes that deepen and shoal the ocean surface boundary layer and develop parametrizations that can be implemented in a state-of-the-art global coupled climate model, facilitating improved weather and climate predictions. Bio-optical sensors mounted on the gliders extended the project's objectives and allowed the study of biophysical interactions in the upper ocean layer. Glider operations and data management were conducted by the University of East Anglia (UEA), the National Oceanography Centre of Southampton (NOCS) and the California Institute of Technology (Caltech).

In this chapter, I give an overview of the OSMOSIS glider mission, describe details of Chl *a* fluorescence data processing, calculation of relevant parameters, such as euphotic zone depth and mixed layer depth, and outline other common data sets used in Chapters 3, 4, 5 and 6.

2.1 Sampling strategy

In the beginning of the OSMOSIS project (September 2012), two gliders were simultaneously deployed ~40 km southeast of the Porcupine Abyssal Plain (PAP) site (Figure 2.1). The PAP sustained observatory is sited in the open North-East Atlantic Ocean (49 °N, 16.5 °W) representing conditions between the sub-polar and sub-tropical gyres of the North Atlantic Ocean and characterized by complex interannual Chl *a* variability (Henson et al. 2009). The location of the PAP site was selected to be away from the continental slope to minimize effects of tides and strong permanent currents (Lampitt et al. 2010). Multidisciplinary observations at the PAP site have been sustained for more than 20 years (Hartman et al. 2010).

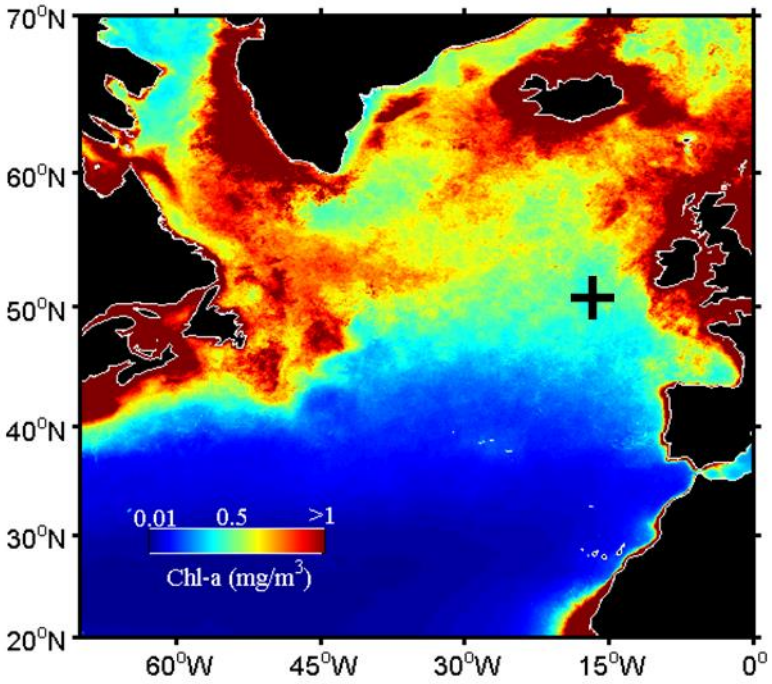

Figure 2.1 Location of the glider sampling site in the North Atlantic Ocean shown on a map of surface Chl *a* (Aqua MODIS mission composite; 2002-2012).

The glider program involved one year (September 2012 – September 2013) of continuous measurements. Every 3-4 months two gliders were recovered and another two were deployed to ensure continuity (Figure 2.2). CTD data collected on process cruises were used to calibrate the glider sensors.

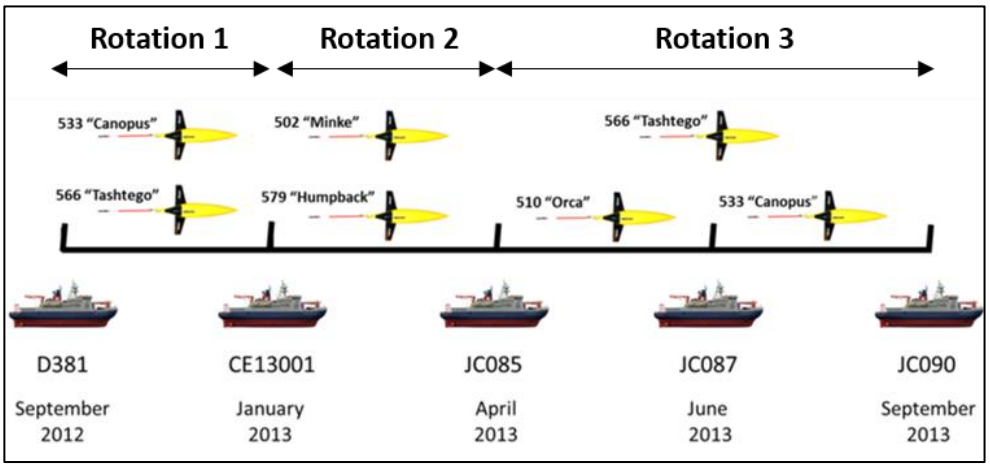

Figure 2.2 Scheme of glider deployments and cruises during the OSMOSIS project.

The gliders collected measurements over a 20 x 20 km^2 sampling area. Both gliders were piloted to follow a "butterfly" trajectory (Figure 2.3). One glider was moving between the northern

and southern sides of the sampling box while another glider was moving between the eastern and western sides. Occasionally the gliders drifted away from the sampling site, being pushed by currents. However, over the course of the mission, the gliders maintained the predefined trajectory well: approximately 88 % of vertical profiles were obtained within the intended sampling area.

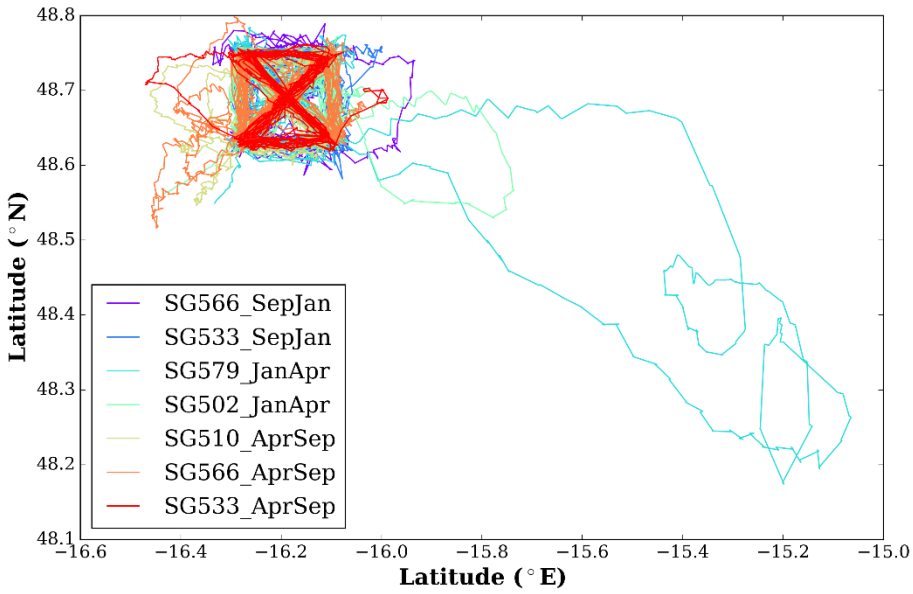

Figure 2.3 Trajectories of the gliders during the OSMOSIS project.

The gliders covered the whole sampling area in approximately 4 days. The time to complete one dive (descent and ascent) to the maximum depth of 1000 meters was 4-5 hours. On average each glider provided 10-12 vertical profiles per day. The gliders were equipped with an un-pumped CT (conductivity, temperature) sensor, a Wetlabs Triplet ECOpuck (including Chl *a* fluorescence, optical backscattering and coloured dissolved organic matter (CDOM) sensors), a spherical PAR sensor and dissolved oxygen optode (Figure 2.4). The ECOpuck components for all deployments are listed in Table 2.1. PAR sensors were mounted on all the gliders except glider 502.

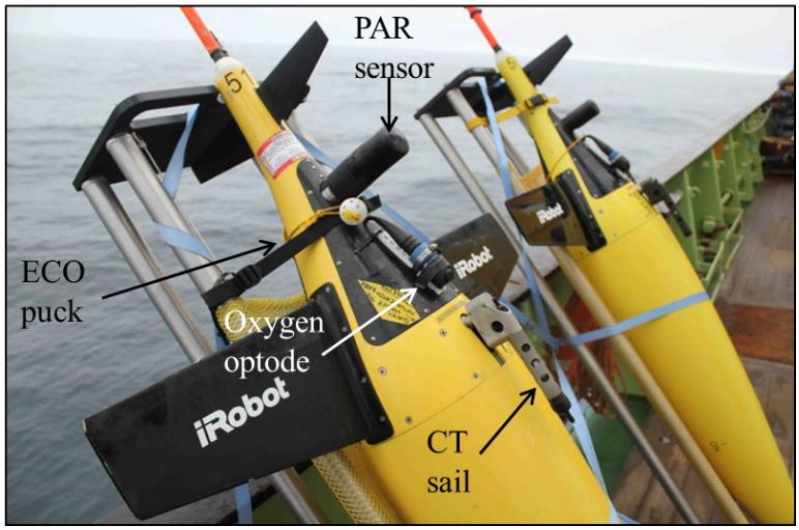

Figure 2.4 Photograph of sensors on one of the gliders (courtesy Dr. Gillian Damerell).

Table 2.1 Bio-optical and PAR sensors on the OSMOSIS gliders

Glider ID	ECOpuck	PAR sensor
SG566	CHL*, CDOM**, BS650***	On
SG533	CHL, CDOM, BS650	On
SG502	CHL, BS700, BS470	Absent
SG579	CHL, CDOM, BS532	On
SG510	CHL, CDOM, BS650	On

*Chl *a* fluorometer
**Colour dissolved organic matter fluorometer
***Volumetric optical backscatter meter (xxx is wavelength in nm)

Bio-optical sensors on gliders result in a significant increase in battery consumption compared to CT sensors. In order to save enough power for 3-4 months of a deployment, sampling depth and resolution for the ECOpuck were constantly adjusted throughout the mission (Figure 2.5) depending on the season, observed vertical distribution of Chl *a* fluorescence and remaining battery levels. ECOpuck sensors were also switched off when gliders drifted away from the sampling site. During a part of the first glider rotation (September 2012 – January 2013) ECOpucks on the two gliders were switched on in turns (Figure 2.5). CT sensors were set to measure down to 1000 m depth with the maximum sampling resolution within the upper 300 m and in the lower 700 m sampling resolution was decreased.

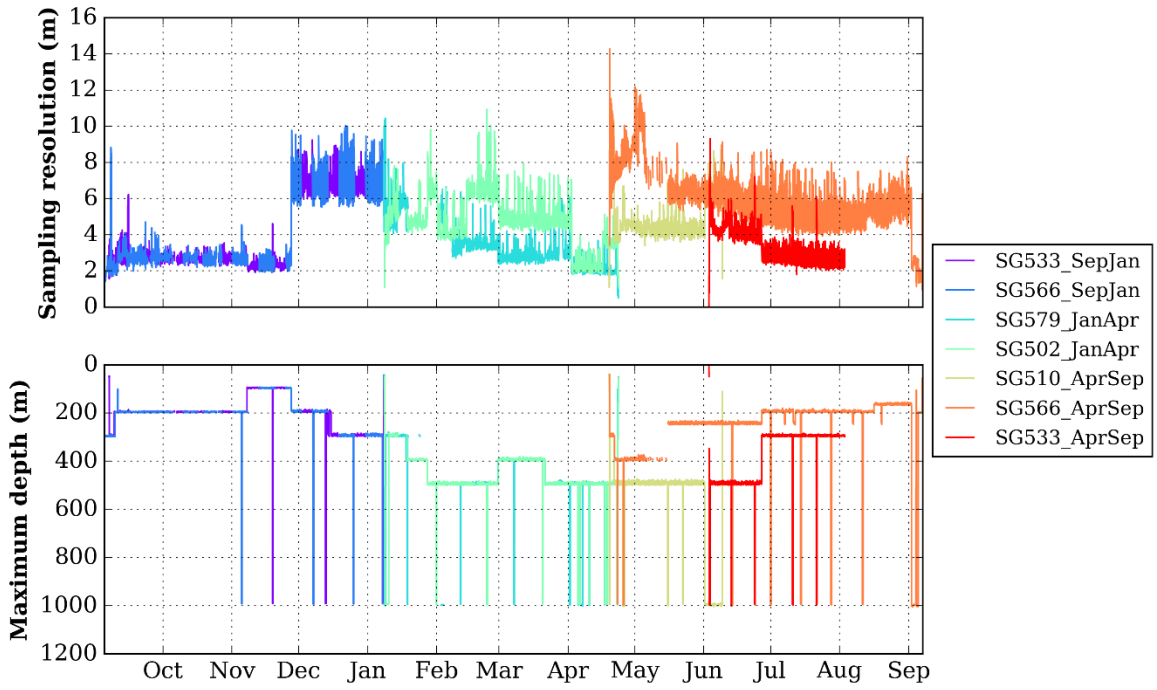

Figure 2.5 Mean per profile sampling resolution (top) and maximum sampling depth (bottom) for the ECOpuck sensors mounted on the OSMOSIS gliders.

The OSMOSIS glider mission resulted in a unique data set containing 8458 vertical profiles of biophysical ocean properties collected throughout the whole annual cycle and representing a wide range of environmental conditions. Gliders provided a large amount of data that requires accurate processing and managing. The methodology implemented for the Chl *a* fluorescence data processing is described in section 2.2.

2.2 Chl *a* fluorescence data processing

Raw data from the ECOpuck is output in digital counts from the sensors. In order to convert raw data from the instruments to scientifically usable format several steps need to be applied. In the current work the data processing involved in situ dark counts evaluation, data quality control, correction for daytime fluorescence quenching and data calibration using in situ Chl *a* samples. Each step is described below. Processing of the optical backscattering data was conducted in a similar way and details are provided in section 2.2.6.

2.2.1 Pre-processing

First, raw data files obtained by the gliders were processed with a glider Matlab toolbox developed in UEA. For each glider deployment, the toolbox aggregated raw data from each dive into one Matlab file and corrected time and pressure readings for the sensors. The sensors mounted on the gliders did not fire all at the same time. Since the glider is in motion, it means that the sensors

were not fired at the same depth. In particular, pressure was measured at different time to other variables. In this regard, scripts in the toolbox apply necessary correction of pressure and time.

2.2.2 In situ dark count evaluation

Dark fluorescence (dark counts) is a fluorometer offset, corresponding to the output of the sensor in deep waters, in the absence of phytoplankton and light. The instrument specific dark counts (hereafter DC) are provided by an instrument manufacturer and usually estimated by covering fluorometers with dark tape. However previous studies (e.g. Thomalla et al. 2015) indicated that DC values observed during glider deployments can differ from factory-provided values. Therefore, DC values for all gliders have to be revaluated during the data processing stage.

To determine in situ DC for OSMOSIS gliders, I calculated the median value of fluorescence over the bottom 10 meters of Chl *a* fluorescence profiles. Histograms of the obtained values are shown in Figure 2.6. The most frequent value in the histograms was assumed to represent in situ DC. For some deployments (e.g. SG566_SepJan) in situ DC significantly differed from the manufacturer's factory provided DC.

The histograms of in situ DC have long right tails. This is due to the fact that sampling depth for the ECOpuck was constantly changing during the mission. As a result, occasionally changes in the sampling depth resulted in undersampling of Chl *a* fluorescence vertical distribution (e.g. Figure 2.7). If Chl *a* fluorescence vertical distribution is not fully sampled, the median value of fluorescence over the bottom 10 meters would be significantly higher than DC.

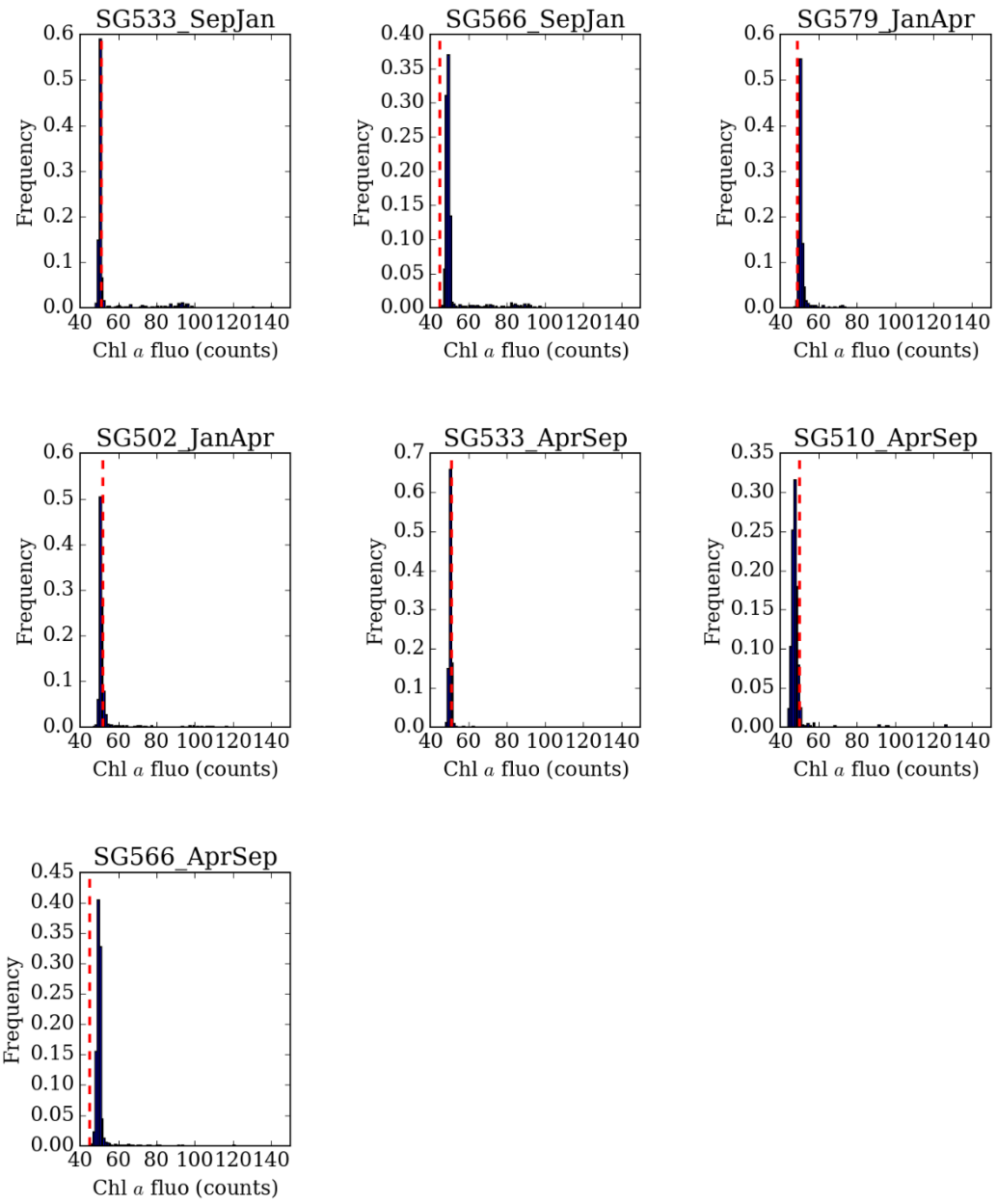

Figure 2.6 Histograms of bottom Chl *a* fluorescence values (median over the deepest 10 m of a profile). Red dashed line on all plots indicates the DC values provided by the glider manufacturer.

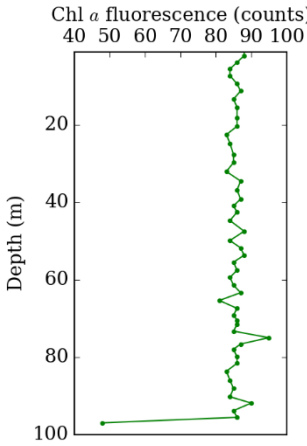

Figure 2.7 An example of an undersampled Chl *a* fluorescence profile collected by glider 566 on the 25th of November 2012.

2.2.3 Quality control

Raw output from the glider fluorescence sensors contained negative values as well extremely high values outside of the realistic range (Figure 2.8), due to instrumental and electronic noise. Therefore, conducting quality control is necessary prior to the scientific analysis of the data. For the Chl *a* fluorescence data quality control, I followed the methodology suggested in "White Book on Oceanic Autonomous Platforms for Biogeochemical Studies: Instrumentation and Measure (PABIM)" (D'Ortenzio et al. 2010). This book summarizes previous experience of the PABIM project team in processing of biochemical data collected by autonomous platforms (such as gliders and profiling floats).

The methodology assigns one of four flags to all Chl *a* fluorescence measurements:

Flag 1 – good data,

Flag 2 – spike,

Flag 3 – potentially correctable data,

Flag 4 – bad data.

Before conducting the quality control, DC was subtracted from all the profiles. Flags were assigned to data based on several tests which assess the quality of the observations.

Test1. Global range

The global range test aims to identify strongly erroneous data in glider fluorescence profiles. This test flags all values outside of a specific range as "bad data". D'Ortenzio et al. (2010) suggested to use 0-50 mg m^3 as a valid range for Chl *a* data collected by autonomous platforms. In the current study, gliders were deployed in the open North Atlantic Ocean generally characterized by Chl *a* concentrations much lower than 50 mg m^{-3}. Therefore, the upper limit of the valid range was reduced. Based on the data distribution (Figure 2.8), the valid data range was set between -5 and 1000 counts (roughly corresponds to Chl *a* concentrations 0-12 mg m^{-3} according to the manufacturer calibrations). Final calibrations using in situ Chl *a* samples (section 2.2.5) changed the range to 0-6.5 mg m^{-3}. Low negative values (from -5 to 0) were observed mostly below the mixed layer depth and corresponded to values slightly lower than determined DC. During the quality control low negative values were assigned to Flag 3 (potentially correctable data). Data that failed the global test were flagged 4.

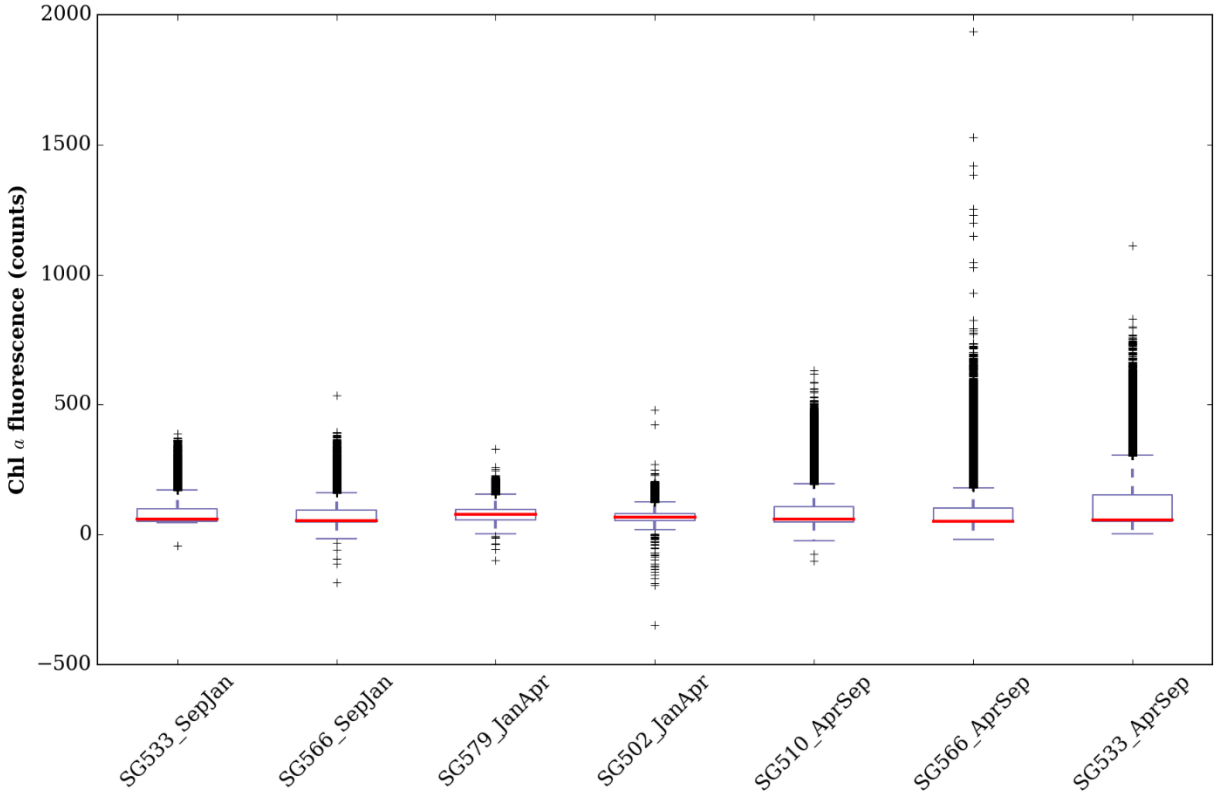

Figure 2.8 Boxplots of raw Chl *a* fluorescence data obtained by the OSMOSIS gliders.

Test2. Spikes

This test aims to identify spikes in Chl *a* fluorescence profiles. Spikes were determined by calculating a "test value" defined as:

$$\text{Test} = |V2 - (V3 + V1)/2| - |(V3 - V1)/2| \quad (2.1)$$

where V2 is a measurement to be tested as a spike, V1 and V3 are the values above and below V2 (D'Ortenzio et al. 2010). Measurements are flagged as spikes when the Test value exceeds a threshold defined as:

$$\text{Threshold} = \text{median}(V0, V1, V2, V3, V4) + \text{std}(V0, V1, V2, V3, V4) \quad (2.2)$$

where VO and V4 are the values respectively above and below V1 and V3. Values which failed the spike test were flagged 2.

After running the tests data points flagged 2 or 4 were replaced with NaN (not-a-number) values. Potentially correctable data points (Flag 3) were replaced with the corresponding evaluated DC values.

Another issue associated with the data set was noted after looking at a time series of water column integrated Chl *a* fluorescence. The time series contained several distinct spikes (Figure 2.9 top). The spikes correspond to "spurious" profiles containing extremely high values of Chl *a* fluorescence compared to other profiles obtained within ~2 hours (Figure 2.9 bottom). This high fluorescence is unlikely explained by biological processes and potentially associated with episodic failure of the ECOpuck fluorometers. The spurious profiles were flagged as "bad data" (Flag 4) and excluded from the subsequent data analysis.

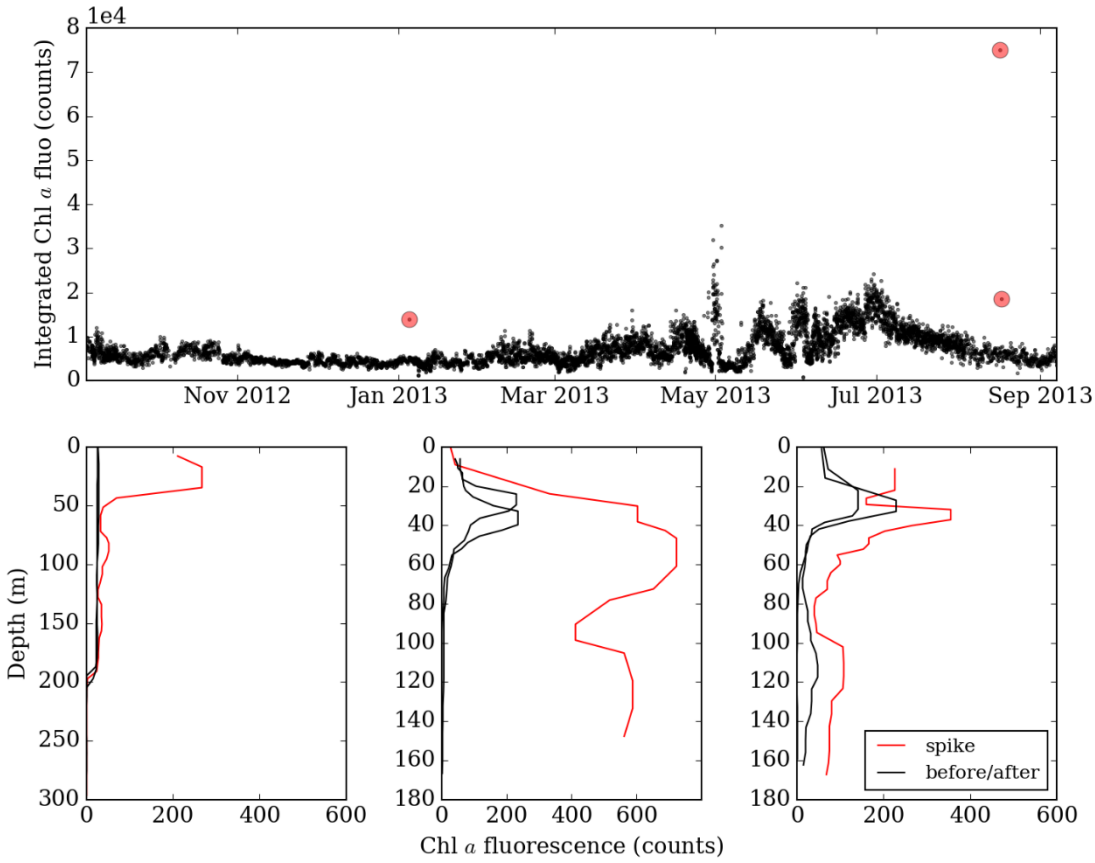

Figure 2.9 Time series of integrated Chl *a* fluorescence (top). Red circles indicate spikes in the time series associated with spurious fluorescence profiles. The spurious profiles are shown at the bottom of the plot (red line). Black lines show fluorescence profiles obtained immediately (within ~2 hours) before and after the spurious profiles.

All Chl *a* fluorescence data obtained from the glider mission before and after quality control are shown in Figure 2.10. The plot shows that the applied quality control procedure significantly reduced the number of spikes in the Chl *a* fluorescence data set.

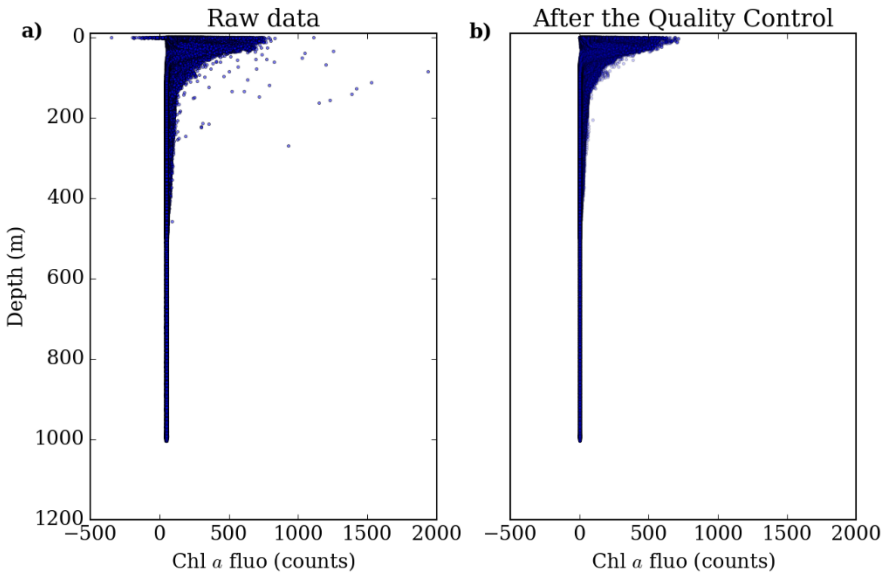

Figure 2.10 Chl *a* fluorescence profiles collected by the OSMOSIS gliders before (a) and after (b) conducting the quality control procedure.

2.2.4 Quenching correction

Marine phytoplankton adapt to fluctuations in solar radiation by changing their pigment composition, pigment morphology and chloroplast shape (Kiefer 1973). These intra-cellular changes can strongly affect fluorescence properties of phytoplankton and result in significant decrease of fluorescence quantum yield during periods of high irradiance (Loftus & Seliger 1975). The diel cycle of in vivo fluorescence is not correlated with diel changes in Chl *a* concentrations and can bias interpretation of fluorescence profiles collected during the daytime. Fluorescence quenching is commonly observed in data sets from autonomous platforms and is a well-known limitation of in vivo fluorescence measurements (Sackmann 2008).

Depression of Chl *a* fluorescence near the surface during daytime was detected in the OSMOSIS glider data set. Daily mean surface (0-20 m) Chl *a* fluorescence for profiles collected between sunrise and sunset was significantly lower compared to the corresponding night-time values (Figure 2.11).

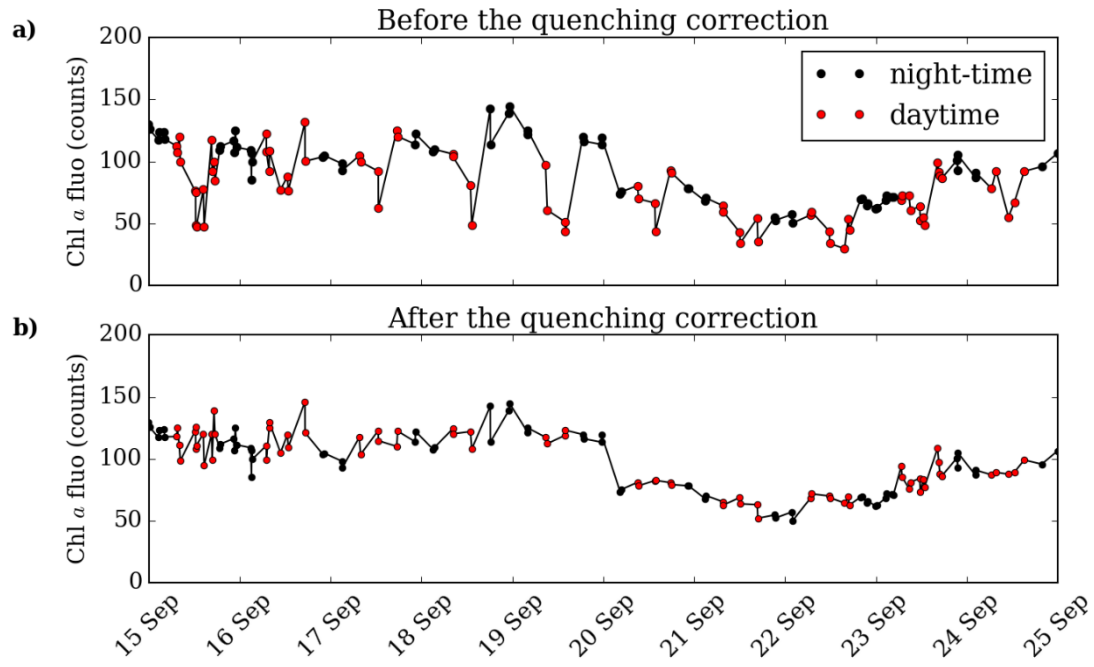

Figure 2.11 Time series of mean surface (0 - 20 m) Chl *a* fluorescence before (a) and after (b) applying quenching correction for a representative 10-day period in September. Black and red dots indicate night-time and daytime profiles respectively.

The ECOpuck triplet mounted on the gliders contained optical backscatter sensors. As shown by previous studies (Stramski et al. 2004), data from optical backscattering sensors correlates well with Chl *a* concentrations in seawater and are not affected by changes in solar irradiance. Based on this fact, Sackmann (2008) proposed to correct quenching in daytime fluorescence profiles using fluorescence to backscatter ratio (FLBS). The quenched part of the Chl *a* fluorescence profile can be corrected by multiplying corresponding values of optical backscatter by FLBS obtained from unquenched fluorescence profiles collected close in time. This approach was implemented in the current work. First, for daytime fluorescence profiles I determined the depth of maximum FLBS ratio within the mixed layer (or the euphotic depth if it was shallower). Following Swart et al. (2014) it was assumed that above this depth the fluorescence profile was affected by quenching. The quenched part of the profile was corrected using mean night-time FLBS ratio within the upper 20 m. An example profile of Chl *a* fluorescence before and after quenching correction is shown in Figure 2.12. Quenching correction significantly decreased the observed offset between surface fluorescence for daytime and night-time profiles and made the values consistent (Figure 2.13).

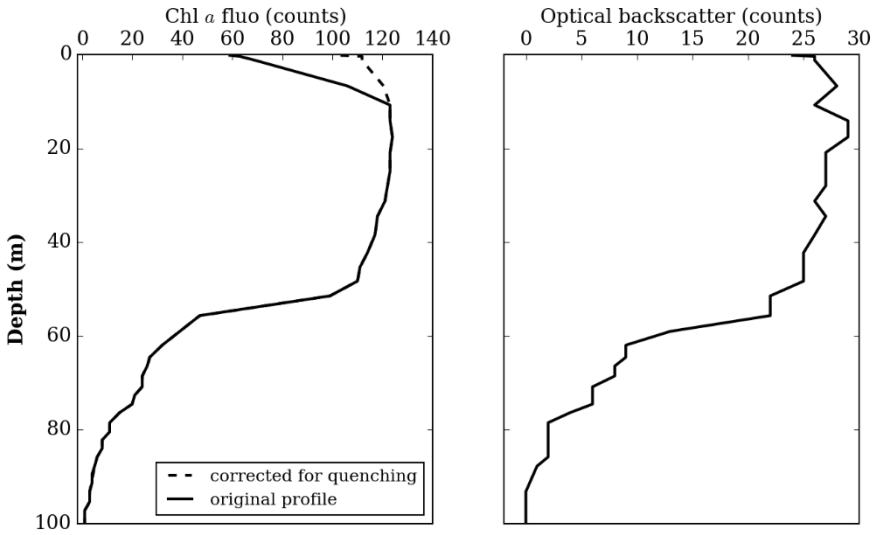

Figure 2.12 An example of applying the quenching corrections to a daytime Chl *a* fluorescence profile: a) Chl *a* fluorescence profile before (solid line) and after (dashed line) quenching correction, b) corresponding profile of optical backscattering. The profiles were collected by glider 566 on September 30 at 10:43.

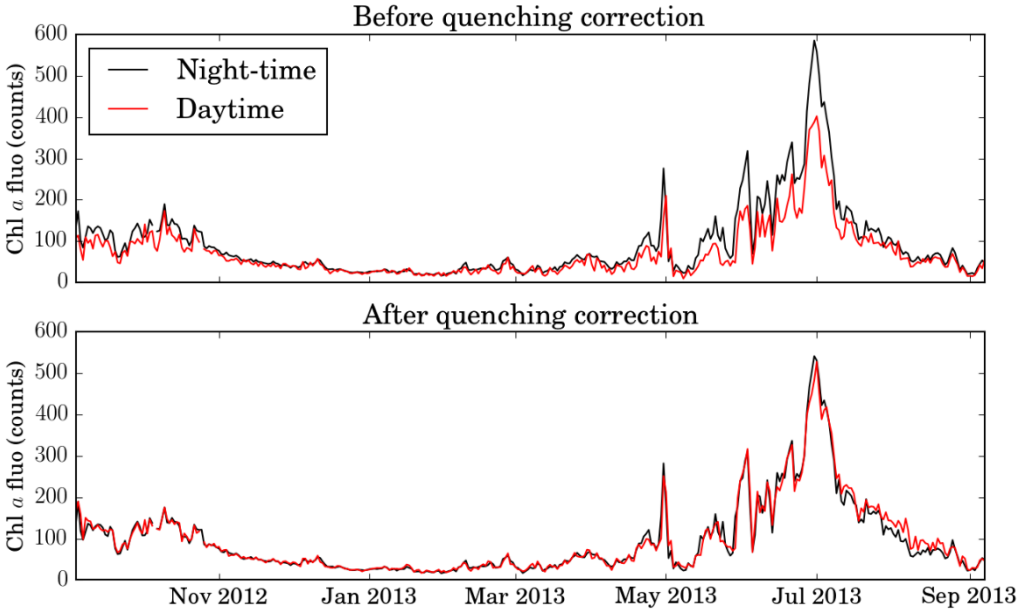

Figure 2.13 Daily mean Chl *a* fluorescence over the upper 20 m calculated separately for daytime (red line) and night-time (black line) profiles before (top) and after (bottom) applying quenching correction for the full year.

2.2.5 Chl *a* fluorescence calibration

Digital counts from fluorescence sensors can be converted to scientifically usable units (Chl *a* in mg m^{-3}) by subtracting dark fluorescence and then multiplying by a scale factor. Manufacturer-provided scale factors are determined based on the sensors' response to a standard solution containing a *Thalassiosira weissflogii* phytoplankton culture of known Chl *a* concentration. However, previous studies (e.g. Frajka-Williams & Rhines 2010) have shown that after applying the manufacturer calibration, Chl *a* concentrations appear high relative to in situ observations and further steps to calibrate the sensor output are necessary.

In this study, the fluorescence sensors on the gliders were calibrated using Chl *a* concentrations obtained from water samples collected from the CTD frame Niskin bottles during the process cruises. Chl *a* concentrations were determined by filtering 250 ml of seawater onto 25 mm GF/F filters (nominal pore size 0.7 µm) and extracting pigments in 90 % acetone at 4 °C over a subsequent 18-20 hours period. The fluorescence of each sample was measured using a Turner Trilogy fluorometer following the method of Welschmeyer (1994).

For each glider, the scaling factor was obtained based on a linear regression of data from co-located glider profiles and CTD casts. CTD and glider measurements of Chl *a* concentrations and fluorescence were matched up in the following way:

- For each CTD cast I selected all glider profiles collected within a time difference less than a day
- For each depth of a CTD profile the corresponding value of glider fluorescence was calculated as a distance-weighted mean of all fluorescence values measured at the same depth (± 5 m).

The calibration outcome (scale factors, the number of match-ups and coefficients of determination) is shown in Figure 2.14-2.17 and summarized in Table 2.2[1].

[1] Chl *a* sampling on cruise CE13001 failed due to mistakes in a sampling protocol.

Table 2.2 Calibration of Chl *a* fluorescence sensors with in situ data obtained during the OSMOSIS cruises (Figure 2.2). Coefficients of determination (R^2) are statistically significant at the 95% confidence intervals.

Glider ID	Manufacturer-provided Scale factor	Re-evaluated Scale factor	R^2	# match ups
D381 cruise (September 2012)				
SG566_SepJan	0.0124	**0.0052**	0.52	64
SG533_SepJan	0.0120	**0.0053**	0.70	33
JC085 cruise (April 2013)				
SG502_JanApr	0.0134	**0.0061**	0.93	19
SG579_JanApr	0.0124	**0.0067**	0.85	19
SG566_AprSep	0.0124	**0.0051**	0.90	42
SG510_AprSep	0.0121	**0.0058**	0.85	43
JC087 cruise (June 2013)				
SG566_AprSep	0.0124	**0.0074**	0.64	135
SG510_AprSep	0.0121	**0.0070**	0.62	87
SG533_AprSep	0.0120	**0.0085**	0.61	135
JC090 cruise (September 2013)				
SG566_AprSep	0.0124	**0.0190**	0.44	36

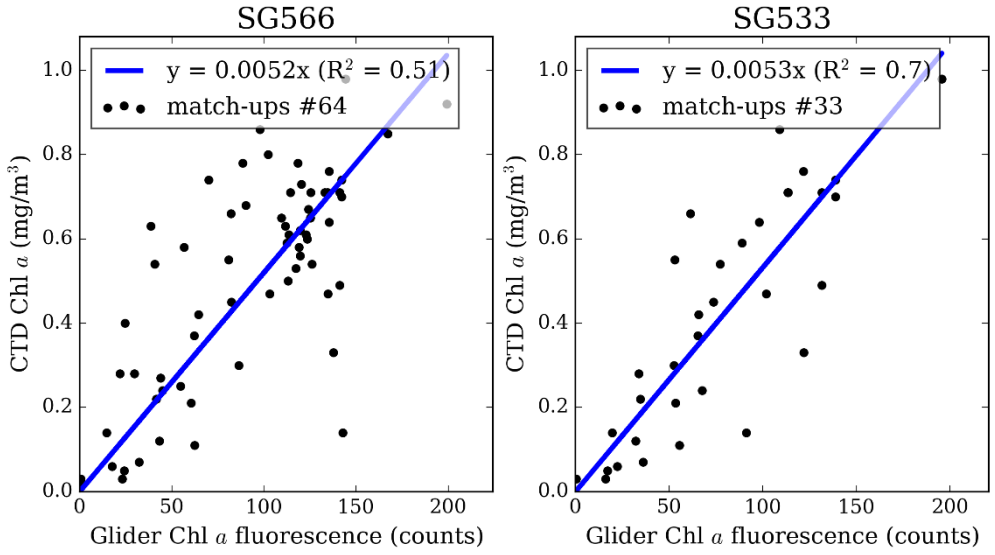

Figure 2.14 Calibration outcome for D381 cruise.

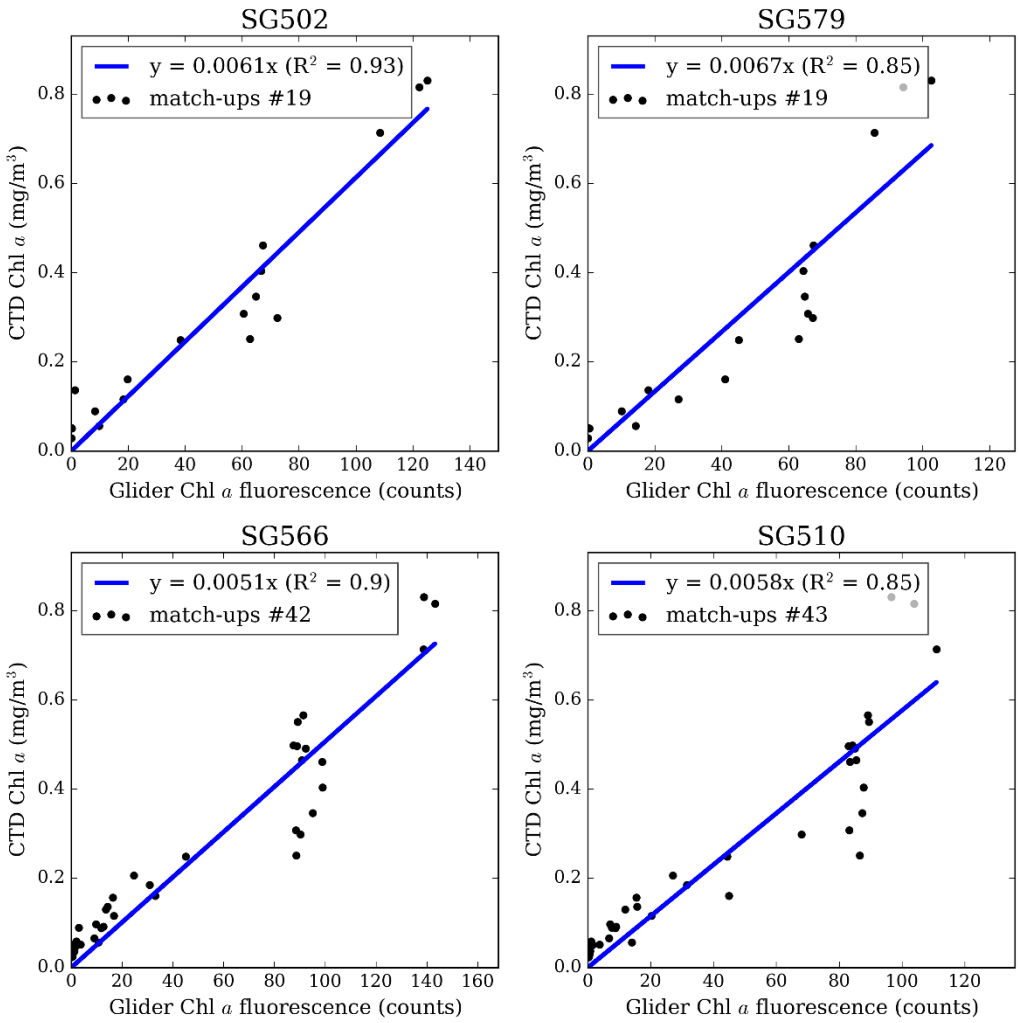

Figure 2.15 Calibration outcome for JC085 cruise.

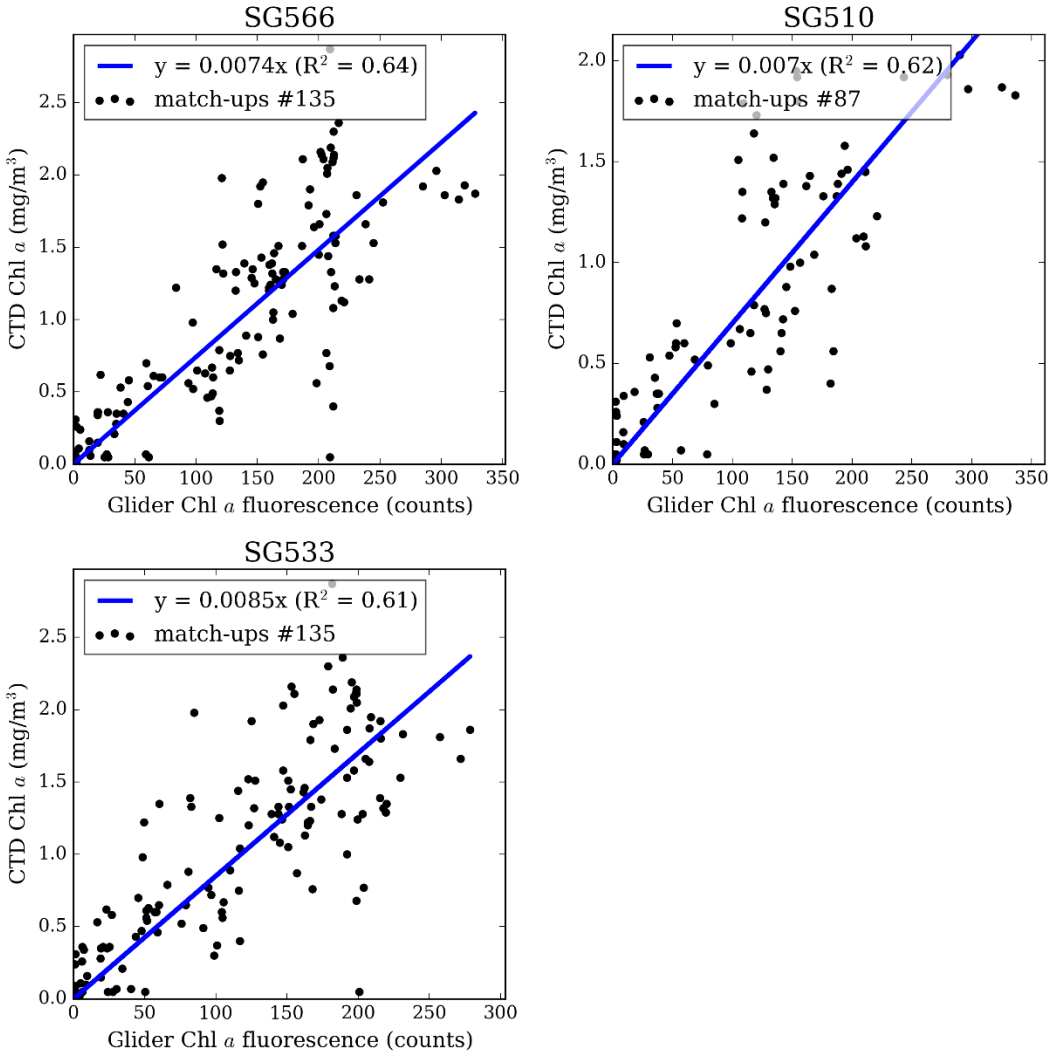

Figure 2.16 Calibration outcome for JC087 cruise.

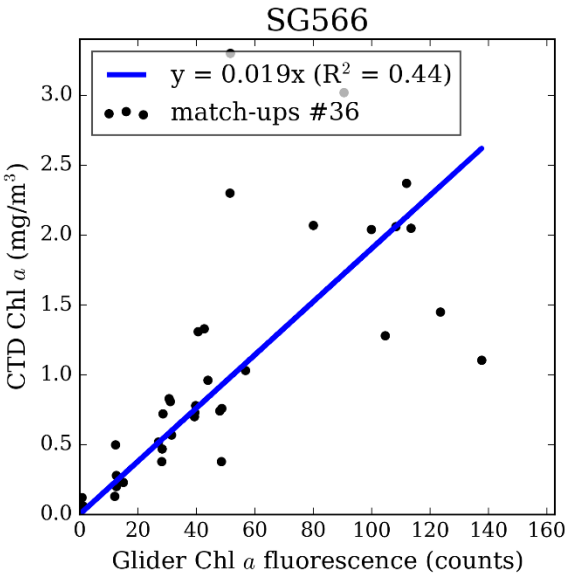

Figure 2.17 Calibration outcome for JC090 cruise.

The scale factors obtained from cruises D381, JC085, JC087 were relatively similar for all the gliders. However, the scale factor obtained from cruise JC090 differed by a factor of ~3. The relationship between Chl *a* concentration and fluorescence can vary throughout the year due to a number of factors such as changes in taxa, physiological state or nutrient conditions (Karabashev & Ohl 1990). Therefore, the outstanding scale factor for JC090 cruise is likely due to a different regime at the sampling site compared to other cruises. A varying relationship between Chl *a* concentrations and fluorescence can introduce uncertainties in the calibration of glider fluorometers. However, this project aims to look at relative changes in Chl *a* concentrations related to physical forcing, light and other drivers rather than evaluate the absolute magnitude of Chl *a*. In this regard, some uncertainties in glider fluorescence calibration are acceptable. The fluorescence was converted to Chl *a* units using the mean scale factor from cruises D381, JC087 and JC087.

To compare satellite and glider measurements of Chl *a*, I estimated daily mean Chl *a* averaged over the intended glider sampling site (Figure 2.3) and daily mean Chl *a* averaged over 100x100 km^2 area around the intended glider sampling site. The comparison between the glider and satellite measurements of Chl *a* is shown in Figure 2.18. There were only 47 days during the glider mission (364 days) when the satellite ocean colour data were available for the glider sampling site and 142 days when satellite ocean colour data were available for the area 100x100 km^2 around the glider sampling site. A number of peaks in surface Chl *a*, particularly in late spring and in summer, were missing in the satellite Chl *a* record. It can be explained by gaps in the satellite data due to the presence of clouds and by the fact that peaks in Chl *a* could be localized in space. For instance, the glider data show a pronounced peak in Chl *a* in the beginning of June (Figure 2.18). However, the satellite data over the glider sampling site only were not available during this time. The satellite-

derived surface Chl *a* data averaged over the larger area does not show a pronounced peak in the beginning of June. This shows that gliders provided a more detailed picture of Chl *a* variability at the PAP site during the year of OSMOSIS mission revealing a number of features missing in the satellite ocean colour data.

Nevertheless, the resulting time series of mean surface Chl *a* was fairly consistent with the corresponding values of surface Chl *a* derived from satellite data (Figure 2.18). Discrepancies between the satellite and glider data can be also explained by changes in fluorescence to chlorophyll ratio, the formation of SCM, phytoplankton patchiness and uncertainties associated with satellite measurements of Chl *a* concentrations. Therefore, calibrated glider fluorescence can be considered as an acceptable representation of Chl *a* concentrations observed at the PAP site during the year of OSMOSIS mission for the purpose of this study.

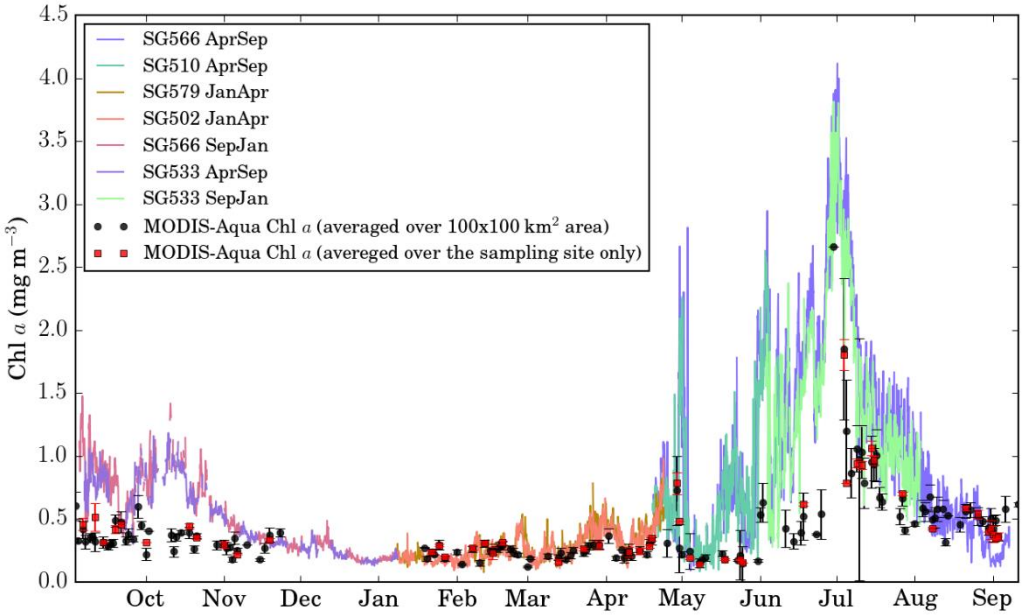

Figure 2.18 Mean surface (0-20 m) Chl *a* derived from the calibrated glider Chl *a* fluorescence measurements and surface Chl *a* concentration from Aqua MODIS satellite averaged over 100x100 km^2 area around the OSMOSIS sampling site (black circles) and averaged over the area corresponding to OSMOSIS sampling site (approximately 20x20 km^2; red circles). Vertical lines correspond to one standard deviation.

2.2.6 Optical backscatter data processing

Processing of the optical backscatter data from the gliders was analogous to the methodology for processing of the Chl *a* fluorescence data and involved the following steps:

- Dark counts re-evaluation (Figure 2.19)
- Data quality control (removing negative values and spikes)
- Detection of spurious profiles

As it can be seen from Figure 2.19, re-evaluated DCs for optical backscatter are significantly higher compared to the manufacturer-provided values. It is explained by the fact, that backscatter signal contains scattering of pure seawater (Dall'Olmo et al. 2009) that is not included in the sensor calibrations provided by the manufacturer. In this study, optical backscatter data were used only to calculate FLBS to correct fluorescence profiles for quenching (section 2.2.4). Therefore, the optical backscatter data were not calibrated against in situ samples.

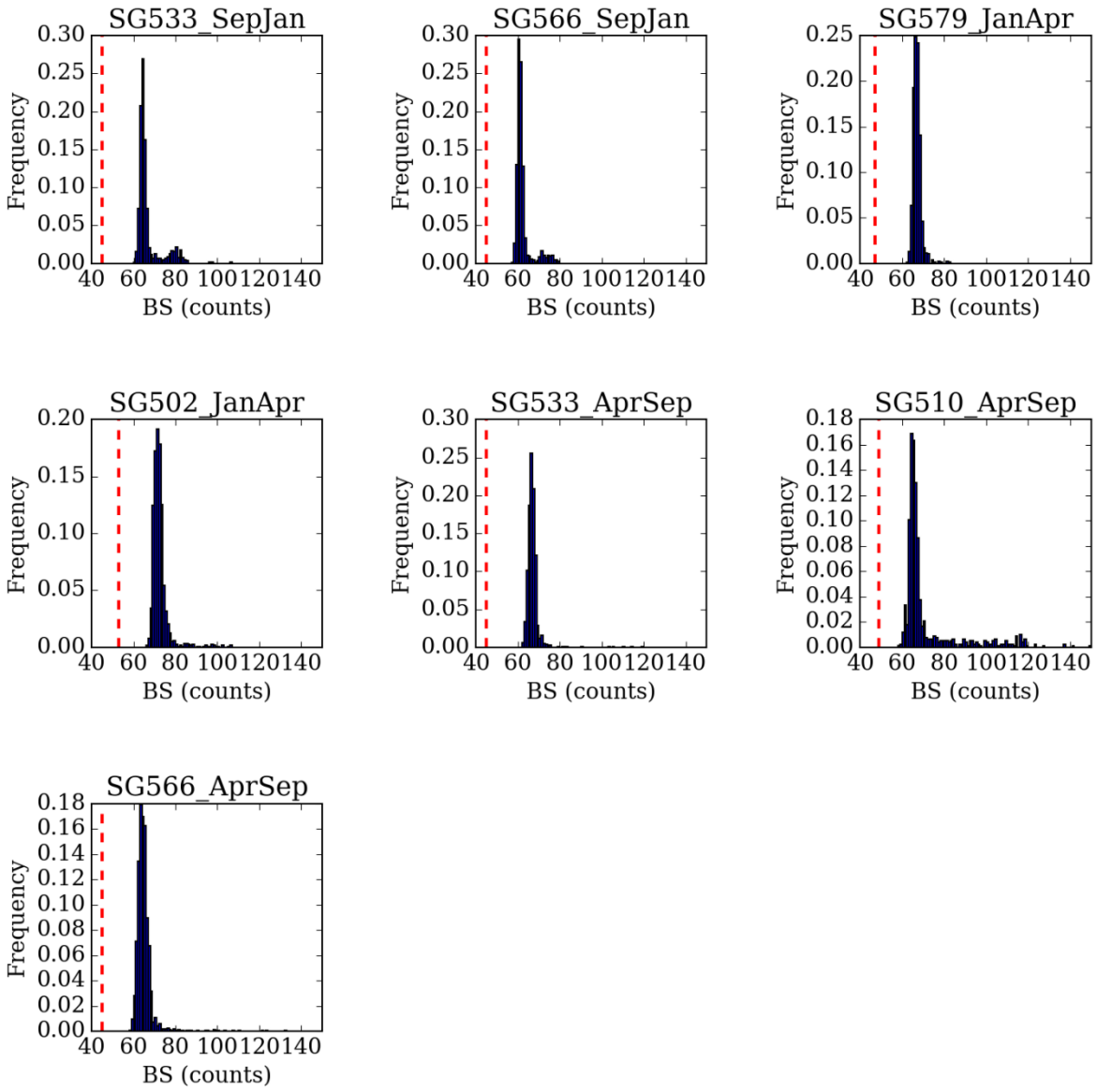

Figure 2.19 Histograms of bottom optical backscatter values (median over the deepest 10 m of a profile) for the OSMOSIS glider deployments. Red dashed line on all plots indicates the values of dark counts provided by the manufacturer.

2.3 Euphotic depth

Estimates of the euphotic depth (defined here as the depth of 1 % of surface irradiance), were obtained from vertical glider profiles of PAR assuming the Lambert-Beer's relationship:

$$E(z) = E_0 e^{-Kz} \tag{2.3}$$

where K is vertical attenuation coefficient of irradiance, E_0 is irradiance just below the sea surface and z is depth. The attenuation coefficients were obtained by fitting an exponential curve to

daytime light profiles (Figure 2.20). By substituting E with $0.01E_0$ in eq. (2.3), the euphotic depth was estimated as 4.6/K.

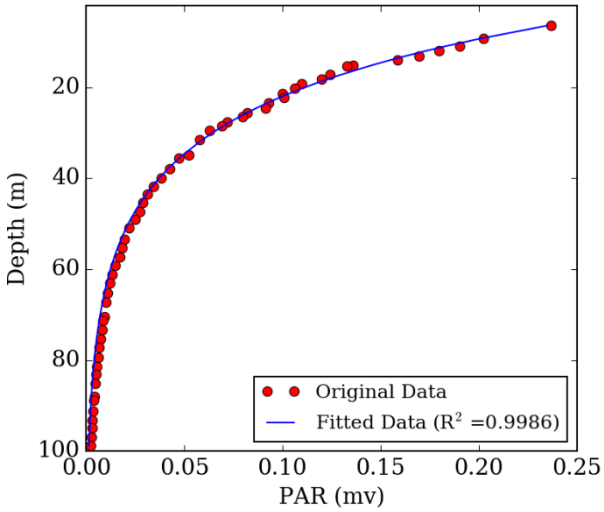

Figure 2.20 An example of an exponential curve (blue line) fitted to a glider PAR profile (red circles) in order to obtain estimates of the euphotic depth and light attenuation coefficient. The PAR profile was obtained by glider 566 on 5 May 2013 at 10:38.

Following Thomalla et al. (2015) exponential curves were fitted only to the part of the profiles above 100 m in order to avoid overfitting to data points in the aphotic layer. For the majority of the profile, the coefficients of determination (R^2) for the curve fitting ranged between 0.90 and 0.99 (Figure 2.21). Vertical PAR profiles with R^2 <0.9 (1% of daytime profiles) were excluded from the subsequent analysis.

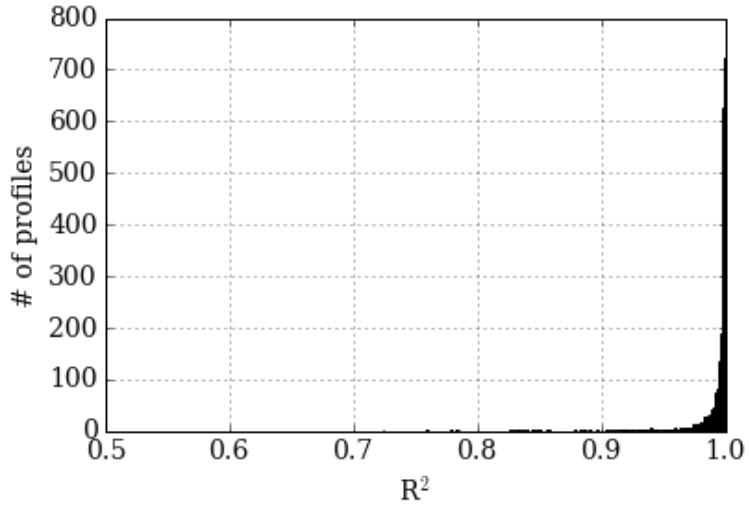

Figure 2.21 Histogram of R^2 for the fitting of exponential curves to the glider PAR profiles.

2.4 Mixed layer depth

The mixed layer depth estimates (provided by Dr. Gillian Damerell) were derived from temperature/salinity glider profiles. The definition of the mixed layer depth was based on de Boyer Montegut et al. (2004) and calculated using two criteria:

- a change in temperature of 0.2 °C relative to the value at 10 m depth
- a change in density of 0.03 kg m^{-3} relative to the value at 10 m depth

For each profile the shallowest value between the two was chosen. Before the calculations the glider salinity data was calibrated with in situ salinity samples and corrected for conductivity cell thermal lag (Garau et al. 2011).

2.5 Additional data sets

Net heat flux. Daily surface heat flux was evaluated using NCEP/NOAA reanalysis data (http://www.esrl.noaa.gov/psd/data/gridded/data.ncep.reanalysis.surfaceflux). Net surface heat flux (Q) was calculated as a sum of net longwave radiation (Q_{lw}), net shortwave radiation (Q_{sw}), sensible heat flux (Q_s) and latent heat flux (Q_l):

$$Q = Q_{lw} + Q_{sw} + Q_s + Q_l \quad (2.4)$$

The spatial resolution of NCEP/NOAA reanalysis data is 2 degrees. The heat flux components were extracted for a grid point centred on 48.6° N, 16.8° W that is the closest point to the sampling site.

Wind data. Daily wind stress data derived from Daily Advanced Scatterometer (ASCAT) Surface Wind Fields (DASCAT) product that implements ASCAT observations and objective time interpolation method in order to obtain regular in space and time daily fields of wind vector fields (Bentamy & Fillon 2012). The spatial resolution of the data is 0.25 degrees. The wind data were extracted for a grid point centred on 48.75° N, 16.25° W.

Ocean colour data. Aqua MODIS Standard Products (http://oceancolor.gsfc.nasa.gov/cgi/l3; Level 3; 4 km resolution) were used to obtain surface Chl *a* in mg m^{-3}. Daily and monthly composite products were used in the project.

Surface PAR data. Aqua MODIS Standard Products (http://oceancolor.gsfc.nasa.gov/cgi/l3; Level 3; 4 km resolution) were used to obtain daily mean photosynthetically available radiation

(PAR; photon flux in E m^{-2} d^{-1}) at the ocean surface averaged over the sampling site. PAR values near the surface were not properly resolved in the glider data set since the gliders perform a surfacing manoeuvre in the upper 10 m of the water column. Therefore, surface PAR values derived from the satellite products were used instead.

Inorganic nutrients. Sampling for inorganic nutrient concentrations was undertaken on cruises D381, JC087 and JC090 from both CTD casts and the underway non-toxic seawater supply (approximate intake depth is 5 m). Analysis of nitrate+nitrite (hereafter nitrate) concentrations was conducted using a Skalar-Sanplus autoanalyser and the method described by Kirkwood (1994). Analysis of the samples was undertaken by Mark Stinchcombe and Dr. Stuart Painter.

Chapter 3: One year of the glider data

The OSMOSIS glider mission provided a unique year long data set of vertical profiles of biophysical properties and light at the PAP site. This chapter presents an exploratory analysis of the data set. The annual cycles of Chl *a* variability, mixed layer depth (hereafter z_{mixed}), euphotic depth (hereafter z_{eu}), net heat flux (hereafter Q) and wind stress (τ) are presented. Nutrient data obtained during cruises D381, JC087 and JC090 are shown. General patterns observed in the data are described. Scientific questions addressed in Chapters 4, 5 and 6 are stated.

3.1 Observed annual cycles

High-resolution glider measurements provided a detailed picture of Chl *a* variability at the PAP site over the annual cycle. Evolution of Chl *a* and z_{mixed} during 3 rotations of the glider mission (Figure 2.2) is shown in Figure 3.1. Time series of surface Chl *a* (hereafter *S*(Chl *a*)), integrated Chl *a* (hereafter *I*(Chl *a*)), z_{eu}, Q and τ are shown in Figure 3.2.

Rotation 1: September - January

This part of the time series captures evolution of phytoplankton populations from September until January. At the start of the mission z_{mixed} was ~30 m deep and shallower than z_{eu} that was ~ 50 m (Figure 3.2c). Until mid-September meteorological conditions were characterized by low wind forcing (τ < 0.2 N m^{-2}; Figure 3.2e) and predominantly net warming of the ocean surface (Q ≈ 0 - 100 W m^{-2}; Figure 3.2d). In the second half of September wind forcing increased dramatically with τ reaching 0.4 N m^{-2} (Figure 3.2e) indicating a passage of a storm over the sampling site. Following the storm event, both *I*(Chl *a*) and *S*(Chl *a*) increased by a factor of ~2 (Figure 3.2a and Figure 3.2b). From October onwards, frequent passage of storms (with τ > 0.4 N m^{-2}) and predominantly net cooling of the ocean surface were observed. Under these meteorological conditions, z_{mixed} gradually deepened below z_{eu} and reached ~200 m by the end of December (Figure 3.2c). As a result, *S*(Chl *a*) and *I*(Chl *a*) decreased from 1.0 mg m^{-3} to 0.2 mg m^{-3} and from 40 mg m^{-2} to 10 mg m^{-2} respectively.

Rotation 2: January – April

The second rotation of the glider mission captured the evolution of the phytoplankton populations during winter and spring. During this time, z_{mixed} ranged between 100 and 400 m (Figure 3.1b) and consistently remained below z_{eu} that varied between 70 and 100 m (Figure 3.2c). *S*(Chl *a*) and *I*(Chl *a*) remained relatively low (0.1-0.2 mg m^{-3} and 10-30 mg m^{-2} respectively) until the

beginning of February (Figure 3.2a and Figure 3.2b). From February onwards pulses of phytoplankton growth can be observed in the Chl *a* data (Figure 3.1b). The meteorological conditions during this period varied substantially. From February until the end of April Q varied between -300 and 100 W m^{-2} and τ changed between 0.05 and 0.9 N m^{-2}. The time series of I(Chl *a*) and S(Chl *a*) indicate a gradual accumulation of phytoplankton stocks and an increase in surface Chl *a* concentrations over February, March and April (Figure 3.2a and Figure 3.2b). At the end of the rotation, when τ decreased below 0.2 N m^{-2} (Figure 3.2e), Q increased above 100 W m^{-2} (Figure 3.2d) and z_{mixed} shoaled above 100 m (Figure 3.1a). The latter corresponds to the formation of seasonal stratification under net warming of the ocean surface and low wind forcing.

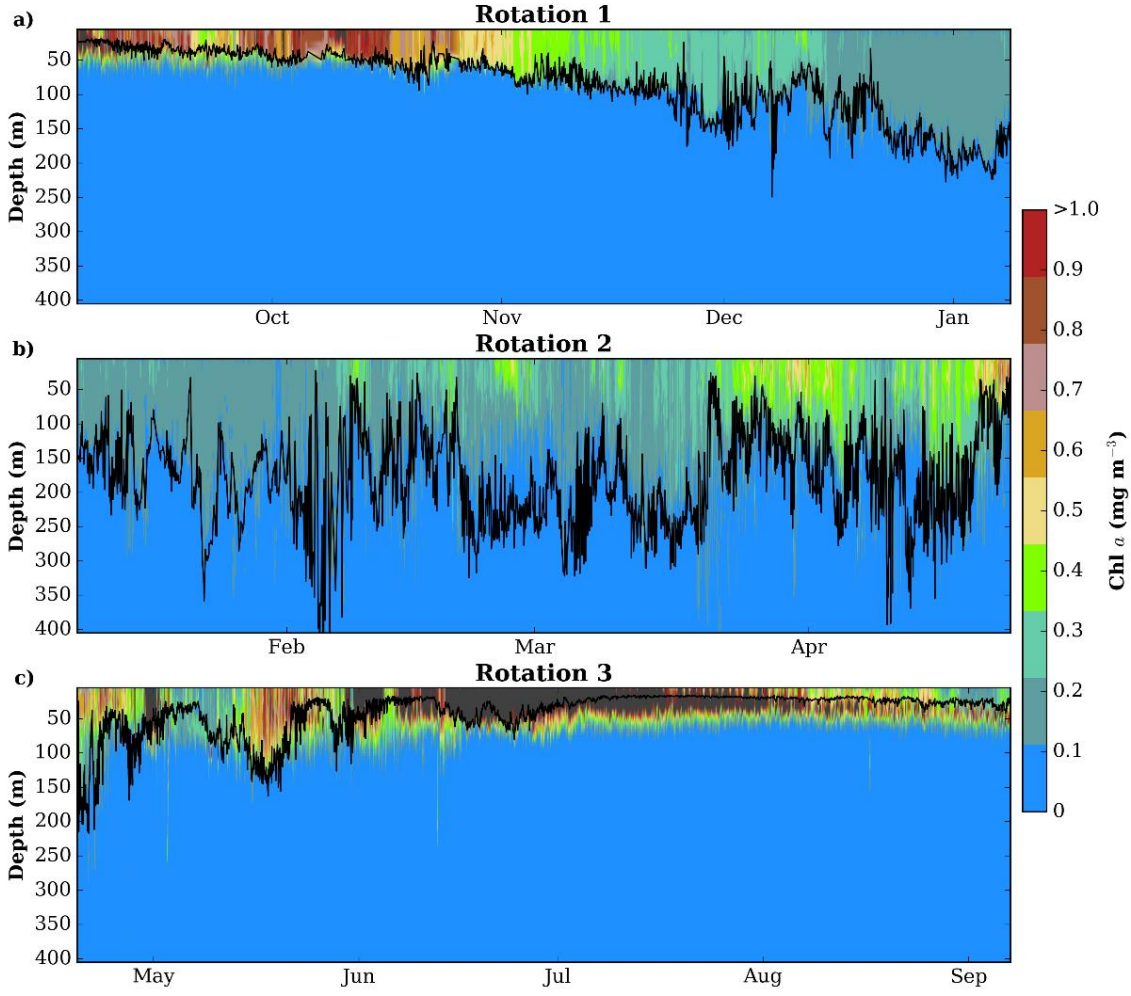

Figure 3.1. Evolution of Chl *a* concentration (colour-coded) during the 3 rotations of the OSMOSIS glider mission: September - January (a), January - April (b), April - September (c). Black lines on the plot correspond to the mixed layer depth.

Rotation 3: April – September

The third rotation of the glider mission captured phytoplankton variability in relatively shallow z_{mixed} (Figure 3.1c). During this time, z_{mixed} was predominantly less than 50 m. Deepening of z_{mixed} was observed in May and June (Figure 3.2c) and correlated well with increases in wind forcing (Figure 3.2e). Chl *a* data obtained during the third rotation indicated complex phytoplankton dynamics (Figure 3.1a, Figure 3.2a, Figure 3.2b). Following the rapid shoaling of z_{mixed} at the end of April, *S*(Chl *a*)/*I*(Chl *a*) first increased to 0.6 mg m^{-3}/60 mg m^{-2} and subsequently to 2 mg m^{-3}/100 mg m^{-2} for a short period of time in the beginning of May (Figure 3.2a and Figure 3.2b). Later, *S*(Chl *a*) and *I*(Chl *a*) rapidly decreased to 0.2 mg m^{-3} and 10 mg m^{-2} respectively. Short-term phytoplankton blooms emerged in mid-May and early June (Figure 3.2c). The highest *S*(Chl *a*) were observed in the beginning of July (~3.5 mg m^{-3}; Figure 3.2a) when z_{mixed} was ~20 m and z_{eu} was ~40 m (Figure 3.2c). The bloom in July subsequently evolved to a SCM that remained at the sampling site until the end of the mission (Figure 3.1c).

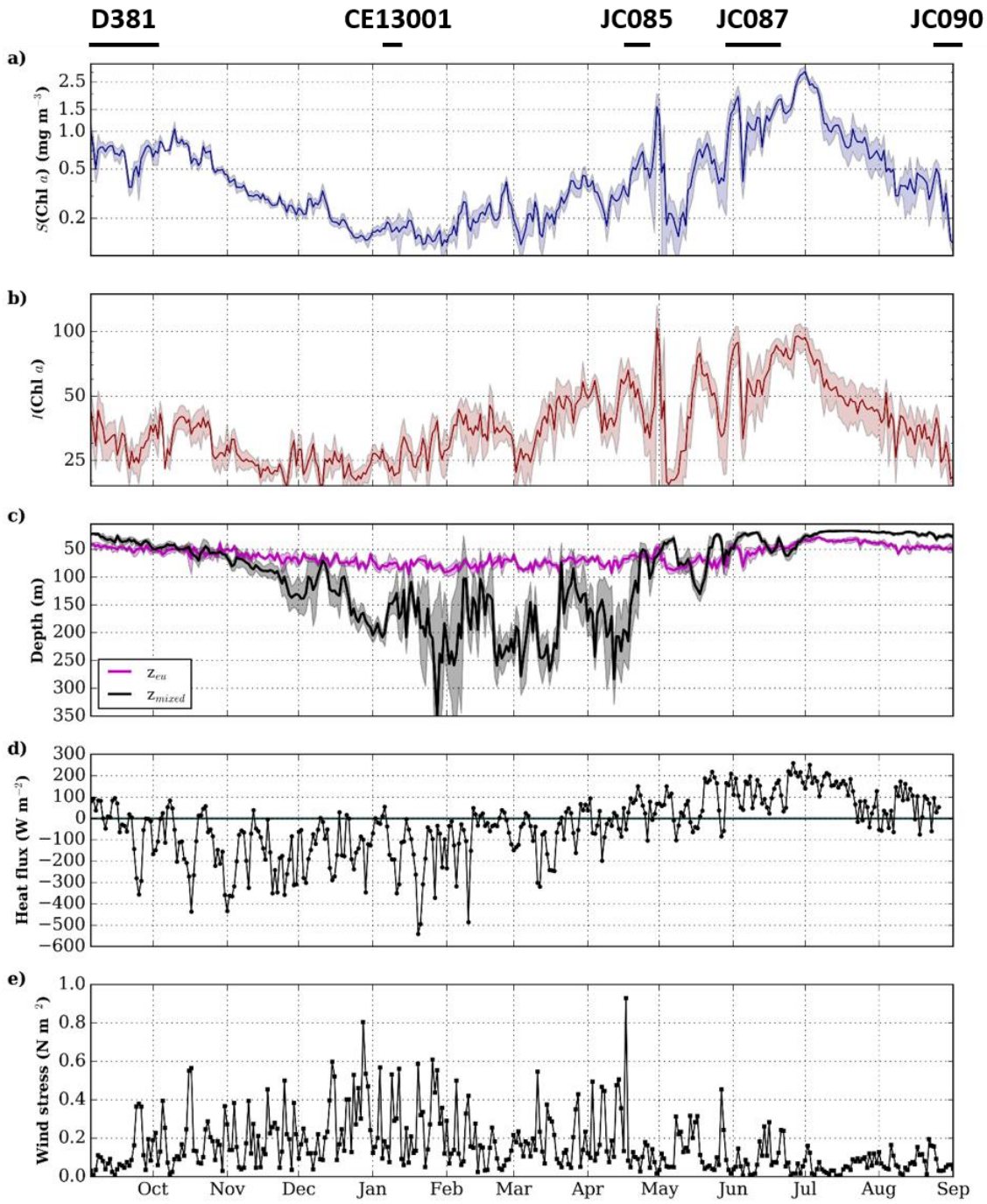

Figure 3.2 Full annual time series of a) daily-mean glider surface (calculated as mean over the upper 20 meters) Chl *a* (±std; blue), b) daily mean glider integrated Chl *a* (±std; red), c) daily-mean mixed layer depth (±std; black) and euphotic depth (±std; violet), d) daily surface heat flux and e) daily wind stress.

3.2 Nutrient data

Figure 3.3 shows nutrient data obtained during cruises D381, JC087, JC090. During cruise D381 (September 2012) nitrate concentrations at the surface varied between 0.1 and 0.5 mmol m^{-3}. Data from JC087 cruises indicated that the nitrate was not completely utilized by June: surface nitrate concentrations ranged between 2 and 6 mmol m^{-3}. In turn, data from JC090 show that nitrate was depleted in the ocean surface layer in the following September. A pronounced nutricline can be observed between 40 and 80 m. The depletion of nutrients might be related to the intense bloom in July. The SCM observed at the sampling site during the third rotation can be associated with accumulation of phytoplankton in the vicinity to the nutricline and at the base of the euphotic depth (Figure 3.2c).

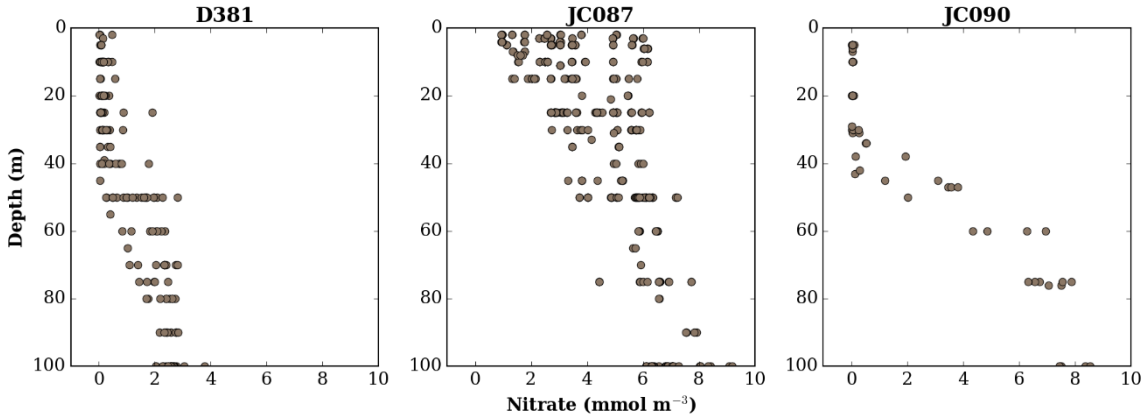

Figure 3.3 Nutrient data obtained from the water samples collected from CTD frame Niskin bottles during D381, JC087 and JC090 cruises.

3.3 Analysis outline for Chapters 4, 5 and 6

The glider data indicated that the year of the OSMOSIS mission at the PAP site was characterized by interesting phytoplankton dynamics: the storm-induced bloom event in autumn, prolonged growth of phytoplankton in deep mixed layers under variable weather conditions, lack of a pronounced bloom associated with the rapid seasonal shoaling of z_{mixed} in spring and short-term sporadic blooms in shallow mixed layers. The scientific questions addressed in the next chapters are stated below.

Chapter 4 analyses the impact of the storm event at the end of September on nutrient fluxes and phytoplankton growth. The analysis of glider observations was complemented by the nutrient, turbulence and meteorological data collected during D381 cruise. Parts of the chapter were

previously published as Rumyantseva et al. (2015), “Ocean nutrient pathways associated with the passage of a storm”, Global Biogeochemical Cycles 29(8), 1179–1189. The paper is included in Appendix 1.

The data showed that the phytoplankton bloom in winter and spring developed in deep mixed layers under variable weather conditions. These observations contradict with Sverdrup’s assumption that spring blooms start when z_{mixed} rapidly shoals in spring due to the onset of surface heating. Which hypothesis can explain the onset of phytoplankton growth in deep mixed layers? Chapter 5 is focused on winter to spring transition and corresponding phytoplankton dynamics observed by the gliders. Variability in mixing regimes corresponding to changes in atmospheric forcing is analyzed. The three widely discussed hypotheses, CDH, CTH and DRH, are tested. The impact of meteorological conditions on phytoplankton specific growth rates and the bloom development is also addressed.

In Chapter 5, the analysis of mixing regimes and their impact on light conditions experienced by phytoplankton mainly focuses on bottom up processes controlling the bloom onset. But, could grazing be responsible for shaping the complex phytoplankton dynamics observed by the gliders? Chapter 6 addresses the potential role of zooplankton grazing in the observed phytoplankton variability during winter and spring. The glider data was complemented by a simple phytoplankton-zooplankton population dynamics model in order to retrieve potential variability in zooplankton grazing underlying the observations.

The most intense phytoplankton bloom formed in shallow z_{mixed} in the beginning of July. Even though this event is of high scientific interest, analysis of mechanisms underlying the July bloom is beyond the scope of this study.

Chapter 4: Storm-induced autumn phytoplankton bloom at the PAP site

Phytoplankton response and nutrient fluxes associated with the storm passage at the end of September 2012 are examined in this chapter. The contribution of storms to local nutrient budgets is assessed. Processing of ocean microstructure data collected during D381 cruise was conducted by Dr. Natasha Lucas (University of Bangor). Parts of the chapter were previously published as Rumyantseva et al. (2015), "Ocean nutrient pathways associated with the passage of a storm", Global Biogeochemical Cycles 29(8), 1179–1189.

4.1 Introduction

Primary production in the temperate and subpolar North Atlantic Ocean plays a crucial role in the global carbon cycle. However, the precise physical mechanisms that supply nutrients to support observed levels of annual primary production and the relative importance of these mechanisms are under debate (McGillicuddy et al. 2003; Oschlies 2002). Many studies have focused on the impact of mesoscale and submesoscale dynamics (Lévy et al. 2012; Martin & Richards 2001; McGillicuddy et al. 1998), the transport of nutrients by major ocean currents (Pelegrí et al. 2006) and winter convection (Williams et al. 2000) as pathways for nutrient supply to support primary production. However, less attention has been given to nutrient fluxes associated with the passage of storms.

Strong wind forcing can be particularly important during the post-spring bloom period when the surface ocean is nitrate-depleted and a well-established pycnocline inhibits the upward flux of nutrients to the euphotic zone. Under these conditions primary production is predominantly fuelled by regenerated forms of nitrogen such as ammonium and urea unless physical re-supply of nutrients occurs. Satellite observations of episodic storm events in summer and autumn have been linked to subsequent phytoplankton increases in otherwise nutrient limited conditions (Babin et al. 2004; Son et al. 2006; Wu et al. 2008). At the same time, it remains uncertain, if the increase in surface Chl *a* is driven by in situ growth or redistribution of phytoplankton from an SCM (Perry et al. 2008; Foltz et al. 2015).

The passage of a storm can initiate transport of nitrate from the ocean interior to the euphotic zone in several ways. The classic interpretation of the wind-induced nutrient supply is that enhanced vertical mixing during strong wind forcing breaks down vertical stratification, erodes the

pycnocline and entrains nutrient rich deeper water into the mixed layer (Findlay et al. 2006; Marra et al. 1990).

Another pathway, rarely documented in observational data, is associated with the interaction between wind stress and surface layer currents, resulting in an intermittent pulsed nutrient flux through the pycnocline (Rippeth et al. 2009). Abrupt changes in wind stress induce near-inertial oscillations (Pollard 1980) that can last for several days before decaying. When the directions of wind stress and these near-inertial oscillations align, enhanced shear production can be sufficient to generate turbulence through Kelvin-Helmholtz instabilities such that the energy dissipation rate across the pycnocline can increase by an order of magnitude (Lenn et al. 2011; Rippeth et al. 2005). This mechanism, referred to as shear-spiking, has been shown to produce near-inertial pulses of high turbulent nitrate flux across the pycnocline (compared to typically low background levels) by previous interdisciplinary studies in temperate shelf seas (Rippeth et al. 2009; Williams et al. 2013). Shear spiking can supply nutrients during high wind forcing as well as in the post-storm period when inertial currents persist in the water column. Open ocean in situ observations of this process have been limited since they require coincident measurements of ocean microstructure and currents over several days.

This chapter presents direct observations of the flux of nutrients to the surface layer resulting from the passage of the autumn storm in the North Atlantic Ocean. Specifically, I show that the storm passage initiated net growth of phytoplankton and quantify the nutrient flux during the storm and additional supply of nutrients after the storm passage associated with the shear-spiking mechanism. The efficiency of the overall storm-induced nutrient supply is compared to other more widely recognised mechanisms in order to assess the storm's contribution to the nutrient budget of the North Atlantic Ocean.

4.2 Data and methods

4.2.1 Observational study

This work is based on an interdisciplinary data set collected aboard RRS Discovery (cruise D381). The sampling campaign was carried out from 31st of August until 1st of October 2012 (year days 244 to 275).

The observations (Figure 4.1) included turbulence measurements using a MSS90 microstructure profiler, standard CTD (conductivity, temperature, depth) profiling using a SeaBird

911, current measurements using a vessel-mounted RDI "Ocean Surveyor" 75 kHz ADCP (Acoustic Doppler Current Profiler), underway water samples from the non-toxic seawater supply (approximate intake depth of 5 m) and surface meteorology. Additionally, the gliders provided vertical profiles of biophysical properties of the ocean boundary layer over the duration of the cruise and beyond. Sampling for inorganic nutrient concentrations was undertaken from both CTD casts and the underway non-toxic seawater supply.

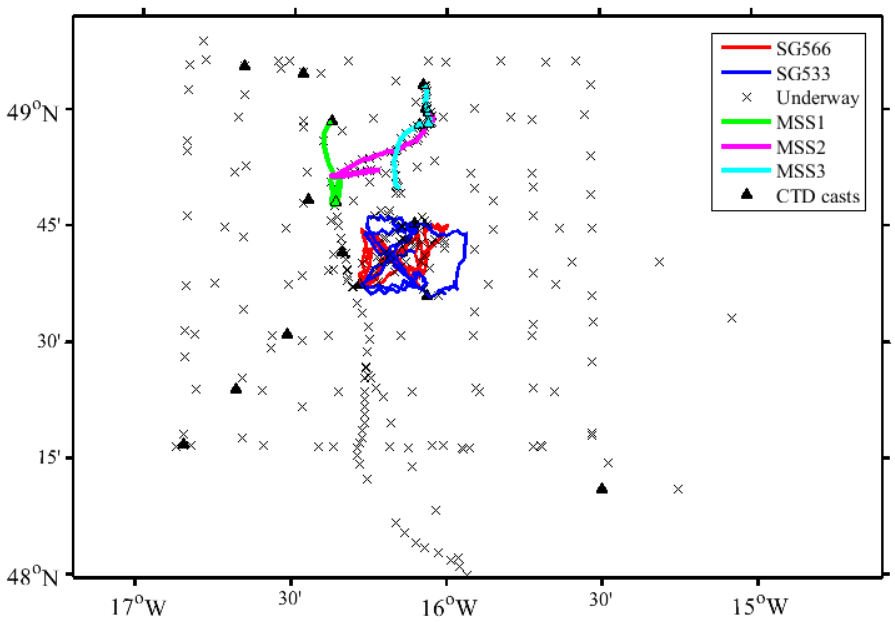

Figure 4.1 Sampling map for cruise D381: gliders 566 and 533 (red and blue lines respectively); underway samples (grey crosses); three series of turbulence measurements: MSS1 (green line), MSS2 (magenta line), MSS3 (light blue line); CTD casts (black triangles).

4.2.2 Turbulent nitrate flux calculations

Estimates of the nitrate flux through the pycnocline were based on vertical profiles of turbulent kinetic energy dissipation. During the course of the cruise, 3 series of turbulence measurements extending to a depth of ~ 200 meters were conducted:

MSS1 - from year day 260.9 to 262.5 (238 profiles)

MSS2 - from year day 265.3 to 266.5 day of year (202 profiles)

MSS3 - from year day 270.8 to 272.0 day of year (175 profiles)

Estimates of the turbulent kinetic energy dissipation rate (ε) were obtained from raw shear data using the MSSPRO software standard processing sequence. All data from the MSS probe for each profile were averaged into 1-m bins. For each bin the vertical eddy diffusivity was calculated from the energy dissipation rate following Osborn (1980):

$$D = 0.2\frac{\varepsilon}{N^2}, \tag{4.1}$$

where *D* is the eddy diffusivity and *N* is the buoyancy frequency. Subsequently, nitrate flux at depth z_d can be defined through multiplying the diffusivity term by the local nitrate gradient:

$$F_{NO_3} = D\frac{\partial NO_3}{\partial z}\Big|_{z=z_d} \tag{4.2}$$

where NO_3 is the nitrate concentration. Following Sharples et al. (2007), CTD bottle data were used to derive a nitrate-density relation and obtain vertically resolved profiles of $\frac{\partial NO_3}{\partial z}$. I found a strong linear relationship between density and nitrate (Figure 4.2a; R^2 = 0.88, p-value < 0.0001) allowing nitrate gradients to be represented in equation (4.2) as $m\frac{\partial \rho}{\partial z}$, where ρ is density measured by the microstructure profiler and *m* = 2.4 ± 0.1 mmol N m^{-3} (kg m^{-3})$^{-1}$ is the nitrate-density gradient. Representative vertical profiles of density and nitrate are shown in Figure 4.2b. Uncertainty associated with the estimated nitrate-density gradient (~5 %) is negligible compared to uncertainties associated with eddy diffusivity measurements in the ocean; therefore m = 2.4 mmol N m^{-3} (kg m^{-3})$^{-1}$ was used in the further calculations of the nitrate flux.

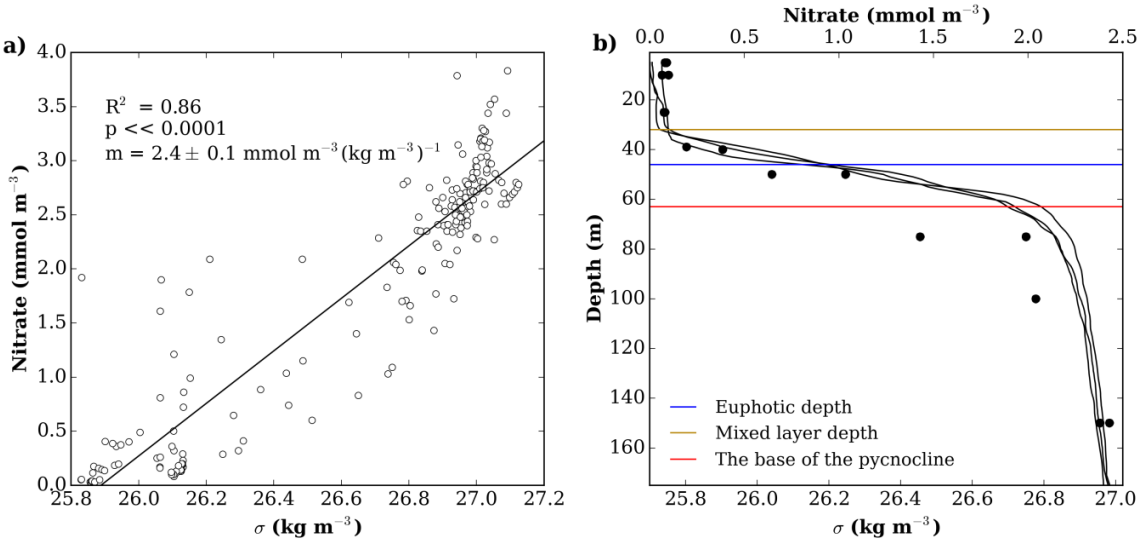

Figure 4.2 a) The nitrate-density relationship within the pycnocline for all CTD casts collected during D381 cruise. *m* is the slope of the linear regression ± 95% confidence intervals. b) CTD profiles collected close in time (decimal days 264-265) illustrating vertical distribution of density

(black lines) and nitrate (black circles) during D381 cruise. Horizontal lines on the plot indicate corresponding mean values of the euphotic depth (blue), mixed layer depth (yellow) and the base of the pycnocline (red).

4.2.3 Bulk shear estimation and theoretical model

Episodic bursts of shear, attributed to alignment and interaction of shear and wind forcing, have been quantified for the open ocean using a modified shear production model as described in Brannigan et al. (2013), which is adapted from a prognostic expression derived from one dimensional momentum equations for stratified tidal shelf seas (Burchard & Rippeth 2009). In this model the authors define a two layer damped-slab model, with the relationship between velocity and bulk shear as:

$$\vec{s} = \frac{\overrightarrow{U_{\mathrm{M}}} - \overrightarrow{U_{\mathrm{L}}}}{h_s} \tag{4.3}$$

where $\overrightarrow{U_{\mathrm{M}}}$ and $\overrightarrow{U_L}$ are the velocities in the mixed layer (z_{mixed}) and lower layer (z_{L}) respectively and h_s is the distance between the centres of mass of these layers, separated by a pycnocline layer. I define a variable pycnocline as the layer between z_{mixed} and the base of the pycnocline. The base of the pycnocline was determined following Johnston & Rudnick (2009), as the depth below the mean mixed layer depth of the deepest isopycnal within one standard deviation of the mean mixed layer depth. In this model the lower layer was defined as a 48 m deep layer immediately below the base of the pycnocline, as this limit was large enough to capture the slab dynamics while falling within the ADCP bin resolution.

Following the derivation in Brannigan et al. (2013) and using the slab layers defined here, a relationship for the rate of change of bulk shear squared with respect to time is obtained with the production or destruction of shear being brought about by the relative orientation between wind and bulk shear directions:

$$\frac{\partial s^2}{\partial t} = 2\left(\frac{\vec{s}}{h_s}\frac{\vec{\tau}}{\rho_0 H} - c_d \frac{h_s}{z_{\mathrm{mixed}}}|s^3|\right), \tag{4.4}$$

where c_d is the drag coefficient, $\vec{\tau}$ is the wind stress and ρ_0 is a reference density. When the dot product is greater than zero (i.e. $\cos(\vec{s},\vec{\tau}) > 0$), directions of wind and shear are favourable for enhanced shear production. If the wind magnitude is constant, the maximum shear production occurs when $\vec{s}$ and $\vec{\tau}$ align.

4.3 Results

4.3.1 Surface dynamics

Atmospheric conditions during the cruise were characterized by the storm that started on day 268 (24th of September 2012) and continued until day 270.6 (27th of September 2012) with typical wind forcing 0.3-0.4 N m^{-2} (Figure 4.3a). Underway nutrient and glider Chl *a* fluorescence data suggest a biochemical response to the storm event (Figure 4.3b, 4.3c). The surface nitrate concentration after the storm had increased from <0.1 mmol N m^{-3} to almost 0.6 mmol N m^{-3}. The time series of change in integrated Chl *a* (*d*(Chl *a*)) showed that replenishment of the surface layer with nutrients was coincident with increased phytoplankton stocks (i.e. *d*(Chl *a*) > 0). The pre-storm period was characterized by mostly negative *d*(Chl *a*) (Figure 4.3d) due to lack of nutrients within the mixed layer (Figure 4.3b) and therefore decreasing phytoplankton growth rate representative of typical conditions in the high latitude North Atlantic Ocean over the post-spring bloom period. Figure 4.4 shows daily mean vertical profiles of Chl *a* collected before, during and after the storm event. Changes in the vertical distribution of phytoplankton show that the storm that started on day 268 eroded SCM observed during days 259-267. The post-storm vertical distribution of phytoplankton was predominantly uniform within the mixed layer.

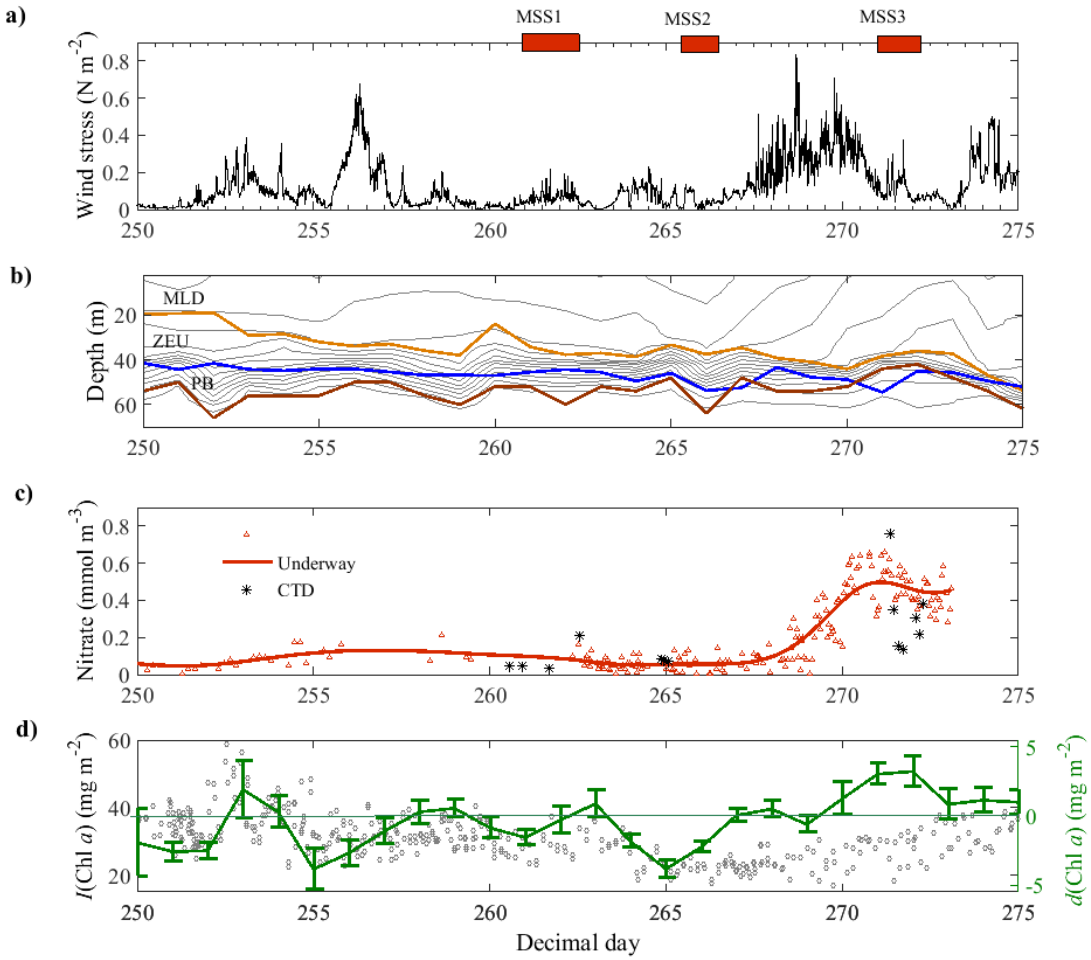

Figure 4.3 Wind and biophysical data collected during cruise D381. a) 10-mins averaged wind stress obtained from the weather station on RRS Discovery. Red rectangles at the top show the timing of three series of turbulence measurements: MSS1, MSS2, MSS3. b) The gliders time series of isopycnal surfaces (grey lines), mixed layer depth (MLD) defined as a temperature differential of 0.2 °C from 10 m depth (orange line), euphotic depth (ZEU; blue line) and the base of the pycnocline (PB; brown line). c) Surface nitrate variability during the cruise: red triangles are surface (~5 m) nitrate concentrations from the ship underway system and the red solid line is fitted smooth spline. Black stars represent mean nitrate concentration within the mixed layer estimated from CTD casts. d) Integrated Chl *a* (*I*(Chl *a*); grey circles) and daily change in integrated Chl *a* (*d*(Chl *a*); green line; gliders data).

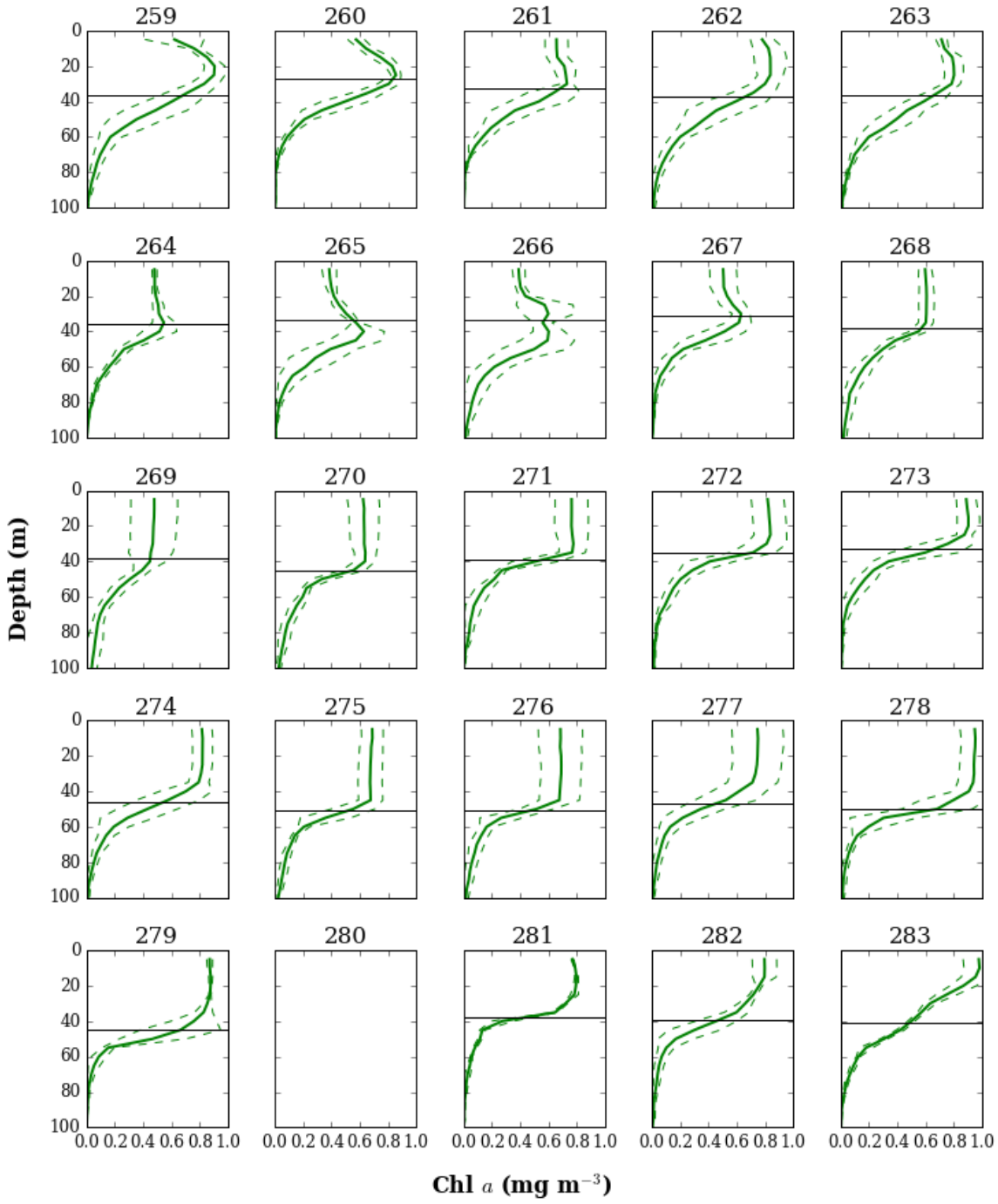

Figure 4.4 Daily mean vertical profiles of Chl *a* (± std) obtained between days 259 and 283. Black horizontal lines on the plots indicate daily mean mixed layer depths.

4.3.2 Nutrient supply during the storm

The ability of gliders to obtain data under challenging weather conditions allowed them to capture the changes in the surface layer dynamics throughout the storm event. The data showed that vertical mixing during the associated strong wind forcing introduced significant changes in the upper ocean density structure: an increase in surface density from ~25.8 kg m^{-3} to ~26.1 kg m^{-3} and erosion of the pycnocline (Figure 4.3b). Entrainment of water from the pycnocline was accompanied by an increase in surface nitrate concentration (Figure 4.3c). This picture is consistent with the classical interpretation of the storm's influence on the upper ocean: thinning of the pycnocline due to high turbulence production at the base of the mixed layer and corresponding intrusion of nutrients. Supply of nutrients during the storm could be also driven by wind-generated inertial oscillation and associated shear instabilities across the pycnocline. Unfortunately, the quality of ADCP data during high wind forcing did not allow clear detection of shear spikes at the ocean pycnocline throughout the storm event. Hence, changes in surface nitrate concentrations during the storm may be the combined effect of both processes.

Meteorological data indicate that high wind speeds were accompanied by a significant decrease in the air temperature, by 2.5 °C. To determine if vertical mixing during the storm was dominated by buoyancy reduction due to cooling or by shear production associated with wind mixing, the Monin-Obukhov length scale (Monin & Obukhov 1954) was used:

$$z_{MO} = -\frac{u_*^3}{k_{vK} B_0}, \tag{4.5}$$

where k_{vK} = 0.41 is the von Karman constant, B_0 is surface buoyancy flux, τ is surface wind stress, $u_* = \left(\frac{\tau}{\rho_0}\right)^{1/2}$ is the friction velocity, and ρ_0 = 1026 kg m^{-3}. Above the Monin-Obukhov length scale shear production of turbulent kinetic energy dominates over buoyant reduction. If the length scale is deeper than the mixed layer depth, turbulence within the surface layer is mainly driven by wind forcing rather than convection (Nagai et al. 2005).

Combined NCEP reanalysis and meteorological data obtained for the cruise period suggest that the net heat flux from the atmosphere to the ocean, Q, was at a minimum of -375 W m^{-2} during the storm (Figure 4.5b). Neglecting effects of evaporation and precipitation, the buoyancy flux can be estimated as:

$$B_0 = \frac{g \lambda Q}{\rho_0 c_p} \tag{4.6}$$

where g = 9.81 m s^{-2} is the acceleration due to gravity, λ = 2.1 x 10-4 °C^{-1} is the coefficient of thermal expansion for seawater and c_p = 3985 J kg^{-1} °C^{-1} is the seawater heat capacity (estimated for typical

values of temperature and salinity within the mixed layer observed during the storm: T ~ 14 °C and S ~ 35.5 psu).

From eq. 4.5 and eq. 4.6, I estimated the weakest wind stress (τ_{cr} ~ 0.2 N m^{-2}) for which wind shear would be the main source of turbulence under the strongest convective conditions during the storm, assuming the mixed layer depth ~40 m. Wind stress values during the storm were generally higher than τ_{cr} (Figure 4.5a). It suggests that turbulent kinetic energy production in the mixed layer and pycnocline erosion observed by gliders were mostly driven by wind forcing, rather than convection.

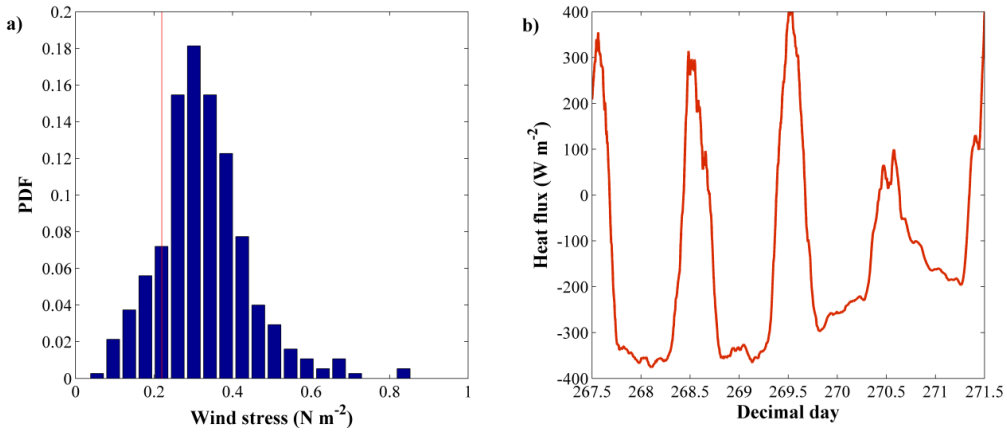

Figure 4.5 Wind stress and surface heat flux data during the observed storm event. a) Histogram of wind stress values throughout the storm. Red vertical line indicates the critical wind stress (τ_{cr}) described in section 4.3.2. b) Surface net heat flux from the atmosphere to the ocean during the storm event that occurred in the course of D381 cruise. Negative heat flux indicates heat loss by the ocean.

Following the passage of the storm, surface nitrate concentrations reached ~0.6 mmol N m^{-3}. Multiplying the increase in concentration (by ~0.5 mmol N m^{-3} compared to the pre-storm values) by the mixed layer depth (~40 m), nutrient supply due to the storm was estimated as ~20 mmol N m^{-2}. The storm lasted about 3 days. Therefore, an increase in mixed layer nitrate by 20 mmol N m^{-2} is equivalent to a nitrate flux of 6-7 mmol N m^{-2} d^{-1}.

4.3.3 Shear spiking after the storm

Turbulence measurements conducted before and after the storm allowed me to estimate the additional supply of nutrients that could occur in the wake of the storm due to the presence of inertial currents in the surface layer and associated shear spiking mechanism. During the pre-storm

period two series of turbulence measurements (MSS1 and MSS2) were conducted providing estimates of the nitrate flux associated with background turbulent diffusion (Figure 4.3a). The third series of turbulence measurements (MSS3) took place immediately after the storm event, capturing interactions between wind stress and inertial currents which affected the magnitude and structure of the turbulent flux. According to the glider data, the base of the euphotic zone was located within the pycnocline (Figure 4.2b and Figure 4.3b). Therefore we assumed that the nitrate flux through the pycnocline represented the flux into the euphotic zone. The nitrate flux was calculated for all 1 m bins within the pycnocline layer. To reduce the influence of outliers, only data points within the interquartile range were considered for each vertical profile.

For the pre-storm turbulence measurements, MSS1 and MSS2, the nitrate flux was relatively constant (Figure 4.6a, 4.6b). The two series gave consistent estimates of the background turbulent diffusive nitrate flux: 0.04 ± 0.03 mmol N m^{-2} d^{-1}. Post-storm (MSS3), three bursts of high nitrate flux (up to 1 mmol N m^{-2} d^{-1}, 32 times the standard deviations for MSS1 and MSS2) were observed (Figure 4.6c). The duration of the bursts was relatively short (O(1 hour)). The time intervals between them were 10.7 and 11 hours. The overall mean flux during MSS3 was 0.11 ± 0.18 mmol N m^{-2} d^{-1}, approximately 3-fold higher than pre-storm (MSS1 and MSS2).

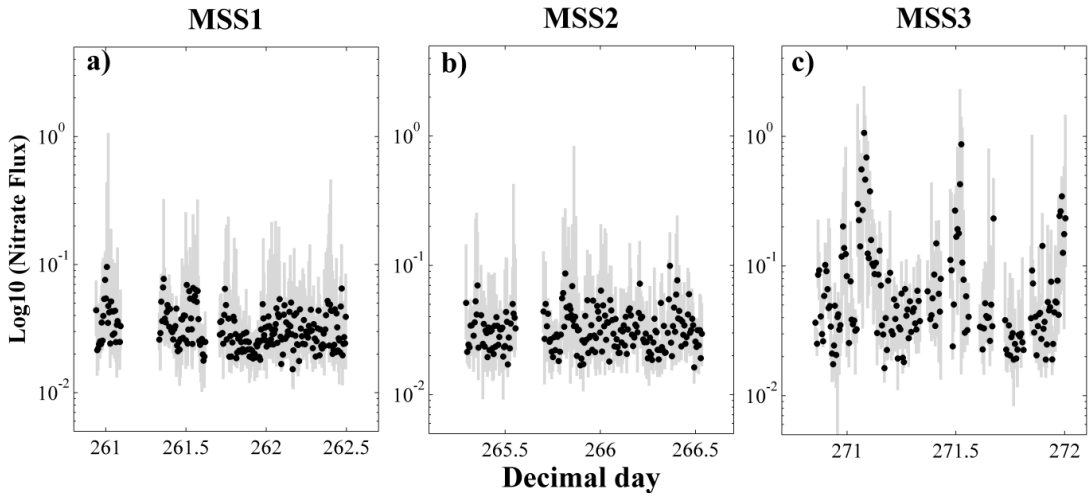

Figure 4.6 Vertical nitrate flux (y-axis is in log scale; units are mmol N m^{-2} d^{-1}) through the pycnocline estimated from the three series of turbulence measurements: a) MSS1, b) MSS2, c) MSS3. Grey lines represent the interquartile range for each profile and black dots indicate the median values.

The data suggest that the variability of the nitrate flux measured during MSS3 was affected by the post-storm inertial currents (Figure 4.7). At the beginning of MSS3 (days 270.9 - 271.6), the ADCP data captured rotation of the bulk shear vector at near the local inertial frequency (~15 hours; Figure 4.7d). The magnitude of the bulk shear oscillated between 0.5 and 2 x 10^{-5} s^{-2} during this time (Figure 4.7b). By day 271.6 slab motion of the surface layer dissipated and the bulk shear value

reduced (Figure 4.7b, 4.7d). The wind direction remained relatively constant throughout (Figure 4.7d). According to the theoretical model (Eq. 4.3), the contribution of the wind to shear production can be assessed by looking at the time series $|\vec{\tau}|\cos(\vec{S},\vec{\tau})$ as this metric encompasses the influence of wind direction relative to the bulk shear as well as the influence of wind magnitude. The time series reveals that wind supported shear production (i.e. $|\vec{\tau}|\cos(\vec{S},\vec{\tau}) > 0$) occurred during days 271–271.2, 271.45–271.75 and at the end of the period of microstructure sampling when the inertial currents dissipated (Figure 4.7c). In agreement with the theory, the bursts of high mixing across the pycnocline occurred during these three periods and were associated with the enhanced bulk shear ($S^2 > 10^{-5}$ s^{-2}). During the bursts, energy dissipation rate (ε) within the pycnocline was at least an order of magnitude higher than the background levels and the mean ε in the 10 m layer above the pycnocline (Figure 4.7a). The latter indicates that it was unlikely that simple deepening of the mixed layer due to surface forcing initiated the spikes in vertical mixing across the pycnocline.

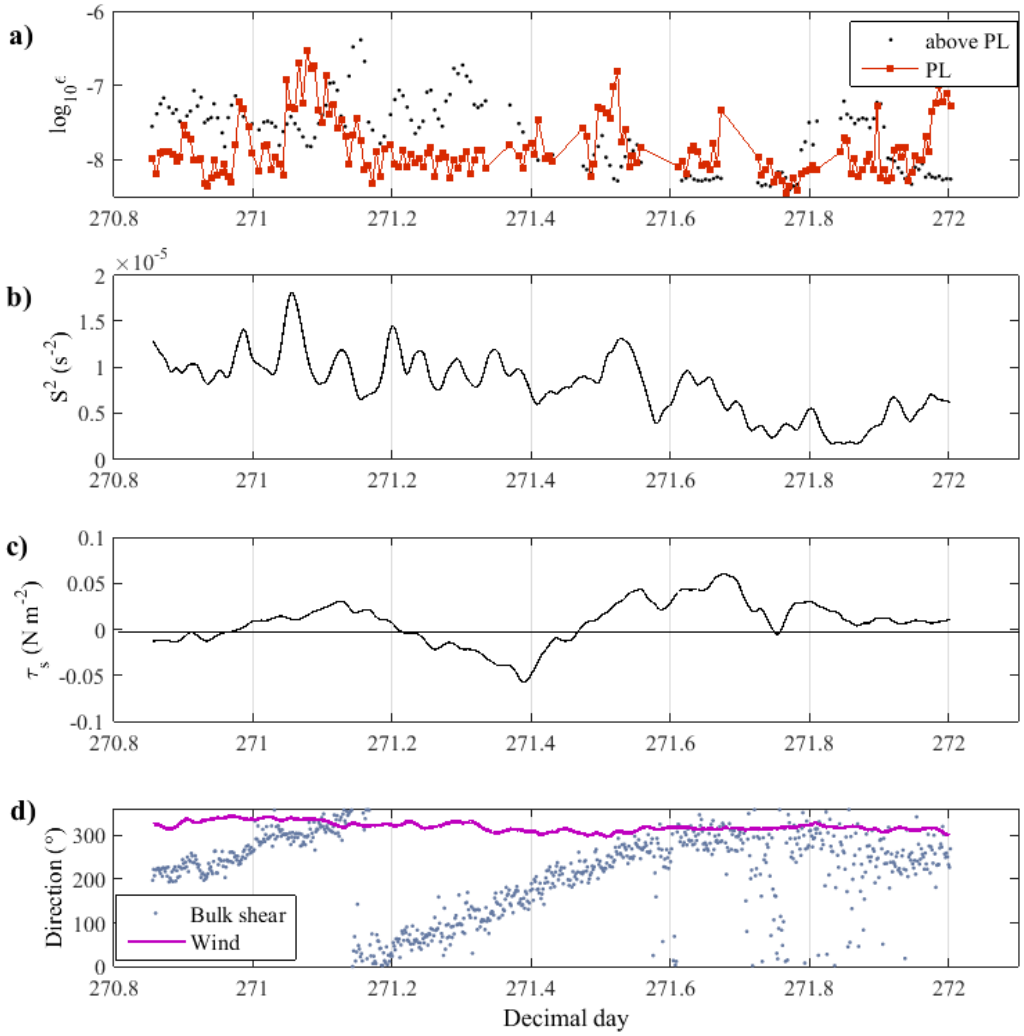

Figure 4.7 Forcing, shear and turbulence characteristics during MSS3 transect during which the bursts of turbulent flux were observed: a) decimal logarithm of median energy dissipation rate ε (units of ε are $m^2\ s^{-3}$) within the pycnocline (red squares) and within the 10 m layer above the pycnocline (grey dots), b) time series of bulk shear magnitude smoothed using 2-h boxcar filter, c) wind stress magnitude multiplied by the cosine between wind and bulk shear directions, d) directions of wind stress (purple line) and bulk shear (blue dots).

4.4 Discussion

Previous studies (Forryan et al. 2012; Martin et al. 2010; Painter et al. 2014) have suggested that the contribution of small-scale diapycnal turbulent diffusion to the overall physical transport of nutrients to the ocean surface layer is relatively minor. However, enhancement of the turbulent flux through the pycnocline associated with wind-driven inertial oscillations has not been considered in previous nitrate budget calculations for the open ocean. Shear spikes are discrete

features and enhancement of the nitrate flux due to them could be missed if measurements do not resolve sub-inertial frequencies.

The data set presented here has allowed direct observation of changes in the turbulent nitrate flux caused by shear spiking following the storm event in the open North Atlantic Ocean. A sequence of pulses of high nitrate flux generated by a wind event longer than the inertial period was observed, in agreement with the sensitivity analysis of the model for shear production presented by Burchard & Rippeth (2009). This model suggests that the period of alignment corresponds to the period of maximum shear production. In the current study the spikes of vertical mixing across the pycnocline occurred during the alignment (the first and the third spikes) and before the alignment (the second spike). In this study it was shown that maximum shear production depends also on the wind magnitude variability and complete alignment is not necessary to produce spikes in vertical mixing across the pycnocline.

Estimates of the background nitrate flux due to turbulent diffusion (~0.04 mmol N m^{-2} d^{-1}) were consistent with the previous similar estimates at the PAP site (Martin et al. 2010). During MSS3 a short-term increase in turbulent nitrate flux (approximately 25 times higher than the background levels) was observed with the mean daily nitrate flux (~0.11 mmol N m^{-2} d^{-1}) being higher only by a factor of 3. The nitrate supply by the post-storm shear spiking was an order of magnitude lower than the estimated nitrate flux during the storm (6-7 mmol N m^{-2} d^{-1}, two orders of magnitude higher than the background flux). Thus, the contribution of the post-storm nitrate supply appears to be low due to the short duration of periods of enhanced nitrate flux and nutrients were delivered to the surface layer mainly during the storm. High values of nitrate flux during enhanced wind forcing (~22 mmol N m^{-2} d^{-1}, 17-fold higher than the background flux) were also reported in previous studies in shelf seas (Williams et al. 2013).

Using the estimates presented in this study, it is worth comparing the storm-driven nutrient supply with other regional physical mechanisms of nutrient transport to the surface ocean. The contribution of winter convection to the nitrate budget of this area of the North Atlantic was previously estimated as between 504 mmol N m^{-2} $year^{-1}$ (Martin et al. 2010) and 1000 mmol N m^{-2} $year^{-1}$ (Williams & Follows 2003). Thus, nutrient intrusion during the storm caused by vertical mixing (20 mmol N m^{-2}) corresponds to 2.5 - 5 % of the total annual nitrate supply by deep winter convection. The PAP site is in the transition region between the mesotrophic subpolar gyre and the oligotrophic subtropical gyre (Henson et al. 2009a). Mesoscale eddy pumping has been estimated to provide approximately 200 mmol N m^{-2} $year^{-1}$ for oligotrophic regions (McGillicuddy et al. 1998; Siegel et al. 1999). However, in subpolar regions the vertical advection by mesoscale eddies can

potentially act as a sink of nutrients (McGillicuddy et al. 2003; Oschlies 2002). Hence, the magnitude, if not sign, of the mesoscale nitrate flux at the study site is uncertain. One instance of the effect of submesoscale filaments on primary production at the PAP site was reported by (Painter et al. 2010), who showed that rates of primary production associated with the passage of an eddy filament could be highly variable with a potential increase of up to 74 mmol C m^{-2} d^{-1}. Assuming a C:N ratio of 6.6 (Redfield 1958) and a lifetime for a submesoscale front of O(1) day (Lévy et al. 2012), the total nitrate supply associated with this filament to support the primary production increase would be 11 mmol N m^{-2}. This is approximately one half of the nitrate associated with the storm pathway. However estimates provided by Painter et al. (2010) are relevant for a single filament observed at the PAP site. In general, submesoscale fronts are ubiquitous features and collectively could be associated with higher nitrate flux.

One can make the point that storms in the high latitude North Atlantic Ocean are localized features compared to basin-wide mechanisms of nutrient supply such as winter convection. However, the spatial scale of storms is relatively large (O(100-1000) km), and comparable to the characteristic scale of the basin (O(1000) km). Their passage is also fairly frequent: model-based estimates of storminess suggest that annually ~30 storms (with maximum wind speed >17 m s^{-1}) occur in the extratropical Northeast Atlantic Ocean (Weisse et al. 2005), although the majority of these storms occur in winter. I looked at the data from the weather mooring deployed at the PAP site from the end of April till November 2013, the time of year when surface nitrate is likely depleted (Figure 4.8). The data showed that during that period of time up to 6 low pressure systems separated by several days with instantaneous wind speed exceeding 17 m s^{-1} passed through the site. A coarse estimate based on the results of the current study suggests that cumulative effects of these storm events can reach up to 30 % of the nitrate supply by winter convection.

Previous studies estimated the impact of tropical cyclones on primary production in the North Atlantic Ocean using satellite ocean colour data and obtained contradictory conclusions on their importance (Foltz et al. 2015; Hanshaw et al. 2008). In this chapter I have assessed the potential significance of extratropical storms for primary production in the temperate North Atlantic Ocean by focussing on nutrient supply. This study shows that the storm induced in situ phytoplankton growth and on an annual scale the passage of storms can potentially support a significant amount of ocean primary production. This fact highlights the importance of further observational and modelling studies of storm contribution to nutrient supply in the ocean surface layer.

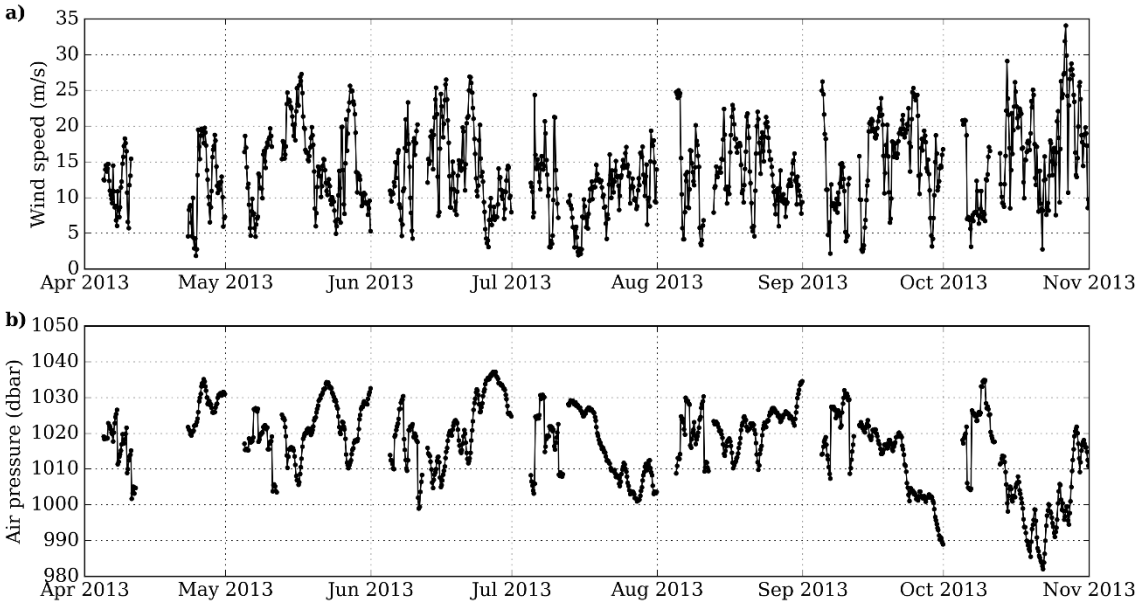

Figure 4.8 Wind speed (a) and air pressure (b) measured between April and November 2013 by the weather mooring at the PAP site.

4.5 Conclusions

Based on the interdisciplinary data set collected at the Porcupine Abyssal Plain Sustained Observatory site a phytoplankton autumn bloom and nutrient fluxes to the ocean surface layer associated with the passage of a storm were examined. The storm passage increased phytoplankton stocks by 50% and eroded a SCM observed at the sampling site before the storm. It was demonstrated that the majority of nutrients were delivered to the mixed layer during the period of strong wind forcing. The turbulence measurements conducted in the wake of a storm allowed quantification of the additional post-storm nitrate flux due to the shear spiking mechanism. Regardless of the dramatic semidiurnal increase of the flux, the overall nitrate supply after the storm was relatively low due to the short duration of the periods of enhanced mixing across the pycnocline. The estimate of the cumulative nitrate supply suggests that storms can form an appreciable component of the local annual nitrate budget.

Chapter 5: The impact of atmospheric forcing on the phytoplankton spring bloom initiation

The aim of this chapter is to analyse the impact of atmospheric conditions and associated mixing regimes in the upper ocean on the spring bloom initiation and development. Three widely discussed hypotheses explaining spring bloom onset in the temperate and subpolar North Atlantic Ocean (CDH, CTH and DRH) are tested. Parts of this chapter have been used in "The impact of atmospheric forcing on the North Atlantic phytoplankton spring bloom" manuscript submitted to "Limnology & Oceanography" journal. The manuscript is in review.

5.1 Introduction

The manifestation of phytoplankton spring blooms in the temperate and subpolar North Atlantic Ocean is highly important for regional trophodynamics and efficiency of carbon export. However, the conditions necessary to trigger phytoplankton spring blooms remain uncertain even after more than 60 years of study (Sathyendranath et al. 2015). To date, three main hypotheses have been proposed: the critical depth hypothesis (CDH), the critical turbulence hypothesis (CTH), and the dilution-recoupling hypothesis (DRH) (Behrenfeld and Boss 2014). The hypotheses predict the onset of blooms under different environmental conditions and put forward different mechanisms responsible for triggering spring blooms. A brief overview of the hypotheses is provided below.

The CDH (Sverdrup 1953) states the start of the phytoplankton spring bloom corresponds to shoaling of the z_{mixed} above a critical depth (hereafter z_{cr}), a threshold based on solar radiation, light attenuation in the water column and algal losses from different sources (Smetacek and Passow 1990). The hypothesis assumes that improving light conditions for phytoplankton is the main factor for triggering spring blooms. To more precisely test the CDH, it is important to consider potential divergence between z_{mixed} and z_{mixing} since z_{mixed} can be an imperfect proxy for a layer where mixing is currently active (Franks 2014). If mixing in the ocean surface layer is driven by surface cooling, convective cells penetrate to the depth of the pycnocline and the entire mixed layer is actively turbulent. However, when surface cooling of the ocean subsides and wind forcing acts as the main source of turbulence, phytoplankton can be trapped within z_{mixing} shallower than z_{mixed}.

According to CTH, the spring bloom can initiate in an arbitrarily deep layer due to changes in mixing intensity rather than in mixing depth (Huisman et al. 1999). Relaxation of turbulence due to weakening atmospheric forcing allows phytoplankton growth near the surface to outpace mixing

and a bloom develops resulting in an uneven vertical distribution of phytoplankton within the mixing layer. The CTH can be expressed in terms of relevant time scales (Taylor and Ferrari 2011a). In this framework, a low mixing rate can result in accumulation of phytoplankton near the surface if

$$t_m \gg t_{\mathrm{g}}, \tag{5.1}$$

where t_{m} is the mixing time scale defined as a mixing layer depth divided by a characteristic turbulent velocity scale and t_{g} is the growth time scale, which is inversely proportional to the phytoplankton growth rate.

The dilution-recoupling hypothesis (DRH) (Behrenfeld 2010) proposes that decreasing grazing pressure is the main factor controlling the bloom onset. Deep mixing in winter dilutes phytoplankton and their grazers. In this scenario, net accumulation of phytoplankton results from decreasing losses of phytoplankton rather than increasing specific growth rates associated with improving light conditions in spring. The hypothesis postulates that net growth of phytoplankton starts in winter, mixing is deep and specific phytoplankton growth rate is low.

The above outlined hypotheses predict the onset of phytoplankton blooms under different atmospheric forcing conditions: (i) subsiding ocean surface cooling and/or weakening wind forcing, associated with a reduction in mixing layer depth and/or a reduction in mixing intensity (CDH and CTH) or (ii) periods of deep mixing layer depths (DRH). Therefore, it remains uncertain which conditions are favourable for the spring bloom onset.

In this chapter, I use glider observations coupled with reanalysis data of atmospheric forcing, to study how meteorological conditions can influence mixing regimes and affect the onset and development of the North Atlantic spring bloom in 2013. The objectives are two-fold. First, I analyze how atmospheric forcing can affect bloom initiation by testing the three main hypotheses: CDH, CTH and DRH. Specifically, I aim to answer the following questions:

- Can the bloom onset be explained by the shoaling of z_{mixing} above the critical depth z_{cr}? (test of CDH)
- Can the bloom onset be explained by decreasing mixing intensity, which leads to an increase in the mixing time scales t_{m}? (test of CTH)
- Can one detect positive net accumulation of phytoplankton in deep mixed layers during strong cooling of the ocean surface and/or during strong wind mixing? (test of DRH)

Second, I also examine how atmospheric forcing can influence the post-initiation development of the bloom.

In the following Method section, I provide an overview of the theoretical framework used to evaluate mixing regimes in the water column, including definitions of z_{mixing}, t_m, z_{cr}, phytoplankton specific growth rate, and net accumulation rates.

5.2 Methods

5.2.1 Turbulence regimes, mixing depth and mixing time scales

Similarly to Brody & Lozier (2014), I characterize turbulence in convective boundary layers with an applied wind stress by calculating the Monin-Obukhov length scale (defined in the previous chapter; eq. 4.5). Previous studies, (e.g. Schmitt et al. 1989), demonstrated that the haline contribution to the surface density flux in the temperate and subpolar North Atlantic Ocean is an order of magnitude lower than the thermal contribution. This was confirmed at the OSMOSIS site by Thompson et al. (2016). Therefore, I assume that the surface buoyancy flux is predominantly regulated by the surface heat flux.

I classify mixing regimes in the ocean surface layer using the framework described by Thorpe (2005):

Case 1: Wind-mixing regime: $z_{mixed} < C_1 z_{MO}$ or $Q > 0$, $C_1 = 0.3$;

Case 2: Convective mixing regime: $z_{mixed} > z_{MO}$ and $Q < 0$.

Under the wind-mixing regime (Case 1), the depth of active mixing (z_{mixing}) can be shallower than z_{mixed} (Franks 2014). The depth of wind mixing can extend to the base of Ekman layer and so can be scaled as

$$z_{\mathrm{mixing}} = \frac{u_*}{C_2 f}, \tag{5.2}$$

where f is the Coriolis parameter, $C_2 = 2$ is a dimensionless constant. Eq. 5.2 was implemented to estimate z_{mixing} under Case 1 conditions during negative surface heat flux ($Q < 0$). During surface warming ($Q>0$, Case 1 conditions), z_{mixing} is additionally suppressed by a positive buoyancy flux. Zilitinkevich et al. (2002) provided the theoretical framework for scaling of the stably stratified Ekman boundary layer in this situation. The scaling was subsequently implemented in numerical studies of phytoplankton spring blooms, e.g. Enriquez & Taylor (2015) in the following form:

$$\frac{1}{z_{\text{mixing}}^2} = \frac{f^2}{(C_3 u_*)^2} + \frac{fB_0}{(C_4 u_*^2)^2}, \quad (5.3)$$

where C_3 and C_4 are prescribed dimensionless constants. The scaling incorporates an increase of z_{mixing} with increasing u_* and a decrease of z_{mixing} due to surface heating (increasing B_0). Values of C_3 and C_4 were determined by Enriquez and Taylor (2015) using LES model output. During the wind-mixing regime, the turbulent diffusivity is assumed to be constant down to z_{mixing}. The vertical mixing time scale associated with wind mixing ($t_{\text{m,wind}}$) can be estimated as:

$$t_{\text{m,wind}} = \frac{z_{\text{mixing}}}{u_*}. \quad (5.4)$$

When surface cooling is the main source of turbulence in the water column (Case 2: convective mixing regime), convective cells develop even under weak surface cooling (Taylor & Ferrari 2011b). Under these conditions, the mixed layer depth can be used as the depth of active mixing. In the convective mixing regime, the vertical eddy diffusivity is assumed to be constant throughout the whole mixing layer and the mixing time scale ($t_{\text{m,convection}}$) can be estimated as:

$$t_{\text{m,convection}} = \frac{z_{\text{mixing}}}{C_5(z_{\text{mixing}} B_0)}. \quad (5.5)$$

where $C_5 = 1$ is a prescribed dimensionless constant. The scaling for the turbulent velocity during the convective mixing regime (the denominator in eq. 5.5) was adopted from Deardorff (1972).

When z_{mixing} falls in the region between $C_1 z_{\text{MO}}$ and z_{MO}, mixing in z_{mixed} is driven by both wind shear and buoyancy, representing transitional conditions between Case 1 and Case 2 regimes. For simplicity, I assumed that the entire mixed layer is turbulent under the transitional conditions. The transitional conditions were not sustained for more than 2 days at a time and represented less than 15% of the time series. Therefore, the mixing time scales were estimated for Case 1 and Case 2 conditions only.

5.2.2 Specific growth rate

Phytoplankton specific growth rate (μ) depends on nutrient abundance, light conditions, and temperature. I assume that nutrients are not limited in the temperate and subpolar North Atlantic Ocean during the period of interest due to deep convective mixing in winter (Williams et al. 2000; Steinhoff et al. 2009). For the glider sampling site, the World Ocean Atlas 2009 gives winter surface nitrate concentration of 7 mmol m^{-3}. The specific growth rate was estimated for the observed temperature conditions assuming a suboptimal light regime similar to Edwards et al. (2013). The

maximum growth rate as a function of temperature under abundant light and nutrient conditions was evaluated following Bissinger et al. (2008):

$$\mu_{\max} = 0.81e^{0.0631T}, \quad (5.6)$$

where μ_{max} is the maximum phytoplankton growth rate (in of d^{-1}) and T is the temperature averaged over z_{mixed}.

Following Evans & Parslow (1985) the phytoplankton specific growth rate as a function of light was determined as:

$$\mu_{\mathrm{E}}\big(E(z,t)\big) = \frac{\mu_{\max}\alpha^{\mathrm{chl}}\theta E(z,t)}{\sqrt{\mu_{\max}^2+(\alpha^{chl}\theta)^2E(z,t)^2}}, \quad (5.7)$$

where α^{chl} is the chlorophyll-specific slope of the phytoplankton-irradiance curve, ϑ is the cellular chlorophyll-to-carbon mass ratio (a conversion factor between productivity and phytoplankton specific growth rate), $E(z,t) = E_0(t)e^{-Kz}$ is the vertical profile of light, K is the light attenuation coefficient (including attenuation by phytoplankton) and E_0 is the surface light intensity. The values of α^{chl} and ϑ (Table 5.1) were adopted from Maraiion & Holligan (1999) and Behrenfeld et al. (2005) respectively.

Surface light intensity changes within a day and can be approximated by a sinusoidal curve (Kirk 1994) such as:

$$E_0 = E_{\max}\sin(\frac{\pi t}{V}), \quad (5.8)$$

where E_{max} is the surface light intensity at noon, t is the time since sunrise, and V is the day length. Time of sunset and sunrise were determined using *ephem* Python module (https://pypi.python.org/pypi/pyephem/). Time-resolved surface light intensity can be obtained using daily average surface PAR values from the satellite products (PAR_s):

$$PAR_s = \frac{1}{V}\int_0^V E_{\max}\sin(\frac{\pi t}{V})dt, \quad (5.9)$$

that leads to the following expression for the surface light intensity at noon:

$$E_{\max} = PAR_s\frac{\pi}{2V}, \quad (5.10)$$

From eq. 5.7-5.10, the daily mean specific growth rate for phytoplankton distributed over a layer of depth H can be estimated as:

$$\mu_{\mathrm{mean}} = \frac{1}{V}\int_0^V \frac{1}{H}\int_H^0 \frac{\mu_{\max}\alpha^{\mathrm{chl}}\theta E(z,t)}{\sqrt{\mu_{\max}^2+(\alpha^{chl}\theta)^2E(z,t)^2}}dzdt, \quad (5.11)$$

From eq. 5.11 the maximum growth rate within a day ($E_0 = E_{\max}$ and z = 0) is:

$$\mu_{\text{day max}} = \frac{\mu_{\max}\alpha^{\text{chl}}\theta E_{\max}}{\sqrt{\mu_{\max}^2+(\alpha^{chl}\theta E_{\max})^2}}. \quad (5.12)$$

5.2.3 Net accumulation rate

The bloom initiation was defined as the onset of net accumulation of phytoplankton following Behrenfeld (2010). The net accumulation rate of phytoplankton (*r*) was calculated using water column integrated Chl *a* inventories, *I*(Chl *a*), and surface Chl *a* concentrations, *S*(Chl *a*) (calculated as mean over glider measurements above 20 m depth). I followed the method described by Behrenfeld (2010) taking into account potential decoupling between the mixed and mixing layers. If z_{mixing} is deepening ($z_{\text{mixing}}(t_1) > z_{\text{mixing}}(t_0)$) and z_{mixing} is deeper than the euphotic depth ($z_{\text{mixing}}(t_1) > z_{\text{eu}}(t_1)$):

$$r = ln\left(\frac{I(\text{Chl } a)_{t_1}}{I(\text{Chl } a)_{t_0}}\right)/\Delta t \quad (5.13)$$

and if z_{mixing} is shoaling or $z_{\text{mixing}}(t_1) < z_{\text{eu}}(t_1)$:

$$r = ln\left(\frac{S(\text{Chl } a)_{t_1}}{S(\text{Chl } a)_{t_0}}\right)/\Delta t \quad (5.14)$$

where *r* is the net accumulation rate over the time interval $\Delta t = t_1 - t_0$. I calculate the net accumulation rates and corresponding uncertainties using Chl *a* data averaged in time over 3 day (r_3), 5 day (r_5) and 8 day (r_8) time intervals. Time intervals for averaging of data were in part chosen to match previous hypothesis tests conducted by Boss & Behrenfeld (2010) using data from a profiling float and by Behrenfeld (2010) using 8 day composites of satellite ocean colour data. In addition, the unsmoothed daily time series of net accumulation rate was significantly affected by short-term variability and which complicated analysis of the biomass accumulation associated with the dilution effect. In this study, I implement a chlorophyll-based approach for calculating phytoplankton net accumulation rate similarly to that followed by Boss & Behrenfeld (2010).

5.2.4 Critical depth

According to Sverdrup's model, the critical depth, z_{cr}, can be defined by the implicit relationship:

$$\frac{1}{Kz_{\mathrm{cr}}}(1-e^{-Kz_{\mathrm{cr}}})=\frac{E_c}{E_0} \quad (5.14)$$

where E_c is the compensation irradiance. I calculated z_{cr} for E_c values (0.96 and 1.75 E m^{-2} d^{-1}) previously obtained for the middle and high latitude North Atlantic Ocean (Siegel et al. 2002) (Table 5.1) from an analysis of spring bloom timing using satellite and hydrographic data sets.

Table 5.1 List of parameters used Chapter 5.

	Symbol	Value
Coriolis parameter (at 49° N latitude)	f	10^{-4} s^{-1}
Chl *a* specific slope of phytoplankton irradiance curve*	α^{chl}	6-17 (mmol m^{-2})$^{-1}$
Chl *a*-to-carbon mass ratio**	θ	0.015
Compensation irradiance (photon flux)***	E_c	0.96 - 1.75 E m^{-2} d^{-1}

*Adopted from Maranon and Holligan (1999) (range of values for 49° N). Similar values were obtained by Uitz (2006) for micro- and nano- plankton.

**Adopted from Behrenfeld et al (2005) (mean value for temperate and subpolar North Atlantic Ocean).

*** The range of values of the middle and high latitude North Atlantic Ocean was taken from Siegel et al. (2002).

5.2.5 Calculation of absolute errors

To calculate absolute errors on the phytoplankton mean specific growth rate (μ_{mean}; eq.5.11), phytoplankton net accumulation rate (r; eq. 5.12 and 5.13), the critical depth (z_{cr}; eq. 5.14) and the growth time scales (t_g) the procedure described, for example, by Cohen (1998) was implemented. For instance, the phytoplankton mean specific growth rate is a function of surface light intensity, attenuation coefficient, surface temperature and the depth of a layer considered:

$$\mu_{\mathrm{mean}}=f(E_0,K,T,H). \quad (5.15)$$

Therefore, the absolute error of can be calculated as follows:

$$\Delta\mu_{\mathrm{mean}}=\sqrt{\left(\frac{\partial f}{\partial E_0}\Delta E_0\right)^2+\left(\frac{\partial f}{\partial K}\Delta K\right)^2+\left(\frac{\partial f}{\partial T}\Delta T\right)^2+\left(\frac{\partial f}{\partial H}\Delta H\right)^2}. \quad (5.16)$$

where ΔT, ΔK and ΔZ are the standard deviations of the daily mean values for T , K and H. ΔE_0 is the standard deviation of E_0 averaged over the sampling site surface light intensity (obtained from Aqua MODIS satellite products). The absolute errors of t_g and z_{cr} were calculated in a similar way.

The net accumulation rate is a function of integrated (or surface mean) Chl a fluorescence at t_0 and t_1 (X_0 and X_1 respectively):

$$r = f(X_0, X_1). \tag{5.17}$$

The absolute error of r, in this case, can be calculated as follows:

$$\Delta r = \frac{\sqrt{\left(\frac{\partial F}{\partial X_0}\Delta X_0\right)^2 + \left(\frac{\partial F}{\partial X_1}\Delta X_1\right)^2}}{\Delta t}. \tag{5.18}$$

where ΔX_1 and ΔX_0 are the standard deviation of the mean for X_1 and X_0 and Δt is the time interval between them. ΔX_1 and ΔX_0 are calculated using measurements collected from selected time bins centred on t_1 and t_0.

5.3 Results

The time evolution of Chl a, z_{mixed}, z_{mixing}, z_{eu}, atmospheric forcing (Q and τ) and E_0 is shown in Figure 5.1. On the plots of atmospheric forcing (Figure 5.1e and 5.1f) red and blue circles show periods of wind (Case 1) and convective (Case 2) mixing regimes respectively. Time-series of daily mean S(Chl a) and I(Chl a) values are presented in Figure 5.1b and Figure 5.1c.

The mixed layer gradually deepened from mid-October until the end of January, during a period of predominantly negative Q (as also previously discussed by Thompson et al. (2016)). This was also a period of frequent passage of atmospheric fronts associated with strong wind forcing (τ > 0.4 N m^{-2}) and gradually decreasing E_0. A convective mixing regime dominated during this period. At the beginning of the time-series S(Chl a) and I(Chl a) were approximately 0.7 mg m^{-3} and 40 mg m^{-2} respectively. Following the mixed layer deepening S(Chl a) and I(Chl a) dropped to 0.1 mg m^{-3} and 25 mg m^{-2} respectively in January.

From February until late April the mixed layer remained relatively deep (100 – 450 m). The net cooling of the ocean surface significantly subsided; the frequent passage of storms persisted. Conditions of wind mixing were more frequent, occasionally interrupted by periods of stronger convective mixing, such as in mid-March (Figure 5.1e). Between February and late April, generally

positive trends in integrated and surface Chl *a* can be observed coinciding with gradually increasing surface light intensity (Figure 5.1d). Over this period, *I*(Chl *a*) increased by a factor of 2.3, from 30 mg m^{-2} in February to 70 mg m^{-2} in April. *S*(Chl *a*) increased by a factor of 3, from 0.2 to 0.6 mg m^{-3}.

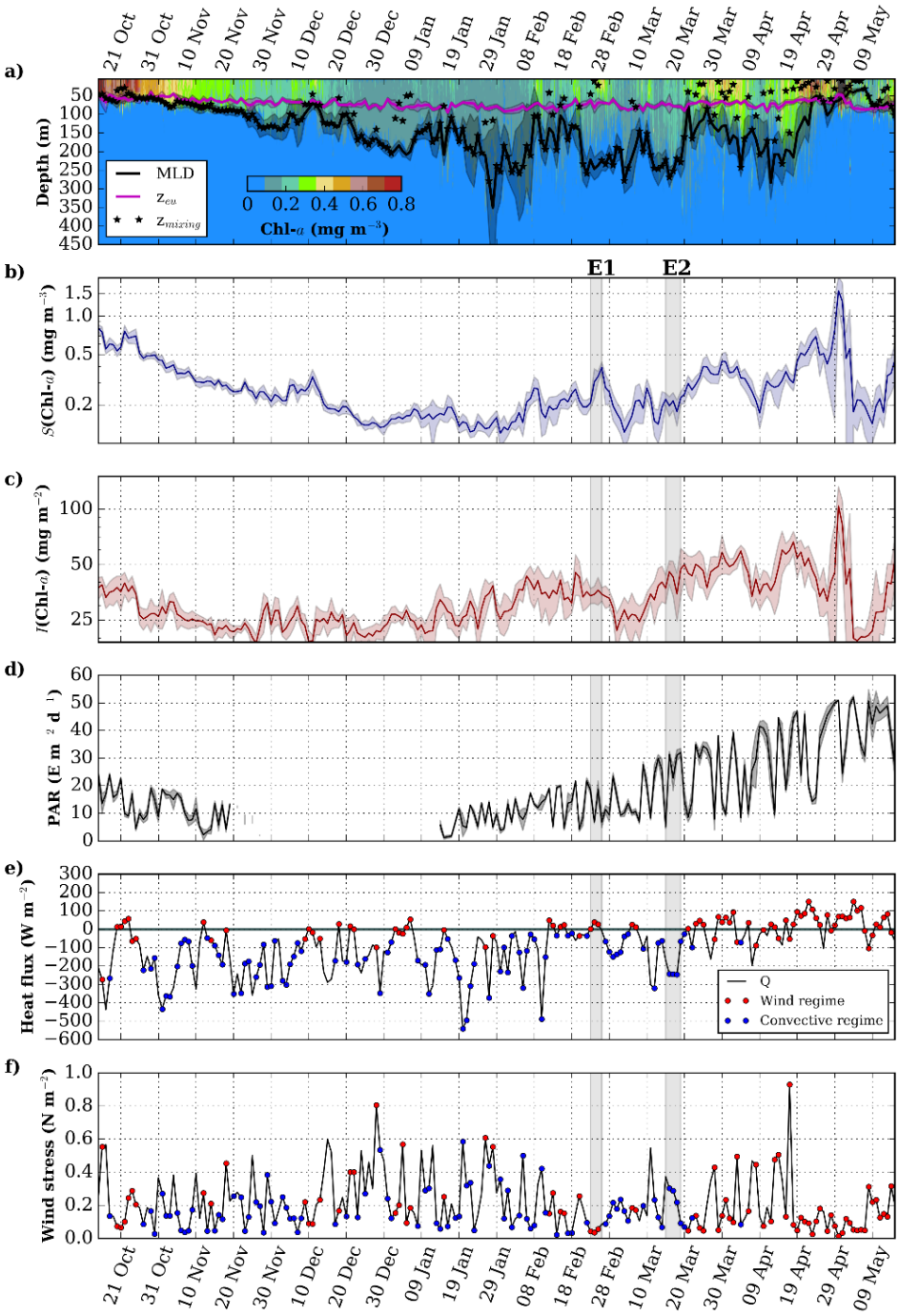

Figure 5.1 Time series of glider Chl *a*, mixed layer depth, euphotic depth, atmospheric forcing and light conditions: a) Chl *a* concentration (mg m^{-3}; colour-coded) with overlaid lines corresponding to daily-mean z_{mixed} (±std; black), z_{mixing} (black stars) and daily mean z_{eu} (±std; violet), b) daily-mean glider surface (calculated as mean over the upper 20 meters) Chl *a* (±std; blue), c) daily-mean glider integrated Chl *a* (±std; red), d) daily mean surface light intensity over the sampling area

(±std), e) surface heat flux and f) surface wind stress. Blue and red circles on panels e) and f) indicate the wind and convective mixing regimes respectively. Vertical shaded areas (E1 and E2) on panel b-f correspond to specific examples from the time series considered in section 5.4.5.

The mixed layer remained consistently deeper than the euphotic depth until the end of April when a rapid transition to surface stratification was observed. The data show that springtime stratification developed in two phases. First, the mixed layer shoaled from 200 m to 50 m in 5 days (19-23 April). Second, the mixed layer deepened below the euphotic zone again for a short period of time (30 April – 1 May) and subsequently shoaled above 100 m for the rest of the time series. The atmospheric data show that strong surface warming and low wind forcing promoted development of seasonal stratification: surface heat flux generally exceeded 100 W m^{-2} and wind stress noticeably decreased after 18th April compared with the rest of the time series (τ < 0.2 N m^{-2}). During the restratification, *S*(Chl *a*) initially reached 0.6 mg m^{-3} and subsequently peaked at 1.5 mg m^{-3} on 1st May. Chl *a* inventories decreased during this period from 60 mg m^{-2} to 30 mg m^{-2} and peaked again to 100 mg m^{-2} at the beginning of May.

5.4 Analysis

The data show that the phytoplankton bloom evolved slowly in weakly-stratified conditions over several months before the ocean mixed layer rapidly stratified at the end of April and remained shallow afterward. Below I test the hypotheses for the bloom onset and analyse how atmospheric forcing could affect the observed bloom dynamics.

The analysis was performed in a one-dimensional framework, interpreting the data as a time series. Data from both of the gliders deployed at a given time were used in the analysis. In order to assess the potential effect of spatiotemporal variability on the interpretation of the data set as a time series, the daily mean *I*(Chl *a*) and *S*(Chl *a*) from five separated areas within the sampling box were constructed implementing the approach described by Alkire et al. (2014). The areas were centred (± 4km) at the corners and at the centre of the glider sampling box. Both *I*(Chl *a*) and *S*(Chl *a*) show similar temporal patterns for all of the five areas (Figure 5.2) suggesting that the signal was dominated by temporal changes in phytoplankton variability rather than spatial heterogeneity within the sampling box due to phytoplankton patchiness.

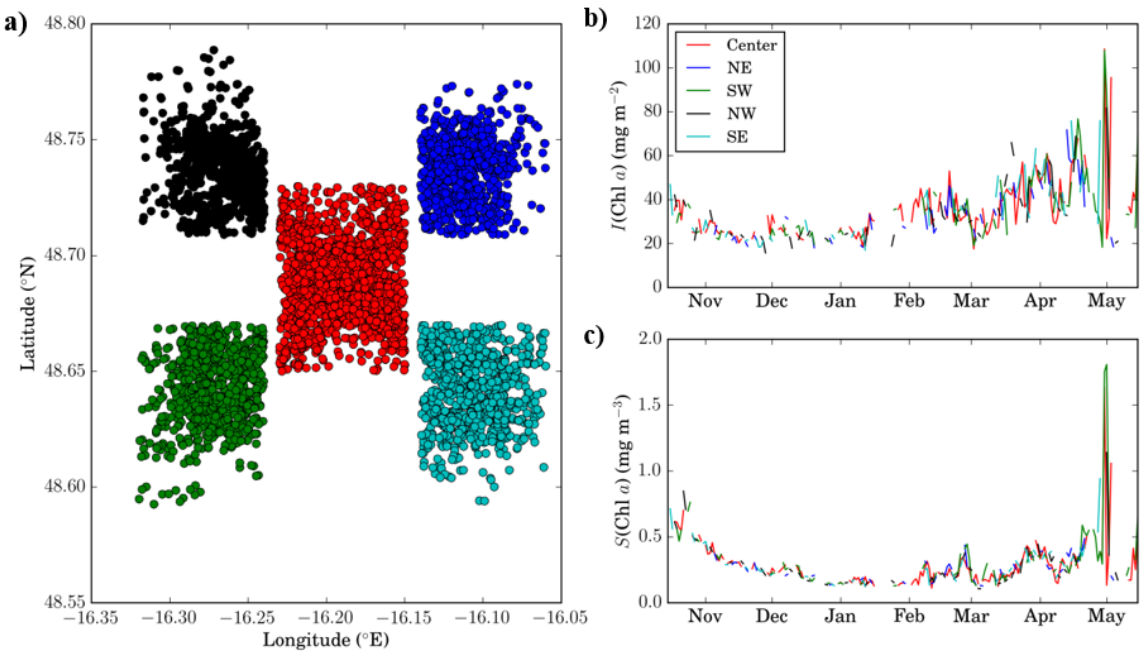

Figure 5.2 Investigation of the spatial heterogeneity within the glider sampling box. The plot on the left (panel a) shows the location of profiles from the five separated areas centred at the corners (NE, SW, SE, NW) and at the centre of the sampling site. The plot on the right shows the corresponding time series of daily mean *I*(Chl *a*) (panel b) and *S*(Chl *a*) (panel c).

It is acknowledged that lateral density gradients and associated submesoscale dynamics can drive increased growth of phytoplankton due to short term (< 1 day) restratification of the ocean mixed layer (Mahadevan et al. 2012) and significant losses in phytoplankton inventories due to export of organic material along isopycnal surfaces to the ocean interior (Omand et al. 2015). The presence of submesoscale features during the OSMOSIS study is discussed by Thompson et al. (2016), but the potential impact of these processes on the sub-daily distribution of phytoplankton is beyond the scope of the study.

5.4.1 Test of the critical depth hypothesis

According to the CDH, shoaling of the mixing layer above a critical depth prompts the onset of spring blooms. A comparison of the estimated range of z_{cr} with z_{mixing} is shown in Figure 5.3a. Figure 5.3b shows the time series of the net phytoplankton accumulation rates derived from the glider data using eq. 5.13-5.14. The critical depth criterion ($z_{mixing} < z_{cr}$) was generally met from February onwards when a period of mostly positive net accumulation rate was observed (Figure 5.3b). In February, z_{mixed} was within the range of the critical depth estimates; however z_{mixing} during the wind-mixing regimes was significantly shallower than the critical depth and positive net accumulation rate can be detected during this time (Figure 5.3a). Negative biomass accumulation rates were observed at the end of February through the beginning of March when z_{mixing} deepened

below the critical depth. The critical depth was sufficiently deep (100-500 m) to allow net phytoplankton to grow for several months before the seasonal restratification. However, estimates of the critical depth are sensitive to the choice of the compensation irradiance value. For the two compensation irradiance values used here (E_c = 1.75 E m^{-2} d^{-1} and E_c = 0.96 E m^{-2} d^{-1}), the difference between z_{cr} estimates was between 50 m and 250 m (Figure 5.3a). The criterion was generally met for both values of E_c. Therefore, the observed accumulation of phytoplankton in deep mixed layers is generally consistent with the CDH, provided the difference between z_{mixed} and z_{mixing} is considered.

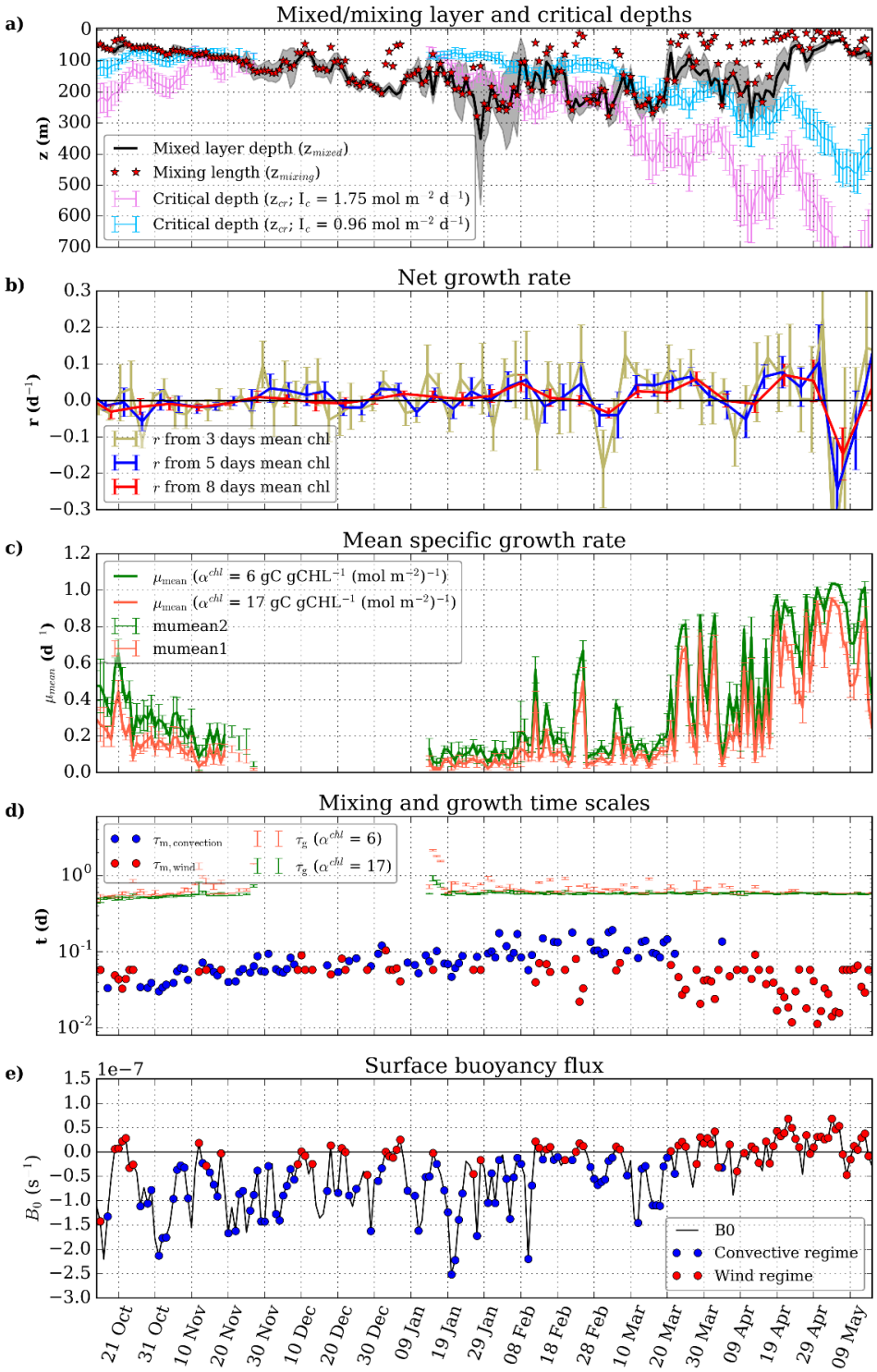

Figure 5.3 Time series of a) critical depth (z_c), mixed layer depth (z_{mixed}) and mixing layer depth (z_{mixing}), b) net accumulation rate of phytoplankton (r) calculated using Chl *a* data from the gliders, c) mean specific growth rate over z_{mixing}, d) growth time scales (t_g) and mixing time scales for the convective ($t_{m,\ convection}$) and the wind ($t_{m,\ wind}$) mixing regimes, e) surface buoyancy flux B_0. The surface light intensity data were not available in winter, therefore the time series of the critical depth, mean specific growth rate and growth time scales contain a gap. Bars on the plots are the estimated range of uncertainty.

5.4.2 Test of the critical turbulence hypothesis

According to the CTH, a spring bloom can start when phytoplankton growth time scales are shorter than mixing time scales. The test of the hypothesis was conducted by comparing estimated mixing (eq. 5.4 and 5.5) and growth time scales (t_m and t_g respectively). I used μ_{daymax} derived from eq. 5.12 to estimate the minimum growth time scale ($t_{g,min} = \frac{1}{\mu_{daymax}}$) that can be achieved under the observed light conditions. In reality, the growth time scales are also affected by various loss factors, therefore $t_g > t_{g,min}$. A comparison of the time scales is shown in Figure 5.3d. For both wind and convective mixing regimes, turbulent mixing time scales are approximately an order of magnitude smaller than calculated growth time scales. The conclusion that mixing time scales are significantly shorter than growth time scales is robust to the choice of values of α^{chl} and θ. The specific growth rate of phytoplankton for the suboptimal light regime is less than μ_{max} irrespective of values taken for α^{chl} and θ (eq. 5.11). For the observed surface temperature values (11-15 °C) during the period considered here μ_{max} was 1.6 – 2.2 d^{-1} (eq. 5.6), corresponding to growth timescales of 0.5 – 0.6 d, which is still significantly higher than the estimated mixing time scales (< 0.1 d; Figure 5.3d). This suggests that for the observed meteorological conditions, the critical turbulence criterion for bloom initiation expressed in terms of relevant time scales (i.e. $t_{g,min} < t_m$) was not met.

5.4.3 Test of the dilution-recoupling hypothesis

The DRH associates the spring bloom onset to decreasing loss rates in winter due to dilution of zooplankton and phytoplankton in deep mixed layers. Positive net accumulation rate during the periods of deepest mixing can indicate the dilution effect and provide support for the hypothesis (as shown by Behrenfeld (2010)). From December until the end of January the convective mixing regime dominated and deepening of the mixed layer was observed (Figure 5.3a, Figure 5.2e). During this time, average net accumulation rates were close to zero (r_3 = 0.01 d^{-1} (STD=0.04 d^{-1}), r_5 <0.01 d^{-1} (STD=0.02 d^{-1}), r_8 < 0.01 d^{-1} (STD=0.01 d^{-1}); Figure 5.3b). Within the quantified range of absolute errors, the sign of *r* was uncertain during December and January, except during a short period at the beginning of January when the net surface heat flux was close to zero (Figure 5.3e). Positive net growth was not evident during the period when mixing was the deepest and when phytoplankton specific growth rate was low (Figure 5.3c). Positive net accumulation rate during deep mixed layers (150 to 280 m) and strong cooling (Q = -200 to -300 W m^{-2}) conditions was observed in March. However, from February onwards, the surface light intensity was gradually increasing (Figure 5.2d) and a corresponding increase in mean specific growth rate (eq. 5.11) for phytoplankton can be

observed (Figure 5.3c). The data suggest that the positive net accumulation rate in March could be attributed to an increasing specific growth rate for phytoplankton rather than decreased grazing pressure. Therefore, predicted by the DRH, net accumulation of phytoplankton under deep mixing and low light conditions cannot be clearly detected in the glider data set.

5.4.4 Net accumulation rate variability derived from satellite Chl *a* data

The data set obtained during the OSMOSIS project allows comparing phytoplankton net accumulation rates derived from the vertically resolved glider data and net accumulations rates derived from the satellite ocean colour data only as described by Behrenfeld (2010). This comparison is interesting since many studies on phytoplankton spring blooms rely on the satellite ocean colour data. In addition, the satellite data ocean colour data is surface limited. To evaluate phytoplankton net accumulations rates following eq. 5.13 and 5.14, Behrenfeld (2010) estimated integrated Chl *a* values by multiplying surface Chl *a* by the mixed layer depth. Due to the potential divergence between z_{mixed} and z_{mixing}, this way of evaluating integrated values of Chl *a* can bias the estimates of phytoplankton net accumulation rates. The comparison allows accessing the consistency between the net accumulation rates variability derived from two data sets.

Satellite-derived surface Chl *a* estimates were calculated as the mean of all satellite observations within 100x100 km^2 area around the glider sampling site. Following Behrenfeld (2010), integrated Chl *a* values for satellite ocean colour data were estimated by multiplying satellite estimates of surface Chl *a* by the mixed layer depth. In this part of the analysis I used glider-derived estimates of the mixed layer depth. Subsequently, net accumulation rates were estimated for satellite-derived surface Chl *a* data averaged in time over 3 day (r_{3s}), 5 day (r_{5s}) and 8 day (r_{8s}) time intervals as described in section 5.2.3.

Figure 5.4 shows time series of r_3, r_{3s}, r_5, r_{5s}, r_8, and r_{8s}. Interestingly, phytoplankton net accumulation rates derived from the glider and satellite data are fairly consistent. Both data sets indicate periods of net positive phytoplankton growth in March and April. The satellite ocean colour data were unavailable in December and January. Therefore, it is not possible to assess the consistency between satellite and glider-derived net accumulation rates in winter. A noticeable discrepancy between the satellite and glider-derived net accumulation rates can be observed from the 1st until 15th of November. The satellite data indicate net positive phytoplankton growth. However, the glider data suggest that the net accumulation rate was close to zero. The discrepancy can be explained by factors like phytoplankton patchiness around the sampling area or changes in phytoplankton physiology discussed in section 2.2.5.

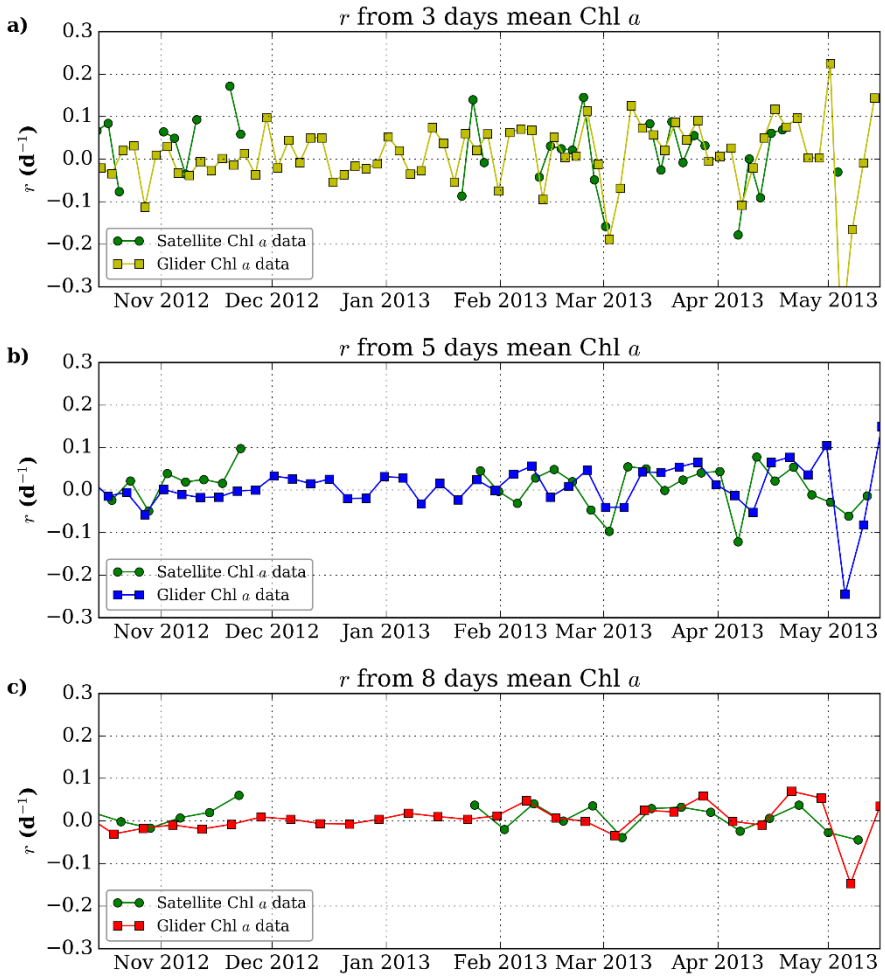

Figure 5.4. Comparison of phytoplankton net accumulation rate variability derived from the satellite ocean colour data (Aqua MODIS Level 3 products) and the glider data obtained during the OSMOSIS mission: a) r_3 (yellow line) and r_{3s} (green line), b) r_5 (blue line) and r_{5s} (green line), c) r_8 (red line) and r_{8s} (green line).

5.4.5 Sensitivity analysis

In this section, I explore the sensitivity of the obtained results to the choice of C_1, C_2, C_3, C_4, and C_5, dimensionless constants used to define mixing regimes and calculate mixing length/time scales. To conduct the sensitivity test, I run Monte-Carlo simulations repeating the classification of mixing regimes and calculations of mixing length/time scales (eq. 5.2-5.5) with randomly chosen values for C_1, C_2, C_3, C_4, and C_5. The distributions for the constants were set as uniform ranging ±50% from the initial values. The simulations were done 10000 times.

The outcome of the simulations (Figure 5.5, Figure 5.6) shows that the results of the hypotheses tests presented in this chapter are robust to the potential uncertainty in the choice of

C_1, C_2, C_3, C_4, and C_5 values. The obtained from simulations mixing time scales (t_m) are still significantly lower than the growth time scales estimated in section 5.4.2 (>0.5 d) (Figure 5.5). The simulations also show that different choice of the constants did not significantly affect estimates of the net accumulation rates (r_3, r_5, r_8) and the comparison of z_{mixing} with z_{cr} (Figure 5.6).

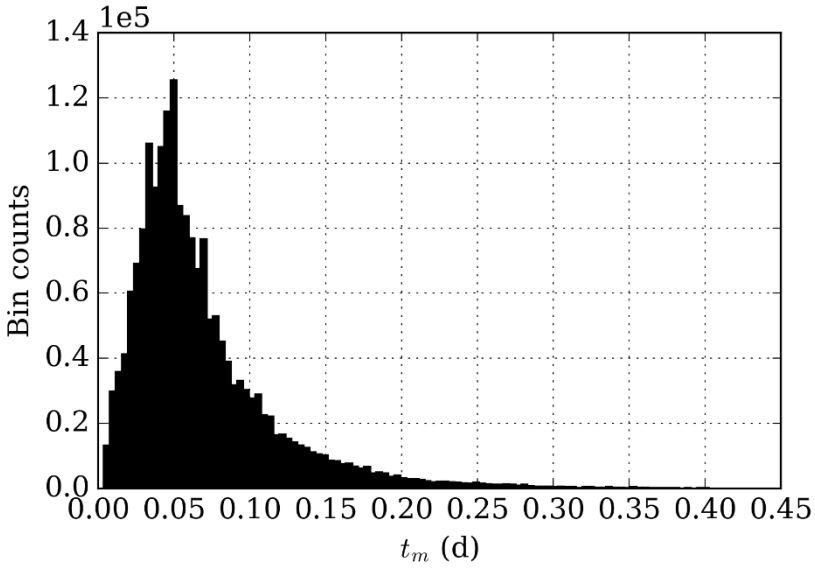

Figure 5.5 Histogram of mixing time scales obtained from the Monte-Carlo simulations.

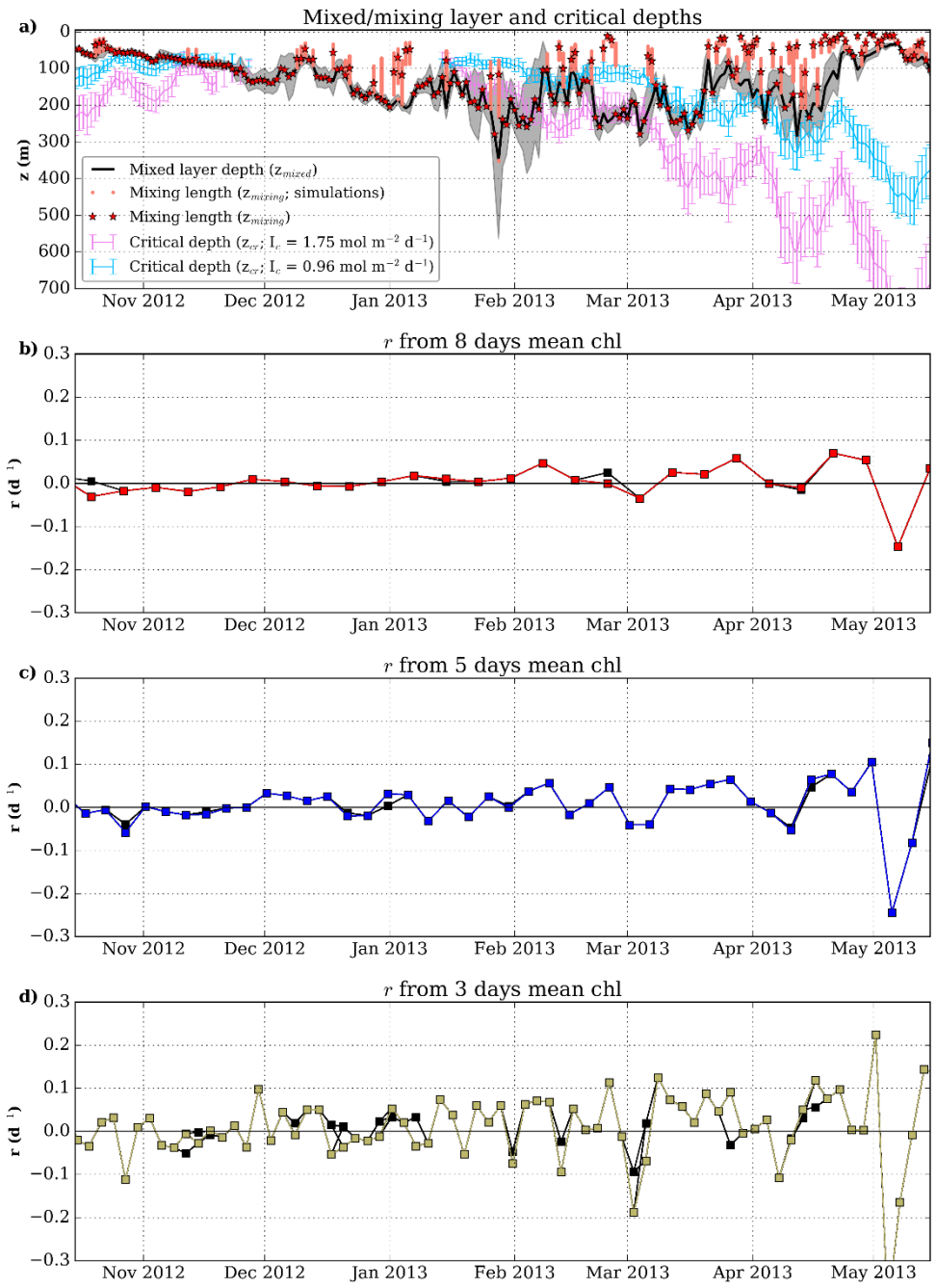

Figure 5.6 Time series of z_c, z_{mixed} and z_{mixing} (a), and the net accumulation rate of phytoplankton calculated using Chl *a* data from the gliders averaged in time over 3 day (b), 5 day (c) and 8 day (d) time intervals. Orange markers in the plot a) correspond to z_{mixing} values derived from the Monte-Carlo simulations. Coloured lines on the plots b), c) and d) correspond to the net accumulation rates presented in Figure 5.3, black lines are the ones derived from the simulations.

5.4.6 Impact of mixing regimes on the bloom development

The test of the bloom onset hypotheses demonstrated that net accumulation of phytoplankton was detected before the upper ocean restratification in spring, in a manner consistent with the CDH combined with increasing mean specific growth rates for phytoplankton due to improving light conditions. However, the observed increase of *S*(Chl *a*) and *I*(Chl *a*) was only a factor of 3 and 2 respectively from February (when $r > 0$ was detected) to the end of April (when seasonal stratification developed). Therefore, the question remains: why did shoaling of z_{mixing} above z_{cr} not result in a rapid and pronounced phytoplankton bloom event? Even though a bloom can be defined as an onset of net growth, some studies (e.g. Platt et al. 1991) consider the rapid accumulation of biomass an essential signature of phytoplankton spring blooms. In this section, I discuss how atmospheric forcing over the winter-spring period and the associated mixing regimes in the ocean boundary layer influenced the mean specific growth rates of phytoplankton and the bloom progression.

The depth of active mixing determines light conditions experienced by phytoplankton cells and influences the specific growth rate (μ_{mean}) for the phytoplankton community (eq. 5.11). Figure 5.7a shows changes in μ_{mean} calculated from eq. 5.11 as a function of z_{mixing} for mean surface irradiance (20 E m^{-2} d^{-1}) and mean light attenuation coefficient (0.066 m^{-1}) observed during the February – April period. The plot shows that for the mixing depth shallower than the euphotic depth, phytoplankton specific growth rate increases abruptly (the inflection points of the curves are close to z_{eu}). The mean specific growth rates calculated for the wind and convective mixing regimes as a function of wind stress and surface heat flux are shown in Figure 5.7b. During the convective mixing regime, convective cells penetrate the whole mixed layer resulting in relatively low mean specific growth rates for the phytoplankton community (0.1-0.3 d^{-1}). Under the wind-mixing regime μ_{mean} is low (0.1-0.4 d^{-1}) for relatively strong wind forcing (τ > 0.2 N m^{-2}) and significantly higher (μ_{mean} >0.5 d^{-1}) for calm weather conditions (τ < 0.2 N m^{-2}). Therefore, in weakly stratified conditions, shoaling of the mixing layer during the wind-mixing regime can significantly increase mean specific growth rate for the phytoplankton community when the wind forcing is weak.

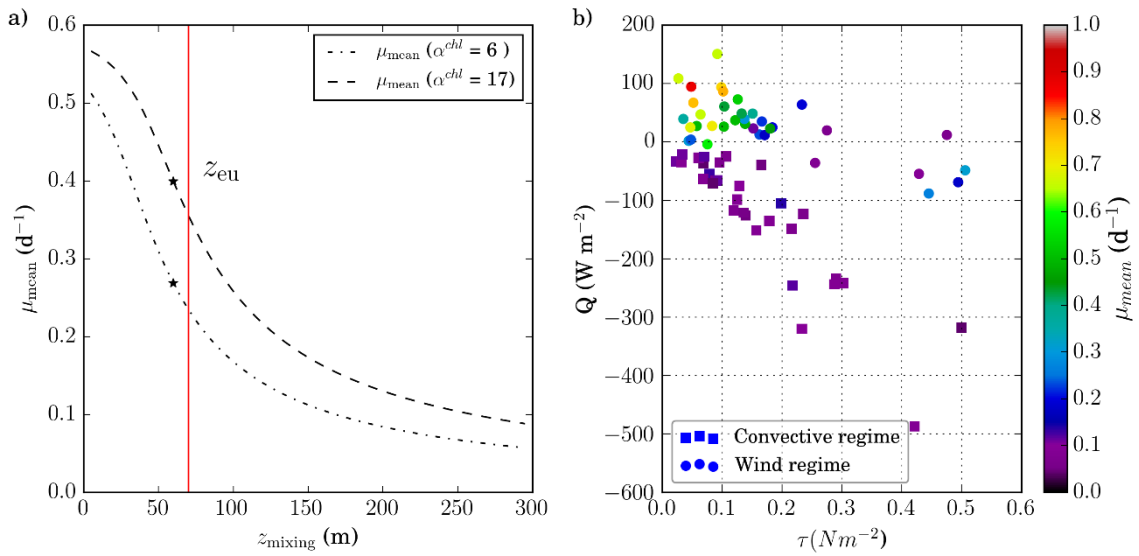

Figure 5.7 a) Mean specific growth rates (μ_{mean}) calculated using eq. 5.11 for α^{chl} = 6 (mmol m^{-2})$^{-1}$ (dashed line) and α^{chl} = 17 (mmol m^{-2})$^{-1}$ (dash-dot line), as a function of the mixing layer depth (z_{mixing}). The values of μ_{mean} were calculated for E_0 = 20 E m^{-2} d^{-1} and K = 0.066 m^{-1} (corresponding to z_{eu} ~ 70 m; vertical red line on the plot). Black stars on the plot represent the inflection points of the curves. b) μ_{mean} (colours) evaluated during the mission as a function of wind stress (τ ; x-axis) and surface heat flux (Q; y-axis). Circles and squares on the plot correspond to the wind and convective mixing regimes respectively.

However, a transition to a wind-mixing regime can have a two-fold effect on phytoplankton inventories. First, growth rates are significantly intensified for the part of the community trapped within z_{mixing} due to increased light exposure. The second effect is trapping of algae within the remnant layer, below z_{mixing}. A decaying mixing intensity below z_{mixing} increases residence time of phytoplankton within the remnant layer (Franks 2014) and potentially below the euphotic zone, where conditions are unfavourable for phytoplankton growth. As an example, if z_{mixed} is 250 m, shallowing of z_{mixing} to 50 m can lead to 80 % of the population being trapped in the aphotic zone (if z_{eu} < 50 m) and potentially being lost from the surface layer. However, the enhanced growth near the surface can rebuild phytoplankton inventories at the same time.

To demonstrate this, I use a simple model for phytoplankton accumulation:

$$\frac{dP(z,t)}{dt} = \mu(z,t)P, \tag{5.19}$$

where P is phytoplankton concentration at time t and depth z. Eq. 5.19 omits vertical diffusion and assumes the initial vertical distribution of phytoplankton is depth-independent. In the case of an

actively turbulent deep mixed layer, the evolution of phytoplankton concentration at any depth within z_{mixed} can be described by the following equation:

$$P_{\mathrm{mixed}}(t) = P_0 e^{\mu_{\mathrm{zmixed}} t}, \tag{5.20}$$

where μ_{zmixed} is the average growth rate in z_{mixed}. When the turbulence structure changes under the wind mixing regime, only the part of the community within z_{mixing} grows, albeit with a higher specific growth rate (μ_{zmixed}) due to increased light exposure:

$$P_{\mathrm{mixing}}(t) = P_0 e^{\mu_{\mathrm{zmixing}} t}, \tag{5.21}$$

where P_{mixing} is phytoplankton concentration within z_{mixing}. If $z_{mixing} < z_{eu}$, phytoplankton also accumulates between z_{mixing} and z_{eu}, although this region is not actively mixed and, therefore, the specific growth rate is not uniform. An example of a vertical profile for the specific growth rate is shown in Figure 5.8a.

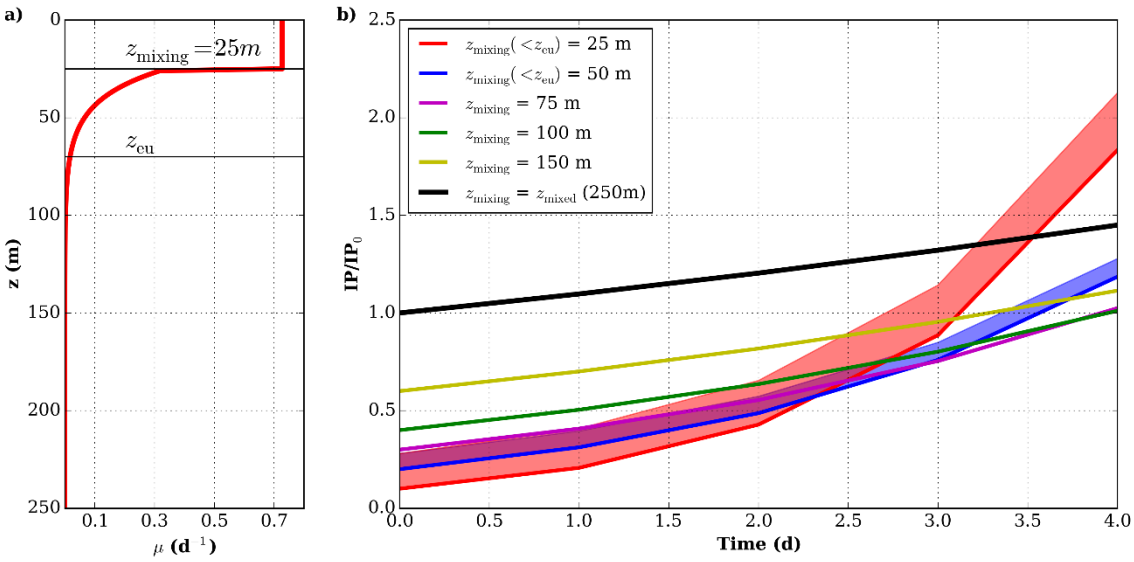

Figure 5.8 a) An example of a vertical profile of phytoplankton specific growth rate (z_{mixing} = 25 m) used to investigate changes in phytoplankton stocks. The growth rate was calculated based on eq. 5.11 for K = 0.066 m^{-1}, E_0 = 20 E m^{-2} d^{-1}, α^{chl} =6 (mmol m^{-2})$^{-1}$ b) Normalized changes in phytoplankton stocks (*IP*) assuming an actively turbulent z_{mixed} (black line) and range of z_{mixing} values (coloured lines on the plot). *IP* values were normalized by IP_0, the initial phytoplankton stock before switching to wind mixing regime. Shaded area indicates additional accumulation of phytoplankton between z_{mixing} and z_{eu}, if $z_{mixing} < z_{eu}$.

Figure 5.8b demonstrates the estimated changes in phytoplankton inventories for the range of z_{mixing} values observed in the glider data (25, 50, 75, 100 and 150 m) as well as for $z_{mixing} = z_{mixed}$ (=

250 m) (Figure 5.8b). In the case of the shallowest z_{mixing}, which generally corresponds to low wind forcing, the fastest accumulation of phytoplankton biomass occurs.

To illustrate the effect of mixing regimes on phytoplankton inventories using in situ data, I compare Chl *a* variability at the end of February, when the surface heat flux was approaching zero and wind intensity was low, to a period of strong convective mixing in March (the selected periods are marked as E1 and E2 respectively in Figure 5.1). The first period is characterized by the significant difference between mixed layer depth (z_{mixed} = 250 m) and mixing layer depth (z_{mixing} = 25 m) (Figure 5.9a). Averaged vertical profiles for this period show surface intensified vertical distribution of Chl *a* within the hydrographically defined mixed layer (Figure 5.9a). Phytoplankton is relatively well mixed down to mean z_{mixing} estimated over the selected period. For the E2 period, when mixing in the water column is driven by convection, the Chl *a* distribution is relatively uniform within z_{mixed} (Figure 5.9b). Figure 5.9c and Figure 5.9d illustrate temporal changes of water column integrated Chl *a*, along with Chl *a* integrated to below and above the euphotic depth during E1 and E2. During E1, below the euphotic depth phytoplankton inventories gradually decrease (Figure 5.9c), reflecting the fact that the divergence between z_{mixing} and z_{mixed} during the wind-mixing regime significantly increases the residence time of phytoplankton in the aphotic zone prompting phytoplankton losses. The opposite effect is observed for the phytoplankton population within the euphotic zone. As a result, overall phytoplankton inventories increase slightly. For the E2 period, the changes in water column integrated Chl *a* correspond to integrated Chl *a* below the euphotic zone (Figure 5.9d) reflecting the fact that the vertically homogeneous turbulent mixed layer results in relatively uniform light conditions for phytoplankton cells.

This analysis shows a convective mixing regime is generally associated with low mean specific growth rates for the phytoplankton community. The shift to a wind mixing regime can significantly increase μ_{mean} especially in the case of low wind forcing, but at the same time, a significant part of the phytoplankton community can be trapped in the aphotic layer and potentially lost.

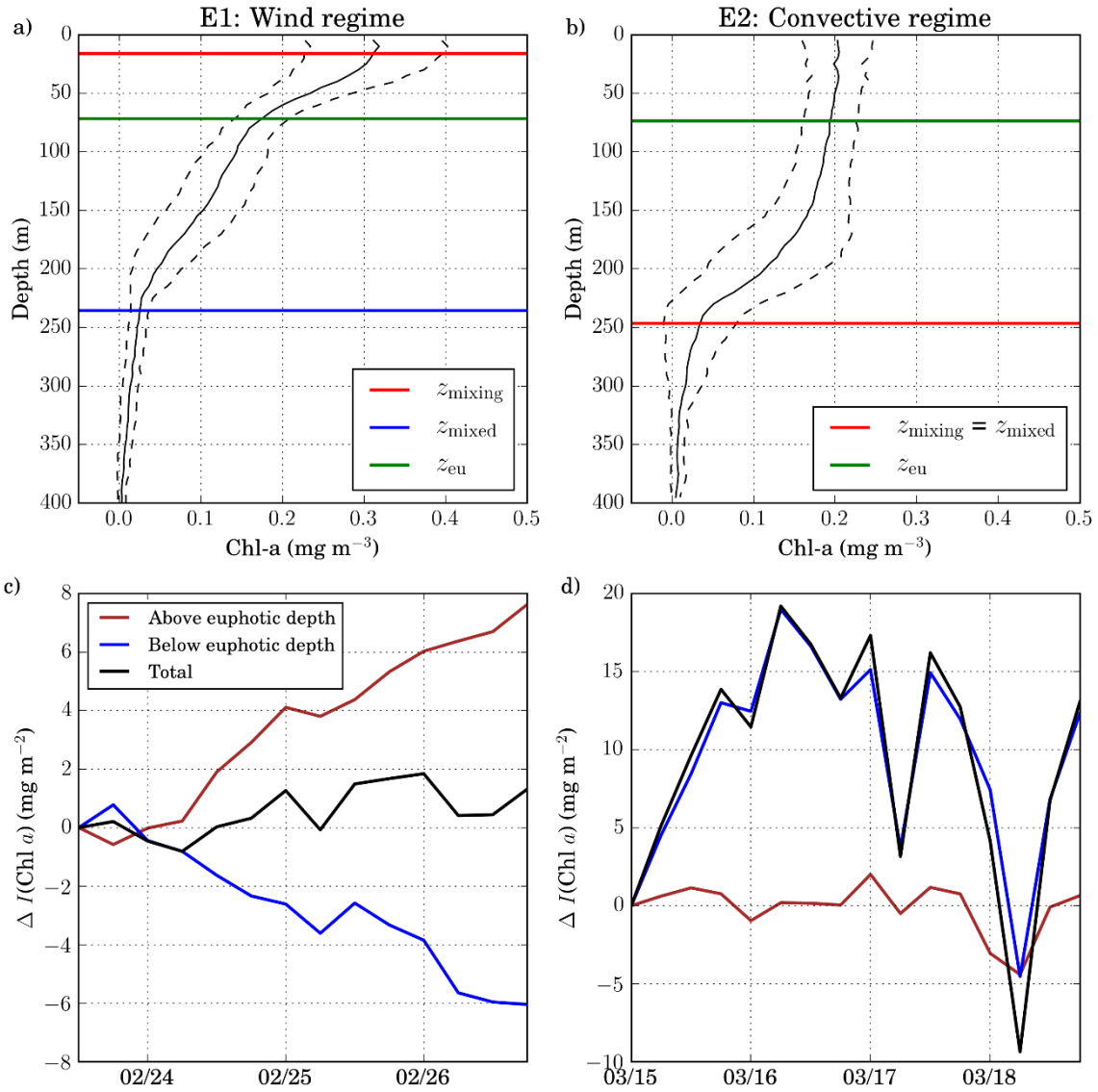

Figure 5.9 Examples of phytoplankton dynamics during wind mixing regime (24-27th of February; marked as E1 on Figure 5.1) and b) convective mixing regime (15-19th of March; marked as E2 on Figure 5.1). The top panels are combined mean vertical profiles of Chl *a* (black solid line) and standard deviation (dashed lines) showing phytoplankton distribution during E1 (a) and E2 (b). Red, blue and green lines on the figure correspond to z_{mixing}, z_{mixed}, and z_{eu} respectively. The bottom panels are changes in phytoplankton stocks integrated over the whole water column (black line), above the euphotic depth (red line) and below the euphotic depth (blue line) during E1 (c) and E2 (d).

5.5 Discussion

In this chapter, the glider data have been used to study the impact of atmospheric forcing on phytoplankton spring bloom dynamics and to test the commonly discussed hypotheses for the spring bloom initiation in the North Atlantic Ocean: CDH, CTH, and DRH.

The analysis performed in this study has not found evidence that CTH and DRH explain the onset of phytoplankton growth in deep mixed layers. The test of the CTH showed that decreasing mixing intensity was unlikely to be driving enhanced phytoplankton growth in winter and spring. The result is consistent with previous investigations of the CTH through theoretical and modelling frameworks. Taylor & Ferrari (2011a) tested the hypothesis for the convective mixing regime and found that spring blooms did not develop in deep mixed layers in the presence of surface cooling. Further exploration of the hypothesis by Enriquez & Taylor (2015) demonstrated that in a wind-mixing regime, shoaling of z_{mixing} rather than decreasing mixing intensity acts as a mechanism of bloom initiation supporting the CDH. Huisman et al. (1999) showed that the phytoplankton spring bloom could develop in an arbitrarily deep mixed layer for vertical eddy diffusivities below 10 cm^2 s^{-1} (10^{-3} m^2 s^{-1}) (Figure 1.6). The critical value of eddy diffusivity derived by Huisman et al. (1999) is an order of magnitude lower than the eddy diffusivity values previously resolved by the LES model (Taylor & Ferrari 2011a; Enriquez & Taylor 2015): 10^{-2} m s^{-1} for Q = -1 W m^{-2} (Figure 5.10a) and 10^{-2} m s^{-1} within the actively mixed layer for Q = 0 W m^{-2} and τ = 0.08 N m^{-2} (Figure 5.10b). Therefore, results of Huisman et al. (1999) might be biased because of the unrealistically low eddy diffusivity needed to initiate a phytoplankton bloom near the ocean surface due to decreasing mixing intensity.

Analysis of the net accumulation rates conducted in this study chapter did not provide support that the phytoplankton bloom started under strong convective mixing in winter due to reduced encounter rates of phytoplankton with grazers. The consistent positive net accumulation rate of phytoplankton was only observed later in the season when the surface light intensity was gradually increasing and the mixing depth was decreasing. However, a more robust test of the hypothesis would require additional data on changes in zooplankton grazing rates in winter that could provide direct evidence for the DRH.

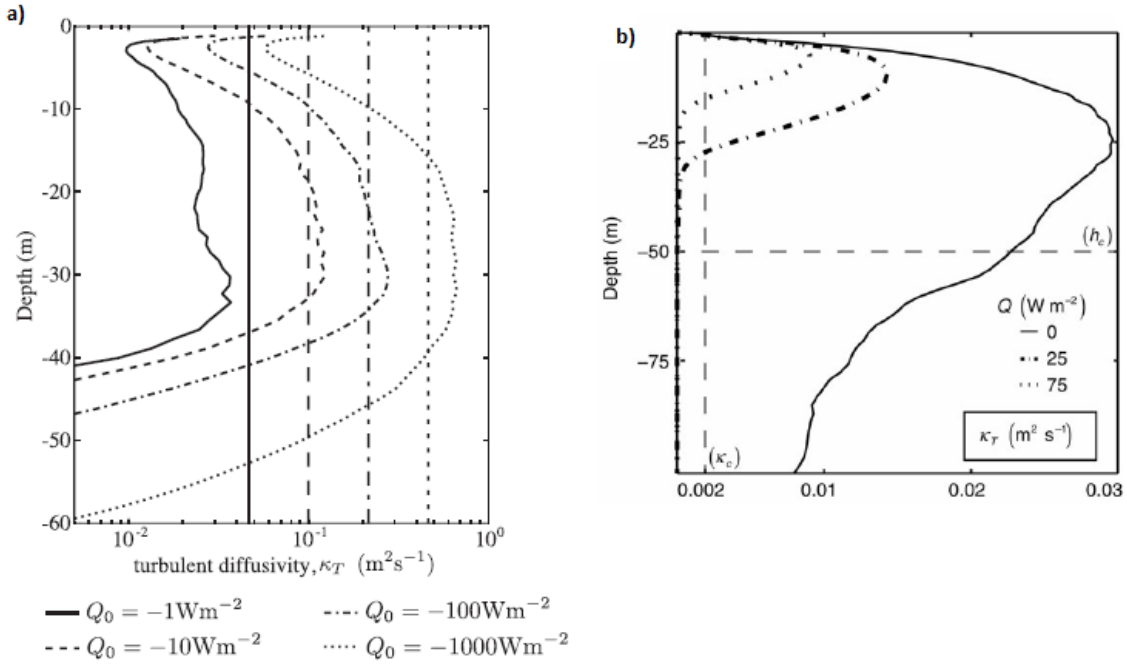

Figure 5.10 Turbulent diffusivity inferred from the LES model: a) simulations forced with a constant negative surface heat flux (Convective mixing regime; taken from Taylor & Ferrari (2011a)), b) simulations forced with constant wind stress (τ = 0.08 N m^{-2}) and positive surface heat flux (Q = 0, 25, 75 W m^{-2}) (Wind mixing regime; taken from Enriquez & Taylor (2015)).

Positive net accumulation rates of phytoplankton were mostly associated with z_{mixing} shoaling above the estimated z_{cr} consistent with Sverdrup's critical depth hypothesis. However, the estimates of z_{cr} heavily depend on the value of the compensation irradiance which I assumed to be constant here. Sverdrup introduced compensation irradiance as a parameter reflecting the loss rates of phytoplankton due to respiration, grazing, sedimentation and other factors during the pre-bloom period. The analysis performed by Platt et al. (1991) demonstrated that the critical depth estimates are highly sensitive to changes in loss terms. Therefore, the compensation irradiance is likely to be a dynamic parameter that changes depending on grazing pressure and other loss factors. Slow spring bloom development can cause a response in the grazing community as shown by Waniek (2003) using a mixed-layer model coupled with a population dynamics model and discussed by Behrenfeld (2014). Indeed, during the JGOFS-NABE experiment (Ducklow & Harris 1993) conducted in the Northeast Atlantic Ocean, low f-ratios (the ratio between new and total primary production) were detected during the onset of stratification suggesting high grazing rates preceded the bloom event associated with restratification (Garside & Garside 1993). Again, gliders did not measure grazing pressure. Potential variability in loss rates can, in part, be addressed by investigation of the phytoplankton spring bloom through a modelling framework (e.g. Lévy 2015).

In their examination of the critical depth framework, Platt et al. (1991) concluded that "*the Sverdrup criterion is necessary but not sufficient*" for predicting rapid phytoplankton accumulation in spring. Simply put, the criterion can only indicate if the net growth of phytoplankton can occur, but not how rapidly the bloom will progress. Platt et al. (1991) suggested that the frequent occurrence of storms prevents the rapid accumulation of phytoplankton biomass. In this chapter, the analysis of the mean specific growth rates under the wind and convective mixing regimes shows how meteorological conditions can affect the development of the spring bloom. For the convective mixing regime, phytoplankton accumulation occurs over the entire mixed layer, but relatively slowly due to low mean specific growth rates. When a shift to a wind-mixing regime takes place, the part of the phytoplankton population within the mixing layer grows more rapidly, but at the same time, losses from the remnant layer can slow down the vertically-integrated accumulation of phytoplankton biomass. It is important to note that this source of losses is not included in the critical depth model. Rapid growth near the surface can rebuild phytoplankton inventories rapidly (over about 4 days; Figure 5.8). From February until late April strong wind forcing occurred every 2-4 days (Figure 5.1f). During high wind forcing (τ > 0.2 N m^{-2}), phytoplankton gets redistributed over a deeper layer and the mean specific growth rate decreases significantly compared to calm weather conditions. Therefore, frequent passage of storms can interrupt the rapid development of the phytoplankton spring bloom. Interestingly, the effect of storms on phytoplankton blooms in the temperate North Atlantic Ocean is different for spring and autumn. In autumn phytoplankton growth is limited by nutrient availability and, as shown in Chapter 4, the passage of storms induces phytoplankton blooms. Here I show that windy conditions in spring can prevent the development of rapid phytoplankton spring blooms by decreasing light-dependent mean specific growth rates for the phytoplankton community.

The correlation between spring bloom characteristics and wind conditions in spring has been noted before. Analysis of satellite data (Ueyama & Monger 2005; Henson et al. 2009b) has shown late, low magnitude phytoplankton spring blooms in the North Atlantic during the positive phase of the North Atlantic Oscillation, commonly associated with strong westerly winds in winter-spring. Waniek (2003) demonstrated that windy weather in spring results in low magnitude interrupted phytoplankton blooms, similar to the one captured during the OSMOSIS mission. The passage of weather systems varies inter-annually and might be affected by future changes in the North Atlantic climate (Gillett et al. 2003). The predicted changes involve increasing sea surface temperature (Allen et al. 2014), variability in surface heat fluxes and increasingly positive North Atlantic Oscillation conditions (Osborn 2004) that would change basin-scale wind forcing patterns. In this

study, it has been shown that atmospheric forcing and associated mixing regimes in the water column have a profound impact on phytoplankton growth rates and manifestation of algal blooms.

5.6 Conclusions

Autonomous underwater gliders deployed at the PAP site provided a unique data set capturing the development of the phytoplankton bloom in the North Atlantic Ocean over winter and spring. Motivated by the long-running debate on Sverdrup's critical depth hypothesis, this chapter concludes that the bloom onset was consistent with the critical depth hypothesis when the divergence between the mixed layer depth and the active mixing layer under a wind-driven mixing regime is considered. The subsequent development of the bloom was interrupted by the meteorological conditions through their effect on phytoplankton specific growth rates. The observed low magnitude of the bloom can be in part explained by the frequent passage of storms and periods of convective mixing after the seasonal onset of net growth.

Chapter 6: Spring bloom dynamics and zooplankton variability

In this chapter a potential impact of zooplankton variability on the observed phytoplankton dynamics in winter and spring is explored. The phytoplankton bloom development was considered as a problem of population dynamics. The glider data were complemented by a simple phytoplankton-zooplankton model.

6.1 Introduction

The pronounced phytoplankton seasonality and formation of seasonal spring blooms in the temperate and subpolar North Atlantic Ocean have been the focus of oceanographic studies for decades. Traditionally the onset of blooms in the region has been attributed to improving light conditions for phytoplankton in spring (Sverdrup 1953). Stabilization of the water column due to surface heating leads to shoaling of the ocean mixed layer and abruptly increasing phytoplankton growth rate. As formulated by Sverdrup in his critical depth hypothesis, during seasonal stratification the mixed layer becomes shallower than the critical depth - the depth at which integrated primary production is equal to integrated phytoplankton losses. However, recent studies have proposed a variety of alternative physical mechanisms that can explain initial improvement of the light conditions and trigger a bloom without seasonal re-stratification of the water column by heating, such as submesoscale processes (Mahadevan et al. 2012), cessation of convection (Taylor & Ferrari 2011b), and decreasing wind-driven mixing in the upper ocean (Brody & Lozier 2015; Brody & Lozier 2014).

On the other hand, analysis of the CDH performed by Platt et al. (1991) highlighted that the spring bloom onset is a multi-factorial problem. Loss factors, such as zooplankton grazing by micro and macro zooplankton, can be essential for promoting or preventing the explosive increase of the phytoplankton population in spring when its growth rate increases dramatically due to seasonal stratification. In Sverdrup's model, loss factors are incorporated in the compensation irradiance, the light level in the water column at which phytoplankton loss rates and phytoplankton growth rates are equal. According to the CDH, the value of compensation irradiance is constant and known before the bloom onset. Therefore, CDH oversimplifies the role of grazing in the bloom initiation process by assuming that losses are constant. Cushing (1959) suggested that the onset of phytoplankton blooms is mainly driven by a disequilibrium between phytoplankton and herbivores, and represents a problem of population dynamics. Nevertheless, the importance of biotic factors

(e.g., grazing by zooplankton) has received significantly less attention in literature on spring blooms in the North Atlantic Ocean compared to abiotic factors such as turbulent mixing and nutrient input (Fischer et al., 2014).

Satellite ocean colour radiometry and measurements of Chl *a* fluorescence from autonomous platforms such as floats and gliders allow phytoplankton distributions to be mapped over large spatial and temporal scales. However, measurements of zooplankton distribution mainly come from short duration research cruises. To counter the lack of data, the impact of zooplankton on phytoplankton seasonality has been addressed using population dynamics models (Evans and Parslow, 1985). In general, the population dynamics models represent a valuable tool for exploring hypotheses regarding plankton variability that underlie the observations (Franks, 2002; Lévy, 2015).

In this chapter I combine the observational data and a population dynamics model in order to address the impact of zooplankton variability and associated changes in loss rates on the observed phytoplankton seasonality at the PAP site. The model was forced with specific phytoplankton growth rate estimated using the obtained data. The lack of a pronounced spring bloom event in the year of sampling can be also explained by phytoplankton-zooplankton interactions. The role of zooplankton in spring bloom manifestation is further explored through a series of simple numerical experiments with variable winter mixed layer depth and timing of seasonal stratification. The experiments emphasize that zooplankton dynamics before the onset of seasonal stratification can have a dramatic effect on phytoplankton spring bloom dynamics.

6.2 Methods

6.2.1 A simple phytoplankton-zooplankton model

In order to investigate the impact of predator-prey interactions on the manifestation of phytoplankton blooms, I used a simple one-dimensional ecosystem model with two state variables: phytoplankton (*P*) and zooplankton (*Z*) (Lotka-Volterra equations). The ecosystem dynamics was assumed to be driven by changes in light conditions and mixed layer depth (Evans and Parslow, 1985). Therefore, the model was forced with a time-varying mean phytoplankton specific growth evaluated based on the observational data. Change in phytoplankton abundance ($\frac{dP}{dt}$) is a function of gross phytoplankton production and losses due to phytoplankton mortality and consumption by zooplankton. Variability of zooplankton concentration ($\frac{dZ}{dt}$) is described as a function of zooplankton

gross production and losses due to mortality and predation by higher trophic levels (quadratic mortality). The model equations are taken from Behrenfeld & Boss (2014):

$$\frac{dP}{dt} = \mu_{\text{mean}}(t)P - bP - c_1 \frac{P^2 Z}{P^2 + c_2}, \tag{6.1}$$

$$\frac{dZ}{dt} = c_1 c_2 \frac{P^2 Z}{P^2 + c_2} - c_4 Z - c_5 Z^2, \tag{6.2}$$

where μ_{mean}(t) is the phytoplankton specific growth rate, b is phytoplankton mortality, c_1 is the maximum zooplankton growth rate, $\sqrt{c_2}$ is grazing half saturation, c_3 is ingestion efficiency, c_4 is zooplankton non-predation mortality and c_5 is zooplankton predation mortality. Zooplankton are assumed to feed on a single type of prey assuming sigmoidal (threshold) response of predator to prey concentration. All stocks are characterized in terms of mmol N m^{-3}.

As described in section 5.2.5 (eq. 5.11), μ_{mean} is a function of surface light intensity (E_0), light attenuation coefficient (K), mixed layer depth (z_{mixed}) and physiological parameters α^{chl} and ϑ. I calculated μ_{mean} based on the observational data for K (glider PAR data; section 2.3), z_{mixed} (based on glider TS data; section 2.4) and E_0 (Aqua MODIS Standard products; section 2.5). The assumed values for α^{chl} and ϑ are given in Table 6.1. The observational data was smoothed using 5-day moving average filter. The list of other constants (b, c_1, c_2, c_3, c_4, c_5) used to run the model is also presented in Table 6.1. Simulations were run with μ_{mean} at t_0 long enough (for 1000 days) to drive the model to a steady state. Then, variability in μ_{mean} was added. The model was executed using Matlab ODE45 solver which uses a variable step Runge-Kutta procedure.

Variability in nutrient concentrations was not included in the model equations. Nutrients were assumed to be replete during the period of interest (January – June). The assumption is supported by in situ data obtained during JC087 cruise to the sampling site that took place from the 31st of May until the 16th of June 2013. Data obtained on JC087 cruise showed nitrate concentration at the sampling site of 2-6 mmol N m^{-3} suggesting that by June nutrients were not completely utilized.

6.2.2 Net accumulation and loss rates

Using the PZ model, phytoplankton net accumulation rate was evaluated as:

$$r = \frac{\ln(P_{t1}/P_{t0})}{\Delta t}, \tag{6.3}$$

where P_{t1} and P_{t0} are phytoplankton population at time steps t_1 and t_0 respectively and $\Delta t = t_1 - t_0$ that equals to 1 day. Phytoplankton loss rates (l) was defined as:

$$l = \mu_{\text{mean}} - r. \tag{6.4}$$

Net accumulation and loss rates were also calculated using the glider Chl *a* time series. Since the gliders provided measurements of surface values of Chl *a* and measurements of Chl *a* inventories, the net accumulation rate was evaluated following the methodology described in section 5.2.3. The loss rate for the glider-derived Chl *a* time series was evaluated using eq. 6.4.

Table 6.1. List of parameters used in the PZ model

	Symbol	**Value**	**Units**
Phytoplankton mortality	b	0.06	d^{-1}
Maximum zooplankton growth rate	c_1	3.24	d^{-1}
Grazing half-saturation	c_2	0.44	$mmol^2\ m^{-6}$
Ingestion efficiency	c_3	0.5	unitless
Zooplankton non-predation mortality	c_4	0.06	d^{-1}
Zooplankton quadratic mortality	c_5	1	$mmol^{-1}\ m^3\ d^{-1}$
Chl *a* specific slope of phytoplankton irradiance curve	α^{chl}	10	$(mmol\ m^{-2})^{-1}$
Chl *a*-to-carbon mass ratio	ϑ	0.015	unitless

6.3 Results

6.3.1 Observed variability in Chl *a*

Variability in *S*(Chl *a*) values derived from the satellite products and the glider data is shown in Figure 6.1. According to the satellite data, the year of the glider mission is characterized by

relatively late phytoplankton seasonality compared to previous years (Figure 6.1). From January until June, Chl *a* concentration mostly remains < 0.5 mg m^{-3}. Monthly satellite data composites show a patch of low Chl *a* around the sampling area which persisted through March, April, May and June (Figure 6.2). In all images the low Chl a patch is observed between 10-20 °W and 48-60 °N, corresponding to an area of O (10^6) km^2 (Figure 6.2). Therefore, the regime observed during the deployment period was characterized by low values of Chl *a*, regardless of replete nitrate concentrations (as suggested by cruise data in June). The glider data show relatively low (< 0.5 mg m^{-3}) surface Chl *a* concentrations from January till the end of April, followed by peaks in May and the beginning of June. The peaks in surface Chl *a* were not clearly resolved in the satellite data.

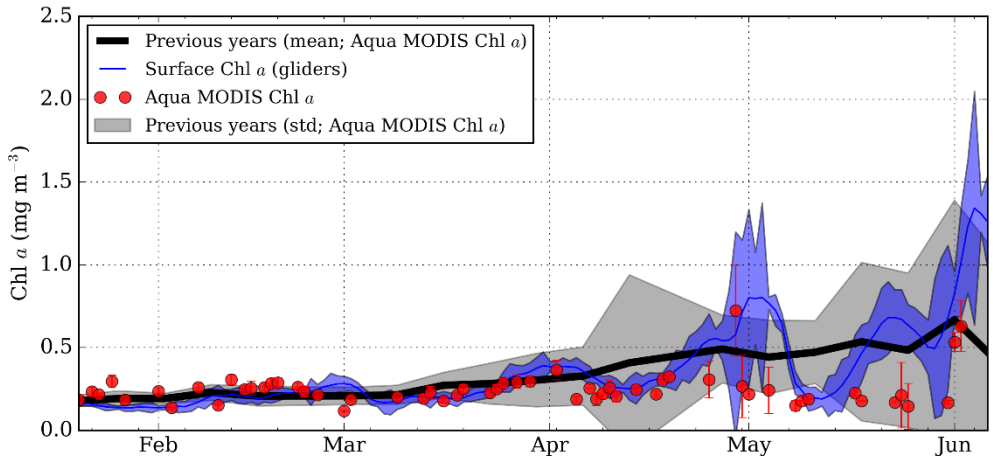

Figure 6.1 Daily mean glider-surface Chl *a* (blue line; blue shaded area ±std), mean over the glider-sampling area satellite Chl *a* (red circles; bars represent ±std) and mean satellite Chl *a* observed over previous yeas during Aqua MODIS mission 2002-2011 (black line; grey shaded area represents ±std).

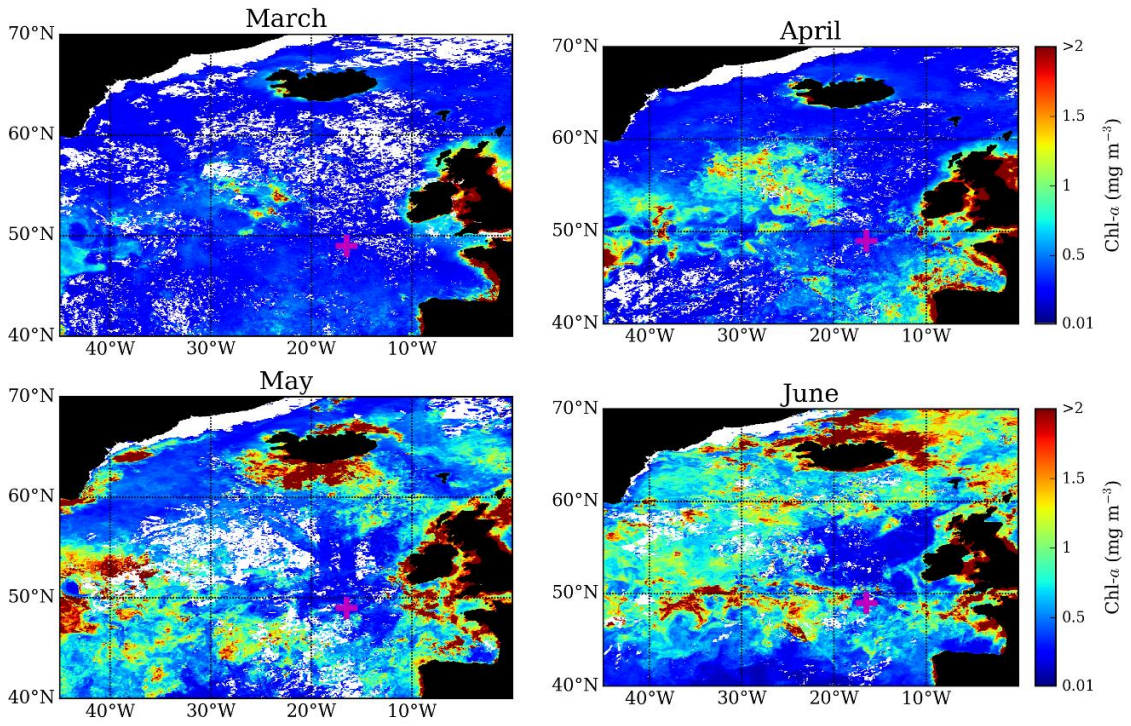

Figure 6.2 Aqua MODIS satellite images (monthly composites) of Chl *a* values over the North Atlantic Ocean for March, April, May and June 2013. Pink cross on the plots indicates the location of the sampling site.

6.3.2 Comparison of model results with observational data

The time series of P, Z, S(Chl *a*), μ_{mean}, K, z_{mixed} and E_0 are shown in Figure 6.3. The data shows that z_{mixed} remained relatively deep from January until the end of April when rapid shoaling of z_{mixed} was observed. The mixed layer remaining < 100 m for the rest of the time series. For clarity I refer to the time period between January and the end of April as the *deep mixed layer phase* and to the rest of the time series as the *shallow mixed layer phase* (Figure 6.3).

Despite its simplicity, the PZ model reproduced well variability in phytoplankton concentration (indexed as Chl *a* fluorescence) measured by the gliders. During the deep mixed layer phase both the model and the data indicated elevated phytoplankton concentrations in mid-February and at the end of March. The three distinct peaks also appear in the model output during the shallow mixed layer phase. Some discrepancy between the model and data (such as in the of February and beginning of April) can be in part explained by the fact that in late winter and spring, when convective mixing subsides, the mixed layer depth can differ from the depth of the layer where mixing is currently active. The impact of the divergence between z_{mixed} and z_{mixing} on the model output is further discussed in section 6.4.1.

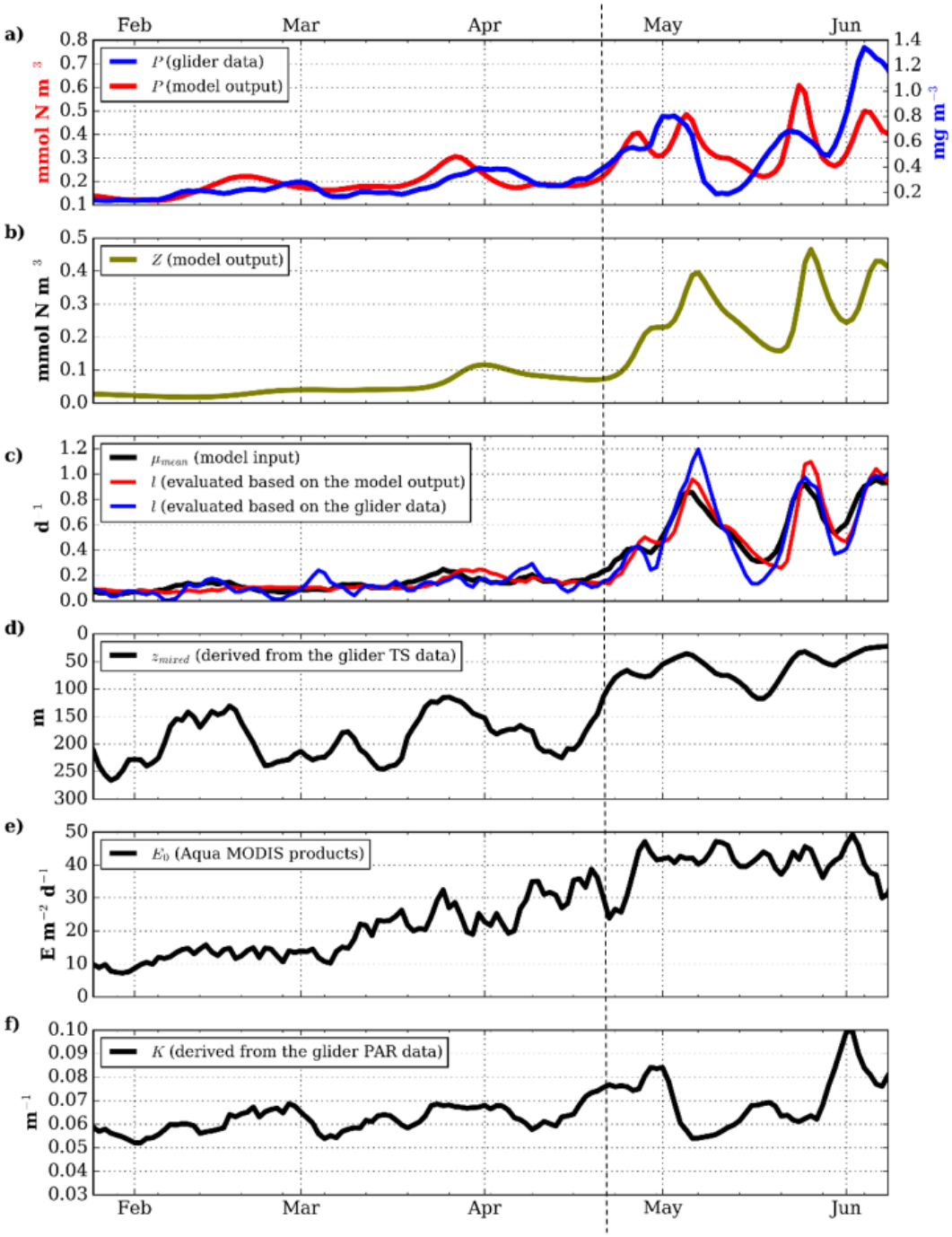

Figure 6.3 a) Phytoplankton variability observed by gliders (surface Chl *a*; blue line) and derived from the PZ model (red line), b) zooplankton variability derived from the PZ model, c) mean over the mixed layer phytoplankton growth rate evaluated based on the observational data (model input; black line), phytoplankton loss rates evaluated based on the output from the PZ model (red line) and based on the glider data (blue line) d) mixed layer depth estimated based on the glider TS data, e) surface light intensity (Aqua MODIS standard surface PAR products) and f) light attenuation coefficient estimated based on the glider PAR data. The vertical dashed line on the plot separates the deep mixed layer phase and the shallow mixed layer phase (section 6.3.2).

6.3.3 Zooplankton variability and loss rates

The model output suggested a tight coupling of the planktonic ecosystem during the mission. Phytoplankton losses evaluated from the model and the data are consistent and correlate well with variability in μ_{mean} (Figure 6.3c). During the deep mixed layer phase l rose from ~0.1 to ~0.2 d^{-1} (Figure 6.3c) that corresponded to the gradual accumulation of zooplankton (Figure 6.3b). However, zooplankton concentrations at that time were significantly lower compared to the ones during the shallow mixed layer phase when three peaks in phytoplankton abundance were observed. The accumulation of phytoplankton and zooplankton in deep mixed layers is related to gradually increasing μ that is driven by the positive trend in surface light intensity (Figure 6.3e).

According to the model output, the peaks in phytoplankton concentration during the shallow mixed layer phase are each followed by peaks in zooplankton concentration (Figure 6.3b). The time lag between P and Z peaks is 2, 3 and 4 days respectively. The formation of the peaks in phytoplankton and zooplankton in the model corresponds to abrupt increases in μ_{mean} that disturb the phytoplankton-zooplankton coupling, and hence permit rapid increases in phytoplankton concentration. The growth rate peaked due to both rapidly shoaling z_{mixed} and decreasing K (Figure 6.3d and Figure 6.3f).

6.3.4 Model experiments

In the previous section, the model output showed significant variability in zooplankton (Figure 6.3b) and loss rates (Figure 6.3c) during the deep mixed layer phase contradicting Sverdrup's assumption on constant loss rates during the pre-bloom period. However, values of l during the deep mixed layer phase (0.1-0.2 d^{-1}) were significantly lower compared to the ones during the shallow mixed layer phase (0.2-1.2 d^{-1}). In order to investigate the role of zooplankton in phytoplankton dynamics two further series (hereafter Series 1 and Series 2) of illustrative modelling experiments were conducted. Each series consisted of 30 experiments. The experiments aim to represent the winter to spring transition with relatively deep z_{mixed} in winter followed by rapid shoaling of z_{mixed} in spring. Variability in winter z_{mixed} and duration of deep mixed layer phase can affect zooplankton dynamics before the onset of the stratification. The experiments examine how sensitive spring bloom characteristics are to changes in zooplankton abundance before the stratification onset. In the experiment set up the rapid shoaling of z_{mixed} corresponding to the onset of spring stratification is the main factor causing disequilibrium between μ and l.

In both of the series the PZ model was forced with the phytoplankton specific growth rate and was run for 200 days. The surface light intensity linearly increased from 5 to 50 E m^{-2} d^{-1} that is a representative range of values for winter and spring time period (Figure 6.3e). The attenuation coefficient was set to a constant value of 0.066 m^{-1}. In Series 1 of experiments z_{mixed} was held constant at between 150 m to 450 m until day 120. After day 120, z_{mixed} linearly decreased to 20 m depth in 20 days (Figure 6.4a). In Series 2, the timing of restratification varied from day 60 to day 180. z_{mixed} was set to 300 m during the deep phase and to 20 m during the shallow phase (Figure 6.4b). The mean phytoplankton specific growth rate was determined based on z_{mixed}, E_0, and K. In the experiments set-up variability in μ was driven by changes in z_{mixed} and E_0. Initial phytoplankton and zooplankton concentrations were the same for the modelling experiments.

The outcome of the experiments demonstrates that phytoplankton blooms form as a response to rapidly shoaling z_{mixed} rather than as a response to the gradually increasing surface light intensity for both Series 1 and Series 2 of experiments (Figure 6.4). Rapid shoaling of z_{mixed} results in a rapid increase of μ. In all of the experiments bloom peaks occurred during, or in close proximity, to the period of rapidly mixed layer shoaling. However, bloom magnitudes vary significantly between the modelling experiments.

The maximum specific growth rate achieved during the stratification is similar for both Series 1 and Series 2 of experiments (Figure 6.4). However, different values of winter mixed layer depth and timings of restratification affected values of the phytoplankton specific growth rate before the onset of the restratification. Such as for modelling experiments corresponding to shallow winter mixed layers (experiments in Series 1; Figure 6.4a) and late restratification timing (experiments in Series 2; Figure 6.4b), μ was higher at the onset of restratification. Changes in μ led to variability in phytoplankton abundance that affects zooplankton abundance before the onset of stratification.

Further examination of the model outputs suggests pre-restratification values of P and Z can affect magnitudes of the subsequent blooms. The outcome of Series 1 (Figure 6.4a) shows that the values of z_{mixed} before the stratification have a profound impact on the magnitude of the bloom. When maximum z_{mixed} increases, that corresponds to lower values for P and Z before the stratification onset, the bloom magnitude increases as well. The peak in phytoplankton concentration is 5-folds greater for the deepest z_{mixed} than for the shallowest one. Series 2 (Figure 6.4b) shows that the response of spring bloom magnitude to changes in the timing of stratification is less pronounced. The peak bloom magnitude stays relatively constant for stratification occurring between days 60 and 120. However, if the stratification occurs between days 120 and 180, the bloom magnitude decreases approximately by the factor of 2.

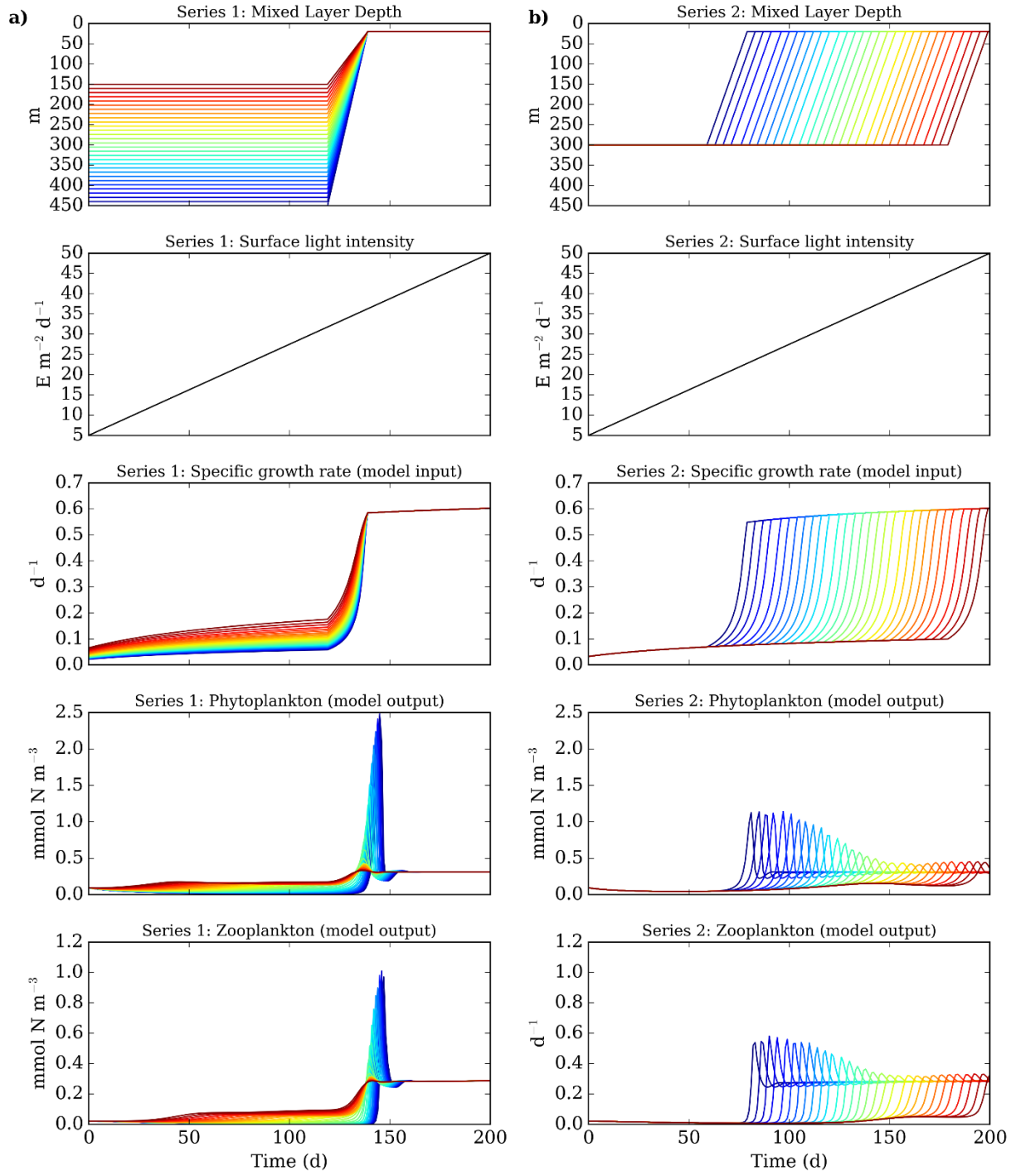

Figure 6.4 Evolution of mixed layer depths, surface light intensity, phytoplankton specific growth rates, phytoplankton and zooplankton concentrations for Series 1 (a) and Series 2 (b) of modelling experiments.

In order to investigate the role of zooplankton variability in setting the magnitude of the bloom, I calculated phytoplankton loss rate to grazing before the onset of stratification. Figure 6.5 shows the derived relationship between the bloom magnitudes and *I* at the onset of stratification.

High magnitude blooms clearly correspond to the lowest values of loss rates ($l < 0.01$ d^{-1}). For $l >$ 0.01 d^{-1}, bloom magnitude is < 0.5mmol N m^{-3} for experiments in both Series 1 and Series 2. When the zooplankton concentration (Figure 6.5a and Figure 6.5b) notably increases before the onset of stratification, relatively low-magnitude blooms form. According to the presented modelling experiments, the zooplankton population can increase most rapidly during relatively shallow winter z_{mixed} and in the case of the late onset of stratification. For low loss rates due to grazing ($l < 0.01$ d^{-1}), the magnitude of the bloom increases abruptly.

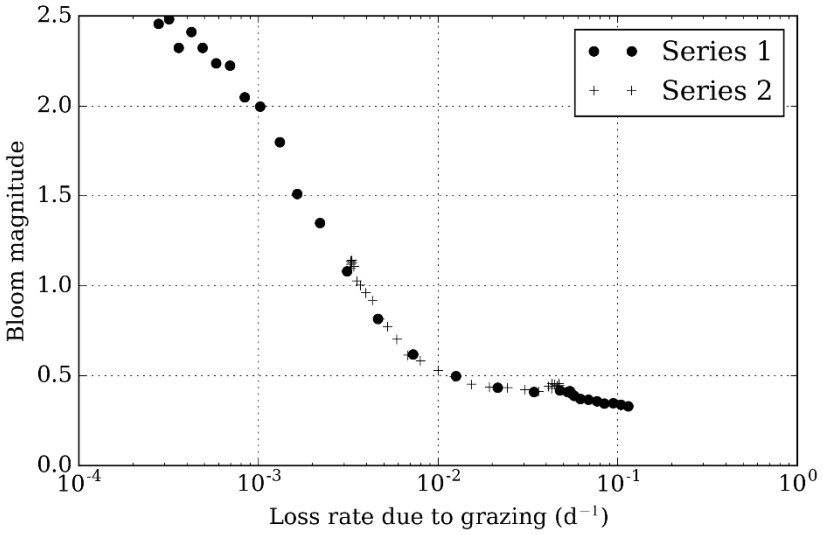

Figure 6.5 Bloom magnitudes obtained during Series 1 and Series 2 of modelling experiments as a function of loss rates at the start of the ocean mixed layer stratification.

The conducted modelling experiments suggest that ecosystem dynamics in deep mixed layers can have a dramatic impact on magnitudes of spring phytoplankton blooms. Enhanced growth of phytoplankton in deep mixed layers leads to increasing zooplankton abundance. In this case, enhanced zooplankton grazing can hamper the development of high-magnitude phytoplankton spring blooms.

6.4 Sensitivity analysis

6.4.1 Mixing layer depth

The PZ model was forced with μ calculated over z_{mixed}. However, as it was discussed in Chapter 5, z_{mixed} does not always represent the layer where the mixing is currently active (z_{mixing}). In this section, the potential impact of the divergence between z_{mixed} and z_{mixing} under wind-driven mixing regime on the model output is explored. The model was forced with μ averaged over z_{mixing}.

Values of z_{mixing} obtained from the Monte-Carlo simulations in section 5.4.4 were used. The results are shown in Figure 6.6.

Phytoplankton variability derived from the PZ model forced with z_{mixing} is generally similar to the one derived from the original model and the one observed by the gliders: the prolonged growth of phytoplankton during the deep mixed layer phase followed by the short-term blooms during the shallow mixed layer phase. There are several pronounced periods of divergence between z_{mixed} and z_{mixing} in the time series: at the end of February, at the end of March and in the second half of April (Figure 6.6b). At the end of February PZ model forced with μ averaged over z_{mixing} indicates higher P compared to the original model. Higher concentrations of P are also observed in the data and correspond to the event (E1) discussed in section 5.4.5. At the end of March and during the second half of April, PZ model forced with z_{mixing} gives significantly higher P compared to the original model and the data. This can indicate the parametrizations of z_{mixing} for these periods are imprecise. If estimates of z_{mixing} are too shallow, it can significantly affect estimates of μ (Figure 6.6c). Accurate estimates of z_{mixing} would require measurements of ocean microstructure in winter and spring (Franks 2014) that were not available in this study.

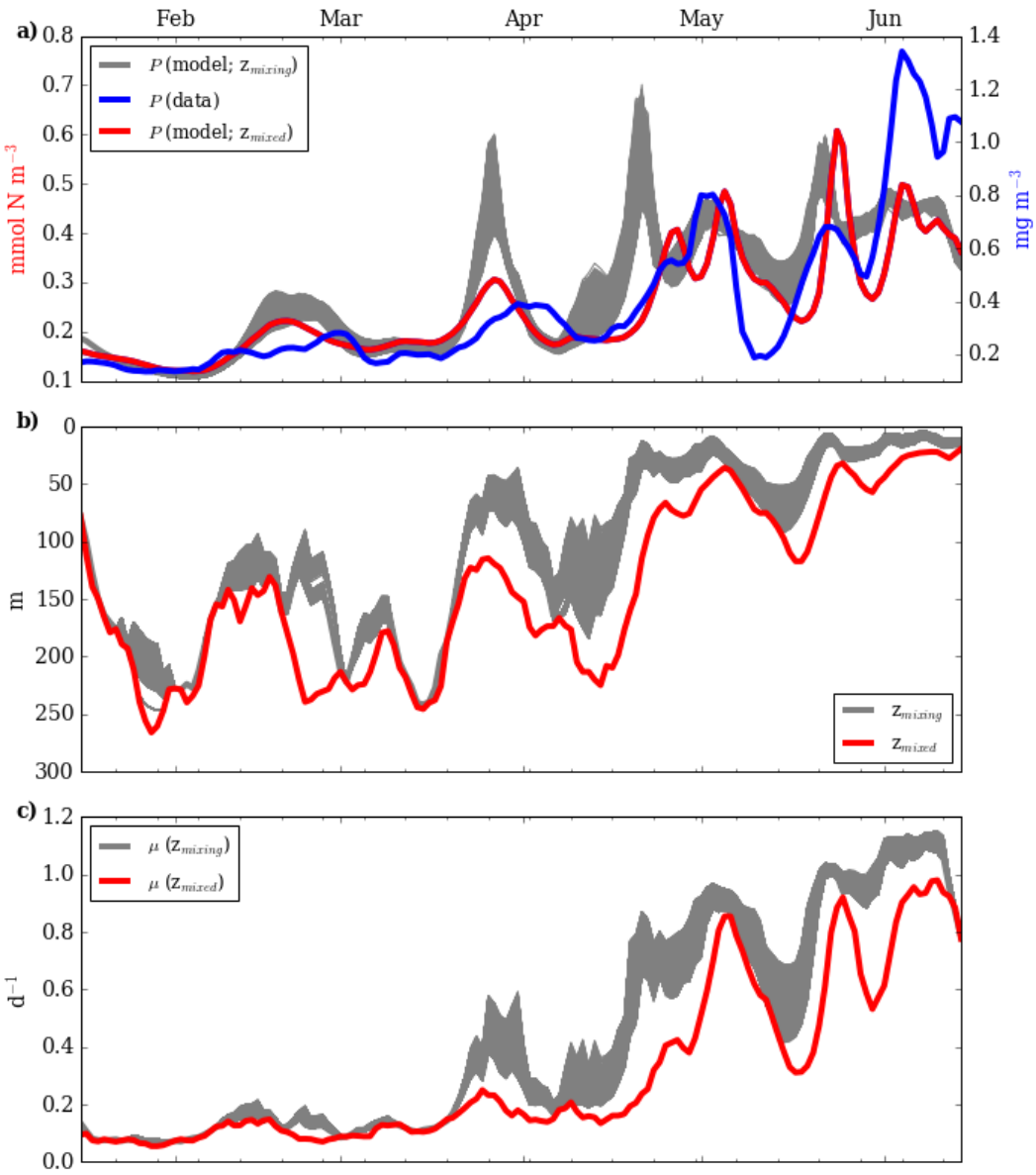

Figure 6.6 Sensitivity test of the PZ model output to the potential divergence between z_{mixed} and z_{mixing}: a) phytoplankton variability (P), b) zooplankton variability (Z) c) phytoplankton growth rate (μ) averaged over z_{mixing} (grey lines) and z_{mixed} (red lines). Red (grey) lines on panels a and b correspond to the model output forced with μ averaged over z_{mixed} (z_{mixing}).

6.4.2 Model parameters

In this section I test how phytoplankton loss rates derived from the model vary depending on changes in b, c_1, c_2, c_3, c_4, c_5, α^{chl} and ϑ parameters used to force the model. The PZ model was run changing one parameter at a time. Results of the sensitivity test are shown in Figure 6.7. The test demonstrated that estimated loss rates are not particularly sensitive to the choice of zooplankton parameters (c_1-c_5) and phytoplankton mortality rate (b) (Figure 6.7a-f). However, substantial variability in the magnitude of I was observed when parameters used in the calculation of μ, such

as α^{chl} and ϑ were changed (Figure 6.7g-h). The test suggests that the magnitude of phytoplankton loss rates to grazing in the PZ model depends on μ rather than zooplankton parameters.

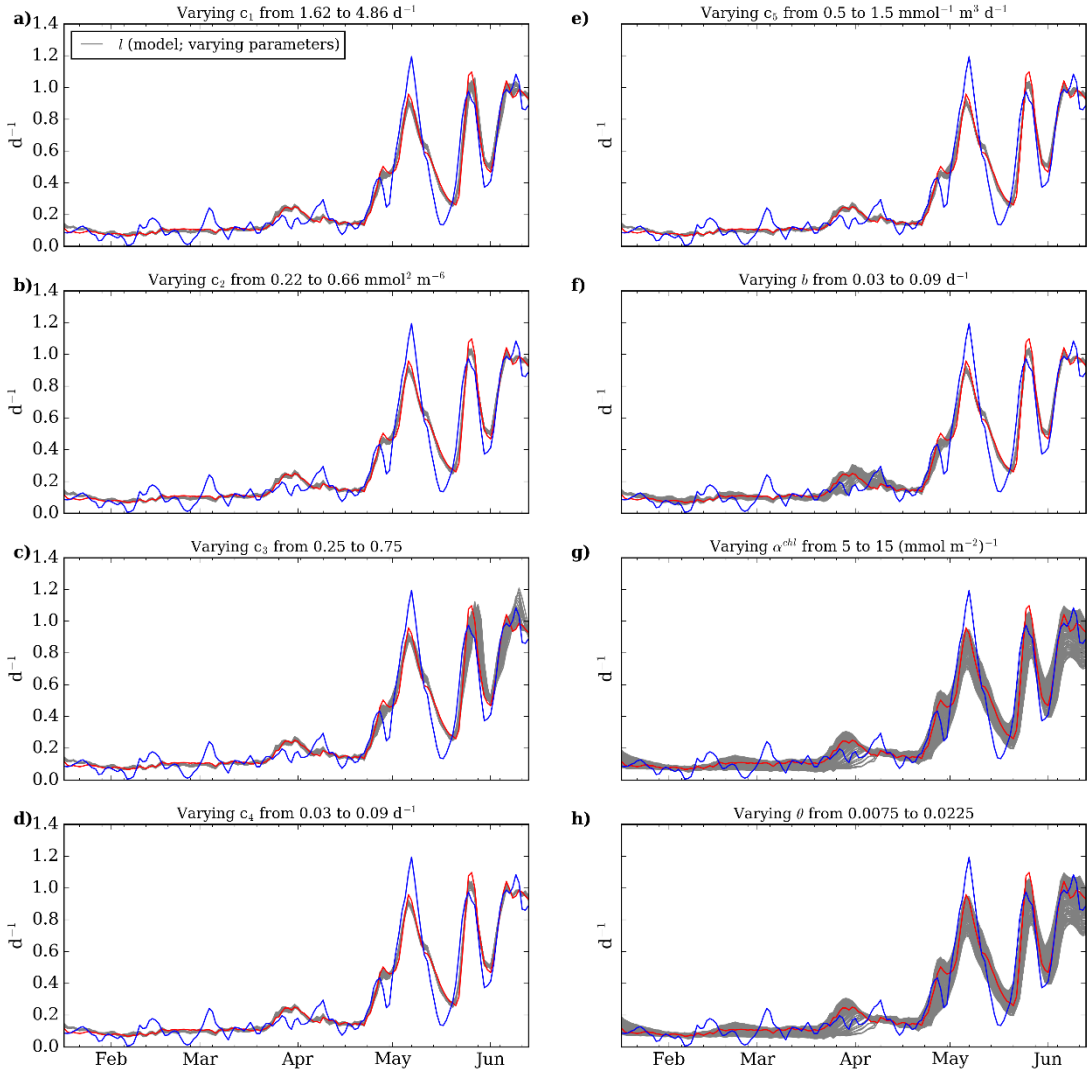

Figure 6.7 Sensitivity test of phytoplankton loss rate to grazing (l) to the choice of the parameter values used in the PZ model: c_1 (a), c_2 (b), c_3 (c), c_4 (d), c_5 (e), b (f), α^{chl} (g) and ϑ (h). Blue lines on the plots represent l evaluated from the glider data. Red line corresponds to l evaluated from the PZ model with the initial set of parameters (Table 6.1). Grey lines are l evaluated from the model outputs with varying parameters.

6.5 Discussion

In this chapter I aimed to address the potential impact of zooplankton grazing on the observed phytoplankton seasonal variability at the PAP site. Satellite and in situ data show that

although nitrate was not depleted, there was no pronounced bloom in spring as in previous years. Instead gradual phytoplankton growth in deep mixed layers and short lived blooms in shallow mixed layers were observed. The implemented PZ model reproduced reasonably well variability in phytoplankton observed by the gliders and provided useful insights on zooplankton dynamics underlying the observations. The model suggests that the ecosystem was tightly coupled. The peaks in phytoplankton were driven by abrupt increases in μ associated with the oscillations in z_{mixed} and K. Substantial variability in loss rates was observed during the deep mixed layer phase that can be considered as a deviation from the CDH framework that assumes constant zooplankton grazing pressure during the pre-bloom period.

The two series of modelling experiments further highlighted that variable grazing rate before the onset of stratification can a have a dramatic effect on the intensity of phytoplankton spring blooms when nutrients are not limited. The highest bloom magnitudes were observed to occur after the deepest winter mixed layers, which corresponded to low pre-bloom phytoplankton concentrations and the lowest grazing rates. This result is in part consistent with the explanation of spring bloom initiation in the North Atlantic Ocean by Behrenfeld (2010). He suggested that occurrence of a pronounced spring bloom depends on the decoupling between phytoplankton and grazers in winter. Behrenfeld (2010) proposed that the main driver causing bloom initiation is a dilution of phytoplankton in deep mixed layers resulting in low encounter rates with grazers. The model set-up implemented in this study could not resolve the potential effect of dilution on spring bloom dynamics. Instead, I show that low growth of phytoplankton in winter leads to low grazing pressure in spring allowing high magnitude phytoplankton blooms to develop. The low grazing pressure at the onset of physical disturbance of the ecosystem prolongs phytoplankton-zooplankton decoupling and results in higher accumulation of phytoplankton biomass. But the bottom line for the results presented here and by Behrenfeld (2010) is similar: the abundance of phytoplankton in spring depends on how rare phytoplankton and zooplankton are in winter.

Previous studies have shown that zooplankton variability regulates seasonal cycles of phytoplankton in the temperate and subpolar North Pacific Ocean (Frost 1991; Parsons & Lalli 1988). Tight coupling between phytoplankton and zooplankton in the high latitude North Pacific Ocean partly leads to the HNLC conditions observed there. A shallow, permanent halocline (100-150 m) in the high latitude North Pacific (Kara et al. 2000) leads to favourable light conditions in winter prompting gradual phytoplankton growth and the corresponding accumulation of micro-zooplankton (Banse & English 1999). In this region, patterns of phytoplankton seasonality are mostly explained by predator-prey interactions (Frost 1991). The North Atlantic Ocean is traditionally characterized as a low nutrient, high chlorophyll regime (LNHC) (Evans & Parslow 1985). However, during the year of the OSMOSIS mission a low chlorophyll regime was observed at

the PAP site and potentially over surrounding areas extending to thousands of kilometres (Figure 6.1, Figure 6.2). Therefore, both HNLC and LNHC regimes can be observed in the North Atlantic Ocean.

Interactions of phytoplankton with zooplankton and resulting spring blooms have important ecological implications for higher trophic levels. Low magnitude blooms of phytoplankton can lead to subsequent low zooplankton abundance. In these conditions, there may be not enough zooplankton for fish larvae to feed on (Cushing, 1975). By combining a phytoplankton–zooplankton model and a zooplankton–larvae–recruitment model, Biktashev et al. (2003) showed that formation of intense plankton blooms was essential for high fish recruitment rates. Moreover, the intensity of phytoplankton blooms can directly affect fish larval survival since the larvae can feed on phytoplankton and timing of the bloom should match the critical period of larval development (Platt et al., 2003). The occurrence of high magnitude blooms results in part of the phytoplankton population being ungrazed forming fast-sinking phytodetrital aggregates (Lampitt 1985) that provide an important food source for benthic organisms.

The results of this study contribute to the ongoing debate on mechanisms responsible for initiation of phytoplankton spring bloom in the North Atlantic Ocean. The significant part of the debate is focused on the various physical mechanisms that can overcome light limitation for phytoplankton in deep mixed layers before the onset of seasonal stratification. But following initial improvement of light conditions for phytoplankton, initiation of bloom can be interrupted by passages of storms (see Chapter 5) or even a moderate increase in wind forcing. Intermittent increases in and corresponding pulses of phytoplankton growth stimulate zooplankton development in deep mixed layers and tight coupling of the planktonic ecosystem that inhibits the formation of pronounced phytoplankton blooms.

6.6 Conclusions

The manifestation of phytoplankton blooms in the temperate and subpolar North Atlantic Ocean have been traditionally explained by improving light conditions for phytoplankton population in winter and early spring (Sverdrup 1953). In this study, I show that variability in zooplankton during the pre-bloom period can have a dramatic impact on the intensity of the spring bloom and patterns of phytoplankton seasonality. In particular, a deep mixed layer depth in winter and/or early onset of seasonal stratification can be of paramount importance for stimulating high magnitude spring blooms in the North Atlantic Ocean. A relatively shallow winter mixed layer depth leads to tight coupling between phytoplankton and zooplankton, resulting in a relatively weak

bloom in the following spring. The study emphasizes that consideration of ecosystem interactions is highly important for the comprehensive understanding of the spring bloom phenomenon in the North Atlantic Ocean.

Chapter 7: Synthesis

This thesis has explored mechanisms underlying the manifestation of phytoplankton spring and autumn blooms in the North Atlantic Ocean using high-resolution in situ glider data collected at the Porcupine Abyssal Plain Observatory site in the framework of the OSMOSIS project. The glider data were complemented by atmospheric forcing reanalysis, satellite-derived Chl *a* and surface PAR data, the population dynamics model and ship-based observations of turbulence, nutrients, Chl *a*, hydrography and meteorology. Below, I outline the main findings obtained in the thesis, discuss challenges of working with glider Chl *a* fluorescence data, describe how the current work contributed to the ongoing debate around phytoplankton spring blooms in the North Atlantic, emphasize the capability of gliders to resolve episodic events, and indicate potential directions for future research.

7.1 Summary of results

The data set collected during the OSMOSIS project allowed analysis of the ecosystem response to an autumnal storm event. Glider observations of variability in Chl *a* inventories showed that the passage of the storm initiated in situ growth of phytoplankton. Following the storm, Chl *a* inventories increased by ~50%. This result confirmed that storms can trigger phytoplankton blooms instead of just redistributing phytoplankton biomass from SCMs. An extensive multi-instrument research campaign conducted during cruise D381 to the sampling site allowed evaluation of nutrient fluxes associated with two physical mechanisms: entrainment during the mixed layer deepening at the time of the storm and shear spiking in the wake of the storm. The post-storm increase in surface layer nitrate (by ~20 mmol m^{-2}) was predominantly driven by the first pathway: nutrient intrusion during the storm. Alignment of post-storm inertial currents and surface wind stress caused shear instabilities at the ocean pycnocline, forming the second pathway for nutrient transport into the euphotic zone. During the alignment period, pulses of high-turbulence nitrate flux through the pycnocline (up to 1 mmol m^{-2} d^{-1}; approximately 25 times higher than the background flux) were detected. However, the impact of the post-storm supply was an order of magnitude lower than during the storm due to the short duration of the pulses. Cumulatively, the storm passage was equivalent to 2.5–5% of the nitrate supplied by winter convection and had a significant effect compared to previously reported (sub)mesoscale dynamics in the region. As storms occur frequently, they can form an important component in local nutrient budgets and represent a significant driver of ocean primary production. A coarse estimate based on the results

suggests that cumulative effects of these storm events can reach up to 30% of the nitrate supply by winter convection.

Chapter 5 focussed on the impact of meteorological conditions on the phytoplankton spring bloom initiation and development. Mixing regimes in the upper ocean layer were characterized using the Monin-Obukhov length scale. During most of the winter, mixing conditions were predominantly driven by convection and the surface light intensity was decreasing. The assumption that these conditions initiate net phytoplankton growth due to decreasing grazing pressure (DRH) was tested. The net positive growth of phytoplankton was observed later in the season, when surface light intensity started to increase and wind-driven mixing conditions with associated shoaling of the mixing layer occurred more frequently. This result suggested that initiation of net phytoplankton growth due to dilution from grazers cannot be detected in the observations.

To test the CTH, mixing and growth time scales were estimated. The mixing time scales (~2-3 hours) were significantly shorter compared to the growth time scales (~12 hours). Therefore, it was concluded that growth of phytoplankton is unlikely to develop through the critical turbulence mechanism. Considering the three main competing hypotheses (CDH, CTH and DRH) initiation of net phytoplankton growth in winter and spring was the most consistent with the critical depth framework if divergence between mixed and mixing layers was considered.

The impact of atmospheric forcing on the mean specific growth rate for the phytoplankton community was evaluated. Windy weather and periods of convective mixing can decrease phytoplankton growth rate and prevent rapid development of phytoplankton spring blooms. Periods of low wind forcing were shown to have a two-fold effect on phytoplankton inventories. Calm weather conditions significantly increase the growth rate for the part of the community within shallow mixing layers. At the same time, a part of the phytoplankton population is trapped below the euphotic zone and potentially lost from the ocean surface layer. The analysis emphasized the complexity of the evolution of phytoplankton population under transient weather conditions associated with changes in mixing regimes.

In this study, the net positive growth of phytoplankton was observed before the seasonal shoaling of the upper ocean layer. The observed bloom developed slowly: over several months both depth-integrated inventories and surface concentrations of Chl *a* increased only by a factor of ~2 and ~3 respectively. Both satellite and glider data indicated the year of the glider mission was characterized by relatively low phytoplankton seasonality. There was no pronounced, high-magnitude seasonal spring bloom event at the PAP site during the year of the glider mission. Basin

scale images of phytoplankton distribution suggest that low seasonality regime observed at the PAP site potentially extended over surrounding areas and with the size of ~10^6 km^2. As shown by satellite record from the previous years, these conditions might be atypical for this region of the North Atlantic Ocean.

Chapter 6 aimed to evaluate the impact of zooplankton grazing on the observed dynamics of the bloom. The glider data was complemented by a simple PZ model that reproduced reasonably well the observed variability in phytoplankton concentration. The model suggested substantial variability in zooplankton populations in winter and spring. In particular, before the seasonal restratification, phytoplankton losses due to grazing increased by a factor of 2 (from 0.1 to 0.2 d^{-1}). Loss rates to grazing significantly increased after the mixed layer permanently shoaled at the end of spring and ranged between 0.2 and 1.2 d^{-1}. Loss rates evaluated from the PZ model and the glider data agreed well. It was concluded that predator-prey coupling played a substantial role in shaping the observed phytoplankton seasonality. A series of modelling experiments aiming to represent the winter to spring transition showed that variability in grazing can have a profound impact on the intensity of spring blooms. In particular, pronounced blooms formed when the mixed layer was deep and/or seasonal stratification occurred early.

7.2 Notes on the debate around spring blooms

This thesis provided a manifold analysis of phytoplankton spring dynamics observed by the gliders. It was shown that the manifestation of phytoplankton spring blooms in the North Atlantic Ocean is a multifactorial phenomenon that requires considerations of both bottom-up and top-down processes. Meteorological conditions modulate mean phytoplankton specific growth rate through changes in mixing layer depth. Variability in phytoplankton growth rates can trigger a response in grazers' population with the subsequent impact on the regional patterns of phytoplankton seasonality. It is highly important to consider trophic interactions and abundance of grazers when rapid increase of phytoplankton cell division rate takes place. In particular, it was shown that pronounced blooms form when zooplankton grazing is low when phytoplankton growth rate starts to increase abruptly.

The analysis questioned several assumptions of Sverdrup's critical depth framework. In particular, it was shown that phytoplankton might not be equally distributed within the mixed layer defined based on hydrography. Glider profiles of Chl *a* fluorescence clearly showed the skewed vertical distribution of phytoplankton within hydrographically defined mixed layers. For example, at the end of February the hydrographically defined mixed layer was ~250 m deep while phytoplankton were uniformly mixed down to a much shallower depth (~25 m). The outcome from

the PZ model suggested that loss rates of phytoplankton to grazing were variable in winter and early spring. In addition, it was shown that significant losses in phytoplankton community can arise under wind-driven mixing regime due to trapping of algae in the aphotic layer. These findings violate Sverdrup's assumptions of constant losses and small influence of grazers on the process of spring bloom initiation.

Finally, the introduction for this thesis presented two conceptual models that moved beyond a "single mechanism" view and attempted to incorporate multiple hypotheses in explaining the onset of phytoplankton spring blooms in the North Atlantic Ocean (section 1.3.7). The inter-seasonal glider observations of phytoplankton variability presented in the current work brought attention to several factors that have not been considered in the conceptual models. The factors are summarised below.

- The data in winter did not provide evidence that strong convective mixing conditions initiate phytoplankton net growth due to dilution from grazers
- The period between strong convective mixing in winter and establishment of seasonal stratification is characterized by variable weather conditions and changeable mixing regimes
- Shoaling of the mixing layer increases phytoplankton growth near the surface, but at the same time traps a significant part of the phytoplankton community in the aphotic layer resulting in losses in phytoplankton inventories
- Slow, prolonged growth of phytoplankton in deep mixed layers can lead to accumulation of grazers
- Enhanced abundance of grazers can hamper phytoplankton biomass accumulation when phytoplankton specific growth rate rapidly increases during the seasonal restratification

7.3 Resolving episodic events

This work emphasized that gliders are capable of efficiently resolving episodic events that are poorly sampled through ship-based observations or remote sensing. During the OSMOSIS mission, gliders captured changes in ocean properties during the passage of an autumnal storm. The observations indicated the transience of the ecosystem response to the storm event: the storm induced net growth of phytoplankton sustained for ~3 days. Due to the cloud coverage during storms, induced phytoplankton growth can be missed in satellite imagery. Ship-based observations are also limited in stormy seas.

During the period of spring bloom initiation, gliders' observations resolved a response in phytoplankton stocks to different turbulence regimes: wind-driven and convective driven mixing regimes. The high-resolution glider observations contrasted how changes in mixing conditions affect phytoplankton stocks. Both of the periods lasted for 3-4 days. Satellite data is surface limited and contains gaps in winter and early spring. Therefore, the ocean colour remote sensing technique is incapable of fully resolving the evolution of phytoplankton population under variable mixing regimes.

Chapter 6 showed that episodic increases in phytoplankton specific growth rate can disturb predator-prey coupling and stimulate short-term blooms in shallow mixed layers. The episodic blooms were not resolved in satellite ocean colour data, which further emphasizes the value of high resolution measurements in advancing our knowledge of phytoplankton seasonality.

7.4 Remarks on mapping phytoplankton with gliders

This thesis showed that autonomous buoyancy-driven gliders represent a powerful technology for studying phytoplankton variability in the upper ocean. The year-long glider mission at the PAP site resulted in 8458 vertical profiles of Chl a fluorescence, light and hydrography. The amount of collected data on phytoplankton distribution is unprecedented compared to ship-based observations. Therefore, it is highly important that data processing procedures are well documented and conducted in a reproducible manner. The latter is essential for the fast implementation of any changes in the pipeline of data processing steps and reproducibility of scientific conclusions drawn from the data.

The main difficulties encountered with the processing of Chl *a* fluorescence data from the gliders were:

- Spikes and negative values in Chl *a* fluorescence profiles
- Random spurious fluorescence profiles containing extremely high values of Chl *a* fluorescence potentially associated with episodic failure of the ECOpuck fluorometers
- Fluorescence quenching near the surface during daytime
- Re-evaluation of manufacturer-provided calibrations

In this study fluorescence was converted to Chl *a* units using a single scale factor for the entire mission. Chl *a* fluorescence is only a proxy for Chl *a* concentration in phytoplankton cells. Fluorescence to Chl *a* ratio can be affected by environmental factors and phytoplankton species composition (Falkowski & Kiefer 1985). Therefore, the applied calibration procedure converted the signal from fluorescence sensors only approximate Chl *a* units. Variable fluorescence to Chl *a* ratio

is a well-known limitation of the in vivo fluorescence technique. In this regard, fluorescence measurements should be used with caution to infer absolute values of Chl *a* concentrations or photosynthetic rates. Nevertheless, fluorescence measurements allow the drawing of scientific conclusions on the temporal and spatial variability of phytoplankton with high certainty (Perry et al. 2008) making them extremely valuable in studies of phytoplankton seasonality.

7.5 Future work

The measurements presented in this thesis were obtained at a single location. However, some findings from this work could be extended further to explain dynamics of phytoplankton blooms over the North Atlantic Ocean basin. For instance, further research can be conducted on links between meteorological conditions and development of blooms. This study hypothesised that windy conditions in spring lead to low-magnitude spring blooms. The hypothesis is testable with satellite ocean colour data and atmospheric forcing reanalysis. The PZ model simulations during the winter to spring transition can also be conducted at locations representative of different oceanic regimes and conditions. Indeed, the main input variables used to calculate phytoplankton specific growth rate in the PZ model can be obtained at the basin scale. Satellite data provide estimates of light attenuation coefficients and surface PAR. Mixed layer depth estimates can be obtained using data from Argo profiling floats. This analysis can provide estimates of variability in phytoplankton loss rates during pre-bloom periods across the entire basin.

This study shows that mid-latitude storms can significantly contribute to the nutrient budgets in the North Atlantic Ocean. This result motivates further investigation of the role of the storms in fuelling ocean primary production and in the global carbon cycle. It has previously been shown that storms can stimulate phytoplankton growth which may result in carbon export via the biological carbon pump (Hung et al. 2009). At the same time storm passage alters surface exchange of CO_2 (Lévy et al. 2012; Bates et al. 1998). Further observations of storms with autonomous platforms potentially equipped with sensors measuring the partial pressure of CO_2 (Atamanchuk et al. 2014) can improve understanding of the impact of storm events on the global carbon cycle.

Additional research can be conducted towards addressing the observation continuum between satellites and gliders. Gliders along with other autonomous platforms and ocean colour remote sensing use measurements of Chl *a* to map phytoplankton distribution in the ocean and represent the largest data sets of phytoplankton variability. Vertically resolved profiles of phytoplankton distribution are capable of extending satellite ocean colour data to the ocean interior. Several methods of homogenising satellite ocean colour and glider Chl a fluorescence data

have been proposed (Lavigne et al. 2012; Sauzède et al. 2015). The methods can be applied to the OSMOSIS data sets and compared.

Further investigation of Chl *a* fluorescence and optical backscatter data sets can be valuable for assessing transfer of carbon to the ocean interior. For instance, observations of aggregate flux events following the diatom bloom in the southeast of Iceland were conducted from autonomous gliders in the framework of NABE08 (Briggs et al. 2011). Sinking aggregates were defined as pronounced spikes in optical backscatter and Chl *a* fluorescence vertical profiles. Carbon export to the mesopelagic zone was also previously studied using bio-optical sensors on profiling floats deployed in the Southern Ocean (Bishop et al. 2004; Bishop & Wood 2009). Similar analysis can be performed on the OSMOSIS glider data set.

The mixed layer variations observed in the data could be partially attributed to the sub-mesoscale dynamics and frontal features at the sampling site. Further exploration of the data set can give valuable insights on the role of sub-mesoscale processes in stimulating pulses of phytoplankton growth under relatively strong surface cooling (Mahadevan et al. 2012; Taylor & Ferrari 2011a) and driving physical transport of phytoplankton out of the surface layer along the isopycnal surfaces (Omand et al. 2015). Analysis of lateral gradients of density and temperature can indicate times when strong fronts are present at the sampling site (e.g. Thompson et al. 2016). Bio-optical data from the gliders can be used to infer response in phytoplankton growth to submesoscale processes.

7.6 Concluding paragraph

This thesis has examined initiation of phytoplankton blooms in the open North Atlantic Ocean using data from the autonomous buoyancy-driven underwater gliders, atmospheric forcing reanalysis, cruise data and a population dynamics model. It was demonstrated that storms trigger autumn phytoplankton blooms and form an important component in local nutrient budgets. The analysis of data collected in winter and spring valuably contributed to the long-lasting debate on mechanisms controlling spring bloom initiation in the temperate and subpolar North Atlantic Ocean. Multi-parameter, depth-resolved, intra-seasonal glider observations provide a new perspective on phytoplankton bloom dynamics. Further ocean observations from autonomous platforms will significantly improve scientific understanding of processes that control ocean primary production and its impact on pelagic ecosystem functioning, fish recruitment rates and ocean carbon sinks.

Bibliography

Alkire, M.B., Lee, C., D'Asaro, E., Perry, M.J., Briggs, N., Cetinić, I. and Gray, A., 2014. Net community production and export from Seaglider measurements in the North Atlantic after the spring bloom. *Journal of Geophysical Research: Oceans*, *119*(9), pp.6121-6139. doi:10.1002/2014JC010105.

Allen, M.R., Barros, V.R., Broome, J., Cramer, W., Christ, R., Church, J.A., Clarke, L., Dahe, Q., Dasgupta, P., Dubash, N.K. and Edenhofer, O., 2014. IPCC Fifth Assessment Synthesis Report-Climate Change 2014 Synthesis Report.

Ardyna, M., Babin, M., Gosselin, M., Devred, E., Bélanger, S., Matsuoka, A. and Tremblay, J.É., 2013. Parameterization of vertical chlorophyll a in the Arctic Ocean: impact of the subsurface chlorophyll maximum on regional, seasonal, and annual primary production estimates. *Biogeosciences*, *10*(6), pp.4383-4404. doi:10.5194/bg-10-4383-2013.

Atamanchuk, D., Tengberg, A., Thomas, P.J., Hovdenes, J., Apostolidis, A., Huber, C. and Hall, P.O., 2014. Performance of a lifetime-based optode for measuring partial pressure of carbon dioxide in natural waters. *Limnology and Oceanography: Methods*, 12(2), pp. 63-73. doi:10.4319/lom.2014.12.63.

Babin, S.M., Carton, J.A., Dickey, T.D. and Wiggert, J.D., 2004. Satellite evidence of hurricane-induced phytoplankton blooms in an oceanic desert. *Journal of Geophysical Research: Oceans*, *109*, C03043, doi:10.1029/2003JC001938.

Banse, K., 1992. Grazing, temporal changes of phytoplankton concentrations, and the microbial loop in the open sea. In: Falkowski PG, Woodhead AD (eds) Primary production and biogeochemical cycles in the sea. Plenum Press, New York, pp. 409-440.

Banse, K., 2013. Reflections about chance in my career, and on the top-down regulated world. *Annual review of marine science*, *5*, pp. 1-19. doi: 10.1146/annurev-marine-121211-172359.

Banse, K. and English, D.C., 1999. Comparing phytoplankton seasonality in the eastern and western subarctic Pacific and the western Bering Sea. *Progress in Oceanography*, *43*(2), pp. 235-288. doi:10.1016/S0079-6611(99)00010-5.

Bates, N.R., Knap, A.H. and Michaels, A.F., 1998. Contribution of hurricanes to local and global estimates of air–sea exchange of CO2. *Nature*, *395*(6697), pp. 58-61. doi:10.1038/25703.

Behrenfeld, M.J., 2010. Abandoning Sverdrup's critical depth hypothesis on phytoplankton blooms. *Ecology*, *91*(4), pp. 977-989. doi:10.1890/09-1207.1.

Behrenfeld, M.J., Boss, E., Siegel, D.A. and Shea, D.M., 2005. Carbon-based ocean productivity and phytoplankton physiology from space. *Global biogeochemical cycles*, *19*(1), GB1006. doi:10.1029/2004GB002299.

Behrenfeld, M.J., 2014. Climate-mediated dance of the plankton. *Nature Climate Change*, *4*(10), pp. 880-887. doi:10.1038/nclimate2349.

Behrenfeld, M.J. and Boss, E.S., 2014. Resurrecting the ecological underpinnings of ocean plankton blooms. *Annual Review of Marine Science*, *6*, pp.167-194. doi:10.1146/annurev-marine-052913-021325.

Belcher, S.E., Grant, A.L., Hanley, K.E., Fox-Kemper, B., Van Roekel, L., Sullivan, P.P., Large, W.G., Brown, A., Hines, A., Calvert, D. and Rutgersson, A., 2012. A global perspective on Langmuir turbulence in the ocean surface boundary layer. *Geophysical Research Letters*, *39*(18), L18605. doi:10.1029/2012GL052932.

Bentamy, A. and Fillon, D.C., 2012. Gridded surface wind fields from Metop/ASCAT measurements. *International journal of remote sensing*, *33*(6), pp. 1729-1754. doi:10.1080/01431161.2011.600348

Bishop, J.K., Wood, T.J., Davis, R.E. and Sherman, J.T., 2004. Robotic observations of enhanced carbon biomass and export at 55 S during SOFeX. *Science*, *304*(5669), pp. 417-420. doi:10.1126/science.1087717.

Bishop, J.K. and Wood, T.J., 2009. Year-round observations of carbon biomass and flux variability in the Southern Ocean. *Global Biogeochemical Cycles*, *23*(2), GB2019. doi:10.1029/2008GB003206.

Bissinger, J.E., Montagnes, D.J., Sharples, J. and Atkinson, D., 2008. Predicting marine phytoplankton maximum growth rates from temperature: Improving on the Eppley curve using quantile regression. *Limnology and Oceanography*, *53*(2), pp. 487-493. doi:10.4319/lo.2008.53.2.0487.

Boss, E. and Behrenfeld, M., 2010. In situ evaluation of the initiation of the North Atlantic phytoplankton bloom. *Geophysical Research Letters*, *37*(18), L18603. doi:10.1029/2010GL044174.

de Boyer Montégut, C., Madec, G., Fischer, A.S., Lazar, A. and Iudicone, D., 2004. Mixed layer depth over the global ocean: An examination of profile data and a profile-based climatology. *Journal of Geophysical Research: Oceans*, *109*(C12), pp. 1-20. doi:10.1029/2004JC002378.

Brainerd, K.E. and Gregg, M.C., 1993. Diurnal restratification and turbulence in the oceanic surface mixed layer: 1. Observations. *Journal of Geophysical Research: Oceans*, *98*(C12), pp.22645-22656. doi:10.1029/93JC02297.

Brainerd, K.E. and Gregg, M.C., 1995. Surface mixed and mixing layer depths. *Deep Sea Research Part I: Oceanographic Research Papers*, *42*(9), pp.1521-1543. doi:10.1016/0967-0637(95)00068-H.

Brannigan, L., Lenn, Y.D., Rippeth, T.P., McDonagh, E., Chereskin, T.K. and Sprintall, J., 2013. Shear at the base of the oceanic mixed layer generated by wind shear alignment. *Journal of Physical Oceanography*, *43*(8), pp.1798-1810. doi:http://dx.doi.org/10.1175/JPO-D-12-0104.1.

Briggs, N., Perry, M.J., Cetinić, I., Lee, C., D'Asaro, E., Gray, A.M. and Rehm, E., 2011. High-resolution observations of aggregate flux during a sub-polar North Atlantic spring bloom. *Deep Sea Research Part I: Oceanographic Research Papers*, *58*(10), pp.1031-1039. doi:10.1016/j.dsr.2011.07.007.

Briggs, N.T., Slade, W.H., Boss, E. and Perry, M.J., 2013. Method for estimating mean particle size from high-frequency fluctuations in beam attenuation or scattering measurements. *Applied optics*, *52*(27), pp.6710-6725. doi:10.1364/AO.52.006710.

Brody, S.R. and Lozier, M.S., 2014. Changes in dominant mixing length scales as a driver of subpolar phytoplankton bloom initiation in the North Atlantic. *Geophysical Research Letters*, *41*(9), pp.3197-3203. doi:10.1002/2014GL059707.

Brody, S.R. and Lozier, M.S., 2015. Characterizing upper-ocean mixing and its effect on the spring phytoplankton bloom with in situ data. *ICES Journal of Marine Science: Journal du Conseil*, *72*, pp. 1961 –1970. doi: 10.1093/icesjms/fsv006.

Burchard, H. and Rippeth, T.P., 2009. Generation of bulk shear spikes in shallow stratified tidal seas. *Journal of Physical Oceanography*, *39*(4), pp.969-985. doi:http://dx.doi.org/10.1175/2008JPO4074.1.

Burkill, P.H., Mantoura, R.F.C., Llewellyn, C.A. and Owens, N.J.P., 1987. Microzooplankton grazing and selectivity of phytoplankton in coastal waters. *Marine Biology*, *93*(4), pp.581-590. doi:10.1007/BF00392796.

Cetinić, I., Perry, M.J., D'Asaro, E., Briggs, N., Poulton, N., Sieracki, M.E. and Lee, C.M., 2014. Optical community index to assess spatial patchiness during the 2008 North Atlantic Bloom. *Biogeosciences Discussions*, *11*(9), pp.12833-12870. doi:10.5194/bgd-11-12833-2014.

Chiswell, S.M., 2011. Annual cycles and spring blooms in phytoplankton: don't abandon Sverdrup completely. *Marine ecology progress series*, *443*, pp. 39-50. doi:10.3354/meps09453.

Chiswell, S.M., Calil, P.H. and Boyd, P.W., 2015. Spring blooms and annual cycles of phytoplankton: a unified perspective. *Journal of Plankton Research*, *37*(3), pp.500–508. doi:10.1093/plankt/fbv021.

Cohen, E.R., 1998. An Introduction to Error Analysis: The Study of Uncertainties in Physical Measurements, 2nd ed., *University Science Books*, 2009.

Cole, H., Henson, S., Martin, A. and Yool, A., 2012. Mind the gap: The impact of missing data on the calculation of phytoplankton phenology metrics. *Journal of Geophysical Research: Oceans*, *117*(C8), C08030. doi:10.1029/2012JC008249.

Cole, H.S., Henson, S., Martin, A.P. and Yool, A., 2015. Basin-wide mechanisms for spring bloom initiation: how typical is the North Atlantic? *ICES Journal of Marine Science: Journal du Conseil*, *72*, pp. 2029–2040. doi:10.1093/icesjms/fsu239.

Cullen, J.J., 1982. The deep chlorophyll maximum: comparing vertical profiles of chlorophyll a. *Canadian Journal of Fisheries and Aquatic Sciences*, *39*(5), pp.791-803. doi:10.1139/f82108/V41EH_krLIU.

Cushing, D.H., 1959. The seasonal variation in oceanic production as a problem in population dynamics. *Journal du Conseil*, *24*(3), pp.455-464. doi:10.1093/icesjms/24.3.455.

D'Ortenzio, F., Thierry, V., Eldin, G., Claustre, H., Testor, P., Coatanoan, C., Tedetti, M., Guinet, C., Poteau, A., Prieur, L. and Lefevre, D., 2010. White Book on Oceanic Autonomous Platforms for Biogeochemical Studies: Instrumentation and Measure (PABIM), http://www.obs-vlfr.fr/OAO/file/PABIM white book version1.3.pdf, February 2010.

Dall'Olmo, G., Westberry, T.K., Behrenfeld, M.J., Boss, E. and Slade, W.H., 2009. Significant contribution of large particles to optical backscattering in the open ocean. *Biogeosciences*, *6*(6), pp. 947-967. doi:10.5194/bg-6-947-2009.

Deardorff, J.W., 1972. Numerical investigation of neutral and unstable planetary boundary layers. *Journal of the Atmospheric Sciences*, *29*(1), pp.91-115. doi:http://dx.doi.org/10.1175/1520-0469(1972)029<0091:NIONAU>2.0.CO;2

Doney, S.C., 2006. Oceanography: Plankton in a warmer world. *Nature*,*444*(7120), pp.695-696. doi:10.1038/444695a.

Ducklow, H.W. and Harris, R.P., 1993. Introduction to the JGOFS North Atlantic bloom experiment. *Deep Sea Research Part II: Topical Studies in Oceanography*, *40*(1), pp.1-8. doi:10.1016/0967-0645(93)90003-6

Dutkiewicz, S., Follows, M., Marshall, J. and Gregg, W.W., 2001. Interannual variability of phytoplankton abundances in the North Atlantic. *Deep Sea Research Part II: Topical Studies in Oceanography*, *48*(10), pp.2323-2344. doi:10.1016/S0967-0645(00)00178-8.

Ebert, U., Arrayás, M., Temme, N., Sommeijer, B. and Huisman, J., 2001. Critical conditions for phytoplankton blooms. *Bulletin of mathematical biology*, *63*(6), pp.1095-1124. doi:10.1006/bulm.2001.0261.

Edwards, K.F., Litchman, E. and Klausmeier, C.A., 2013. Functional traits explain phytoplankton community structure and seasonal dynamics in a marine ecosystem. *Ecology letters*, *16*(1), pp. 56-63. doi:10.1111/ele.12012.

Eilertsen, H.C., Schei, B. and Taasen, J.P., 1981. Investigations on the plankton community of Balsfjorden, Northern Norway: The phytoplankton 1976–1978. Abundance, species composition, and succession. *Sarsia*, *66*(2), pp. 129-141. doi:10.1080/00364827.1981.10414530.

Enriquez, R.M. and Taylor, J.R., 2015. Numerical simulations of the competition between wind-driven mixing and surface heating in triggering spring phytoplankton blooms. *ICES Journal of Marine Science: Journal du Conseil*, *72*, pp. 1926–1941. doi:10.1093/icesjms/fsv071.

Eriksen, C.C., Osse, T.J., Light, R.D., Wen, T., Lehman, T.W., Sabin, P.L., Ballard, J.W. and Chiodi, A.M., 2001. Seaglider: A long-range autonomous underwater vehicle for oceanographic research. *IEEE Journal of oceanic Engineering*, *26*(4), pp.424-436. doi:10.1109/48.972073.

Evans, G.T. and Parslow, J.S., 1985. A model of annual plankton cycles. *Biological oceanography*, *3*(3), pp.327-347. doi:10.1080/01965581.1985.10749478.

Fairall, C.W., Bradley, E.F., Rogers, D.P., Edson, J.B. and Young, G.S., 1996. Bulk parameterization of air-sea fluxes for tropical ocean-global atmosphere coupled-ocean atmosphere response experiment. *Journal of Geophysical Research: Oceans*, *101*(C2), pp. 3747-3764. doi:10.1029/95JC03205.

Falkowski, P. and Kiefer, D.A., 1985. Chlorophyll a fluorescence in phytoplankton: relationship to photosynthesis and biomass. *Journal of Plankton Research*, *7*(5), pp.715-731. doi:10.1093/plankt/7.5.715.

Ferrari, R., Merrifield, S.T. and Taylor, J.R., 2015. Shutdown of convection triggers increase of surface chlorophyll. *Journal of Marine Systems*, *147*, pp.116-122. doi:10.1016/j.jmarsys.2014.02.009.

Field, C.B., Behrenfeld, M.J., Randerson, J.T. and Falkowski, P., 1998. Primary production of the biosphere: integrating terrestrial and oceanic components. *Science*, *281*(5374), pp.237-240. doi:10.1126/science.281.5374.237.

Findlay, H.S., Yool, A., Nodale, M. and Pitchford, J.W., 2006. Modelling of autumn plankton bloom dynamics. *Journal of Plankton Research*, *28*(2), pp.209-220. doi:10.1093/plankt/fbi114.

Fischer, A., Moberg, E., Alexander, H., Brownlee, E., Hunter-Cevera, K., Pitz, K., Rosengard, S. and Sosik, H., 2014. Sixty years of Sverdrup: a retrospective of progress in the study of phytoplankton blooms. *Oceanography*, *27*, pp. 222–235. http://dx.doi.org/10.5670/oceanog.2014.26.

Foltz, G.R., Balaguru, K. and Leung, L.R., 2015. A reassessment of the integrated impact of tropical cyclones on surface chlorophyll in the western subtropical North Atlantic. *Geophysical Research Letters*, *42*(4), pp.1158-1164. doi:10.1002/2015GL063222.

Forryan, A. et al., 2012. Turbulent nutrient fluxes in the Iceland Basin. *Deep Sea Research Part I: Oceanographic Research Papers, 63*, pp.20–35. doi:10.1016/j.dsr.2011.12.006.

Frajka-Williams, E., Eriksen, C.C., Rhines, P.B. and Harcourt, R.R., 2011. Determining vertical water velocities from Seaglider. *Journal of Atmospheric and Oceanic Technology*, *28*(12), pp.1641-1656. doi:http://dx.doi.org/10.1175/2011JTECHO830.1.

Frajka-Williams, E. and Rhines, P.B., 2010. Physical controls and interannual variability of the Labrador Sea spring phytoplankton bloom in distinct regions. *Deep Sea Research Part I: Oceanographic Research Papers*, *57*(4), pp.541-552. doi:10.1016/j.dsr.2010.01.003.

Frajka-Williams, E., Rhines, P.B. and Eriksen, C.C., 2009. Physical controls and mesoscale variability in the Labrador Sea spring phytoplankton bloom observed by Seaglider. *Deep Sea Research Part I: Oceanographic Research Papers*, *56*(12), pp.2144-2161. doi:10.1016/j.dsr.2009.07.008.

Franks, P.J.S., 2014. Has Sverdrup's critical depth hypothesis been tested? Mixed layers vs. turbulent layers. *ICES Journal of Marine Science: Journal du Conseil*, *72*, pp. 1897–1907. doi:10.1093/icesjms/fsu175.

Frost, B.W., 1991. The role of grazing in nutrient-rich areas of the open sea. *Limnology and Oceanography*, 36(8), pp.1616–1630. doi:10.4319/lo.1991.36.8.1616.

Garau, B. et al., 2011. Thermal lag correction on Slocum CTD glider data. *Journal of Atmospheric and Oceanic Technology*, 28(9), pp.1065–1071. doi:http://dx.doi.org/10.1175/JTECH-D-10-05030.1.

Garside, C. & Garside, J.C., 1993. The "f-ratio" on 20 W during the North Atlantic Bloom Experiment. *Deep Sea Research Part II: Topical Studies in Oceanography*, 40(1), pp.75–90. doi:10.1016/0967-0645(93)90007-A

Gillett, N.P., Graf, H.F. & Osborn, T.J., 2003. Climate change and the North Atlantic oscillation. *Geophysical Monograph-American Geophysical Union*, 134, pp.193–210. doi:10.1029/134GM09.

Gran, H.H. & Braarud, T., 1935. A quantitative study of the phytoplankton in the Bay of Fundy and the Gulf of Maine (including observations on hydrography, chemistry and turbidity). *Journal of the Biological Board of Canada*, 1(5), pp.279–467. doi:10.1139/f35-012.

Guihen, D., Fielding, S., Griffiths, G., Creed, E. and Heywood, K., 2012. Assessing the performance of seaglider based acoustics in detecting krill swarms. http://scar2012.geol.pdx.edu.

Hanshaw, M.N., Lozier, M.S. and Palter, J.B., 2008. Integrated impact of tropical cyclones on sea surface chlorophyll in the North Atlantic. *Geophysical Research Letters, 35(1)*, L01601. doi:10.1029/2007GL031862.

Hartman, S.E. et al., 2010. Seasonal and inter-annual biogeochemical variations in the Porcupine Abyssal Plain 2003-2005 associated with winter mixing and surface circulation. *Deep-Sea Research Part Ii-Topical Studies in Oceanography*, 57(15), pp.1303–1312. doi:10.1016/j.dsr2.2010.01.007.

Henson, S.A., Dunne, J.P. & Sarmiento, J.L., 2009. Decadal variability in North Atlantic phytoplankton blooms. *Journal of Geophysical Research*, 114(C4), C04013. doi:10.1029/2008JC005139.

Hirche, H.J., 1996. Diapause in the marine copepod, Calanus finmarchicus—a review. *Ophelia*, *44*(1-3), pp.129-143. doi:10.1080/00785326.1995.10429843.

Huisman, J., van Oostveen, P. & Weissing, F.J., 1999. Critical depth and critical turbulence: two different mechanisms for the development of phytoplankton blooms. *Limnology and Oceanography*, pp.1781–1787. doi:10.4319/lo.1999.44.7.1781.

Hung, C.C. et al., 2009. Enhancement of particulate organic carbon export flux induced by atmospheric forcing in the subtropical oligotrophic northwest Pacific Ocean. *Marine Chemistry*, 113(1-2), pp.19–24. doi:10.1016/j.marchem.2008.11.004.

Huot, Y. et al., 2007. Does chlorophyll a provide the best index of phytoplankton biomass for primary productivity studies? *Biogeosciences Discussions*, 4(2), pp.707–745. doi:10.5194/bgd-4-707-2007.

Irigoien, X., Flynn, K.J. & Harris, R.P., 2005. Phytoplankton blooms: A “loophole” in microzooplankton grazing impact? *Journal of Plankton Research*, 27(4), pp.313–321. doi:10.1093/plankt/fbi011.

Johnston, T.M.S. & Rudnick, D.L., 2009. Observations of the transition layer. *Journal of Physical Oceanography*, 39(3), pp.780–797. doi:http://dx.doi.org/10.1175/2008JPO3824.1.

Kalnay, E. et al., 1996. The NCEP/NCAR 40-year reanalysis project. *Bulletin of the American Meteorological Society*, 77(3), pp. 437–471. doi:10.1175/1520-0477(1996)077<0437:TNYRP>2.0.CO;2.

Kane, J., 1984. The feeding habits of co-occurring cod and haddock larvae from Georges Bank. *Marine Ecology Progress Series*, 16, pp. 9–20.

Kara, A.B., Rochford, P.A. & Hurlburt, H.E., 2000. Mixed layer depth variability and barrier layer formation over the North Pacific Ocean. *Journal of Geophysical Research*, 105(C7), pp. 16783–16801. doi:10.1029/2000JC900071/full.

Karabashev, G.S. & Ohl, K.A., 1990. *Fluorescence in the ocean*, Gidrometeoizdat,Leningrad, 200 pp.

Kiefer, D.A., 1973. Chlorophyll a fluorescence in marine centric diatoms: responses of chloroplasts to light and nutrient stress. *Marine Biology*, 23(1), pp.39–46. doi:10.1007/BF00394110.

Kirk, J.T., 1994. *Light and photosynthesis in aquatic ecosystems*. Cambridge university press.

Kirkwood, D., 1994. Nutrients: Practical notes on their determination in seawater. In *Proc. ICES/HELCOM workshop on quality assurance of chemical analytical procedures for the Baltic monitoring programme. Baltic Sea Environ. Proc*. pp. 23–47.

Koeller, P. et al., 2009. Basin-scale coherence in phenology of shrimps and phytoplankton in the North Atlantic Ocean. *Science*, 324(5928), pp. 791–793. doi:10.1126/science.1170987.

Koeve, W., 2001. Wintertime nutrients in the North Atlantic—new approaches and implications for new production estimates. *Marine chemistry*, 74(4), pp.245–260. doi:10.1016/S0304-4203(01)00016-0.

Lampitt, R.S. et al., 2010. Long-term variability of downward particle flux in the deep northeast Atlantic: Causes and trends. *Deep-Sea Research Part Ii-Topical Studies in Oceanography*, 57(15), pp. 1346–1361. doi:10.1016/j.dsr2.2010.01.011.

Large, W.G., Morzel, J. & Crawford, G.B., 1995. Accounting for surface wave distortion of the marine wind profile in low-level ocean storms wind measurements. *Journal of Physical Oceanography*, 25(11), pp. 2959–2971. doi:http://dx.doi.org/10.1175/15200485(1995)025<2959:AFSWDO>2.0.CO;2.

Lavigne, H. et al., 2012. Towards a merged satellite and in situ fluorescence ocean chlorophyll product. *Biogeosciences*, 9(6), pp. 2111–2125. doi:10.5194/bg-9-2111-2012.

Legendre, L., 1990. The significance of microalgal blooms for fisheries and for the export of particulate organic carbon in oceans. *Journal of Plankton Research*, 12(4), pp. 681–699. doi:10.1093/plankt/12.4.681.

Leggett, W.C. & Deblois, E., 1994. Recruitment in marine fishes: is it regulated by starvation and predation in the egg and larval stages? *Netherlands Journal of Sea Research*, 32(2), pp. 119–134. doi:10.1016/0077-7579(94)90036-1.

Lenn, Y.-D. et al., 2011. Intermittent Intense Turbulent Mixing under Ice in the Laptev Sea Continental Shelf. *Journal of Physical Oceanography*, 41(3), pp. 531–547. doi:http://dx.doi.org/10.1175/2010JPO4425.1.

Lévy, M., Ferrari, R., Franks, P.J., Martin, A.P. and Rivière, P., 2012. Bringing physics to life at the submesoscale. *Geophysical Research Letters*, *39*(14), L14602. doi:10.1029/2012GL052756.

Lévy, M., Lengaigne, M., et al., 2012. Contribution of tropical cyclones to the air-sea CO2 flux: A global view. *Global Biogeochemical Cycles*, 26(2), GB2001. doi:10.1029/2011GB004145.

Lévy, M., 2015. Exploration of the critical depth hypothesis with a simple NPZ model. *ICES Journal of Marine Science: Journal du Conseil*, 72(6), pp. 1916–1925. doi:10.1093/icesjms/fsv016.

Lévy, M., Mémery, L. & Madec, G., 2000. Combined effects of mesoscale processes and atmospheric high-frequency variability on the spring bloom in the MEDOC area. *Deep Sea Research Part I: Oceanographic Research Papers*, 47(1), pp.27–53. doi:10.1016/S0967-0637(99)00051-5.

Lévy, M., Mémery, L. & Madec, G., 1999. The onset of the Spring Bloom in the MEDOC area: Mesoscale spatial variability. *Deep-Sea Research Part I: Oceanographic Research Papers*, 46(7), pp. 1137–1160. doi:10.1016/S0967-0637(98)00105-8.

Lindemann, C. and St John, M.A., 2014. A seasonal diary of phytoplankton in the North Atlantic. *Frontiers in Marine Science*, 1, pp. 1-6. doi:10.3389/fmars.2014.00037.

Loftus, M.E. & Seliger, H.H., 1975. Some limitations of thein vivo fluorescence technique. *Chesapeake Science*, 16(2), pp. 79–92. doi:10.2307/1350685.

Mahadevan, A. et al., 2012. Eddy-Driven Stratification Initiates North Atlantic Spring Phytoplankton Blooms. *Science*, 337(6090), pp.54–58. doi:10.1126/science.1218740.

Maraiion, E. & Holligan, P.M., 1999. Photosynthetic parameters of phytoplankton from 50° N to 50° S in the Atlantic Ocean. *Marine Ecology Progress Series*, 176, pp. 191–203.

doi:10.3354/meps176191.

Marra, J., Bidigare, R.R. & Dickey, T.D., 1990. Nutrients and mixing, chlorophyll and phytoplankton growth. *Deep Sea Research Part A. Oceanographic Research Papers*, 37(1), pp. 127–143. doi:10.1016/0198-0149(90)90032-Q.

Martin, A.P. et al., 2010. The supply of nutrients due to vertical turbulent mixing: A study at the Porcupine Abyssal Plain study site in the northeast Atlantic. *Deep Sea Research Part II: Topical Studies in Oceanography*, 57(15), pp. 1293–1302. doi:10.1016/j.dsr2.2010.01.006.

Martin, A.P. & Richards, K.J., 2001. Mechanisms for vertical nutrient transport within a North Atlantic mesoscale eddy. *Deep Sea Research Part II: Topical Studies in Oceanography*, 48(4), pp. 757–773. doi:10.1016/S0967-0645(00)00096-5.

Martinez, E. et al., 2011. Phytoplankton spring and fall blooms in the North Atlantic in the 1980s and 2000s. *Journal of Geophysical Research: Oceans*, 116, C11029. doi:10.1029/2010JC006836.

McGillicuddy, D.J. et al., 2003. Eddy-driven sources and sinks of nutrients in the upper ocean: Results from a 0.1 resolution model of the North Atlantic. *Global Biogeochemical Cycles*, 17(2), 1035. doi:10.1029/2002GB001987.

McGillicuddy, D.J. et al., 1998. New evidence for the impact of mesoscale eddies on biogeochemical cycling in the Sargasso Sea. *Nature*, 394, pp. 263–266.

Mills, E.L., 2011. *Biological oceanography: An early history, 1870-1960*, University of Toronto Press.

Monin, A.S. & Obukhov, Am., 1954. Basic laws of turbulent mixing in the surface layer of the atmosphere. *Contrib. Geophys. Inst. Acad. Sci. USSR*, 151, pp. 163–187.

Nagai, T. et al., 2005. Field and numerical study of entrainment laws for surface mixed layer. *Deep Sea Research Part II: Topical Studies in Oceanography*, 52(9), pp.1109–1132. doi:10.1016/j.dsr2.2005.01.011.

Olita, A. et al., 2014. Observations of a phytoplankton spring bloom onset triggered by a density front in NW Mediterranean. *Ocean Science*, 10(4), pp. 657–666. doi:10.5194/os-10-657-2014.

Omand, M.M. et al., 2015. Eddy-driven subduction exports particulate organic carbon from the spring bloom. *Science*, 348(6231), pp.222–225. doi:10.1126/science.1260062.

Osborn, T.J., 2004. Simulating the winter North Atlantic Oscillation: the roles of internal variability and greenhouse gas forcing. *Climate Dynamics*, 22(6-7), pp.605–623. doi:10.1007/s00382-004-0405-1.

Osborn, T.R., 1980. Estimates of the local rate of vertical diffusion from dissipation measurements. *Journal of Physical Oceanography*, 10(1), pp. 83–89. doi:http://dx.doi.org/10.1175/1520-0485(1980)010<0083:EOTLRO>2.0.CO;2.

Oschlies, A., 2002. Nutrient supply to the surface waters of the North Atlantic: A model study. *Journal of Geophysical Research: Oceans (1978–2012)*, 107(C5), pp. 13–14. doi:10.1029/2000JC000275.

Painter, S.C. et al., 2014. An assessment of the vertical diffusive flux of iron and other nutrients to

the surface waters of the subpolar North Atlantic Ocean. *Biogeosciences*, 11, pp. 2113–2130. doi:10.5194/bg-11-2113-2014.

Painter, S.C., Pidcock, R.E. & Allen, J.T., 2010. A mesoscale eddy driving spatial and temporal heterogeneity in the productivity of the euphotic zone of the northeast Atlantic. *Deep Sea Research Part II: Topical Studies in Oceanography*, 57(15), pp. 1281–1292. doi:10.1016/j.dsr2.2010.01.005.

Parsons, T.R. & Lalli, C.M., 1988. Comparative oceanic ecology of the plankton communities of the subarctic Atlantic and Pacific oceans. *Oceanogr. Mar. Biol. Ann. Rev*, 26, pp.317–359.

Pelegrí, J.L., Marrero-Díaz, A. & Ratsimandresey, A.W., 2006. Nutrient irrigation of the North Atlantic. *Progress in Oceanography*, 70(2), pp.366–406. doi:10.1016/j.pocean.2006.03.018.

Perry, M.J., Sackmann, B.S., Eriksen, C.C. and Lee, C.M., 2008. Seaglider observations of blooms and subsurface chlorophyll maxima off the Washington coast. *Limnology and Oceanography*, *53*, pp. 2169-2179. doi:10.4319/lo.2008.53.5_part_2.2169.

Platt, T., Bird, D.F. & Sathyendranath, S., 1991. Critical depth and marine primary production. *Proceedings of the Royal Society of London B: Biological Sciences*, 246, pp.205–217. doi:10.1098/rspb.1991.0146

Platt, T., Fuentes-Yaco, C. & Frank, K.T., 2003. Spring algal bloom and larval fish survival. *Nature*, 423, pp. 398–399. doi:10.1038/423398b.

Pollard, R.T., 1980. Properties of near-surface inertial oscillations. *Journal of Physical Oceanography*, 10(3), pp.385–398. doi:http://dx.doi.org/10.1175/15200485(1980)010<0385:PONSIO>2.0.CO;2.

Racault, M.F. et al., 2012. Phytoplankton phenology in the global ocean. *Ecological Indicators*, 14(1), pp. 152–163. doi:10.1016/j.ecolind.2011.07.010.

Raven, J.A. & Falkowski, P.G., 1999. Oceanic sinks for atmospheric CO2. *Plant, Cell and Environment*, 22(6), pp.741–755. doi:10.1046/j.1365-3040.1999.00419.x.

Redfield, A.C., 1958. The biological control of chemical factors in the environment. *American scientist*, 46(3), pp. 230-221.

Rippeth, T.P. et al., 2009. The diapcynal nutrient flux and shear-induced diapcynal mixing in the seasonally stratified western Irish Sea. *Continental Shelf Research*, 29(13), pp. 1580–1587. doi:10.1016/j.csr.2009.04.009.

Rippeth, T.P., Palmer, M.R., Simpson, J.H., Fisher, N.R. and Sharples, J., 2005. Thermocline mixing in summer stratified continental shelf seas. *Geophysical Research Letters*, 32(5), L05602. doi:10.1029/2004GL022104.

Sackmann, 2008. Seaglider observations of variability in daytime fluorescence quenching of chlorophyll-a in Northeastern Pacific coastal waters. *Biogeosciences Discussions*, 5(40), pp. 2839–2865. doi:10.5194/bgd-5-2839-2008.

Sathyendranath, S., Ji, R. & Browman, H.I., 2015. Revisiting Sverdrup's critical depth hypothesis. *ICES Journal of Marine Science: Journal du Conseil*, 72(6), pp. 1892–1896. doi:10.1093/icesjms/fsv110.

Sauzède, R. et al., 2015. Retrieving the vertical distribution of chlorophyll a concentration and phytoplankton community composition from in situ fluorescence profiles: A method based on a neural network with potential for global-scale applications. *Journal of Geophysical*

Research: Oceans, 120(1), pp. 451–470. doi:10.1002/2014JC010355.

Schmitt, R.W., Bogden, P.S. & Dorman, C.E., 1989. Evaporation minus precipitation and density fluxes for the North Atlantic. *Journal of Physical Oceanography*, 19(9), pp. 1208–1221. doi:10.1175/1520-0485(1989)019<1208:EMPADF>2.0.CO;2.

Sharples, J. et al., 2007. Spring-neap modulation of internal tide mixing and vertical nitrate fluxes at a shelf edge in summer. *Limnology and Oceanography*, 52(5), pp. 1735–1747. doi: 10.4319/lo.2007.52.5.1735.

Siegel, D.A., Doney, S.C. & Yoder, J.A., 2002. The North Atlantic spring phytoplankton bloom and Sverdrup's critical depth hypothesis. *Science*, 296(5568), pp. 730–733. doi:10.1126/science.1069174.

Siegel, D.A., McGillicuddy, D.J. & Fields, E.A., 1999. Mesoscale eddies, satellite altimetry, and new production in the Sargasso Sea. *Journal of Geophysical Research: Oceans (1978–2012)*, 104, pp.13359–13379. doi:10.1029/1999JC900051.

Siegenthaler, U. & Sarmiento, J.L., 1993. Atmospheric carbon dioxide and the ocean. *Nature*, 365, pp. 119–125. doi:10.1038/365119a0.

Son, S., Platt, T., Bouman, H., Lee, D. and Sathyendranath, S., 2006. Satellite observation of chlorophyll and nutrients increase induced by Typhoon Megi in the Japan/East Sea. *Geophysical research letters*, 33(5), L05607. doi:10.1029/2005GL025065.

Steinhoff, T. et al., 2009. Estimating mixed layer nitrate in the North Atlantic Ocean. *Biogeosciences Discussions*, 6(5), 795–807. doi:10.5194/bg-7-795-2010.

Stramski, D. et al., 2004. The role of seawater constituents in light backscattering in the ocean. *Progress in Oceanography*, 61(1), pp. 27–56. doi:10.1016/j.pocean.2004.07.001.

Strom, S., 2002. Novel interactions between phytoplankton and microzooplankton: their influence on the coupling between growth and grazing rates in the sea. *Hydrobiologia*, 480, pp. 41–54. doi:10.1023/A:1021224832646.

Strom, S.L. et al., 2001. Phytoplankton blooms are strongly impacted by microzooplankton grazing in coastal North Pacific waters. *Marine Biology*, 138(2), pp. 355–368. doi:10.1007/s002270000461.

Suttle, C. a., Chan, A.M. & Cottrell, M.T., 1990. Infection of phytoplankton by viruses and reduction of primary productivity. *Nature*, 347(6292), pp.467–469. doi:10.1038/347467a0.

Sverdrup, H.U., 1953. On conditions for the vernal blooming of phytoplankton. *Journal du Conseil*, 18(3), pp. 287–295. doi:10.1093/icesjms/18.3.287.

Swart, S., Thomalla, S.J. & Monteiro, P.M.S., 2014. The seasonal cycle of mixed layer dynamics and phytoplankton biomass in the sub-antarctic zone: a high-resolution glider experiment. *Journal of Marine Systems*. doi:10.1016/j.jmarsys.2014.06.002.

Taylor, J.R. & Ferrari, R., 2011a. Shutdown of turbulent convection as a new criterion for the onset of spring phytoplankton blooms. *Limnology and Oceanography*, 56(6), pp. 2293-2307. doi:10.4319/lo.2011.56.6.2293.

Taylor, J.R. and Ferrari, R., 2011b. Ocean fronts trigger high latitude phytoplankton blooms. *Geophysical Research Letters*, 38(23), L23601. doi:10.1029/2011GL049312.

Thomalla, S.J. et al., 2015. High-resolution view of the spring bloom initiation and net community production in the Subantarctic Southern Ocean using glider data. *ICES Journal of Marine Science: Journal du Conseil*, *72*, pp. 1999–2020. doi:10.1093/icesjms/fsv105.

Thompson, A.F., Lazar, A., Buckingham, C., Naveira Garabato, A.C., Damerell, G.M. and Heywood, K.J., 2016. Open-ocean submesoscale motions: A full seasonal cycle of mixed layer instabilities from gliders. *Journal of Physical Oceanography*, *46*(4), pp.1285-1307. doi:http://dx.doi.org/10.1175/JPO-D-15-0170.1.

Thorpe, S.A., 2005. *The turbulent ocean*. Cambridge University Press.

Tillmann, U., 2004. Interactions between planktonic microalgae and protozoan grazers. *Journal of eukaryotic microbiology*, *51*(2), pp.156-168. doi:10.1111/j.1550-7408.2004.tb00540.x.

Ueyama, R. & Monger, B.C., 2005. Wind-induced modulation of seasonal phytoplankton blooms in the North Atlantic derived from satellite observations. *Limnology and Oceanography*, 50(6), pp.1820–1829. doi:10.4319/lo.2005.50.6.1820.

Uitz, J. (2006), Structure des communautés phytoplanctoniques et propriétés photophysiologiques dans l'océan ouvert: Paramétrisation en vue d'applications à la couleur de l'océan, Ph.D. thesis, 230 pp., Univ. de la Méditerranée Lab. de Océanogr., Villefranche-sur-Mer, France.

Volk, T. and Hoffert, M.I., 1985. Ocean carbon pumps: Analysis of relative strengths and efficiencies in ocean-driven atmospheric CO2 changes. *The Carbon Cycle and Atmospheric CO: Natural Variations Archean to Present*, pp.99-110. doi:10.1029/GM032p0099.

Waniek, J.J., 2003. The role of physical forcing in initiation of spring blooms in the northeast Atlantic. *Journal of Marine Systems*, 39(1), pp. 57–82. doi:10.1016/S0924-7963(02)00248-8.

Watras, C.J. et al., 1985. The effect of zooplankton grazing on estuarine blooms of the toxic dinoflagellate Gonyaulax tamarensis. *Journal of Plankton Research*, 7(6), pp. 891–908. doi:10.1093/plankt/7.6.891.

Weisse, R., von Storch, H. & Feser, F., 2005. Northeast Atlantic and North Sea storminess as simulated by a regional climate model during 1958-2001 and comparison with observations. *Journal of Climate*, 18(3), pp. 465–479. doi:http://dx.doi.org/10.1175/JCLI-3281.1.

Weisse, T. & Scheffel-Möser, U., 1990. Growth and grazing loss rates in single-celledPhaeocystis sp.(Prymnesiophyceae). *Marine biology*, 106(1), pp. 153–158. doi:10.1007/BF02114686.

Welschmeyer, N.A., 1994. Fluorometric analysis of chlorophyll a in the presence of chlorophyll b and pheopigments. *Limnology and Oceanography*, 39(8), pp. 1985–1992. doi:10.4319/lo.1994.39.8.1985.

Williams, C., Sharples, J., Mahaffey, C. and Rippeth, T., 2013. Wind-driven nutrient pulses to the subsurface chlorophyll maximum in seasonally stratified shelf seas. *Geophysical Research Letters*, 40(20), pp. 5467-5472. doi:10.1002/2013GL058171.

Williams, R.G. and Follows, M.J., 2003. Physical transport of nutrients and the maintenance of biological production. In *Ocean Biogeochemistry* (pp. 19-51). Springer Berlin Heidelberg. doi:10.1007/978-3-642-55844-3_3.

Williams, R.G., McLaren, A.J. & Follows, M.J., 2000. Estimating the convective supply of nitrate and implied variability in export production over the North Atlantic. *Global Biogeochemical Cycles*, 14(4), pp. 1299–1313. doi:10.1029/2000GB001260.

Wu, Y. et al., 2008. A summer phytoplankton bloom triggered by high wind events in the Labrador Sea, July 2006. *Geophysical research letters*, 35(10), L10606. doi:10.1029/2008GL033561.

Zilitinkevich, S. et al., 2002. Diagnostic and prognostic equations for the depth of the stably stratified Ekman boundary layer. *Quarterly Journal of the Royal Meteorological Society*, 128(579), pp. 25–46. doi:10.1256/00359000260498770.

Appendix A

Rumyantseva, Anna, et al. "Ocean nutrient pathways associated with the passage of a storm." *Global Biogeochemical Cycles* 29.8 (2015): 1179-1189.

AGU PUBLICATIONS

Global Biogeochemical Cycles

RESEARCH ARTICLE
10.1002/2015GB005097

Key Points:
- Storms significantly contribute to annual nitrate budgets
- Poststorm inertial currents produce spikes of high diffusive nitrate flux
- Their impact on nitrate supply is low compared to wind mixing during a storm

Supporting Information:
- Text S1
- Figure S1

Correspondence to:
A. Rumyantseva,
asr1g12@soton.ac.uk

Citation:
Rumyantseva, A., N. Lucas, T. Rippeth, A. Martin, S. C. Painter, T. J. Boyd, and S. Henson (2015), Ocean nutrient pathways associated with the passage of a storm, *Global Biogeochem. Cycles*, *29*, 1179–1189, doi:10.1002/2015GB005097.

Received 16 JAN 2015
Accepted 13 JUL 2015
Accepted article online 16 JUL 2015
Published online 14 AUG 2015

Ocean nutrient pathways associated with the passage of a storm

Anna Rumyantseva[1,2], Natasha Lucas[3], Tom Rippeth[3], Adrian Martin[1], Stuart C. Painter[1], Timothy J. Boyd[4], and Stephanie Henson[1]

[1]National Oceanography Centre, Southampton, UK, [2]Ocean and Earth Science, University of Southampton, Southampton, UK, [3]School of Ocean Sciences, Bangor University, Menai Bridge, UK, [4]The Scottish Association for Marine Science, Scottish Marine Institute, Argyll, UK

Abstract Storms that affect ocean surface layer dynamics and primary production are a frequent occurrence in the open North Atlantic Ocean. In this study we use an interdisciplinary data set collected in the region to quantify nutrient supply by two pathways associated with a storm event: entrainment of nutrients during a period of high wind forcing and subsequent shear spiking at the pycnocline due to interactions of storm-generated inertial currents with wind. The poststorm increase in surface layer nitrate (by ~20 mmol m^{-2}) was predominantly driven by the first pathway: nutrient intrusion during the storm. Alignment of poststorm inertial currents and surface wind stress caused shear instabilities at the ocean pycnocline, forming the second pathway for nutrient transport into the euphotic zone. During the alignment period, pulses of high-turbulence nitrate flux through the pycnocline (up to 1 mmol m^{-2} d^{-1}; approximately 25 times higher than the background flux) were detected. However, the impact of the poststorm supply was an order of magnitude lower than during the storm due to the short duration of the pulses. Cumulatively, the storm passage was equivalent to 2.5–5% of the nitrate supplied by winter convection and had a significant effect compared to previously reported (sub)mesoscale dynamics in the region. As storms occur frequently, they can form an important component in local nutrient budgets.

1. Introduction

Primary production in the temperate and subpolar North Atlantic Ocean plays a crucial role in the global carbon cycle [*Sabine et al.*, 2004]. However, the precise physical mechanisms that supply nutrients to support observed levels of annual primary production and the relative importance of these mechanisms are still under debate [*McGillicuddy et al.*, 2003; *Oschlies*, 2002a]. Many studies have focused on the impact of mesoscale and submesoscale dynamics [*Lévy et al.*, 2012; *Martin and Richards*, 2001; *McGillicuddy et al.*, 1998], the transport of nutrients by major ocean currents [*Pelegrí et al.*, 2006], and winter convection [*Williams et al.*, 2000] as pathways for nutrient supply to support primary production. However, less attention has been given to nutrient fluxes associated with the passage of storms.

In temperate and high-latitude oceans, strong wind forcing can be particularly important during the postspring bloom period when the surface ocean is nitrate-depleted and a well-established pycnocline inhibits the upward flux of nutrients to the euphotic zone. Under these conditions primary production is predominantly fuelled by regenerated forms of nitrogen such as ammonium and urea unless physical resupply of nutrients occurs. Satellite observations of episodic storm events in summer and autumn have been linked to subsequent phytoplankton increases in otherwise nutrient-limited conditions [*Babin et al.*, 2004; *Son et al.*, 2006; *Wu et al.*, 2008].

The passage of a storm can initiate transport of nitrate from the ocean interior to the euphotic zone in several ways. The classic interpretation of the wind-induced nutrient supply is that enhanced vertical mixing during strong wind forcing breaks down vertical stratification, erodes the pycnocline, and entrains nutrient-rich deeper water into the mixed layer [*Findlay et al.*, 2006; *Marra et al.*, 1990].

Another pathway, rarely documented in observational data, is associated with the interaction between wind stress and surface layer currents, resulting in an intermittent pulsed nutrient flux through the pycnocline [*Rippeth et al.*, 2009]. Abrupt changes in wind stress induce near-inertial oscillations [*Pollard*, 1980] that can last for several days before decaying. When the directions of wind stress and these near-inertial oscillations

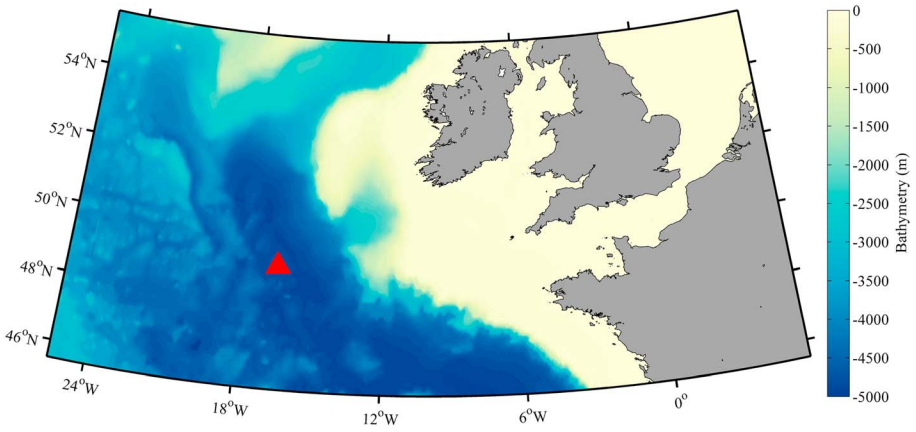

Figure 1. Bathymetry map of the northeast Atlantic Ocean showing the location of the sampling site during D381 cruise.

align, enhanced shear production can be sufficient to generate turbulence through Kelvin-Helmholtz instabilities such that the energy dissipation rate across the pycnocline can increase by an order of magnitude [*Lenn et al.*, 2011; *Rippeth et al.*, 2005]. This mechanism, referred to as shear spiking, has been shown to produce near-inertial pulses of high-turbulence nitrate flux across the pycnocline (compared to typically low background levels) by previous interdisciplinary studies in temperate shelf seas [*Rippeth et al.*, 2009; *Williams et al.*, 2013]. Shear spiking can supply nutrients during high wind forcing as well as in the poststorm period when inertial currents persist in the water column. Open ocean in situ observations of this process have been limited since they require coincident measurements of ocean microstructure and currents over several days.

This paper presents direct observations of the flux of nutrients to the surface layer resulting from the passage of an autumn extratropical storm in the open North Atlantic Ocean. Specifically, we quantify the nutrient flux during the storm and additional supply of nutrients after the storm passage associated with the shear-spiking mechanism. The efficiency of the overall storm-induced nutrient supply is compared to other more widely recognized mechanisms in order to assess the storm's contribution to the nutrient budget of the North Atlantic Ocean.

2. Data and Methods

2.1. Observational Study

This study is based on an interdisciplinary data set collected aboard RRS Discovery (cruise D381) in the framework of the UK Natural Environment Research Council (NERC) OSMOSIS (Ocean Surface Mixing Ocean Submesoscale Interaction Study) project. The sampling campaign was carried out 40 km southeast of the Porcupine Abyssal Plain (PAP) Sustained Observatory (49°N, 16.5°W; Figure 1 [*Lampitt et al.*, 2010]), from 31 August to 1 October 2012 (year days 244 to 275).

The observations (Figure 2) included turbulence measurements using a MSS90 microstructure profiler, standard CTD (conductivity-temperature-depth) profiling using a SeaBird 911, current measurements using a vessel-mounted RDI "Ocean Surveyor" 75 kHz ADCP (acoustic Doppler current profiler), and underway water samples from the nontoxic seawater supply (approximate intake depth of 5 m) and surface meteorology. Additionally, two Seagliders surveyed the area for a year (September 2012 to September 2013), equipped with an unpumped conductivity-temperature sensor, a Wetlabs ECOpuck (including chlorophyll *a*, hereafter chl *a*, fluorescence sensor), and a spherical photosynthetically available radiation sensor, providing vertical profiles of biophysical properties of the ocean boundary layer over the duration of the cruise and beyond. Details of Seaglider data processing and calibration are presented in the supporting information. Sampling for inorganic nutrient concentrations was undertaken from both CTD casts and the underway nontoxic seawater supply. Analysis of nitrate + nitrite (hereafter nitrate) concentrations was conducted using a Skalar-Sanplus autoanalyzer and the method described by *Kirkwood* [1996].

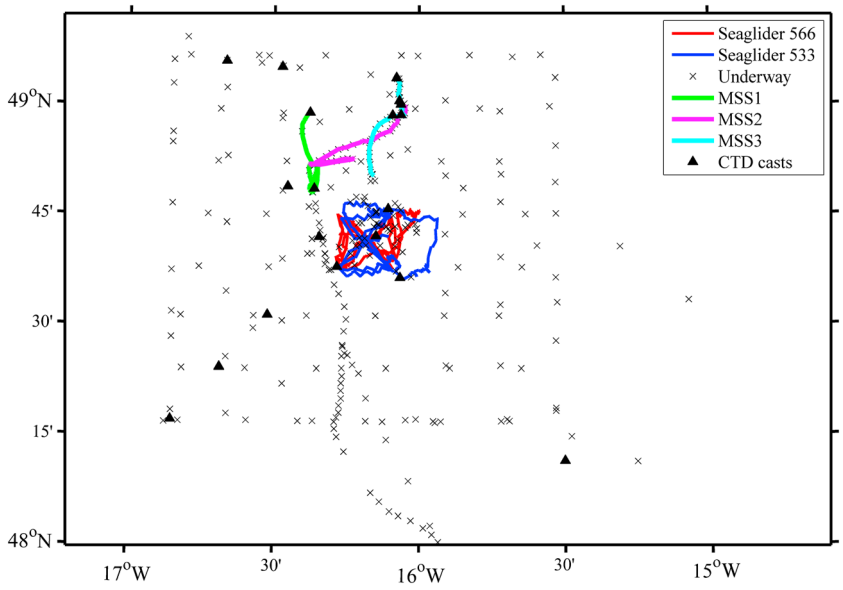

Figure 2. Sampling map for cruise D381: Seagliders 566 and 533 (red and blue lines, respectively); underway samples (grey crosses); three series of turbulence measurements: MSS1 (green line), MSS2 (magenta line), and MSS3 (light blue line); CTD casts (black triangles).

2.2. Turbulent Nitrate Flux Calculations

Estimates of the nitrate flux through the pycnocline were based on vertical profiles of turbulent kinetic energy dissipation. During the course of the cruise, three series of turbulence measurements extending to a depth of ~200 m were conducted:

MSS1 From year day 260.9 to 262.5 (238 profiles)

MSS2 From year day 265.3 to 266.5 day of year (202 profiles)

MSS3 From year day 270.8 to 272.0 day of year (175 profiles)

Estimates of the turbulent kinetic energy dissipation rate (ε) were obtained from raw shear data using the MSSPRO software standard processing sequence. All data from the MSS probe for each profile were averaged into 1 m bins. For each bin the eddy diffusivity was calculated from the energy dissipation rate following *Osborn* [1980]:

$$K = 0.2\frac{\varepsilon}{N^2} \tag{1}$$

where K is the eddy diffusivity and N is the buoyancy frequency. Subsequently, nitrate flux at depth d can be defined through multiplying the diffusivity term by the local nitrate gradient:

$$F = K\frac{\partial \mathrm{NO_3}}{\partial z}\bigg|_{z=d} \tag{2}$$

where NO_3 is the nitrate concentration. Following *Sharples et al*. [2007], CTD bottle data were used to derive a nitrate-density relation and obtain vertically resolved profiles of $\frac{\partial \mathrm{NO_3}}{\partial z}$. We found a strong linear relationship between density and nitrate (Figure 3a; $R^2 = 0.88$, $P < 0.0001$), allowing nitrate gradients to be represented in equation (2) as $m\frac{\partial \rho}{\partial z}$, where ρ is the density measured by the microstructure profiler and $m = 2.4 \pm 0.1$ mmol N m^{-3} (kg m^{-3})$^{-1}$ is the nitrate-density gradient. Representative vertical profiles of density and nitrate are shown in Figure 3b. Uncertainty associated with the estimated nitrate-density gradient (~5%) is negligible compared to uncertainties associated with eddy diffusivity measurements in the ocean; therefore, $m = 2.4$ mmol N m^{-3} (kg m^{-3})$^{-1}$ was used in the further calculations of the nitrate flux.

2.3. Bulk Shear Estimation and Theoretical Model

Episodic bursts of shear, attributed to alignment and interaction of shear and wind forcing, have been quantified for the open ocean using a modified shear production model as described in *Brannigan et al*. [2013], which is

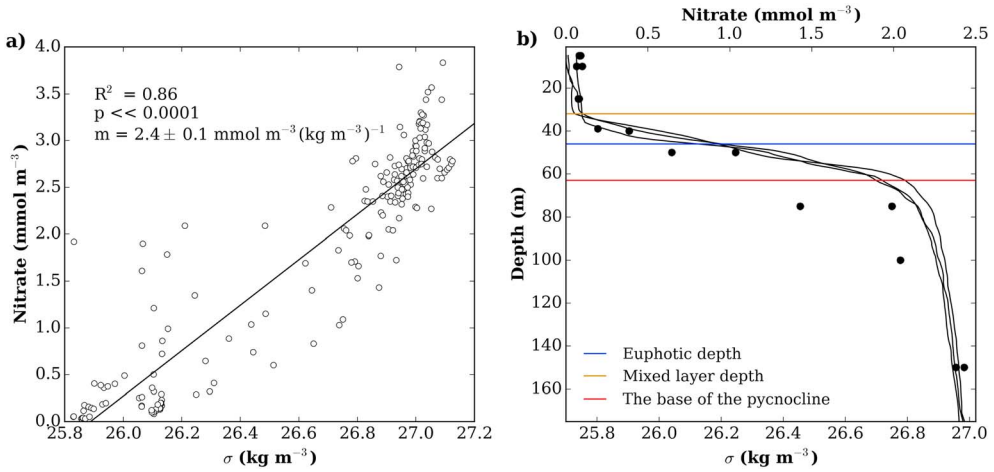

Figure 3. (a) The nitrate-density relationship within the pycnocline for all CTD casts collected during D381 cruise. *m* is the slope of the linear regression ±95% confidence intervals. (b) CTD profiles collected close in time (decimal days 264–265) illustrating vertical distribution of density (black lines) and nitrate (black circles) during D381 cruise. The horizontal lines on the plot indicate the corresponding mean values of the euphotic depth (blue), mixed layer depth (yellow), and the base of the pycnocline (red).

adapted from a prognostic expression derived from one-dimensional momentum equations for stratified tidal shelf seas [*Burchard and Rippeth*, 2009]. In this model the authors define a two-layer damped-slab model, with the relationship between velocity and bulk shear as

$$\vec{S} = \frac{\vec{u}_H - \vec{u}_L}{h_s} \tag{3}$$

where $\vec{u}_H$ and $\vec{u}_L$ are the velocities in the mixed layer H and lower layer L, respectively, and h_s is the distance between the centers of mass of these layers, separated by a pycnocline layer. In this work we define a variable pycnocline as the layer between the mixed layer depth (MLD) and the base of the pycnocline. The definition of MLD was based on *de Boyer Montégut et al.* [2004] and calculated using a change in temperature of 0.2°C relative to the value at 10 m depth. The base of the pycnocline was determined following *Johnston and Rudnick* [2009], as the depth below the mean mixed layer depth of the deepest isopycnal within one standard deviation of the mean mixed layer depth. In this model the lower layer was defined as a 48 m deep layer immediately below the base of the pycnocline, as this limit was large enough to capture the slab dynamics while falling within the ADCP bin resolution.

Following the derivation in *Brannigan et al.* [2013] and using the slab layers defined here, a relationship for the rate of change of bulk shear squared with respect to time is obtained with the production or destruction of shear being brought about by the relative orientation between wind and bulk shear directions:

$$\frac{\partial S^2}{\partial t} = 2\left(\frac{\vec{S}\,\vec{T}_w}{h_s \rho H} - c_i \frac{h_S}{H}|S^3|\right) \tag{4}$$

where c_i is the drag coefficient, $\vec{T}_w$ is the wind stress, and ρ is a reference density. When the dot product is greater than zero (i.e., $\cos\left(\vec{S}, \vec{T}_w\right) > 0$), directions of wind and shear are favorable for enhanced shear production. If the wind magnitude is constant, the maximum shear production occurs when $\vec{S}$ and $\vec{T}_w$ align.

3. Results

3.1. Surface Dynamics

Atmospheric conditions during the cruise were characterized by a storm that started on day 268 (24 September 2012) and continued until day 270.6 (27 September 2012) with typical wind forcing 0.3–0.4 N m^{-2} (Figure 4a). Underway nutrient and Seaglider chl *a* fluorescence data suggest a biochemical response to the storm event (Figures 4c and 4d). The surface nitrate concentration after the storm had increased from <0.1 mmol N m^{-3}

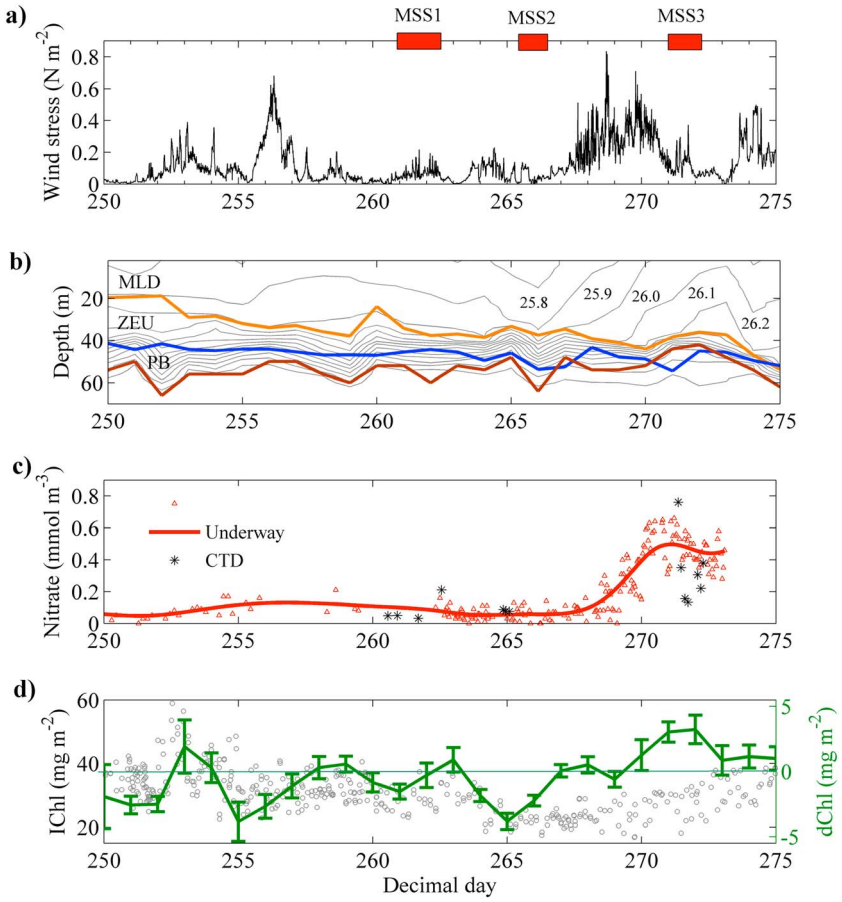

Figure 4. Wind and biophysical data collected during cruise D381. (a) The 10 min averaged wind stress was calculated as in *Large et al.* [1995] using wind speed data measured by the weather station on RRS Discovery. The red rectangles at the top show the timing of three series of turbulence measurements: MSS1, MSS2, and MSS3. (b) The Seagliders time series of isopycnal surfaces (grey lines), mixed layer depth (MLD) defined as a temperature differential of 0.2°C from 10 m depth (orange line), euphotic depth (ZEU; blue line; details of the calculations are presented in the supporting information), and the base of the pycnocline (PB; brown line). (c) Surface nitrate variability during the cruise: the red triangles are the surface (~5 m) nitrate concentrations from the ship underway system, and the red solid line is the fitted smooth spline. The black stars represent the mean nitrate concentration within the mixed layer estimated from CTD casts. (d) Integrated chl *a* (IChl; grey circles) and daily change in integrated chl *a* (dChl; green line; Seagliders data).

to almost 0.6 mmol N m^{-3}. The time series of change in integrated chl *a* (dChl) showed that replenishment of the surface layer with nutrients was coincident with increased phytoplankton stocks (i.e., dChl > 0). The prestorm period was characterized by mostly negative dChl (Figure 4d) due to lack of nutrients within the mixed layer (Figure 3b) and therefore decreasing phytoplankton growth rate representative of typical conditions in the high-latitude North Atlantic Ocean over the postspring bloom period.

3.2. Nutrient Supply During the Storm

The ability of Seagliders to obtain data under challenging weather conditions allowed them to capture the changes in the surface layer dynamics throughout the storm event. The data showed that vertical mixing during the associated strong wind forcing introduced significant changes in the upper ocean density structure: an increase in surface density from ~25.8 kg m^{-3} to ~26.1 kg m^{-3} and erosion of the pycnocline (Figure 4b). Entrainment of water from the pycnocline was accompanied by an increase in surface nitrate concentration (Figure 4c). This picture is consistent with the classical interpretation of the storm's influence on the upper ocean: thinning of the pycnocline due to high-turbulence production at the base of the mixed layer and corresponding intrusion of nutrients. Supply of nutrients during the storm could be also driven by wind-generated inertial oscillation and associated shear instabilities across the pycnocline. Unfortunately, the

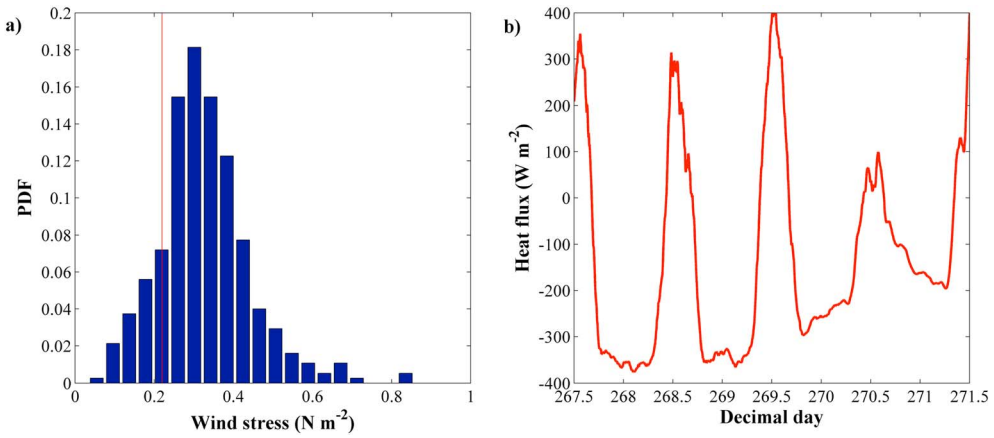

Figure 5. Wind stress and surface heat flux data during the observed storm event. (a) Histogram of wind stress values throughout the storm. The red vertical line indicates the critical wind stress (τ_{cr}) described in section 3.2. (b) Surface net heat flux from the ocean to the atmosphere during the storm event that occurred in the course of D381 cruise. The components of the net heat flux were calculated using meteorological data obtained on the cruise applying TOGA COARE 2.0 algorithm [*Fairall et al.*, 1996]. The negative heat flux indicates the heat loss by the ocean.

quality of ADCP data during high wind forcing did not allow clear detection of shear spikes at the ocean pycnocline throughout the storm event. Hence, changes in surface nitrate concentrations during the storm may be the combined effect of both processes.

Meteorological data indicate that high wind speeds were accompanied by a significant decrease in the air temperature, by 2.5°C. To determine if vertical mixing during the storm was dominated by buoyancy reduction due to cooling or by shear production associated with wind mixing, the Monin-Obukhov length scale [*Monin and Obukhov*, 1954] was used:

$$L_{MO} = -\frac{u_*^3}{k_{vK}B} \tag{5}$$

where $k_{vK} = 0.41$ is the von Karman constant, B is the surface buoyancy flux, $u_* = \left(\frac{\tau_w}{\rho_0}\right)^{1/2}$ is the friction velocity, $\rho_0 = 1026\,\mathrm{kg\,m^{-3}}$ is the reference density, and τ_w is the wind stress. Above the Monin-Obukhov length scale shear production of turbulent kinetic energy dominates over buoyant reduction. If the length scale is deeper than the mixed layer depth, turbulence within the surface layer is mainly driven by wind forcing rather than convection [*Nagai et al.*, 2005].

Combined National Centers for Environmental Prediction reanalysis and meteorological data obtained for the cruise period suggests that the net heat flux from the ocean to the atmosphere, Q, was at a minimum of $-375\,\mathrm{W\,m^{-2}}$ during the storm (Figure 5b). The components of the net heat flux were calculated using the Tropical Ocean–Global Atmosphere (TOGA) Coupled Ocean-Atmosphere Response Experiment (COARE) 2.0 algorithm [*Fairall et al.*, 1996]. Neglecting effects of evaporation and precipitation, the buoyancy flux can be estimated as

$$B = \frac{g\alpha Q}{\rho_0 c_p} \tag{6}$$

where $g = 9.81\,\mathrm{m\,s^{-2}}$ is the acceleration due to gravity, $\alpha = 2.1 \times 10^{-4}\,^{\circ}\mathrm{C}^{-1}$ is the coefficient of thermal expansion for seawater, and $c_p = 3985\,\mathrm{J\,kg^{-1}\,^{\circ}C^{-1}}$ is the seawater heat capacity (estimated for typical values of temperature and salinity within the mixed layer observed during the storm: T~14°C and S~35.5 practical salinity unit).

From equations (5) and (6), we estimated the weakest wind stress (τ_{cr}~$0.2\,\mathrm{N\,m^{-2}}$) for which wind shear would be the main source of turbulence under the strongest convective conditions during the storm, assuming the mixed layer depth ~40 m (Figure 4b). Wind stress values during the storm were generally higher than τ_{cr} (Figure 5a). It suggests that turbulent kinetic energy production in the mixed layer and pycnocline erosion observed by Seagliders were mostly driven by wind forcing, rather than convection.

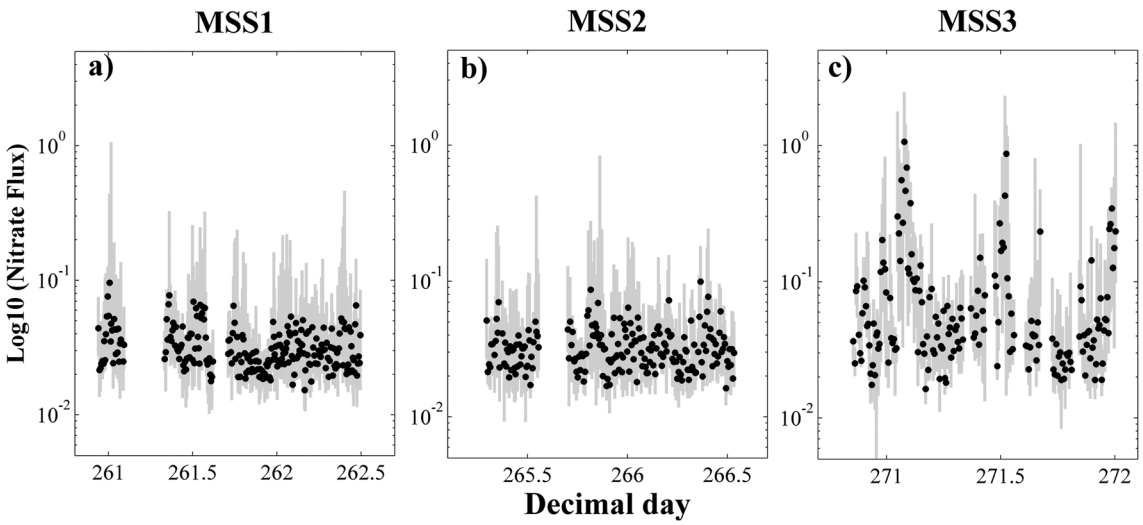

Figure 6. Vertical nitrate flux (*y* axis is in log scale; units are mmol N m^{-2} d^{-1}) through the pycnocline estimated from the three series of turbulence measurements: (a) MSS1, (b) MSS2, and (c) MSS3. The grey lines represent the interquartile range for each profile, and the black dots indicate the median values.

Following the passage of the storm, surface nitrate concentrations reached ~0.6 mmol N m^{-3}. Multiplying the increase in concentration (by ~0.5 mmol N m^{-3} compared to the prestorm values) by the mixed layer depth (~40 m), nutrient supply due to the storm was estimated as ~20 mmol N m^{-2}. The storm lasted about 3 days. Therefore, an increase in mixed layer nitrate by 20 mmol N m^{-2} is equivalent to a nitrate flux of 6–7 mmol N m^{-2} d^{-1}.

3.3. Shear Spiking After the Storm

Turbulence measurements conducted before and after the storm allowed us to estimate the additional supply of nutrients that could occur in the wake of the storm due to the presence of inertial currents in the surface layer and associated shear-spiking mechanism. During the prestorm period two series of turbulence measurements (MSS1 and MSS2) were conducted, providing estimates of the nitrate flux associated with background turbulent diffusion (Figure 4a). The third series of turbulence measurements (MSS3) took place immediately after the storm event, capturing interactions between wind stress and inertial currents which affected the magnitude and structure of the turbulent flux. According to the Seaglider data, the base of the euphotic zone was located within the pycnocline (Figures 3b and 4b). Therefore, we assumed that the nitrate flux through the pycnocline represented the flux into the euphotic zone. The nitrate flux was calculated for all 1 m bins within the pycnocline layer. To reduce the influence of outliers, only data points within the interquartile range were considered for each vertical profile.

For the prestorm turbulence measurements, MSS1 and MSS2, the nitrate flux was relatively constant (Figures 6a and 6b). The two series gave consistent estimates of the background turbulent diffusive nitrate flux: 0.04 ± 0.03 mmol N m^{-2} d^{-1}. Poststorm (MSS3), three bursts of high nitrate flux (up to 1 mmol N m^{-2} d^{-1}, 32 times the standard deviations for MSS1 and MSS2) were observed (Figure 6c). The duration of the bursts was relatively short (O(1 h)). The time intervals between them were 10.7 and 11 h. The overall mean flux during MSS3 was 0.11 ± 0.18 mmol N m^{-2} d^{-1}, approximately 3-fold higher than prestorm (MSS1 and MSS2).

The data suggest that the variability of the nitrate flux measured during MSS3 was affected by the poststorm inertial currents (Figure 7). At the beginning of MSS3 (days 270.9–271.6), the ADCP data captured rotation of the bulk shear vector at near the local inertial frequency (~15 h; Figure 7d). The magnitude of the bulk shear oscillated between 0.5 and 2×10^{-5} s^{-2} during this time (Figure 7b). By day 271.6 slab motion of the surface layer dissipated and the bulk shear value reduced (Figures 7b and 7d). The wind direction remained relatively constant throughout (Figure 7d). According to the theoretical model (equation (3)), the contribution of wind to shear production can be assessed by looking at the time series $\left|\vec{T}_w\right|\cos(\vec{S},\vec{T}_w)$ as this metric encompasses the influence of wind direction relative to the bulk shear as well as the influence of wind magnitude. The time

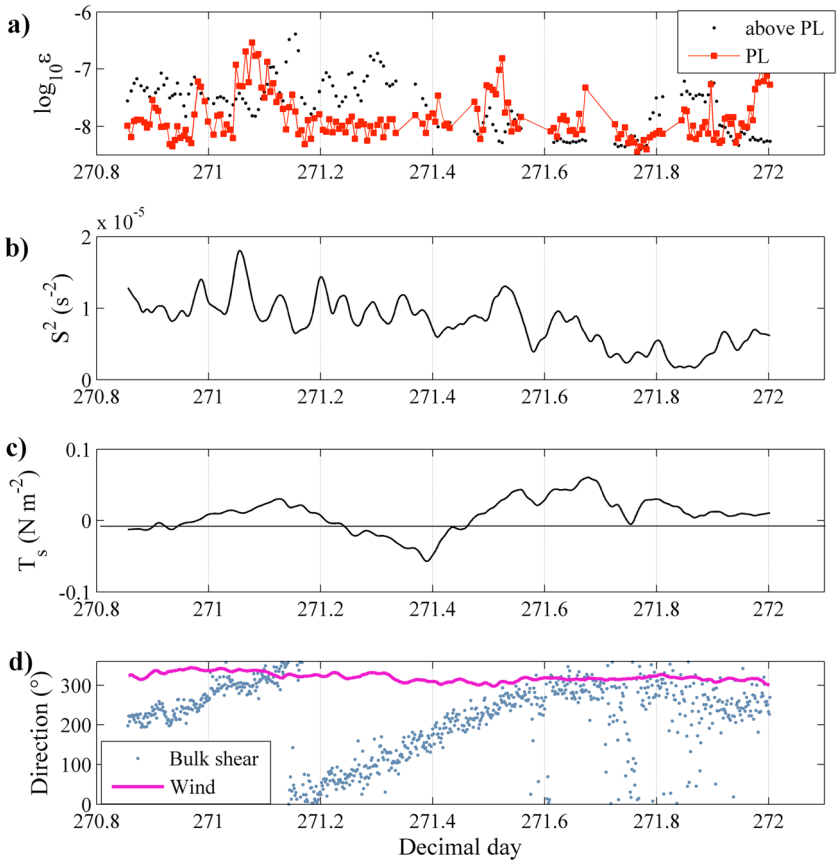

Figure 7. Forcing, shear, and turbulence characteristics during MSS3 transect during which the bursts of turbulent flux were observed: (a) decimal logarithm of median energy dissipation rate ε (units of ε are $m^2\ s^{-3}$) within the pycnocline (red squares) and within the 10 m layer above the pycnocline (grey dots), (b) time series of bulk shear magnitude smoothed using 2 h boxcar filter, (c) wind stress magnitude multiplied by the cosine between wind and bulk shear directions, and (d) directions of wind stress (purple line) and bulk shear (blue dots).

series reveals that wind-supported shear production (i.e., $\left|\vec{T}_w\right|\cos(\vec{S},\vec{T}_w)>0$) occurred during days 271–271.2, 271.45–271.75, and at the end of the period of microstructure sampling when the inertial currents dissipated (Figure 7c). In agreement with the theory, the bursts of high mixing across the pycnocline occurred during these three periods and were associated with the enhanced bulk shear ($S^2>10^{-5}\ s^{-2}$). During the bursts, energy dissipation rate (ε) within the pycnocline was at least an order of magnitude higher than the background levels and the mean ε in the 10 m layer above the pycnocline (Figure 7a). The latter indicates that it was unlikely that simple deepening of the mixed layer due to surface forcing initiated the spikes in vertical mixing across the pycnocline.

4. Discussion

Previous studies [*Forryan et al.*, 2012; *Martin et al.*, 2010; *Painter et al.*, 2014] have suggested that the contribution of small-scale diapycnal turbulent diffusion to the overall physical transport of nutrients to the ocean surface layer is relatively minor. However, enhancement of the turbulent flux through the pycnocline associated with wind-driven inertial oscillations has not been considered in previous nitrate budget calculations for the open ocean. Shear spikes are discrete features, and enhancement of the nitrate flux due to them could be missed if measurements do not resolve subinertial frequencies.

The data set presented here has allowed direct observation of changes in the turbulent nitrate flux caused by shear spiking following the storm event in the open North Atlantic Ocean. A sequence of pulses of high nitrate flux generated by a wind event longer than the inertial period was observed, in agreement with

the sensitivity analysis of the model for shear production presented in *Burchard and Rippeth* [2009]. This model suggests that the period of alignment corresponds to the period of maximum shear production. In the current study the spikes of vertical mixing across the pycnocline occurred during the alignment (the first and the third spikes) and before the alignment (the second spike). In this study it was shown that maximum shear production depends also on the wind magnitude variability and complete alignment is not necessary to produce spikes in vertical mixing across the pycnocline.

Estimates of the background nitrate flux due to turbulent diffusion (~0.04 mmol N m^{-2} d^{-1}) were consistent with the previous similar estimates at the PAP site [*Martin et al*., 2010]. During MSS3 a short-term increase in turbulent nitrate flux (approximately 25 times higher than the background levels) was observed with the mean daily nitrate flux (~0.11 mmol N m^{-2} d^{-1}) being higher only by a factor of 3. The nitrate supply by the poststorm shear spiking was an order of magnitude lower than the estimated nitrate flux during the storm (6–7 mmol N m^{-2} d^{-1}, 2 orders of magnitude higher than the background flux). Thus, the contribution of the poststorm nitrate supply appears to be low due to the short duration of periods of enhanced nitrate flux, and nutrients were delivered to the surface layer mainly during the storm. High values of nitrate flux during enhanced wind forcing (~22 mmol N m^{-2} d^{-1}, 17-fold higher than the background flux) were also reported in previous studies in shelf seas [*Williams et al*., 2013].

Using the estimates presented in this study, it is worth comparing the storm-driven nutrient supply with other regional physical mechanisms of nutrient transport to the surface ocean. The contribution of winter convection to the nitrate budget of this area of the North Atlantic was previously estimated as between 504 mmol N m^{-2} yr^{-1} [*Martin et al*., 2010] and 1000 mmol N m^{-2} yr^{-1} [*Williams and Follows*, 2003]. Thus, nutrient intrusion during the storm caused by vertical mixing (20 mmol N m^{-2}) corresponds to 2.5–5% of the total annual nitrate supply by deep winter convection. The PAP site is in the transition region between the mesotrophic subpolar gyre and the oligotrophic subtropical gyre [*Henson et al*., 2009]. Mesoscale eddy pumping has been estimated to provide approximately 200 mmol N m^{-2} yr^{-1} for oligotrophic regions [*McGillicuddy et al*., 1998; *Siegel et al*., 1999]. However, in subpolar regions the vertical advection by mesoscale eddies can potentially act as a sink of nutrients [*McGillicuddy et al*., 2003; *Oschlies*, 2002b]. Hence, the magnitude, if not sign, of the mesoscale nitrate flux at the study site is uncertain. One instance of the effect of submesoscale filaments on primary production at the PAP site was reported by *Painter et al*. [2010], who showed that rates of primary production associated with the passage of an eddy filament could be highly variable with a potential increase of up to 74 mmol C m^{-2} d^{-1}. Assuming a C:N ratio of 6.6 [*Redfield*, 1958] and a lifetime for a submesoscale front of O(1) day [*Lévy et al*., 2012], the total nitrate supply associated with this filament to support the primary production increase would be 11 mmol N m^{-2}. This is approximately one half of the nitrate associated with the storm pathway. However, estimates provided by *Painter et al*. [2010] are relevant for a single filament observed at the PAP site. In general, submesoscale fronts are ubiquitous features and collectively could be associated with higher nitrate flux.

One can make the point that storms in the high-latitude North Atlantic Ocean are localized features compared to basin-wide mechanisms of nutrient supply such as winter convection. However, the spatial scale of storms is relatively large (O(100–1000) km) and comparable to the characteristic scale of the basin (O(1000) km). Their passage is also fairly frequent: model-based estimates of storminess suggest that annually ~30 storms (with maximum wind speed >17 m s^{-1}) occur in the extratropical northeast Atlantic Ocean [*Weisse et al*., 2005], although the majority of these storms occur in winter. We looked at the data from the weather mooring deployed at the PAP site from the end of April to November 2013, the time of year when surface nitrate is likely depleted. The data showed that during that period of time up to six low-pressure systems separated by several days with instantaneous wind speed exceeding 17 m s^{-1} passed through the site. A coarse estimate based on the results of the current study suggests that cumulative effects of these storm events can reach up to 30% of the nitrate supply by winter convection.

Previous studies estimated the impact of tropical cyclones on primary production in the North Atlantic Ocean using satellite ocean color data and obtained contradictory conclusions on their importance [*Foltz et al*., 2015; *Hanshaw et al*., 2008]. In this paper we have assessed the potential significance of extratropical storms for primary production in the high-latitude North Atlantic Ocean by focusing on nutrient supply. This study shows that on an annual scale the passage of storms can potentially support a significant amount of

ocean primary production and highlights the importance of further observational and modeling studies of storm contribution to nutrient supply in the ocean surface layer.

5. Conclusions

Based on the interdisciplinary data set collected at the Porcupine Abyssal Plain Sustained Observatory site we estimated nutrient fluxes to the ocean surface layer associated with the passage of a storm. Our observations demonstrated that the majority of nutrients were delivered to the mixed layer during the period of strong wind forcing. The turbulence measurements conducted in the wake of a storm allowed quantification of the additional poststorm nitrate flux due to the shear-spiking mechanism. Regardless of the dramatic semidiurnal increase of the flux, the overall nitrate supply after the storm was relatively low due to the short duration of the periods of enhanced mixing across the pycnocline. The estimate of the cumulative nitrate supply suggests that storms can form an appreciable component of the local annual nitrate budget.

Acknowledgments

The authors would like to thank L. Brannigan, M. Toberman, G. Damerell, K. Heywood, A. Thompson, J. Kaiser, V. Hemsley, M. Stinchcombe, the crew of RRS Discovery for their help with the data collection and processing, and two anonymous reviewers for their constructive comments, which helped us to improve the manuscript. OSMOSIS project was supported by NERC grant NE/I020083/1. A. Rumyantseva was funded by a University of Southampton PhD studentship. The data set used in this study will be lodged with the British Oceanographic Data Centre (enquiries@bodc.ac.uk). In memory of Timothy Boyd.

References

Babin, S. M., J. A. Carton, T. D. Dickey, and J. D. Wiggert (2004), Satellite evidence of hurricane-induced phytoplankton blooms in an oceanic desert, *J. Geophys. Res.*, *109*, C03043, doi:10.1029/2003JC001938.

Brannigan, L., Y.-D. Lenn, T. P. Rippeth, E. McDonagh, T. K. Chereskin, and J. Sprintall (2013), Shear at the base of the oceanic mixed layer generated by wind shear alignment, *J. Phys. Oceanogr.*, *43*(8), 1798–1810, doi:10.1175/JPO-D-12-0104.1.

Burchard, H., and T. Rippeth (2009), Generation of bulk shear spikes in shallow stratified tidal seas, *J. Phys. Oceanogr.*, *39*(4), 969–985, doi:10.1175/2008JPO4074.1.

de Boyer Montégut, C., G. Madec, A. S. Fischer, A. Lazar, and D. Iudicone (2004), Mixed layer depth over the global ocean: An examination of profile data and a profile-based climatology, *J. Geophys. Res.*, *109*, C12003, doi:10.1029/2004JC002378.

Fairall, C. W., E. F. Bradley, D. P. Rogers, J. B. Edson, and G. S. Young (1996), Bulk parameterization of air-sea fluxes for Tropical Ocean-Global Atmosphere Coupled-Ocean Atmosphere Response Experiment, *J. Geophys. Res.*, *101*, 3747–3764, doi:10.1029/95JC03205.

Findlay, H. S., A. Yool, M. Nodale, and J. W. Pitchford (2006), Modelling of autumn plankton bloom dynamics, *J. Plankton Res.*, *28*(2), 209–220, doi:10.1093/plankt/fbi114.

Foltz, G. R., K. Balaguru, and L. Ruby Leung (2015), A reassessment of the integrated impact of tropical cyclones on surface chlorophyll in the western subtropical North Atlantic, *Geophys. Res. Lett.*, *42*, 1158–1164, doi:10.1002/2015GL063222.

Forryan, A., A. P. Martin, M. A. Srokosz, E. E. Popova, S. C. Painter, and M. C. Stinchcombe (2012), Turbulent nutrient fluxes in the Iceland Basin, *Deep Sea Res., Part I*, *63*, 20–35, doi:10.1016/j.dsr.2011.12.006.

Hanshaw, M. N., M. S. Lozier, and J. B. Palter (2008), Integrated impact of tropical cyclones on sea surface chlorophyll in the North Atlantic, *Geophys. Res. Lett.*, *35*, L01601, doi:10.1029/2007GL031862.

Henson, S. A., J. P. Dunne, and J. L. Sarmiento (2009), Decadal variability in North Atlantic phytoplankton blooms, *J. Geophys. Res.*, *114*, C04013, doi:10.1029/2008JC005139.

Johnston, T. M. S., and D. L. Rudnick (2009), Observations of the transition layer, *J. Phys. Oceanogr.*, *39*, 780–797, doi:10.1175/2008JPO3824.1.

Kirkwood, D. S. (1996), *Nutrients: Practical Notes on Their Determination in Seawater*, *ICES Tech. Mar. Environ. Sci. Rep.*, vol. 17, 25 pp., International Council for the Exploration of the Seas, Copenhagen.

Lampitt, R. S., D. S. M. Billett, and A. P. Martin (2010), The sustained observatory over the Porcupine Abyssal Plain (PAP): Insights from time series observations and process studies, *Deep Sea Res., Part II*, *57*(15), 1267–1271, doi:10.1016/j.dsr2.2010.01.003.

Large, W. G., J. Morzel, and G. B. Crawford (1995), Accounting for surface wave distortion of the marine wind profile in low-level ocean storms wind measurements, *J. Phys. Oceanogr.*, *25*, 2959–2971, doi:10.1175/15200485.

Lenn, Y., T. Rippeth, C. Old, S. Bacon, I. Polyakov, V. Ivanov, and J. Holemann (2011), Intermittent intense turbulent mixing under ice in the Laptev Sea continental shelf, *J. Phys. Oceanogr.*, *41*(3), 531–547, doi:10.1175/2010JPO4425.1.

Lévy, M., R. Ferrari, P. J. S. Franks, A. P. Martin, and P. Rivière (2012), Bringing physics to life at the submesoscale, *Geophys. Res. Lett.*, *39*, L14602, doi:10.1029/2012GL052756.

Marra, J., R. Bidigare, and T. Dickey (1990), Nutrients and mixing, chlorophyll and phytoplankton growth, *Deep-Sea Res., Part A*, *37*(1), 127–143, doi:10.1016/0198-0149(90)90032-Q.

Martin, A. P., and K. J. Richards (2001), Mechanisms for vertical nutrient transport within a North Atlantic mesoscale eddy, *Deep Sea Res., Part II*, *48*(4), 757–773, doi:10.1016/S0967-0645(00)00096-5.

Martin, A. P., M. I. Lucas, S. C. Painter, R. Pidcock, H. Prandke, H. Prandke, and M. C. Stinchcombe (2010), The supply of nutrients due to vertical turbulent mixing: A study at the Porcupine Abyssal Plain study site in the northeast Atlantic, *Deep Sea Res., Part II*, *57*(15), 1293–1302, doi:10.1016/j.dsr2.2010.01.006.

McGillicuddy, D., A. Robinson, D. Siegel, H. Jannasch, R. Johnson, T. Dickey, J. McNeil, A. Michaels, and A. Knap (1998), New evidence for the impact of mesoscale eddies on biogeochemical cycling in the Sargasso Sea, *Nature*, *394*, 263–266.

McGillicuddy, D., L. Anderson, S. Doney, and M. Maltrud (2003), Eddy-driven sources and sinks of nutrients in the upper ocean: Results from a 0.1 resolution model of the North Atlantic, *Global Biogeochem. Cycles*, *17*(2), 1035, doi:10.1029/2002GB001987.

Monin, A., and A. Obukhov (1954), Basic laws of turbulent mixing in the surface layer of the atmosphere, *Contrib. Geophys. Inst. Acad. Sci. USSR*, *151*, 163–187.

Nagai, T., H. Yamazaki, H. Nagashima, and L. Kantha (2005), Field and numerical study of entrainment laws for surface mixed layer, *Deep Sea Res., Part II*, *52*(9), 1109–1132, doi:10.1016/j.dsr2.2005.01.011.

Osborn, T. (1980), Estimates of the local rate of vertical diffusion from dissipation measurements, *J. Phys. Oceanogr.*, *10*(1), 83–89, doi:10.1175/1520-0485(1980)010<0083:EOTLRO>2.0.CO;2.

Oschlies, A. (2002a), Nutrient supply to the surface waters of the North Atlantic, *J. Geophys. Res.*, *107*(C5), 3046, doi:10.1029/2000JC000275.

Oschlies, A. (2002b), Can eddies make ocean deserts bloom?, *Global Biogeochem. Cycles*, *16*(4), 1106, doi:10.1029/2001GB001830.

Painter, S. C., R. E. Pidcock, and J. T. Allen (2010), A mesoscale eddy driving spatial and temporal heterogeneity in the productivity of the euphotic zone of the northeast Atlantic, *Deep Sea Res., Part II*, *57*(15), 1281–1292, doi:10.1016/j.dsr2.2010.01.005.

Painter, S., S. Henson, A. Forryan, S. Steigenberger, J. Klar, M. Stinchcombe, N. Rogan, A. Baker, E. P. Achterberg, and C. Moore (2014), An assessment of the vertical diffusive flux of iron and other nutrients to the surface waters of the subpolar North Atlantic Ocean, *Biogeosciences*, *11*, 2113–2130, doi:10.5194/bgd-10-18515-2013.

Pelegrí, J. L., A. Marrero-Díaz, and A. Ratsimandresy (2006), Nutrient irrigation of the North Atlantic, *Prog. Oceanogr.*, *70*(2), 366–406, doi:10.1016/j.pocean.2006.03.018.

Pollard, R. (1980), Properties of near-surface inertial oscillations, *J. Phys. Oceanogr.*, *10*(3), 385–398, doi:10.1175/1520-0485(1980)010<0385:PONSIO>2.0.CO;2.

Redfield, A. C. (1958), The biological control of chemical factors in the environment, *Am. Sci.*, *46*, 205–221.

Rippeth, T. P., M. R. Palmer, J. H. Simpson, N. R. Fisher, and J. Sharples (2005), Thermocline mixing in summer stratified continental shelf seas, *Geophys. Res. Lett.*, *32*, L05602, doi:10.1029/2004GL022104.

Rippeth, T. P., P. Wiles, M. R. Palmer, J. Sharples, and J. Tweddle (2009), The diapcynal nutrient flux and shear-induced diapcynal mixing in the seasonally stratified western Irish Sea, *Cont. Shelf Res.*, *29*(13), 1580–1587, doi:10.1016/j.csr.2009.04.009.

Sabine, C. L., R. A. Feely, N. Gruber, R. M. Key, K. Lee, J. L. Bullister, R. Wanninkhof, C. S. Wong, D. W. R. Wallace, and B. Tilbrook (2004), The oceanic sink for anthropogenic CO_2, *Science*, *305*(5682), 367–371, doi:10.1126/science.1097403.

Sharples, J., J. F. Tweddle, J. Mattias Green, M. R. Palmer, Y.-N. Kim, A. E. Hickman, P. M. Holligan, C. Moore, T. P. Rippeth, and J. H. Simpson (2007), Spring-neap modulation of internal tide mixing and vertical nitrate fluxes at a shelf edge in summer, *Limnol. Oceanogr.*, *52*(5), 1735–1747, doi:10.4319/lo.2007.52.5.1735.

Siegel, D. A., D. J. McGillicuddy, and E. A. Fields (1999), Mesoscale eddies, satellite altimetry, and new production in the Sargasso Sea, *J. Geophys. Res.*, *104*(C6), 13,359–13,379, doi:10.1029/1999JC900051.

Son, S., T. Platt, H. Bouman, D. Lee, and S. Sathyendranath (2006), Satellite observation of chlorophyll and nutrients increase induced by Typhoon Megi in Japan/East Sea, *Geophys. Res. Lett.*, *33*, L05607, doi:10.1029/2005GL025065.

Weisse, R., H. von Storch, and F. Feser (2005), Northeast Atlantic and North Sea storminess as simulated by a regional climate model during 1958–2001 and comparison with observations, *J. Clim.*, *18*(3), 465–479, doi:10.1175/JCLI-3281.1.

Williams, C., J. Sharples, C. Mahaffey, and T. Rippeth (2013), Wind-driven nutrient pulses to the subsurface chlorophyll maximum in seasonally stratified shelf seas, *Geophys. Res. Lett.*, *40*, 5467–5472, doi:10.1002/2013GL058171.

Williams, R. G., and M. J. Follows (2003), Physical transport of nutrients and the maintenance of biological production, in *Ocean Biogeochemistry: A JGOFS Synthesis*, edited by M. Fasham, 19–50, Springer, New York.

Williams, R. G., A. J. McLaren, and M. J. Follows (2000), Estimating the convective supply of nitrate and implied variability in export production over the North Atlantic, *Global Biogeochem. Cycles*, *14*(4), 1299–1313, doi:10.1029/2000GB001260.

Wu, Y., T. Platt, C. C. Tang, S. Sathyendranath, E. Devred, and S. Gu (2008), A summer phytoplankton bloom triggered by high wind events in the Labrador Sea, July 2006, *Geophys. Res. Lett.*, *35*, L10606, doi:10.1029/2008GL033561.